Sorbonne Université

Ecole doctorale 560 - StepUp

Laboratoire de Physique Nucléaire et des Hautes Energies / Groupe ATLAS

Recherche de particules de type axion à longue durée de vie dans l'expérience ATLAS et contribution au logiciel de réinterprétation MadAnalysis5.

Par Artur CORDEIRO OUDOT CHOI

Thèse de doctorat de Physique de l'Univers

Sous la direction du Pr. Bertrand Laforge

Présentée et soutenue publiquement le 30/09/2024

Devant un jury composé de :

SCOTTO-LAVINA Luca, Directeur de Recherche - Président du jury
DAMAZIO Denis, Senior Physicist – Rapporteur
MALCLÈS Julie, Directrice de Recherche - Rapporteuse
GEMME Claudia, Directrice de Recherche – Examinatrice
SALA Filippo, Assistant Professor – Examinateur
LAFORGE Bertrand, Professeur des Universités - Directeur de thèse

Searching for Axion-Like Long-Lived Particles at the ATLAS Experiment and a Contribution to the MadAnalysis5 Recasting Framework

Artur Cordeiro Oudot Choi

Acknowledgements

The work presented here was conducted at LPNHE over three years. It would not have been possible without the support of many people, to whom I am deeply grateful.

Firstly, I want to thank the people with whom I have worked. My supervisor, Bertrand Laforge, provided important scientific input and feedback throughout the different projects that allowed me to improve my knowledge of many aspects of our research field. Additionally, Benjamin Fuks and Mark Goodsell played a crucial guidance role in the final project of my work.

I would also like to thank many coworkers who played a role in the outcome of this thesis, including Yara do Amaral Coutinho, Edmar de Souza, José Ocariz, Romain Van Den Broucke, Mateus Hufnagel, Andre Malvezzi, Luiz Balabram, Giorgia Calì, Cristiano Sebastiani, and the A3LP team, Bogdan Malaescu, José Seixas, with Juan, PC, Eduardo, and so many more people from our Brazil-France Friday meetings, Giovanni Calderini, Francesco Crescioli, Paul Chabrillat, Šejla Hadžić, Francesco Guescini, and Yajun He. Their direct collaboration and expertise have been invaluable to me.

I would also like to express my gratitude to my jury members—Julie Malcles, Denis Damazio, Luca Scotto-Lavina, Filippo Sala, and Claudia Gemme—for agreeing to be part of my defense. I am especially thankful to Julie and Denis for taking the time to thoroughly review my dissertation and for providing valuable feedback.

I extend my thanks to the entire LPNHE community, which has created a great environment for me to develop my projects. I want to thank Sébastien Bongard and Matthew Charles for taking the time to help me with diverse matters. I would also like to thank the PhD students who made these years so enjoyable! While there are many names I could mention, I want to especially thank Enya, Tommaso, Paul, and Line. Also, I would like to greatly thank Anthony for that one time I could not produce a very specific plot!

I want to thank the Harmoniques Sphériques for organizing so many great musical events with many students!

My final thanks go to my family, who have always supported me, and to my friends. In particular, I want to thank Laura Michel for making my life better in every way.

Résumé Substantiel

La problématique de la matière noire a été découverte dans les années 70 et demeure aujourd'hui une question majeure de la physique contemporaine. En effet, si la relativité générale est une description exacte de la gravité, la matière noire représente environ 27% du contenu masse-énergétique de l'univers. De nombreuses observations et modèles cosmologiques, comme ΛCDM, établissent les propriétés de la matière noire nécessaires pour expliquer l'évolution de l'Univers et des grandes structures. Cependant, le modèle standard des particules élémentaires ne présente aucune particule (élémentaire ou composite) ayant ces propriétés. De nouvelles théories proposent diverses particules candidates telles que les particules massives faiblement interactives (WIMPs) et les particules de type axion (ALPs). Ces dernières peuvent être décrites dans le cadre des théories effectives des champs et peuvent présenter des durées de vie longues pour certaines combinaisons de masses, couplages et échelles d'énergie. Ceci donne lieu à des particules de longue durée de vie (LLPs) qui peuvent être interprétées comme médiateurs vers le secteur sombre et présentent de nouvelles opportunités expérimentales concernant leur observation. Malgré de nombreuses approches expérimentales — détection directe, indirecte et via des recherches en collisionneurs — aucune preuve directe de la matière noire à des échelles microscopiques n'a été obtenue à ce jour. Le travail réalisé pendant cette thèse se concentre sur la recherche d'ALPs en explorant des signatures expérimentales uniques liées aux longues durées de vie en développant de nouvelles méthodes d'analyse dans l'expérience ATLAS.

Les expériences au grand collisionneur d'hadrons (LHC), notamment à travers les détecteurs ATLAS et CMS, offrent des opportunités uniques d'explorer les signatures potentielles de la matière noire, y compris celles issues de couplages avec le boson de Higgs. Cependant, les signatures inhabituelles associées à ce type de recherches défient les algorithmes standards d'identification des particules. Cette thèse met en lumière l'importance de concevoir de nouveaux outils utilisant les informations bas niveau des sous-détecteurs d'ATLAS pour surmonter ces limitations, en particulier dans le cas des LLPs.

En effet, ATLAS peut être décomposé en 4 sous-détecteurs majeurs. Il s'agit, dans l'ordre croissant de distance par rapport au point de collisions des protons, du trajectographe, baignant dans un champ magnétique, qui permet de reconstruire la trajectoire des particules et d'en déduire leur charge et quantité de mouvement; du calorimètre électromagnétique (EM), qui permet l'absorption et la mesure de l'énergie des électrons, photons et composants EM des gerbes QCD; du calorimètre hadronique, qui absorbe et mesure l'énergie des hadrons stables; et du système muonique qui identifie les muons ayant traversé les premiers sous-détecteurs.

Les signatures investiguées dans cette thèse sont focalisées sur des ALPs à longues durées de vie (LL-ALP) se désintégrant en paire de photons à l'intérieur des calorimètres. Naturellement, les techniques d'identification de photons actuelles atteignent des efficacités de 0 lorsqu'on considère des productions de photons aussi éloignées du point de collision. Effectivement, ATLAS et ses méthodes d'analyse ont été développées pour des particules produites au point de collision. Les recherches de cette thèse ont alors mené à la création d'un nouveau groupe d'analyse ATLAS qui développe des techniques basées sur l'apprentissage automatique (ML) et des données calorimétriques bas niveau pour rechercher des LL-ALPs dans les données acquises par ATLAS pendant le Run 3 du LHC.

Les désintégrations possibles en paires de photons dans les calorimètres génèrent des formes de gerbes exotiques difficilement imitables par les processus standards. Cette thèse explore l'utilisation des variables Calorings pour pouvoir lire ces formes exotiques. Ces variables, initialement développées pour le système de déclenchement, permettent d'obtenir une description longitudinale et latérale des dépôts d'énergie dans les calorimètres plus générale que les variables standards. Elles peuvent alors devenir une base alternative pour identifier des paires de photons collimatés ainsi que reconstruire la position de désintégration d'ALP dans les calorimètres, ouvrant la voie à une régression des vertex secondaires pour les LLPs.

Le travail de cette thèse a également développé des extensions asymétriques des Calorings, nommés Quad-Rings, qui ont mené à l'observation d'une dépendance entre l'asymétrie du dépôt d'énergie causé par une gerbe de photons collimatés et la masse invariante du système. Ceci ouvre alors la possibilité de régression de masse de l'ALP dans le cas de photons collimatés, ce qui était une limitation majeure d'analyses précédentes. De plus, d'autres analyses ATLAS souffrent des difficultés de reconstruction de masse de photons collimatés comme la recherche de bosons de Higgs en di-photon où la réjection de π^0 est difficile.

Ces avancées techniques pour l'identification de photons permettent d'élargir les capacités de détection d'ATLAS vers les particules de longue durée de vie et vers les paires de photons collimatées. Ceci peut augmenter la sensibilité du détecteur dans l'espace des paramètres de divers modèles, incluant les ALPs où ATLAS pourrait alors combler des lacunes par rapport à d'autres expériences.

Par ailleurs, cette thèse a également contribué à la préparation d'ATLAS pour les conditions plus exigeantes de la phase haute luminosité de LHC prévue pour 2030 (HL-LHC). Notamment, un travail de qualification pour devenir auteur de la collaboration a été effectué sur le projet ITk (Inner Tracker) qui remplacera le trajectographe actuel. Ce sous-détecteur, composé de modules de pixels en silicium, est conçu pour résister aux radiations accrues et maintenir une reconstruction précise des trajectoires. Le travail de thèse s'est focalisé sur les campagnes de tests en faisceau menées en 2022 au CERN, et a permis de valider les capteurs atteignant des efficacités de détection supérieures à 98%. En outre, des investigations sur les résultats obtenus avec le nouveau logiciel de reconstruction ont été introduites pour garantir une cohérence méthodologique et une robustesse dans l'analyse des résultats. Ces améliorations sont essentielles pour garantir la qualité des données collectées au HL-LHC et maximiser l'efficacité des recherches sur la nouvelle physique, comme celles impliquant des LLPs.

Finalement, durant cette thèse un projet a été développé sur la réinterprétation d'analyses expérimentales (*recasting*). Le recasting joue un rôle clé pour évaluer la compatibilité des résultats expérimentaux existants avec de nouveaux modèles théoriques. Cette thèse a contribué à intégrer des fonctionnalités d'apprentissage automatique (ML) dans le cadre du logiciel de réinterprétation MadAnalysis5, grâce à l'utilisation de l'outil d'inférence ONNX. Cette intégration a permis de reproduire une analyse ATLAS axée sur la supersymétrie violant la parité R. Cette réalisation valide la possibilité de réinterpréter des analyses basées sur des modèles ML complexes, tout en soulignant l'importance des ressources auxiliaires détaillées pour garantir une inférence précise de ces derniers. Les conclusions de cette étude devraient inciter la collaboration ATLAS à standardiser la publication des outils ML et à améliorer la documentation de ses analyses, renforçant ainsi les capacités de recasting de la communauté phénoménologique.

Conclusion

Cette thèse illustre plusieurs approches pour repousser les limites des recherches sur la physique au-delà du modèle standard en développant de nouvelles techniques basées sur les Calorings pour les signatures LLPs, en contribuant au projet ITk pour améliorer la performance du détecteur ATLAS, et en intégrant des outils ML dans les cadres de réinterprétation de résultats. Ces contributions montrent comment les expériences du LHC comme ATLAS nécessitent constamment d'améliorations pour garantir qu'aucune nouvelle physique n'échappe aux analyses expérimentales passées et futures.

Abstract

If general relativity is a valid description of gravity, Dark Matter (DM) makes up about 27% of the universe's energy content, posing one of the most profound questions in modern physics. Numerous Beyond Standard Model (BSM) theories propose new particle candidates and mediators for dark matter, including weakly interacting particles (WIMPs) and axion-like particles (ALPs) as prominent examples that have possible masses spanning over 30 orders of magnitude. ALPs, usually described in the framework of effective field theories, could exhibit long lifetimes, leading to long-lived particles (LLPs) possibly acting as mediators to the dark sector. These LLPs could generate exotic signals in collider experiments like ATLAS and CMS, challenging conventional identification and reconstruction algorithms. This thesis focuses on developing novel calorimeter-based techniques to detect ALPs decaying into photon pairs within the ATLAS detector, addressing the unique challenges posed by displaced decay vertices to enhance the sensitivity of LLP searches.

In addition to the primary focus on dark matter and LLP searches, this work includes significant contributions to the MadAnalysis 5 (MA5) framework for reinterpreting ATLAS and CMS experimental results. The framework now supports efficient ML-based analysis recasting by integrating machine learning (ML) models through the ONNX inference software utility. This development facilitates the accurate reproduction and reinterpretation of complex analyses that use ML-driven event selection methods and ensures consistent performance across different environments. As a demonstration of this enhanced capability, an ATLAS search for R-parity violating Supersymmetry has been reproduced within MA5. This project exhibits possible progress in the way the LHC experiments publish auxiliary material used to allow easy reinterpretation and provide interesting legacy data for future LHC analyses recasting.

Furthermore, this thesis discusses the upgrades to ATLAS subsystems to prepare for the HL-LHC run and details the progress in pixel detector technology accomplished through the future Inner Tracker (ITk) test-beam campaigns conducted in 2022. These campaigns evaluated sensor performances, achieving detection efficiencies exceeding 98%. The insights gained were crucial in establishing better reconstruction software and workflows to guarantee consistency and robustness in the measured performances.

Overall, this thesis presents a comprehensive approach to advancing ALP research through new LLP detection techniques, enhanced recasting capabilities for ML-based analyses, and contributions to detector technology development.

Contents

Acknowledgements iii

Résumé Substantiel v

1 The open problem of Dark Matter 1
- 1.1 Introduction . . . 1
- 1.2 Experimental evidence for Dark Matter . . . 2
  - 1.2.1 Rotation Curves of Stars in Galaxies . . . 3
  - 1.2.2 Cosmic Microwave Background . . . 4
  - 1.2.3 Gravitational Lensing and the Bullet Cluster . . . 5
- 1.3 Why the Standard Model fails to explain Dark Matter. . . . 6
  - 1.3.1 Important Structures of the Standard Model . . . 6
  - 1.3.2 Field Theories and Symmetries . . . 8
  - 1.3.3 Electroweak Symmetry Breaking and the Higgs Mechanism . . . 9
  - 1.3.4 Effective Field Theory approach . . . 10
  - 1.3.5 Limitations in Explaining Dark Matter . . . 11
- 1.4 Invisible Matter or the need for a new theory of gravity ? . . . 11
  - 1.4.1 Post-Einsteinian gravitation possible models . . . 11
  - 1.4.2 Macroscopic Dark Matter candidates . . . 11
  - 1.4.3 Microscopic Dark Matter candidates . . . 12
- 1.5 Collider Searches for Dark Matter . . . 21
  - 1.5.1 Dark Matter Production Mechanisms . . . 21
  - 1.5.2 Search Strategies and Experimental Signatures . . . 22
  - 1.5.3 Current Results and Constraints . . . 23
  - 1.5.4 Prospects at the HL-LHC and beyond . . . 24
- 1.6 Mediator Searches at Colliders . . . 25
  - 1.6.1 Vector and Axial Mediators . . . 26
  - 1.6.2 Pseudo-Scalar Mediators . . . 28
- 1.7 ALP and long-lived particles . . . 29
  - 1.7.1 ALP motivations . . . 29
  - 1.7.2 Effective Field Theory of ALPs . . . 30
  - 1.7.3 Higgs sector . . . 31
  - 1.7.4 Long life times . . . 32
  - 1.7.5 LLP challenges at the LHC . . . 32
- 1.8 Summary . . . 33

2 The ATLAS detector and the tracker upgrade 35

2.1 The Large Hadron Collider . . . 35
2.2 The ATLAS detector . . . 36
2.2.1 The Tracking system . . . 38
2.2.2 The Calorimeter system . . . 40
2.2.3 The Muon detector . . . 45
2.2.4 Forward detectors . . . 45
2.2.5 Long-lived particles can decay in different sub-systems . . . 45
2.3 Data acquisition and analysis workflow . . . 46
2.3.1 Hardware-based and software triggers . . . 46
2.3.2 Reconstruction and analysis model . . . 46
2.3.3 Reconstructed objects . . . 48
2.4 ATLAS upgrades . . . 50
2.5 The High Luminosity phase of the LHC . . . 51
2.6 The need for a new tracker . . . 52
2.7 Silicon semiconductor detectors for ITk . . . 53
2.8 Pixel detectors . . . 54
2.9 The ITk layout . . . 55
2.10 Quad and Triplet modules . . . 57
2.11 Hybrid modules and readout . . . 57
2.12 Summary . . . 58

3 Contributions to the ITk project 61
3.1 Overview of hardware activities . . . 61
3.2 Production . . . 63
3.3 Modules Assembly . . . 64
3.3.1 Gluing . . . 64
3.3.2 Wire bonding . . . 64
3.4 Electrical tests . . . 65
3.4.1 I-V Curves . . . 65
3.4.2 SLDO qualification . . . 66
3.5 Pixel calibration . . . 67
3.5.1 Yarr tuning . . . 68
3.6 Testbeam characterization : . . . 70
3.6.1 Test beam facilities . . . 71
3.6.2 Test beam main activities of 2022 . . . 72
3.6.3 Challenges and opportunities . . . 73
3.7 Experimental setup at CERN: . . . 73
3.8 Testbeam data reconstruction . . . 76
3.8.1 Corryvreckan and data analysis workflow . . . 76
3.9 Results . . . 82
3.9.1 Single Chip Card . . . 82
3.9.2 Prototype Quad . . . 85
3.9.3 Pre-production Quad . . . 86
3.10 Conclusion . . . 87
3.A Data analysis consistency issues . . . 89
3.A.1 min_hits_on_track . . . 89

3.A.2 chi2ndof_cut . . . 89
3.A.3 Masking . . . 90
3.A.4 Other parameters . . . 92
3.A.5 A new workflow . . . 92
3.B Detection efficiency dependence on operating parameters . . . 94

4 ATLAS long-lived ALP search **97**
4.1 ALP at high energy colliders . . . 97
4.1.1 Production mechanisms . . . 97
4.1.2 Decay channels . . . 98
4.2 Photon Channel . . . 99
4.2.1 Two-Body Geometrical Distribution . . . 100
4.2.2 Challenges of a di-photon decay . . . 100
4.2.3 Challenges of a displaced di-photon decay . . . 101
4.2.4 Two strategies . . . 102
4.3 LLPs in ATLAS . . . 104
4.3.1 General LLP Signatures . . . 104
4.3.2 Decays in Calorimeters . . . 106
4.4 ALP phenomenology studies . . . 109
4.4.1 ALP decay in ATLAS . . . 109
4.4.2 Calorimeter geometries . . . 111
4.4.3 A new Python tool to predict ALP production . . . 114
4.4.4 Parameter-Space scan . . . 116
4.4.5 Compatible parameter-space . . . 118
4.4.6 Run3 expected number of events . . . 119
4.5 Full Simulation Datasets . . . 121
4.5.1 MonteCarlo simulations . . . 122
4.5.2 ATLAS data . . . 125
4.6 A3LP . . . 126
4.6.1 Analysis Strategy . . . 126
4.6.2 Jet based analysis . . . 127
4.7 Conclusion and prospects . . . 134
4.A Analysis of Parameter Choices . . . 135
4.A.1 Energy Scale Λ and Coupling $C_{\gamma\gamma}$ . . . 135

5 The Caloring approach **137**
5.1 Review on Jets and e/γ Showers in ATLAS . . . 137
5.1.1 Hadrons and e/γ interact through different forces . . . 138
5.1.2 Radiation and Interaction Lengths . . . 139
5.1.3 Electromagnetic and Hadronic Shower Development . . . 139
5.1.4 Reminder of Jet and e/γ Reconstruction . . . 140
5.1.5 ALP into Two Merged Photons Search . . . 140
5.2 Standard electron and photon identification . . . 140
5.2.1 Shower-Shape Variables . . . 141
5.2.2 Limits . . . 144
5.3 Caloring variables . . . 145
5.3.1 Ring construction procedure . . . 148

5.3.2 Electron identification at HLT . . . 149
5.4 Using rings for LL-ALPs . . . 151
5.4.1 Building jet rings . . . 151
5.4.2 QCD jets vs di-photons . . . 151
5.4.3 Decay length sensitivity . . . 155
5.4.4 Sensitivity to EM layers . . . 159
5.4.5 Extended barrel and end caps . . . 162
5.5 Asymmetric topologies . . . 163
5.6 Asymmetries in double showers . . . 165
5.6.1 Quad-Ring reliability . . . 167
5.6.2 Removing noise . . . 168
5.6.3 Asymmetry computation . . . 169
5.7 Results . . . 170
5.7.1 Asymmetry on event by event basis . . . 170
5.7.2 Jets and ALP discrepancies . . . 172
5.7.3 Limitations . . . 176
5.7.4 ML tool . . . 176
5.8 Conclusion and perspectives . . . 180

6 Recasting an ML-based SUSY search 183
6.1 Recasting Frameworks . . . 184
6.2 Developing ML capabilities in MadAnalysis5 . . . 187
6.2.1 ONNX . . . 187
6.2.2 ONNX Runtime . . . 188
6.2.3 Madanalysis SampleAnalyser . . . 189
6.2.4 Madanalysis packages . . . 189
6.3 Recasting an ML-based SUSY search . . . 191
6.3.1 R-parity and R-parity Violation . . . 192
6.3.2 Benchmark models . . . 192
6.4 Signal event generation . . . 194
6.5 NN discriminator . . . 196
6.6 Recasting Validation . . . 198
6.6.1 Sensitive steps . . . 198
6.6.2 Results . . . 202
6.7 Conclusion . . . 207

Bibliography 209

Chapter 1

The open problem of Dark Matter

1.1 Introduction

The existence and nature of Dark matter (DM) are major questions of modern Physics. This problem involves many fields, such as astrophysics, particle physics, and cosmology, connecting the universe's physics and microscopic physics. The possible existence of DM emerges from observations that cannot be explained by visible matter alone under the framework of general relativity as a description of gravity. The current understanding suggests that DM outweighs visible matter by about 5. More precisely, within the general relativity framework, the universe matter-energy content is only 5% ordinary matter and 26.8% dark matter [1] [2] [3]. This form of matter does not interact with the electromagnetic field, so it neither emits, absorbs, nor reflects light, making it invisible and detectable only through its gravitational effects. This is the reason for its substantive "dark". If general relativity holds, it is understood that the presence of dark matter is essential for explaining the formation and evolution of the universe and the origin of its current structures. [4] [5].

Experimentally, there are three primary methods to possibly detect dark matter at microscopic scales: direct detection, indirect detection, and collider searches. Direct detection aims to observe dark matter particles interacting with standard matter through rare scattering events. These searches mainly investigate atom or electronic recoils from DM scattering in ultra-sensitive experiments. Experiments like Xenon [6] or Darkside [7] are of interest. They are among the significant direct detection experiments utilizing two target atoms, xenon and argon. These experiments have excluded many ranges of mass and cross-sections of DM in the past years. Main direct DM search detectors plan upgrades to further investigate DM with a higher sensitivity that eventually reaches the neutrino floor (detailed in 1.4.3) when directionality becomes an essential experimental signature.

Other indirect techniques involving bolometers or silicon-based detectors, such as DAMIC [8], contribute to this research together with experiments searching for lighter DM such as helioscopes or Madmax [9]. Indirect detection searches for products of dark matter annihilation or decays into Standard Model (SM) particles under certain conditions. Mainly, searches for gamma rays are conducted in regions with high dark matter density, like the galactic center. Experiments like Nustar [10] search for X-ray decays

from low mass DM while BESS analyses anti-matter excesses in cosmic rays [11] to probe DM indirectly. Other experiments like HESS [12], CTA [13], and Fermi-LAT [14] are also of interest in this field.

Collider searches, such as those conducted at the Large Hadron Collider (LHC), look for dark matter particles produced in high-energy collisions, which would manifest as missing transverse energy in the detectors or particular signatures, as will be discussed in this thesis. At LHC experiments, this search type is also strongly motivated by the Higgs portal [15] to the dark sector through Higgs-DM couplings. Figure 1.1 illustrates these three different methods to exploit an interaction of DM with standard matter. All these searches are based on the hypothesis that the Dark sector and standard matter interact via another interaction than gravity.

No detection of DM at microscopic scales has been established yet. Consequently, direct, indirect, and collider searches provide more than 30 years of constraints on the many theoretical models proposed to give particle rationality to DM.

Although experiments have never observed DM, many astrophysical and cosmological observations provide reliable and convergent evidence of its existence. The results provided by such observations show that the crucial properties of DM can be understood. The primary experimental evidence of DM is presented in the following section.

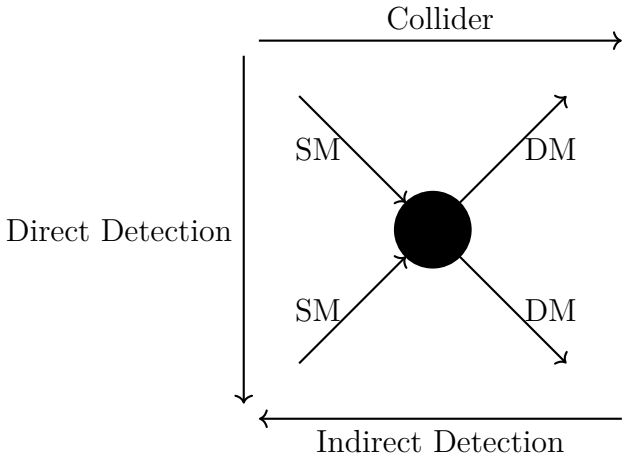


Figure 1.1: Schematic representation of dark matter detection methods at microscopic scales based on an unknown effective interaction of DM with standard model particles.

1.2 Experimental evidence for Dark Matter

The evidence for dark matter is robust and comes from various astrophysical and cosmological observations. One of the earliest and most convincing pieces of evidence comes from galactic rotation curves but was later completed by several phenomena that are coherently well described using the ΛCDM model [16].

1.2.1 Rotation Curves of Stars in Galaxies

Equation 1.1 shows the expected behavior of stars' rotation velocity as a function of their radial distance from the galactic center according to Newtonian mechanics. This Newtonian approach is a good approximation of general relativity at low gravity and low speeds compared to c. From the equation, two phenomena must be taken into account. The first concerns the radial mass term $M(r)$. Indeed, the mass amount between a given star and the galaxy center directly impacts its rotation velocity. This is because the centripetal and gravitational forces must compensate for the star to maintain its orbit. Thus, a greater gravitational pull yields a higher rotation velocity. This mass quantity increases with distance up to a specific radial limit (R) where most matter is confined. M(r) reflects this mass distribution model and is further subdivided into gas and stellar mass terms. The second phenomenon to consider is the decrease of gravitational attraction with distance at a pace $\frac{1}{r}$. When these two phenomena are taken into account, one expects the velocity to decrease as $\frac{1}{r}$ for $r > R$. Indeed, at these great distances, the mass term is considered constant. However, observations show that the velocity remains constant or even increases beyond R. These results imply the presence of more unseen mass and a mass density that should be non-negligible even for large distances $r > R$.

Figure 1.2 shows experimental measurements of stars' velocities concerning the radial distance to the galactic center of M33 [17]. This observation contradicts the expected $\frac{1}{r}$ velocity decrease at distances much more significant than the volume containing most visible matter.

$$v(r) = \sqrt{\frac{GM(r)}{r}}. \tag{1.1}$$

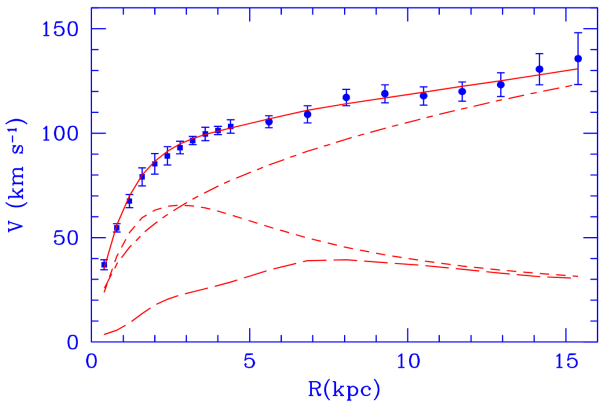


Figure 1.2: Evolution of experimental star rotation velocities as a function of the radial distance to the galactic center. Velocities are measured using the Doppler effect of the starlight in the galaxy. Large dashed lines represent the gas mass contribution. Short dashed lines are the stellar disk contribution. The fitted DM halo contribution is presented in dashed-dotted lines [17]

.

Rotation curves provide critical evidence for dark matter. These results imply that the galaxy mass distribution only differs from the visible matter distribution. The almost constant speeds at large r indicate that the unseen mass is distributed linearly to counter

the $\frac{1}{r}$ decrease. This suggests that the galaxy incorporates a dark matter halo that expands beyond usual matter.

1.2.2 Cosmic Microwave Background

The cosmic microwave background (CMB) radiation is a relic radiation signature of the universe structure 380,000 years after the Big Bang. Shortly after the Big Bang, the universe was dense enough that the temperature was above the binding energy of electrons and protons. In this period, no stable atom formation was possible, implying that photons could not travel freely. Matter and light were coupled. With the universe's expansion, temperatures cooled down, allowing electron and proton combinations into hydrogen atoms. This recombination instant marks the moment when matter and photons decouple, and the universe becomes transparent to light. With time and further temperature decreases, this initial emission of electromagnetic radiation was red-shifted to the microwave wavelength. Multiple CMB surveys were conducted to detect microwave radiation and sky maps of temperature fluctuations at recombination were produced (see figure 1.3). The high precision of these measurements allows for an exemplary description of the CMB map. The average temperature of CMB photons is of the order of $T = 2.7$ K while fluctuations can be seen to the 10^{-5} level [1].

The tiny fluctuations in the CMB's temperature correspond to density variations in the early universe, which, according to our understanding, grew into the large-scale structures observed today. Small density fluctuations are the seeds that enable matter agglomeration that finally forms these structures. Decomposing the temperature fluctuations into spherical harmonics yields the figure 1.4. This power spectrum can be fitted to the ΛCDM model [16], which describes, with a single energy-matter density content of the universe, the different data discussed in this chapter. This model includes cosmological parameters for dark energy, dark matter, baryonic matter, and space curvature that experimental results can constrain.

Detailed measurements of these fluctuations by experiments such as the Planck satellite have provided precise values for cosmological parameters, including the densities of dark matter and ordinary matter. The CMB data strongly supports the presence of dark matter. The ΛCDM model fits with a very high agreement with the experimental data points.
The resulting matter density([2], [3]) is :

$$\Omega_m h^2 = 0.1428 \pm 0.0011 \tag{1.2}$$

Where h is the Hubble constant. ΛCDM fits the CMB and also shows that the DM contribution to matter density is of the order of 86%.

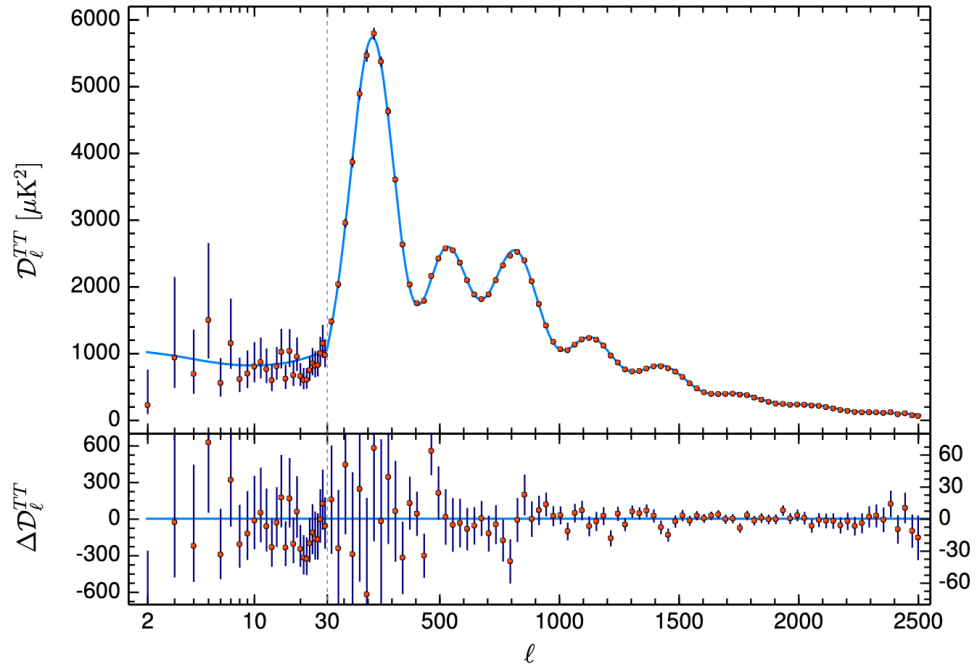


Figure 1.4: The temperature power spectrum of the CMB, with data points fitted by the ΛCDM model. From Placnk 2018 results [3].

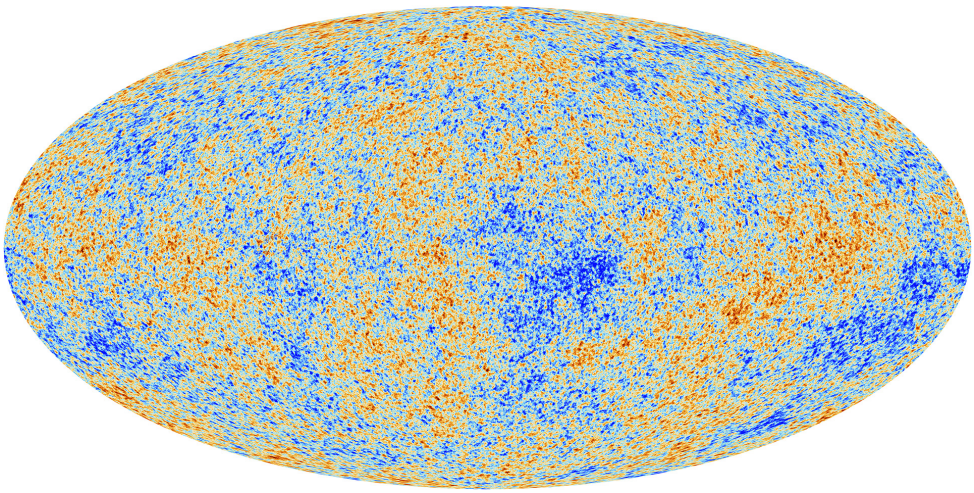


Figure 1.3: An intensity map of the CMB, showing temperature fluctuations. Maximun and minium flutiations are : -300μK (blue) + 300μK (red). Credit ESA and the Planck Collaboration.

1.2.3 Gravitational Lensing and the Bullet Cluster

The gravitational lensing effect provides another powerful tool to establish further evidence for dark matter. Massive objects like galaxy clusters bend the light path from background objects, creating distorted and magnified images. This effect allows us to map the mass distribution in these clusters. One of the most striking examples is the Bullet Cluster [18], where observations show a separation between the visible matter, pri-

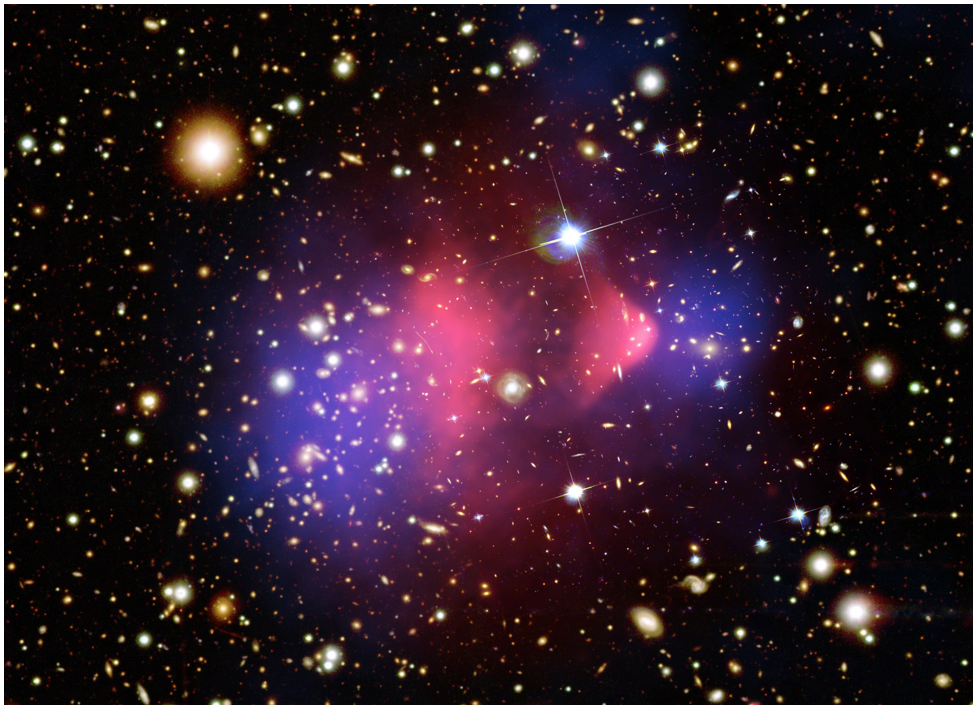


Figure 1.5: The Bullet Cluster: X-ray emission (pink) shows the hot gas, while gravitational lensing (blue) reveals the mass distribution, indicating a separation between visible and dark matter. [18].

marily in the form of hot gas, and the total mass inferred from lensing. This separation is a clear indication of dark matter, which interacts weakly with itself and ordinary matter, allowing the dark matter components of the colliding clusters to pass through each other largely unaffected.

1.3 Why the Standard Model fails to explain Dark Matter.

The Standard Model (SM) of particle physics is a remarkably successful theory that describes the known fundamental particles and their interactions, excluding gravity. However, despite its successes, the SM fails to provide a dark matter candidate. This section provides a brief reminder of critical points of the particle physics theoretical framework, the SM key components, and why it cannot explain DM, thereby motivating the search for new physics beyond the Standard Model (BSM).

1.3.1 Important Structures of the Standard Model

The SM comprises two main types of particles: fermions and bosons. They are categorized as matter components and interaction carrier particles. Fermions are further organized into three generations, while bosons are separated into vectorial gauge bosons mediating the fundamental forces and the Higgs boson, the only spin-0 particle in the SM.

Fermions Fermions are often called the "building blocks" of matter, consisting of quarks and leptons. Quarks come in six flavors (up, down, charm, strange, top, bottom) and experience electromagnetic, weak, and strong interactions, leading to confinement within protons, neutrons, and other hadrons. Leptons include electrons, muons, tau particles, and their associated neutrinos, which do not experience strong interactions.

Bosons Bosons are force carriers. The SM includes the photon (γ) for electromagnetism, the W and Z bosons for the weak force, the gluons (g) for the strong force, and the Higgs boson (h) responsible for the mass generation of both vector bosons and fermions through the Higgs mechanism.

Standard Model Spectrum These particles are presented as a table containing information on their mass, electrical charge, spin, and associated categories. Figure 1.6 depicts the SM table. One identifies a different organization in fermions concerning bosons, organized in three families of increasing masses. Figure 1.6 also highlights the possible interactions between a vector boson and fermions.

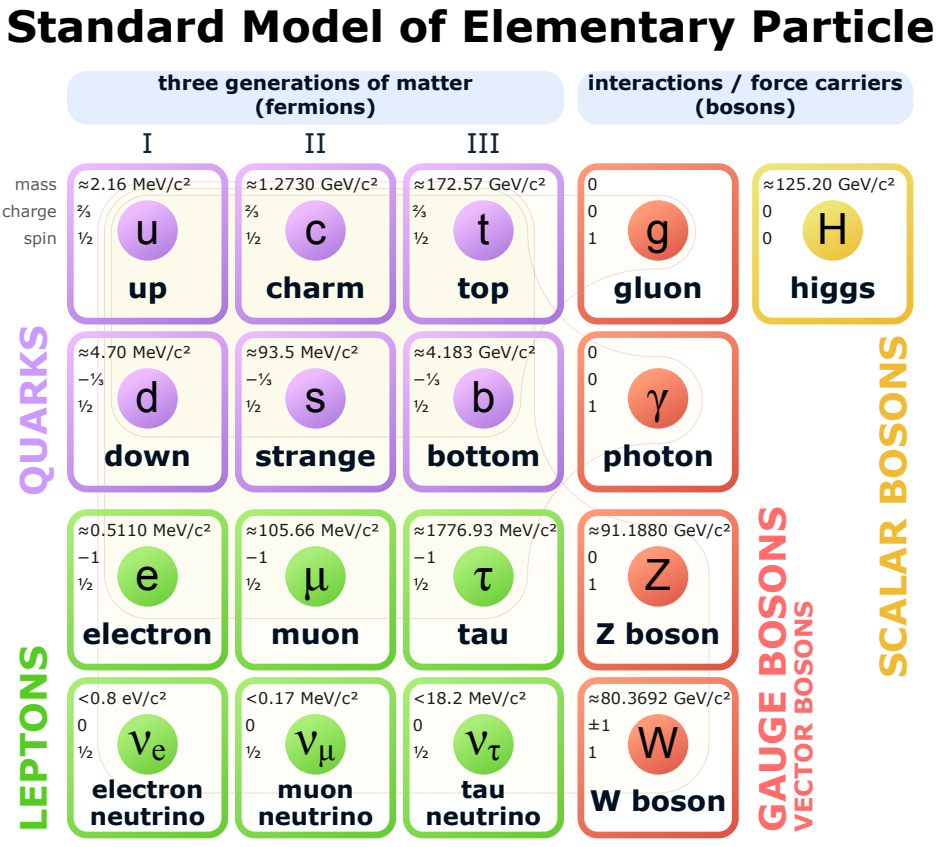


Figure 1.6: Standard model table presenting the full spectrum of established elementary particles [19].

To fully understand the particle spectrum, one must consider the anti-particles, which present quantum numbers opposite to their partners, such as the electric charge.

1.3.2 Field Theories and Symmetries

The Standard Model is a quantum field theory governed by the principles of gauge symmetry. The interactions between particles are described by the SM Lagrangian, which is invariant under the SM gauge group $SU(3)_C \times SU(2)_L \times U(1)_Y$. This symmetry group dictates elementary particles' allowable interactions, particle masses, and confinement properties.

The SM theory is written under the Lagrangian formalism. The fully developed Lagrangian is too long to be presented in this section. However, fundamental structures are given below.

Gauge Field Kinetic Terms

These terms describe the dynamics of the gauge fields associated with the fundamental interactions strong and electroweak (before electroweak is decoupled into weak and electromagnetic) :

$$\mathcal{L}_{\text{gauge}} = -\frac{1}{4} G^a_{\mu\nu} G^{\mu\nu a} - \frac{1}{4} W^i_{\mu\nu} W^{\mu\nu i} - \frac{1}{4} B_{\mu\nu} B^{\mu\nu}$$

where $G^a_{\mu\nu}$, $W^i_{\mu\nu}$, and $B_{\mu\nu}$ are the field strength tensors for $SU(3)_C, SU(2)_L, U(1)_Y$, respectively.

Covariant derivative and gauge invariance

Implementing a gauge invariance onto the Lagrangian is technically done using covariant derivatives. This derivative D_μ ensures the theory's stability and invariance under gauge transformation by incorporating gauge-related terms. The covariant derivative D_μ is defined for each type of gauge field by:

$$D_\mu = \partial_\mu - i g_s \frac{\lambda^a}{2} G^a_\mu - i g \frac{\tau^i}{2} W^i_\mu - i g' Y B_\mu$$

Fermion Kinetic Terms and gauge interactions

While the classical Lagrangian describes fermions free propagation with a ∂_μ derivative term, the SM Lagrangian describes their complex dynamics with D_μ as :

$$\mathcal{L}_{\text{fermion}} = \sum_\psi \bar{\psi} i \gamma^\mu D_\mu \psi$$

where ψ represents the fermion fields. Additionally, the presence of the covariant derivative in this term introduces interactions between the fermion fields and the different gauge fields. These interaction strengths are determined by a coupling associated with each gauge group.

Higgs Kinetic and Potential Terms

The Higgs field is a scalar field denoted as ϕ. These terms describe the dynamics of the Higgs field and its potential:

$$\mathcal{L}_{\text{Higgs}} = (D_\mu \phi)^\dagger (D_\mu \phi) - V(\phi)$$

with the potential $V(\phi)$ given by:

$$V(\phi) = \mu^2 \phi^\dagger \phi + \lambda (\phi^\dagger \phi)^2$$

Yukawa Interactions

The interactions between the Higgs field and the fermions named Yukawa interactions are imposed to the theory by the Higgs mechanism and generate the fermion masses. These interactions correspond to the following Lagrangian term :

$$\mathcal{L}_{\text{Yukawa}} = -\sum_f y_f \bar{\psi}_f \phi \psi_f$$

where y_f are the Yukawa couplings for each fermion and ψ_f are the different fermion fields.

1.3.3 Electroweak Symmetry Breaking and the Higgs Mechanism

The gauge group $SU(2)_L \times U(1)_Y$ allows the implementation of the electroweak force. The weak and electromagnetic interactions were united and driven by the associated massless gauge bosons in the early universe phase. The EM and weak couplings are equal at a given energy scale, which implies a unification of both interactions. In this electroweak phase, the Lagrangian remains symmetric under this group. However, the Higgs mechanism breaks this symmetry down to $U(1)_{em}$, giving rise to different gauge bosons: the massive W and Z bosons and the massless photon mediating the weak and electromagnetic interactions. This mechanism, known as Brout-Englert-Higgs [20], is achieved through the Higgs field acquiring a non-zero vacuum expectation value (VEV) for its potential.

Effectively, this breaking reorganizes the degrees of freedom of the gauge bosons but also generates mass terms for the fermions with the Yukawa interactions couplings. The gauge fields before and after electroweak symmetry breaking are reorganized as follows:

Gauge Fields Before Symmetry Breaking:

- W_μ^1, W_μ^2, W_μ^3 (from $SU(2)_L$) : gauge symmetry associated to fermionic left component
- B_μ (from $U(1)_Y$) : gauge symmetry associated to hypercharge conservation.

Gauge Fields After Symmetry Breaking:

- **Massive Gauge Bosons (Weak force mediators):**

$$W_\mu^\pm = \frac{1}{\sqrt{2}}(W_\mu^1 \mp iW_\mu^2) \tag{1.3}$$

$$Z_\mu = \cos\theta_W W_\mu^3 - \sin\theta_W B_\mu \tag{1.4}$$

- **Massless Gauge Boson (EM force mediator):**

$$A_\mu = \sin\theta_W W_\mu^3 + \cos\theta_W B_\mu \tag{1.5}$$

The gauge fields from $SU(2)_L$ and $U(1)_Y$ mix to form these physical gauge bosons after the Higgs mechanism breaks the symmetry, where θ_W is the weak mixing angle (Weinberg angle).

1.3.4 Effective Field Theory approach

From the first principles on the possible structures of the Lagrangian, an effective description of interactions can be achieved as an Effective Field Theory (EFT), which includes terms beyond the ones present in the SM. Such an approach provides a framework for describing interactions below a given energy scale where the dynamics of fields can be neglected. It is done by supposing contact interactions between particles without needing gauge boson mediators, which are supposed to have a mass larger than the energy scale of interest. This is represented in figure 1.7. This figure shows how a mediator propagation term in the gauge interaction model replaces a single coupling strength G describing a contact interaction. This G coupling is suppressed by the mediator mass square, allowing a perturbative approach where coefficients are universal and called Wilson coefficients.

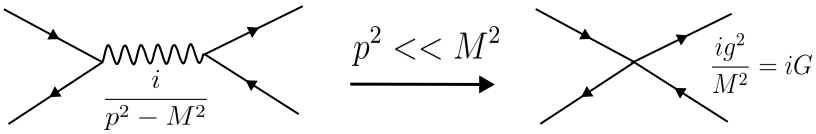


Figure 1.7: Illustration of EFTs replacing a mediator term by a point-like interaction.

As their name suggests, they are "effective" since their power to describe physics phenomena is limited to a maximum energy scale. One classic example is Fermi's theory of beta decay [21] at low energy, described by a four-fermion contact interaction:

$$\mathcal{L}_{\text{Fermi}} = -\frac{G_F}{\sqrt{2}}(\bar{\psi}_e\gamma^\mu\psi_\nu)(\bar{\psi}_p\gamma_\mu\psi_n), \tag{1.6}$$

Where G_F is the Fermi constant. This Lagrangian predicted and approximated the behavior of Neutron beta decay and was the first step toward the Weak force discovery. EFTs allow one to describe physics without needing the details of higher energy theories. This universal description enables the use of Wilson coefficient measurements as precision tests of the SM. Current experimental LHC results provide information on the lower limits of possible energy scales for new physics, including the dark matter sector.

1.3.5 Limitations in Explaining Dark Matter

Despite the comprehensive nature of the Standard Model, it does not account for dark matter, which constitutes about 27% of the universe's mass-energy content. The SM does not have a suitable DM candidate. Neutrinos have some of the right properties to be a dark matter candidate. It is electrically neutral, stable on cosmological timescales, and is not massless. However, they are too relativistic to explain large structure formation and fail to explain the measured DM density. A detailed list of DM candidate's properties is presented in the next section.

This significant limitation highlights the need for new physics. Various BSM theories and extensions, such as supersymmetry, extra dimensions, and the introduction of new particles like WIMPs (Weakly Interacting Massive Particles) and Axions, are being explored to address this open question and provide a viable candidate for dark matter.

1.4 Invisible Matter or the need for a new theory of gravity ?

This section provides a spectrum of theoretical proposals to solve the DM question, focusing on the particle-physics approach.
Indeed, an alternative to the dark matter hypothesis is the possibility that our understanding of gravity is incomplete. Modified gravity theories propose changes to general relativity to account for the observed phenomena without invoking dark matter. These theories include MOND (Modified Newtonian Dynamics) and TeVeS (Tensor-Vector-Scalar gravity), which modify the laws of gravity at large scales.

1.4.1 Post-Einsteinian gravitation possible models

Post-Einsteinian models seek to adjust general relativity to explain the galactic rotation curves and other observations. MOND, for example, modifies Newton's laws at low accelerations to reproduce the flat rotation curves of galaxies. TeVeS extends this by incorporating tensor, vector, and scalar fields to match a broader range of astrophysical phenomena. This approach will not be discussed further in this thesis, but references [22] [23] provide extra material. Nevertheless, such theories perform worse to answer DM as they fail to offer viable solutions simultaneously at multiple scales. In addition, some require a lot of fine-tuning, resulting in non-natural theories.

1.4.2 Macroscopic Dark Matter candidates

Macroscopic candidates for dark matter include MACHOs (Massive Compact Halo Objects) [24] such as brown dwarfs or neutron stars. These objects do not emit significant light and could account for some of the missing mass in galaxies. However, extensive searches have ruled mainly out MACHOs as the primary dark matter component due to their insufficient abundance. Primordial black holes (PBH) are a leading macroscopic candidate for the DM issue. Small PBHs that have not evaporated yet by Hawkings

radiation could contribute significantly to the universe's matter content. Recent searches heavily constrain the PBH hypothesis to the mass ranges of 10^5 to 10^{50} g. [25] [26]

1.4.3 Microscopic Dark Matter candidates

Many microscopic descriptions are hypothesized and matched with DM density observations by defining specific cosmological-scale production mechanisms to understand this new form of matter.

The main properties a microscopic DM candidate has to respect are the following :

- **Stability:** Dark matter must have a lifetime significantly longer than cosmological timescales.
- **Electric Charge:** The "darkness" of DM can be evaluated based on constraints from the Cosmic Microwave Background (CMB) and large-scale structures [27]. Charged or milli-charged DM would affect the baryon-photon plasma during recombination and suppress the DM density fluctuations. The found limits [28] require DM to a maximal charge of :
  - $3.5 \times 10^{-7} \left(\frac{m_{DM}}{1\,\mathrm{GeV}}\right)^{0.58}$ for $m_{DM} > 1\,\mathrm{GeV}$
  - $4.0 \times 10^{-7} \left(\frac{m_{DM}}{1\,\mathrm{GeV}}\right)^{0.35}$ for $m_{DM} < 1\,\mathrm{GeV}$
- **Lower Mass Limits:** Quantum effects set lower bounds on tiny DM masses. Pauli's exclusion principle limits the phase-space density for fermionic DM. Observations of velocity dispersion and physical density in dwarf galaxies provide a lower limit on fermionic DM masses, which is: $m_F > 70\,\mathrm{eV}$ [29].

  For bosonic DM, the Compton wavelength of ultra-light particles could erase small-scale structure, conflicting with CMB, large-scale structure data, Lyman-α observations, and High-redshift galaxy luminosity functions.
  These observations [30], impose a lower mass bound of: $m_B \gtrsim 10^{-22}\,\mathrm{eV}$.
- **Upper Mass Limits:** The stability against tidal disruption of structures within DM halos determines the upper mass limit for DM particles. Constraints are derived from analyzing wide halo binaries and the stability of star clusters. These limits indicate that a single, point-like DM constituent, if it constitutes 100% of the DM, should be lighter than approximately $5\,M_\odot$ [31].
- **Self-Interactions:** Observations of merging clusters and ellipticity of galaxies constrains DM-DM self-interactions. The key parameter is the ratio of the DM-DM cross-section to the DM mass:
  - $\sigma_{DM-DM}/m_{DM} < 0.47\,\mathrm{cm}^2/\mathrm{g} \approx 0.84\,\mathrm{barn/GeV}$ at 95% CL [32].

  However, self-interacting DM has been proposed to solve specific small-scale structure problems.

Many theories propose the existence of a single DM particle, while some hypothesize a full spectrum composed of multiple particles [33], making up the "dark sector."

Apart from having the correct DM particle-level properties, these different models must also find robust theoretical proposals for the DM particle production in the universe since the Big Bang. Several theories satisfy all these requirements in natural extensions of the SM.

Regarding thermodynamics, the microscopic DM candidates are categorized into three forms: cold, warm, and hot DM.

- **Cold Dark Matter**: Cold Dark Matter (CDM) refers to dark matter particles that are non-relativistic (*i.e.*, moving slowly compared to the speed of light) at the time of structure formation in the universe. This allows them to clump together under gravity and form the intermediate-scale structures we observe today, such as galaxies and clusters of galaxies. WIMPs (Weakly Interacting Massive Particles) are a primary example of CDM candidates. CDM models successfully explain the observed distribution of galaxies and the cosmic microwave background.

- **Warm Dark Matter**: Warm Dark Matter (WDM) particles are somewhat intermediate regarding velocity at the time of structure formation. They are relativistic at early times but become non-relativistic later. This results in a suppression of small-scale structure formation compared to CDM. Sterile neutrinos are often considered as WDM candidates. WDM can potentially resolve small-scale structure issues in CDM models, such as the missing satellites problem [34].

- **Hot Dark Matter**: Hot Dark Matter (HDM) particles are relativistic (*i. e.*, moving close to the speed of light) at the time of structure formation. Due to their high velocities, HDM particles do not clump together easily under gravity, leading to a smooth distribution of matter. Neutrinos are an example of HDM candidates. HDM is not favored as the primary form of dark matter because it cannot explain the observed structures in the universe by itself.

The leading candidates for dark matter are microscopic particles predicted by extensions of the Standard Model. These include WIMPs, sterile neutrinos, and axions.

The WIMP miracle

Weakly Interacting Massive Particles (WIMPs) are a popular dark matter candidate. As the name suggests, these particles could provide the relic DM density with masses and cross-sections around the EW scale. Thus, it represents a significant contribution to the mass content of the universe while interacting very weakly with the rest of matter. They are hypothesized to have masses between a few GeV and several TeV to be stable.

Furthermore, if WIMPs were produced in the early universe, among the other SM particles, they would be expected to freeze to a given relic density due to the universe's expansion. It was understood that WIMPs' relic density would match the DM's measure densities. This is called the WIMP miracle and greatly motivates WIMP searches.

More precisely, WIMPs are expected to have been in thermal equilibrium with ordinary matter in the early universe. This means that at this stage, the rate of WIMP production is the same as the rate of WIMP annihilation. Thus, the WIMP abundance remains constant. The thermal production of WIMPs is possible through collisions of SM particles; indeed, when the universe temperature is higher than the WIMP mass, such processes are possible. The annihilation of WIMPs, on the other hand, does not depend on the universe's temperature; it only requires two WIMPs to be close enough to interact. However, these rates can evolve during the universe's evolution, thus breaking the thermal equilibrium and changing the abundance of WIMPs. As the universe expanded and cooled down, WIMPs left the thermal equilibrium until reaching a relic density. In fact, at a threshold of temperature of $T < m_\chi$ (χ being the WIMP), the production of WIMPs starts dropping since the collision energy of SM particles is not enough to produce them. When temperatures further cool down and become significantly lower than m_χ, the production processes do not occur. At this point, the number density of WIMPs can only decrease through annihilation processes.
However, the expansion rate should impact the WIMP annihilation rate. With an expanding universe, the probability of interaction between WIMPs decreases. Therefore, the annihilation also decreases. At a given time, the expansion effect becomes significantly higher than the annihilation rate; thus, no more annihilation processes occur. This renders a constant relic density of WIMPs since they cannot be produced thermally, nor can they annihilate due to the universe's expansion.

This relic density can reach different values depending on the cross-section of annihilation processes. Looking at figure 1.8, the multiple phases of the freeze-out mechanisms can be identified, and the achieved relic densities seem to differ depending on the order of cross-section. In this plot, the x-axis represents the ratio of mass to temperature and starts at a moment where $T = m_\chi$. As explained, the abundance remains constant before this moment and then starts decreasing due to a lower production rate. This decrease is visible in the middle part of the plot. But at around x=[20-50], the annihilation processes are suppressed due to the expansion that reduces the volume density of WIMPs. The resulting relic density stabilizes between x=[50-1000], and stronger interactions yield lower frozen abundances. If the interactions are strong, the decreasing phase due to annihilation will significantly reduce the final number of WIMPs compared to weak interactions. Furthermore, if those cross-sections are of the order of the Weak force, one finds that the final WIMP relic abundance matches what is expected to explain the DM density in the universe.

Additionally, theories such as supersymmetry (SUSY) [36], motivated by many different open questions of physics, predict the existence of a WIMP candidate when R-parity is conserved. The neutralino lightest χ^0 is a prime WIMP candidate investigated at the LHC in SUSY processes searches. Constraints from ATLAS and CMS exclude SUSY particle masses below a few hundred GeV [37].

Direct experiments fail to probe WIMPs and exclude significant ranges of WIMP masses and cross-section interaction with ordinary matter. Figure 1.9 shows how DM detectors have excluded large regions of the parameter space. In the future, more sensitive

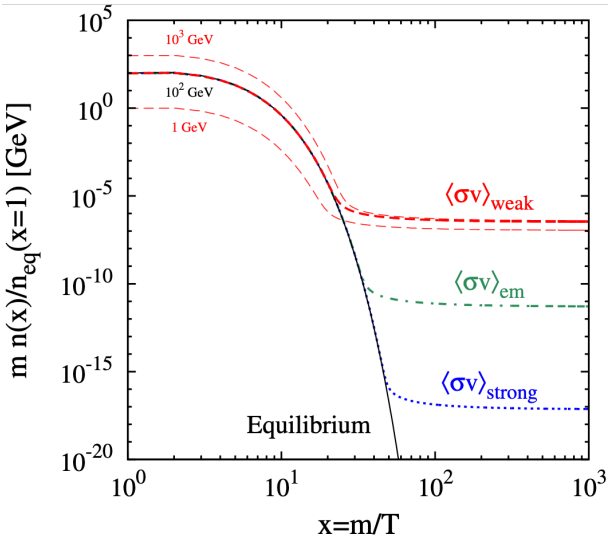


Figure 1.8: Evolution of WIMP abundance for different choices of annihilation cross section σv [35]. The number of WIMPs normalizes the abundance during the equilibrium phase. Three different final abundances depend on σv, with v being the velocity of particles. This is used instead of σ as it represents an interaction rate for a volume unit.

detectors will be able to dig the remaining regions to a fraction of GeV. However, at a low enough cross-section, the WIMPs that such detectors can probe cannot be discriminated from the expected neutrino scattering predicted by the SM. Collider experiments can also constrain DM(WIMP)-Nucleon interactions cross-sections, as seen in a later section's figure 1.13 of a later section.

The lack of evidence of WIMPs, as predicted by the WIMP miracle, has called for alternative theories. These new DM WIMP variations include non-thermal production models, where freeze-out production of a relic density is taken out [38] and other freeze-in models such as FIMP (Feabily Interacting Massive Particles) [39].

In contrast to the freeze-out mechanism, the freeze-in mechanism involves the gradual production of dark matter particles over cosmic time through out-of-equilibrium processes. In the freeze-in scenario, dark matter particles are produced slowly and never reach thermal equilibrium with the standard model particles. Instead, their abundance increases over time due to rare decays and collisions of SM particles in the early universe.

The freeze-in dark matter production rate is proportional to the associated cross-section and the Hubble expansion rate. These particles are typically much more weakly interacting than WIMPs, meaning they can evade the constraints from direct detection experiments designed to detect more strongly interacting particles. Thus explaining the passage of WIMPs to FIMPs models.

Other than FIMPs, an example of a freeze-in dark matter candidate is the Gravitino [40]. Gravitinos, which are supersymmetric partners of the graviton, can be produced via decay processes involving a Planck-suppressed coupling. This leads to the accumulation of Gravitinos over time without them ever coming into thermal equilibrium with other

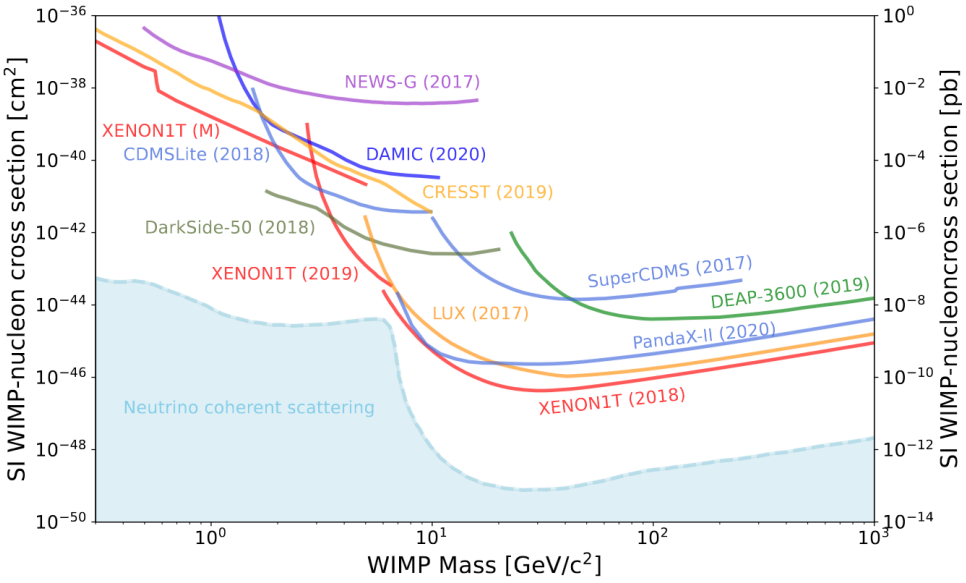


Figure 1.9: Overview of WIMP searches at direct detection experiments. From [41]

particles in the universe.

In summary, while the freeze-out mechanism relies on dark matter particles being in thermal equilibrium and then decoupling as the universe cools, the freeze-in mechanism depends on the gradual production of dark matter particles through very weak interactions that accumulate over time. This latter theory offers an alternative explanation for the observed relic density of dark matter, especially in cases where direct detection of WIMPs has failed to provide evidence of their actual existence.

Sterile neutrinos

Sterile neutrinos are another compelling candidate for dark matter [42]. Unlike regular (active) neutrinos, which interact via the weak nuclear force and can be detected through their weak interactions, sterile neutrinos do not interact through any of the Standard Model forces except gravity. This makes them exceedingly difficult to detect directly with current technologies, as they are essentially invisible to the detectors.

The concept of sterile neutrinos extends the SM by introducing right-handed neutrinos, which do not participate in weak interactions. These sterile neutrinos can mix with the active neutrinos, leading to a variety of potential astrophysical and cosmological signatures.

In the early universe, sterile neutrinos could be produced through oscillations with active neutrinos. The production rate of sterile neutrinos is highly sensitive to their mixing angle with active neutrinos and their square mass difference [43].

Sterile neutrinos can exist in a wide range of masses and are generally categorized as:

- **light sterile neutrinos** with masses around the eV scale could potentially explain anomalies in neutrino experiments [43] with sterile-active neutrino mixing. However, their contribution to the overall dark matter density would be minimal.

- **Intermediate-mass sterile neutrinos** with masses in the keV range are particularly interesting as they could serve as a warm dark matter candidate. They can influence the formation of structures in the universe, such as dwarf galaxies, and leave imprints on the cosmic microwave background and large-scale structure [44] [45] [46].

- **Heavy sterile neutrinos** with higher masses are also considered. These particles could be DM candidates with a significant contribution to DM density. Intermediate and high-mass sterile neutrinos could decay into SM particles via active neutrino mixing, potentially producing detectable signals in the form of X-rays or other radiations [47].

Several experimental and observational efforts have been, and are still, made to detect sterile neutrinos indirectly using different probes :

- **X-ray observations**: If sterile neutrinos have high enough masses, their decay could produce X-rays. Observatories like Chandra have conducted searches for such signals, looking for unexplained X-ray lines in astrophysical sources [48].

- **CMB and Large-Scale Structure (LSS)**: Precision measurements of the CMB by Planck and observations of the LSS provide constraints on the properties of sterile neutrinos.

- **Laboratory experiments**: Experiments such as KATRIN (Karlsruhe Tritium Neutrino Experiment) [49] and future projects aim to detect the effects of sterile neutrinos on beta decay spectra or through other indirect methods [43].

Despite the lack of direct detection, the theoretical framework for sterile neutrinos remains robust; the relevant bounds can be found in [50]. Sterile neutrinos provide a solution to several problems in particle physics and cosmology, including the observed neutrino masses and mixings, and the nature of dark matter. The search for sterile neutrinos continues to be an important area of DM research.

Axions

Axions are another class of compelling dark matter candidates. These particles are neutral pseudo-scalar and can arise from the breaking of any new U(1) symmetries added to the SM as pseudo-nambu-glodstone-bosons. They show straightforward cosmological production mechanisms enhancing their "naturalness" as a BSM theory.

The strong CP problem Axions were originally proposed to solve the strong CP problem in quantum chromodynamics (QCD) [51]. The strong CP problem arises from the fact that the QCD Lagrangian can include a term that violates CP symmetry. When expanding the QCD Lagrangian, one finds the kinetic terms of the quark and gauge fields, the quark mass term, and an extra CP-violating term known as the θ-term, shown below:

$$\mathcal{L} = \theta \frac{1}{16\pi^2} G^a_{\mu\nu} \tilde{G}^{\mu\nu a} \tag{1.7}$$

The intensity of this CP-violating term is dictated by its pre-factor θ angle. This angle can essentially have a value between 0 and 2π, as there is no theoretical constraint. However, experimentally, no such violation is observed, with the CP-violating parameter θ being constrained to be extremely small ($|\theta| < 10^{-11}$) [52]. This small value appears unnatural and suggests the need for an additional mechanism to explain it.

The θ parameter is then introduced as related to the vacuum expectation value of the axion field protected by a new global U(1) symmetry, known as the Peccei-Quinn (PQ) symmetry [51]. When the PQ symmetry is spontaneously broken at a high energy scale, it gives rise to a pseudo-Nambu-Goldstone boson, which is the axion particle.

The axion field, a, dynamically adjusts the value of the θ parameter to effectively zero, thus solving the strong CP problem. The following Lagrangian describes the axion's interaction with gluons:

$$\mathcal{L}_{\text{axion-gluon}} = \frac{a}{f_a} \frac{1}{16\pi^2} G^a_{\mu\nu} \tilde{G}^{\mu\nu a} \tag{1.8}$$

where f_a is linked to the vacuum expectation value energy that breaks the PQ symmetry. Effectively, as one can see in the above equation, the axion field a raises the θ parameter to the rank of field. This field adjusts to minimize the potential energy of the system driving the θ parameter to 0.

Axion production as Dark Matter Due to their mass and extremely weak interactions with ordinary matter, axions are great DM candidates. Axions could have been produced in the early universe through various mechanisms, both thermal and non-thermal. All following mechanisms are detailed in [53], a review of the axion creation mechanism. The most well-studied non-thermal production mechanism is the so-called misalignment mechanism [53], where the axion field starts with a random initial value and, as the universe cools, begins to oscillate around the minimum of its potential, contributing to the cold dark matter density.

In addition, the breaking of the Peccei-Quinn symmetry can lead to the formation of topological defects, such as cosmic strings and domain walls [54], which can emit axions during their evolution, further changing the number density of axions in the universe. Depending on whether the PQ symmetry breaks before or after inflation, the cosmological implications and resulting axion abundance vary significantly.

In the pre-inflation scenario, the universe is homogeneous with a uniform misalignment angle, whereas, in the post-inflation scenario, the axion field takes different values in causally disconnected regions, leading to a more complex density distribution.

Thermal production mechanisms also play a role, where axions are produced in thermal equilibrium with the primordial plasma, though this typically results in hot or warm dark matter contributions. Overall, these production mechanisms ensure that axions remain a viable and natural candidate for dark matter, with ongoing experiments aiming to detect their presence through various astrophysical and laboratory searches.

Furthermore, axion-like particles (ALPs), which are similar to axions but not necessarily tied to the solution of the strong CP problem, also emerge in various extensions of the Standard Model. ALPs (deeper described in 1.7) can be seen as a generalization of the QCD Axion. One can expand the model building of Axions and replace the PQ symmetry with other U(1) symmetries. This yields ALPs that share very similar features with the original axion without a necessary bond to the strong CP problem. This allows for further phenomenologies to be probed as well as a much wider parameter space to explore with masses ranging from 10^{-12} to 10^{10} eV.

Experimental searches for axions and ALPs The axion can decay into photons through QCD loops, where quarks radiate electromagnetically. Such processes allow for many laboratory and astrophysical searches.

Various experiments and observations highly constrain the mass of axions and ALPs, and their interactions intensity:

- **Haloscopes**: These detectors aim to detect axions from the galactic halo by converting them into microwave photons in a strong magnetic field, such as in the ADMX experiment [55] and MADMAX [9]. The benefit of haloscopes is their sensitivity to dark matter axions that are believed to make up the local dark matter density, allowing direct detection of dark matter axions present in our galaxy.

- **Axion Helioscopes**: These instruments look for axions produced in the Sun, which would convert to X-rays in a magnetic field, as seen in the CAST experiment [56]. Helioscopes benefit from the relatively high flux of solar axions, providing a continuous and predictable source of axions for detection, thus allowing the study of axion interactions with solar matter. A future international axion observatory using such techniques is currently under study [57].

- **Laboratory Experiments**: Light-shining-through-wall experiments attempt to produce and detect axions in the lab by converting photons to axions and back again to photons. These experiments benefit from being able to control experimental conditions precisely and test theoretical predictions about axion properties in a controlled environment without relying on astrophysical sources.
  Additionally, light-by-light scattering phenomena can include an axion contribution and are investigated using high-power laser pulses or in e^+e^- particle collisions [58] [59].

- **Other indirect observation**: Polarisation measurements of photons in neutron stars can also probe axions. The axion-photon resonant conversions in the magnetic field of neutron stars can modify photons' polarisation. If a magnetosphere exists, plasma in this region can enhance this effect significantly. [60]

Figure 1.10 shows current boundaries on ALP masses and photon coupling through different experiments.

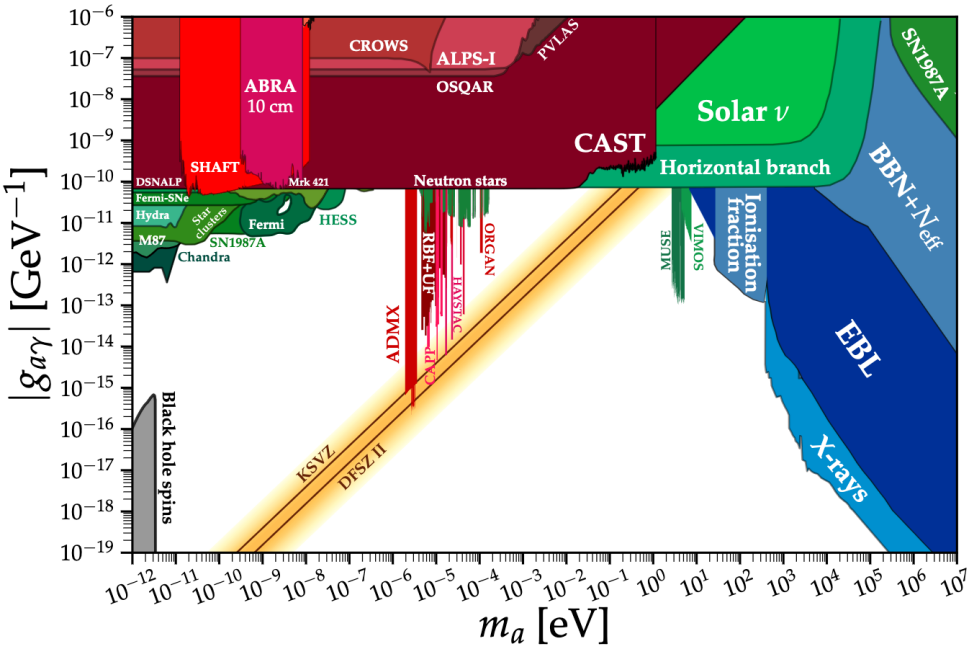


Figure 1.10: ALP parameter space with current experimental constraints [61].

Additionally, other models allow for dark matter portal research at colliders using pseudo-scalar mediators like the ALP [62] [63]. Further motivating ALP searches in the context of Dark Matter.

In conclusion, axions provide an elegant and natural solution to the strong CP problem and are compelling candidates for dark matter. The introduction of the PQ symmetry and axions is considered a natural solution to the strong CP problem because it explains the smallness of θ without requiring fine-tuning. The Axion and ALP fields are driving a significant portion of current experimental and theoretical research in particle physics and cosmology.

Other Models

Beyond the presented, well-known models of WIMPs, sterile neutrinos, and axions, there are many other intriguing dark matter models. The two other principal interesting theories that will not be explained in detail include **Multi-Component Dark Matter** and **Dark Photons**.

Multi-Component Dark Matter proposes that dark matter may consist of a complex hidden sector [33] with its particles and forces analogous to the visible sector. These models often include additional particles and mediators that can have different spin properties, such as (pseudo-)scalars and vector mediators, which can interact weakly with the standard model particles through various portals, providing novel detection opportunities.

Dark Photons are hypothetical light vector bosons that can mix kinetically with regular photons. These dark photons could be produced in the early universe and might be stable over cosmological timescales. They can convert into photons in the presence of a magnetic field, and their parameter space is constrained by a combination of astrophysical

observations and laboratory experiments [64].

These models expand the range of potential dark matter candidates and provide new avenues for experimental searches.

1.5 Collider Searches for Dark Matter

Collider experiments, particularly those conducted at the Large Hadron Collider (LHC), play a crucial role in the search for dark matter. These searches are based on the hypothesis that dark matter particles can be produced in high-energy collisions similar to those that occurred in the early universe. If dark matter particles are produced at colliders, they would typically manifest as missing transverse energy (E_T^{miss}) in the detectors since they would not interact with the detector material.

Recent searches by the CMS and ATLAS collaborations have focused on proton-proton collisions at a center-of-mass energy of 13 TeV. These searches look notably for an imbalance in transverse momentum, indicative of undetectable dark matter particles produced alongside Standard Model particles. No significant deviations from SM predictions have been observed, but these searches have set important limits on the couplings and masses of dark matter particles and associated mediators. Unfortunately, these searches are very model-dependent in opposition to direct detection.

1.5.1 Dark Matter Production Mechanisms

Dark matter particles can be produced in a variety of processes at colliders. The main DM searches in ATLAS consider a production through the Higgs portal or postulate the existence of a (axial-)vector boson mediator denoted Z'. The mediator approach is a "simplified-model" interpretation of DM [65] allowing to define benchmark signals at the LHC. To avoid having very oriented analysis strategies that depend heavily on a specific model, it is optimal to look for general model-independent signals. This maximizes the potential for reinterpretation and the potential of constraining general DM descriptions.

The most common production mechanisms include:

- **Direct Pair Production**: Dark matter particles can be produced directly in pairs through processes such as gluon fusion ($gg \to \chi\chi$) or quark-antiquark annihilation ($q\bar{q} \to \chi\chi$). These processes often result in events with significant missing energy (E_T^{miss}) as the dark matter particles escape the detector. However, this production is difficult to capture due to the lack of hard SM particles used for selecting events.

- **Associated Production**: Dark matter particles can be produced alongside other SM particles. For example, a dark matter particle pair can be produced in association with a jet ($q\bar{q} \to \chi\chi + j$), a photon ($q\bar{q} \to \chi\chi + \gamma$) or a Higgs boson ($q\bar{q} \to \chi\chi + h$). The associated standard particles provide a visible signature that can be used to infer the presence of dark matter particles. Figure 1.11 illustrates two of these possible production processes.

- **Higgs Portal**: In models where dark matter particles interact with the Higgs, the boson can decay into a pair of dark matter particles ($h \to \chi\chi$). These events are

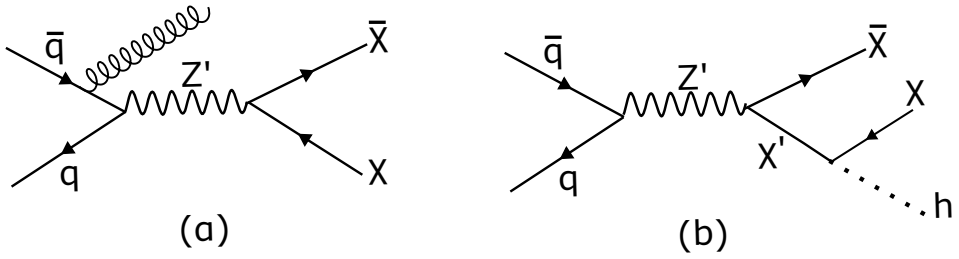


Figure 1.11: Feynman diagrams of DM pair production at the LHC with the emission of an associated SM particle. Z' is a massive vectorial mediator linking the SM to the dark sector. X' represents an excited state of the DM particle. (a) represents mono-jet + E_T^{miss} events and (b) illustrates possible mono-Higgs +E_T^{miss} events

referred to as Higgs to invisible since the DM escapes the detector. The Higgs portal mechanism is particularly interesting because it connects dark matter searches with the Higgs boson properties, providing a complementary probe to Higgs physics.

1.5.2 Search Strategies and Experimental Signatures

As mentioned, searches for DM particle candidates at colliders focus on identifying events with large missing transverse energy accompanied by other visible particles. Possible DM mediators are searched using different signatures that are covered lower in the Chapter. The key strategies and signatures include:

- **Mono-X Searches**:
  These searches look for events with a single high-energy SM particle (X) recoiling against missing transverse energy formed by elusive DM particles. The main searches include mono-jet, mono-photon, mono-Higgs, and mono-Z searches. [66]

  - Mono-jet searches ($pp \to \chi\chi + j$) are among the most sensitive due to the high production cross-section of jets at the LHC. The signature is a high-energy jet plus significant E_T^{miss}. These searches are the main mono-X search but offer a low signal over background ratio. [67] [68]
  - Mono-photon searches [69] are challenged by the probability of emitting a photon from initial state radiation (ISR) is less important than in mono-jet searches. However, the ID of photons through shower-shapes is used to strongly reject the QCD background. Overall yielding a better signal over background ratio. In mono-photon searches, the main background includes $Z \to \nu\nu + \gamma$ and $W \to \ell\nu + \gamma$ processes, as well as single electrons or jets reconstructed as photons.
  - Mono-Z searches focus on events with two opposite-sign leptons with invariant mass compatible with the Z boson and large E_T^{miss}. Backgrounds are estimated using control regions with tightly or loosely identified lepton pairs. These

lepton constraints significantly improve the background rejection. However, the cross sections remain small for this type of process [70]. Other Z decay processes are also investigated, such as hadronic decays [71]

– Mono-Higgs searches are similar to mono-Z but exploit the possible Higgs decay channels to better reject background. Higgs interactions with light quarks are very weak; the sensitivity is dominated by $h \to bb$ [72] and $h \to \gamma\gamma$ [73]. By selecting photon decay, channel cuts can be implemented on the two photons' invariant mass. This greatly reduces the background impact on the search.

- **Invisible Higgs Decays**:
  In Higgs portal models, the Higgs boson can decay into dark matter particles, resulting in invisible decays. These decays can be inferred from the missing energy balance in events where the Higgs is produced alongside other visible particles. Searches for invisible Higgs decays complement other analyses and provide constraints on the Higgs-dark matter coupling.

- **Multijet + E_T^{miss} Signatures**:
  Some dark matter models predict events with multiple jets and missing transverse energy. These signatures are challenging due to the large backgrounds from SM processes but can be very powerful with advanced analysis techniques. Multijet + E_T^{miss} searches probe scenarios with strong interaction between dark matter and quarks/gluons, offering complementary information to mono-jet searches. DM production in association with a $t\bar{t}$ pair is a very interesting channel in such signatures. [74]

1.5.3 Current Results and Constraints

The LHC experiments, ATLAS and CMS, have conducted extensive searches for dark matter particles using the above-mentioned strategies [75]. These searches have placed parameter-space limits on various dark matter models.

- **Mono-X constraints**:
  ATLAS and CMS Mono-X searches set limits on the production cross-section and masses of DM particles and mediators, as represented in figure 1.12. For example, mono-jet searches have excluded dark matter-nucleon cross-sections down to the level of direct detection experiments for certain mass ranges, as presented in figure 1.13. Mono-Z searches have set limits on the production of vector and axial-vector mediators, excluding mediator masses up to 680 GeV and dark matter particle masses up to 250 GeV (for the vector-mediator interpretation) [70].

- **Invisible Higgs constraints**:
  The combination of Higgs measurements and searches for invisible decays has constrained the branching ratio of the Higgs to invisible particles. ATLAS run 2 searches have set an upper limit on the investigated branching ratio, $Br_{h\to inv} < 0.145$ [76]. This value remains within a 1σ range of the expected SM limit; thus, it does not exclude SM predictions.

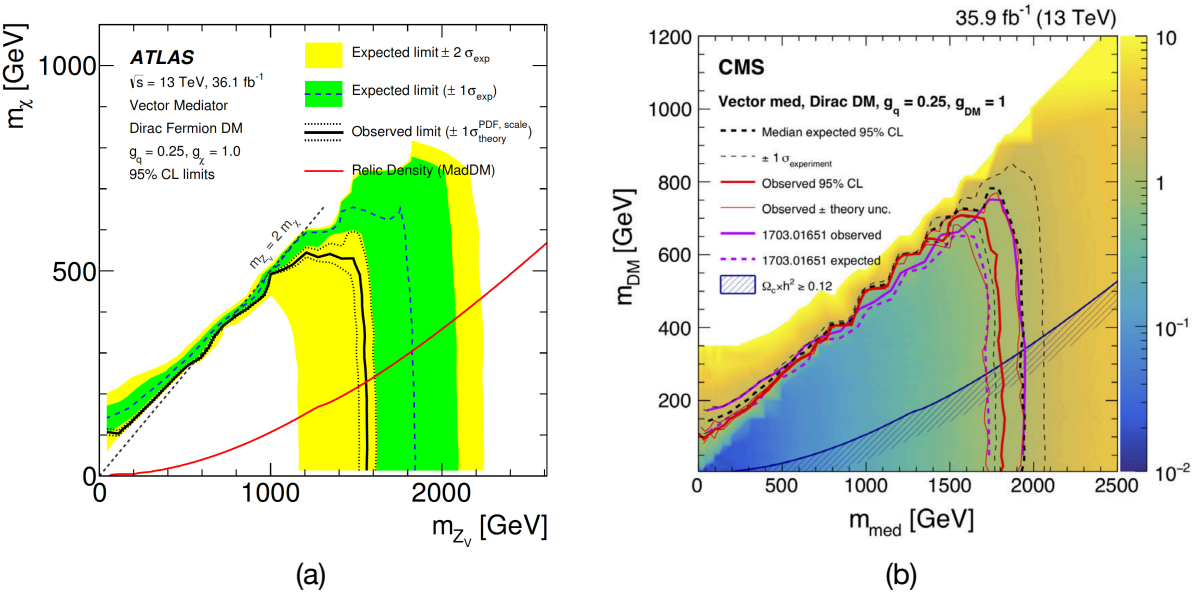


Figure 1.12: Limits on DM models as a function of DM particle mass and mediator mass on mono-jet + E_T^{miss} searches [68] [71]. (a) is from ATLAS results, and (b) is from CMS.

- **Multijet + E_T^{miss} constraints**:
  These searches have set limits on models with strong interactions between DM and quarks/gluons. They are susceptible to scenarios where DM particles are produced in cascade decays involving new heavy states. The constraints from these searches help to narrow down the parameter space of theories involving strongly interacting DM particles.

1.5.4 Prospects at the HL-LHC and beyond

The ongoing upgrades to the LHC and future colliders like the High-Luminosity LHC (HL-LHC) and the proposed Future Circular Collider (FCC) would significantly enhance the sensitivity of dark matter searches.

The **HL-LHC** aims to increase the integrated luminosity by a factor of 10, allowing for much larger datasets and improving the sensitivity to rare processes. This upgrade would enhance the discovery potential for DM particles and provide more constraints on their properties. The **FCC** is a proposed next-generation collider that would operate at significantly higher energies than the LHC, opening new kinematic regimes for heavy DM production or heavier mediators. The increased energy and luminosity of the FCC would enable the exploration of heavier candidates and interactions that are currently beyond the reach of the LHC.

Furthermore, the FCC-ee (electron-positron collider) would also allow for further studies of the axion model through light-by-light scattering searches [59]. In particular, the

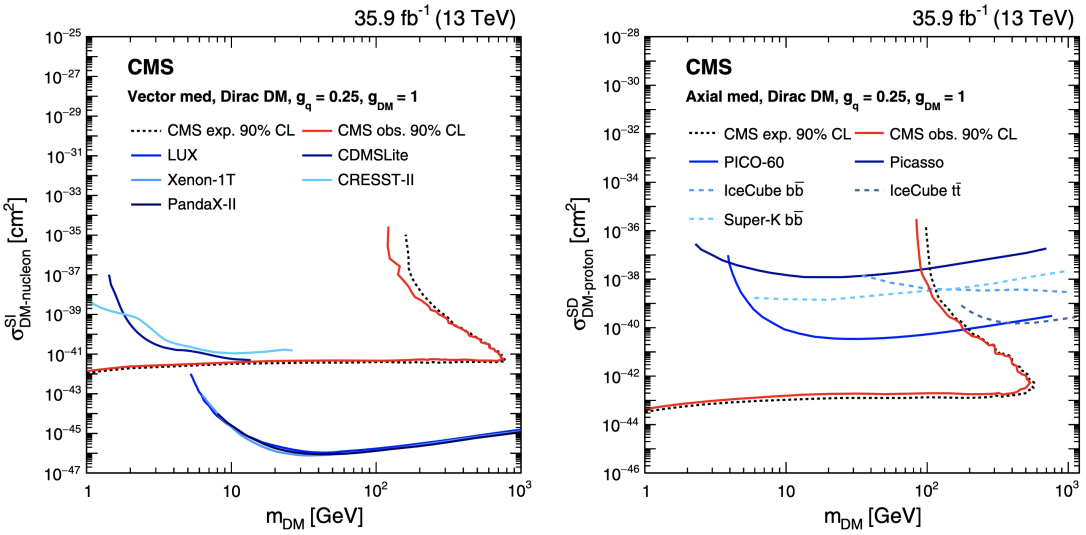


Figure 1.13: DM-nucleon interaction limits set by CMS with mon-X searches [71].

effective coupling to photons could be probed with higher precision and overall sensitivities for 2-8GeV ALPs were enhanced compared to the LHC.

In conclusion, collider experiments are a vital component of the multi-faceted approach to dark matter detection. While no direct evidence has been found yet, the constraints provided by these searches are essential for guiding theoretical model building and future experimental efforts. This discussion demonstrates the essential complementarity between collider experiments and direct and indirect searches for Dark Matter.

1.6 Mediator Searches at Colliders

In LHC Run 1 results, due to the relatively low collision energy of 8 TeV, resonant production of heavy mediators linking both sectors was not limited. Consequently, contact interactions were finally used to search for potential DM signals. This means that mediator propagators were integrated out of the cross-section calculations. Although EFT approaches provide model-independent limits, at energy scales where the momentum transfer is comparable to the mediator mass, a simple contact interaction was insufficient to tackle possible dynamic effects. Including a mediator in the model description (as in Figure 1.11) changes the final state kinematics, considering this mediator is necessary for a realistic analysis strategy.

The Z' mediator searches, considered in the above-presented collider searches, are interpreted by fixing various combinations of mediator couplings to quarks and DM g_q and g_χ. The spin-1 Z' mediator is preferred as it introduces electroweak-like portals. However, scalar mediators S are also considered by ATLAS and CMS. The S couplings to the SM are Yukawa-like and mass-dependent, thus yielding extra difficulties. The S mediator will not be covered in this thesis.

Independently of DM particle searches, ATLAS and CMS analysis can also directly target these BSM boson resonances. This is done by considering only SM interactions of

the Z' boson as illustrated in figure 1.14.

1.6.1 Vector and Axial Mediators

The Z' boson can be considered as a vector or axial-vector mediator which alters the event kinematics.

Vector Mediators

Vector mediators are spin-1 particles that couple to the vector current, preserving parity. They interact with fermions through terms like $\bar{f}\gamma^{\mu}f$. Searches for vector mediators typically focus on resonances in invariant mass distributions of fermion-antifermion pairs, such as di-jet (for $q\bar{q}$) or di-lepton (for $l^{+}l^{-}$) final states. The production cross-section of vector mediators is generally higher due to their parity-conserving interactions, making them easier to detect in processes like $pp \to Z' \to jj$.

Axial Vector Mediators

Axial vector mediators are also spin-1 particles but couple to the axial-vector current, violating parity. They interact with fermions through Lagrangian terms like $\bar{f}\gamma^{\mu}\gamma^{5}f$. While the searches for axial-vector mediators also look for resonances, the kinematic distributions of the decay products might differ due to the parity-violating nature of the interaction. This causes spin dependencies and can affect angular distributions and polarization of the final states. Thus requiring different result interpretations from vector mediators. Additionally, cross-sections are suppressed due to the P-violating nature of the interaction.

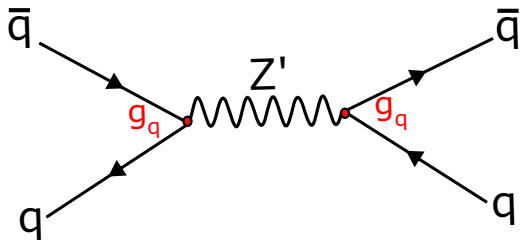


Figure 1.14: Resonant production of a Z' decaying into a pair of quarks. Producing di-jets with invariant mass $m_{jj} = m_{Z'}$

Mediator Searches

Mediator searches are conducted by examining processes where the mediator decays into a resonant pair of SM particles. These searches help to probe the mediator's properties and interactions with SM particles, enabling a deeper understanding of the potential

connections between the visible and dark sectors. Assuming that a DM mediator can be produced by quark-quark annihilation implies that it can also decay into a pair of quarks. Mediator searches focus on final states with two jets, typically looking for a bump in the di-jet invariant mass spectrum due to the presence of a new resonance (see figure 1.14).

The di-jet production at the LHC is very abundant, allowing these searches to inspect high mass ranges and put important limits [77]. However, due to the high production rate, traditional di-jet searches are not sensitive to low-mass mediators, as high jet-p_T thresholds must be set to avoid saturating the trigger bandwidth. To address this, minimal information trigger-level analysis and searches for boosted mediators recoiling against hard ISR jets have been implemented [78]. This efficiently increases the sensitivity to lighter mediators. Additionally, to reach higher masses sensitivity, that are hard to distinguish from the SM QCD di-jet background, angular distribution criteria are forced. SM jet pairs are typically produced in the forward region of the detector, while heavy mediators' di-jet distributions would peak in the barrel. These searches can thus be used to put constraints on the mediator mass and the coupling values.
This type of search is necessary since it is only capable of directly probing the coupling to SM (no intervention of g_χ).

The Z' exclusion limits are dominated by the di-jet analyses, which benefit from the large di-jet production cross-section and do not depend on the mass of the DM particles. Figure 1.15 illustrates constraints on Z' mass and coupling to quarks. These constraints further reduce the phase space excluded by mono-X analyses [73].

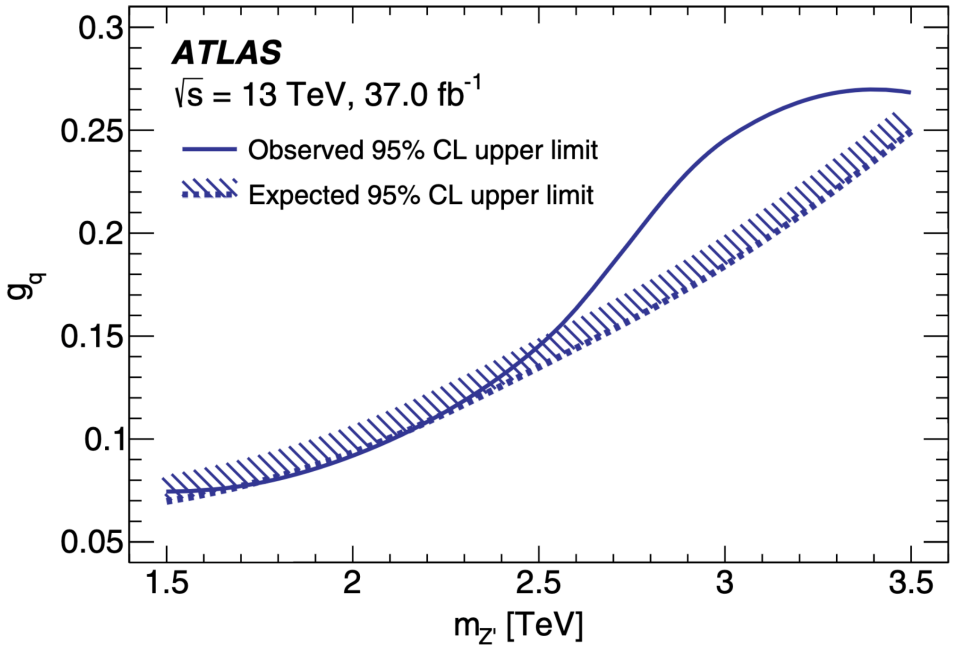


Figure 1.15: Limits on mediator mass and couplings emerging from ATLAS di-jet searches [77]

1.6.2 Pseudo-Scalar Mediators

Additionally to Z' and S mediators, pseudo-scalar mediators were also investigated [62] [63]. This is the case of axion-like particles. ALPs are spin-0 particles and couple to the pseudo-scalar current involving a γ^5 matrix. These mediators offer different decay modes, as discussed in the dedicated Chapter 4. For instance, ALPs can decay into two photons ($a \to \gamma\gamma$) due to their coupling to the dual field strength tensor, leading to clean and identifiable experimental signatures.

Pseudo-scalar mediators allow for interaction with the Higgs field and allow gluon fusion production processes. Considering this, ALP mediators can be incorporated into many mono-X signals. Figure 1.16 illustrates two pseudo-scalar mediator processes contributing to mono-j + E_T^{miss} events.

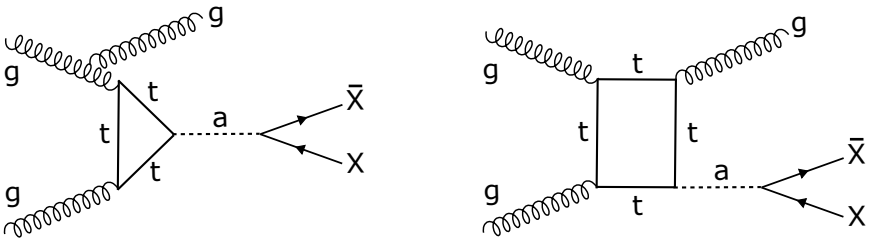


Figure 1.16: Processes contributing to DM plus one jet events through a pseudo-scalar mediator.

Searches of Pseudo-Scalars

Due to direct Higgs coupling, ALPs can also be produced via exotic decays of the Higgs boson [79]. Each production process severely impacts the final state, resulting in different kinematic situations with different cross-sections. Furthermore, the nature of its couplings to the SM allows for a high diversity in decay possibilities.

Searches for pseudo-scalar mediators focus on distributions of specific channel decay products, such as $a \to \gamma\gamma$ or $a \to gg$, for a given ALP production process. Specific Higgs decay could also produce ALP pairs $H \to aa$, which can then decay in different ways as represented in figure 1.17. Due to specific choices of decay channels and the unique back-to-back topology offered by the $H \to aa$ decay, this type of event yields very special signatures, which helps reduce the SM background.

The variety of decays and production possibilities within the Higgs sector makes for a high number of phenomenologies to be probed. ATLAS and CMS analysis strategies are to target all possible final states and are necessary for consistent model testing.
These analyses include : $H \to aa \to \mu^+\mu^- b\bar{b}$, $H \to aa \to \gamma\gamma\gamma\gamma$, $H \to Za \to l^+l^- gg$, and more. Pseudo-scalar mediators ATLAS analysis examples can be found in [80] [81] [82] [83] [84].

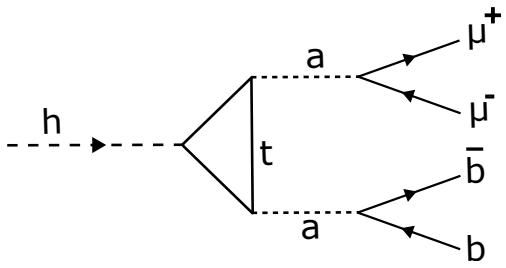


Figure 1.17: Double ALP Higgs boson decay producing a final state with a pair of bottom quarks and a pair of muons.

The published analysis of CMS and ATLAS found no significant excesses concerning SM background. However, pseudo-scalar searches remain a hot topic at the LHC and promise various future analysis strategies. In particular, some regions of the ALP's parameter space allow for long lifetimes. This enhances the search for ALPs by extending analyses to the domain of long-lived particles (LLP). These LLP cases yield extremely unusual event signatures in need of new probing solutions using alternative techniques.

The search for long-lived ALPs at the LHC is the main focus of this thesis. A detailed description of the investigated decay modes and production mechanisms at the LHC is presented in Chapter 4.

1.7 ALP and long-lived particles

This section provides a more detailed description of ALP phenomenology and of the long-lived search opportunities that it offers.

1.7.1 ALP motivations

Axions and ALPs searches are motivated by the strong CP problem and the Dark Matter question. They can be DM candidates or considered as a mediator to the dark sector. However, due to the simplicity of expanding the SM with ALPs by adding a new broken U(1) symmetry and due to the flexibility allowed by EFT approaches, many open problems of particle physics can find solutions through an ALP extension. This creates more motivation to investigate this hypothetical particle

In addition, other motivations for the existence of ALPs are given by:
String theory, in which ALPs naturally arise as in other models with extra dimensions [85] [86]. Furthermore, regarding the muon g-2 anomaly, recent results show significant (4.2σ) deviations from the SM, which are thought to be related to theory uncertainties [87] but could show signs of new physics. A plausible explanation considers ALP models with one loop a-μ corrections of muons [88]. Finally, ALPs can be considered as a possible solution to inflation, playing both a role in the inflation mechanism and in the DM density [89].

1.7.2 Effective Field Theory of ALPs

The ALP EFT Lagrangian (in the EW symmetric phase) is given by equation 1.9 [90] [91] [92].

$$\begin{aligned}\mathcal{L}_{\text{eff}}^{D\leq 5} = &\frac{1}{2}(\partial_\mu a)(\partial^\mu a) - \frac{m_a^2}{2}a^2 + \frac{\partial_\mu a}{4\pi f_a}\sum_F \bar{\psi}_F C_F \gamma^\mu \psi_F \\ &+ \frac{\alpha_s C_{GG}}{4\pi f_a} a G_{\mu\nu}\tilde{G}^{\mu\nu} + \frac{\alpha C_{WW}}{4\pi f_a} a W_{\mu\nu}\tilde{W}^{\mu\nu} + \frac{\alpha' C_{BB}}{4\pi f_a} a B_{\mu\nu}\tilde{B}^{\mu\nu}\end{aligned} \tag{1.9}$$

The terms in the Lagrangian are dimension 5 (maximum) and are regulated by the spontaneous breaking energy scale f_a of the U(1) symmetry associated with the axion field. The Lagrangian describes the kinetic term of the ALP, its mass term, interactions with SM fermions, and couplings to the gauge fields. Where $G_{\mu\nu}$, $W_{\mu\nu}$, and $B_{\mu\nu}$ are the field strength tensors of $SU(3)_c$, $SU(2)_L$, and $U(1)_Y$, respectively. The dual field strength tensors are defined as $\tilde{X}^{\mu\nu} = \frac{1}{2}\epsilon^{\mu\nu\alpha\beta}X_{\alpha\beta}$ (with $\epsilon^{0123} = 1$). The Levi-Civita matrix ϵ includes the γ^5 matrix, highlighting the pseudo-scalar nature of the ALP interactions.

After the EW symmetry breaking, one can find ALP couplings between the EM tensor $F_{\mu\nu}$ and Z bosons :

$$\mathcal{L}_{\text{eff}} \ni \frac{\alpha_{\text{em}} C_{\gamma\gamma}}{4\pi f_a} a F_{\mu\nu}\tilde{F}^{\mu\nu} + \frac{2\alpha_{\text{em}}}{s_w c_w}\frac{C_{\gamma Z}}{4\pi f_a} a F_{\mu\nu}\tilde{Z}^{\mu\nu} + \frac{\alpha_{\text{em}}}{s_w^2 c_w^2}\frac{C_{ZZ}}{4\pi f_a} a Z_{\mu\nu}\tilde{Z}^{\mu\nu} \tag{1.10}$$

The Wilson coefficients have nontrivial relations to the couplings before EW symmetry breaking that can be written as :

$$\begin{aligned} C_{\gamma\gamma} &= C_{WW} + C_{BB}, \\ C_{\gamma Z} &= c_w^2 C_{WW} - s_w^2 C_{BB}, \\ C_{ZZ} &= c_w^4 C_{WW} + s_w^4 C_{BB}, \end{aligned} \tag{1.11}$$

where s_w and c_w are the sine and cosine of the weak mixing angle.

The EW breaking also gives rise to Yukawa-like interactions with fermions :

$$\mathcal{L}_{\text{eff}} \ni i C_{a\psi} a \sum_F m_\psi \bar{\psi}_F \gamma^5 \psi_F \tag{1.12}$$

where m_ψ relates to the fermion mass matrix, and F runs over all SM fermions (excluding neutrinos). Note the presence of γ^5, which differs from standard scalar Higgs Yukawa interactions.

This ALP EFT description offers a high number of possible analysis channels. It allows for a wide range of masses and couplings, making it a usable general framework for exploring new physics and interpreting results. This diversity of interactions renders various possible production mechanisms at particle colliders, including both pp collisions and electron-positron collisions. As presented below, ALPs can also be produced via the Higgs.

1.7.3 Higgs sector

Interaction between the Higgs field and the ALP is not present in equation 1.9. These interactions involving ϕ arise at higher-dimensional operators. These operators are suppressed by higher powers of the energy scale f_a, indicating that they only become significant at very high energies.

The effective Lagrangian $\mathcal{L}_{\text{eff}}^{D\geq 6}$ Higgs related terms are:

$$\begin{aligned}\mathcal{L}_{\text{eff}}^{D\geq 6} \ni & \frac{C_{ah}}{(4\pi f_a)^2}(\partial_\mu a)(\partial^\mu a)\phi^\dagger\phi \\ & + \frac{C_{Zh}}{(4\pi f_a)^3}(\partial_\mu a)\left(\phi^\dagger i D^\mu \phi + \text{h.c.}\right)\phi^\dagger\phi + \cdots ,\end{aligned} \tag{1.13}$$

The first term allows for kinetic mixing between the ALP and the Higgs field with a coupling strength C_{ah}. Thus allowing for $h \to aa$ mechanisms and Higgs radiation if $m_a > m_h$. The second term involves a covariant derivative D_μ, which allows for coupling to the Z boson gauge field and would be responsible for a possible $h \to Za$ decays.

There are additional higher-dimensional terms that are not explicitly written but follow a similar pattern of suppression by higher powers of f_a.

Branching ratio : The Higgs portal is an interesting process to investigate. Indeed, CMS and ATLAS results indicate a non-negligible possible branching ratio of Higgs decays to new physics. Current constraints put a high upper limit of [93] :

$$\text{Br}(h \to \text{BSM}) = \frac{\Gamma_{\text{BSM}}}{\Gamma_{\text{BSM}} + \Gamma_{\text{SM}}} \leq 0.34 \tag{1.14}$$

This motivates special ALP searches that can only be performed at the LHC.

As demonstrated, ALPs have multiple decay and production modes but could also have different possible lifetimes. Prompt ALPs can decay within a few mm, while stable ALPs could escape the detector and induce missing energy exactly like a DM candidate. The lifetime drastically changes the expected signatures given by the same process. If ALPs escape the detector it becomes impossible to differentiate them as "long-lived" mediators of DM or directly as a DM particle. However, between prompt ALPs and ALPs escaping ATLAS rises the domain of long-lived particles (LLP), which creates significant displacements of decay inside the detector.

1.7.4 Long life times

ALPs can exhibit long lifetimes if their decay widths are small. The decay width Γ is inversely related to its lifetime τ through the relation:

$$\tau = \frac{\hbar}{\Gamma} \tag{1.15}$$

For ALPs with $m_a < m_h$, the main decay modes include di-photons, di-jets, and lepton pairs. The combined decay widths can result in a long-lived particle. Suppose the ALP primarily decays into photons, meaning the associated branching ratio is sizable. In that case, the decay width can be approximated to the channel-specific one $\Gamma_{a\to\gamma\gamma}$, which is expressed as:

$$\Gamma_{\gamma\gamma} = \frac{\alpha_{\text{em}}^2 C_{\gamma\gamma}^2 m_a^3}{64\pi^3 f_a^2}, \tag{1.16}$$

If the coupling $C_{\gamma\gamma}$ is small or the mass m_a is low, the decay width becomes small. This property makes ALPs promising candidates for LLP searches at colliders [94] [79].

Long Lived DM Mediators Long-lived Pseudoscalar mediators for DM can impact searches in several ways. Long-lived scalar S and mediators can provide reinterpretations of astrophysical observations through γ-ray telescopes. Long-lived ALP decays could contribute to excesses in gamma-ray spectra observed by instruments such as the Cherenkov Telescope Array (CTA) [13] [95] [96]. This offers new insights and constraints on DM models in a complementary search for axion dark matter.

1.7.5 LLP challenges at the LHC

Searching for LLPs at the LHC presents unique challenges. Standard identification, reconstruction, and calibration techniques are based on the assumption that final state particles are produced promptly. However, if an LLP decay arises at significant distances from the collision point, it results in displaced vertices and other unconventional signatures in the detectors. A detailed overview of LLPs and associated challenges and opportunities is further discussed in Chapter 5.

The identification of LLPs requires novel techniques and methodologies. For instance, new calorimeter-based techniques will be presented in Chapter 5 to improve the identification efficiency of photons from LLP decays. Traditional photon reconstruction algorithms often fail when confronted with displacements of the decay position. To investigate these new hypothetical events, new projects propose to build new detectors placed further away from the collision point to detect decaying LLPs, as the Mathusla [97] experiment, for instance.

Additionally, leveraging Machine Learning (ML) techniques can greatly enhance LLP searches. Since the detectors and original software were not meant to reconstruct such particles, ML algorithms can be trained to recognize patterns in experimental signatures specific to LLP events, increasing the sensitivity of the associated searches.

LLP searches at the LHC are only partially explored compared to other DM mediator searches. They hold significant potential for discovering new physics, as some signatures

are so exotic that even a few detected events could indicate a ground-breaking discovery. With their high-energy collisions and advanced detection capabilities, the LHC experiments are well-positioned to explore these territories, especially through the Higgs portal. Future research and development in this area are crucial for uncovering the full potential of LLP searches at the LHC.

1.8 Summary

Dark Matter is a pillar question of modern physics. It is very well-motivated and has gathered a great number of experimental observations today, as presented in this chapter. Since the SM cannot explain the universe DM density, many new BSM theories are built around the idea of proposing microscopic DM candidates and mediators to the dark sector. Some particle candidates can arise from a given theory offering a multitude of other non-DM-related particles, while others were only built in a strict DM solution approach. Additionally, other non-microscopic solutions are investigated. Many research fields, such as astrophysics, cosmology, astroparticles, colliders, and other particle laboratory experiments, have deployed considerable efforts for probing either DM particles or mediators in the dark sector. Their combined results offer great complementarity and have constrained the parameter space of many different models. Among these models are axions and ALPs. It has been understood, through an EFT description of ALPs, that their lifetimes can be important, which can yield to LLP. This long lifetime further extends the possible domain of mediators to be constrained. From the point of view of collider experiments, such LLPs render very unusual signals that are hard for the SM to mimic, as will be explained in this thesis. This implies that LLP searches of ALPs can considerably reject the SM background and become ultra-sensitive to this new physics. However, these displaced signals in detectors such as ATLAS or CMS are incompatible with most identification and reconstruction algorithms. New techniques must be developed and implemented to extend the detector sensitivity to these LLPs. Additionally, the variety of ALP decay modes and production through the Higgs portal provide exciting complementary signals to probe at LHC experiments.

This thesis will focus on the search for long-lived ALPs in the ATLAS experiment. The standard workflow for data analysis is questioned because of the challenges displaced signals induce in ATLAS-like detector reconstruction. New solutions based on calorimeter shower-shape descriptions are developed to search for ALPs decaying in a photon pair with a long lifetime.

Chapter 2

The ATLAS detector and the tracker upgrade

Multiple high-energy physics (HEP) experiments are conducted through proton collisions using the Large Hadron Collider (LHC). These explore a new domain of energy in which physics beyond the Standard Model could be produced. However, when this strategy fails, Standard Model precision measurements can be conducted, and deviations from what the theory expects are computed. Potential new physics signatures, which include new particles or interactions, are investigated using modern techniques. The main LHC particle detectors are LHCb, ALICE, ATLAS, and CMS. These detectors were built to target specific particle physics investigations. ATLAS and CMS are commonly referred to as "general-purpose" detectors, while LHCb and ALICE focus on more specific physics. LHCb is dedicated to studying CP violation and searching for rare decays that may reveal new physics in the beauty sector. ALICE, on the other hand, is designed to study high-energy collisions between lead nuclei. These collisions mimic the extreme temperature and energy density that would have been present shortly after the Big Bang by forming a quark–gluon plasma, a state of matter in which quarks and gluons are unbound.

This chapter provides a brief recap of the LHC and the ATLAS detector. In a second step, ATLAS upgrades are presented, notably the next version of the inner tracker sub-detector.

2.1 The Large Hadron Collider

The LHC, by the European Organization for Nuclear Research (CERN), is today the world's largest and most powerful particle accelerator. It has a 27 km circumference and is located beneath the France–Switzerland border near Geneva. It can accelerate particles such as protons and lead nuclei to significant energy levels. The LHC is part of a broad complex of accelerators. The acceleration process of protons is done through multiple steps that require different-sized particle accelerators. The protons initially come from bottled dihydrogen, where the hydrogen atoms are ionized and separated. These protons are then injected into the first accelerator, LINAC 2, accelerating them to 50 MeV. Next, the protons enter the BOOSTER synchrotron, increasing their energy to 1.4 GeV. In the Proton Synchrotron (PS), they form ultra-relativistic proton bunches with an energy of 25 GeV and a bunch structure of 81 packets with 25 ns intervals. Afterward, the protons

are directed to the Super Proton Synchrotron (SPS) and further accelerated to 450 GeV. Ultimately, the LHC is filled with over 2000 bunches per beam, each containing approximately 10^{11} protons, and these beams are then accelerated to 6.8 TeV. The acceleration of particles is done using Radio Frequency cavities [98] that present electric fields that boost passing protons.

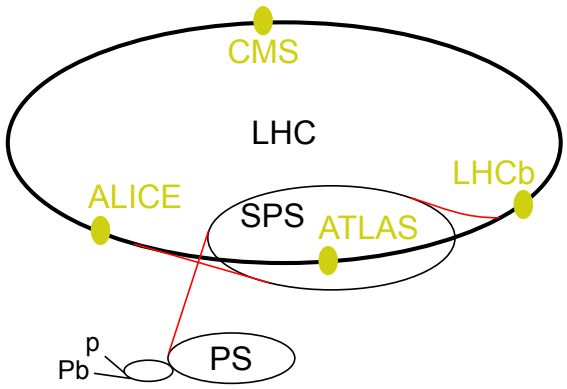


Figure 2.1: The LHC accelerator complex. From [99]

The LHC is made of two beamlines, with protons circulating in opposite directions, allowing collisions every 25 ns. Proton collisions reach energies up to $\sqrt{s} = 13.6TeV$ in the current Run 3; where $\sqrt{s}$ is the total amount of energy in the center of the mass frame. The LHC has undergone three major runs, with improvements in luminosity and collision energy each time.

The instantaneous luminosity is a key parameter of an accelerator's performance. It is defined as the number of produced interactions per second per unit cross-sectional area (barn). For a given process, the relationship between the number of produced events per second $\frac{dN}{dt}$, luminosity L, and cross-section σ is given by:

$$\frac{dN}{dt} = L \cdot \sigma$$

The luminosity directly reflects the expected statistics that a given experiment can collect. It is directly linked to the frequency of bunch crossings, the number of protons per bunch, and the probability of proton-proton interaction due to the beam width. For a total period of data-taking, one considers the integrated luminosity over time $L_{\text{int}} = \int L\, dt$, as it reflects the total amount of statistics of a given data set.

The LHC features four main collision points, named interaction points (IP), corresponding to four detectors: ATLAS, CMS, ALICE, and LHCb.

2.2 The ATLAS detector

This section will quickly introduce all important aspects of the detector that help understand the subsequent discussions present in this thesis.

The ATLAS detector [100], A Toroidal LHC ApparatuS, is a multi-purpose detector designed to explore a wide range of physics phenomena, from precision measurements of the SM to searches for new physics. The detector is a large and complex instrument, measuring 46 meters in length, 25 meters in diameter, and weighing about 7,000 tonnes. Its cylindrical shape design maximizes the detector acceptance for particles generated at the IP. The cylindrical shape is referred to as the barrel, while both ends of the detector are the end-caps. A standard ATLAS coordinate system is defined and used as a convention. The z-axis points along the beam direction, the y-axis points upwards, and the x-axis towards the center of the LHC ring. Cylindrical coordinates are often used in ATLAS. (r, ϕ) are the basis axis of the transverse plane (same as the xy plane), and the pseudorapidity η provides the 3rd dimension and is related to the polar angle θ as:

$$\eta = -\ln\left(\tan\frac{\theta}{2}\right)$$

This coordinate is commonly used in ATLAS to describe sub-detector acceptance and physics process event topologies. In this definition, the central barrel region coverage is $|\eta| < 1.5$, and the end-caps coverage is $1.5 < |\eta| < 3.2$.

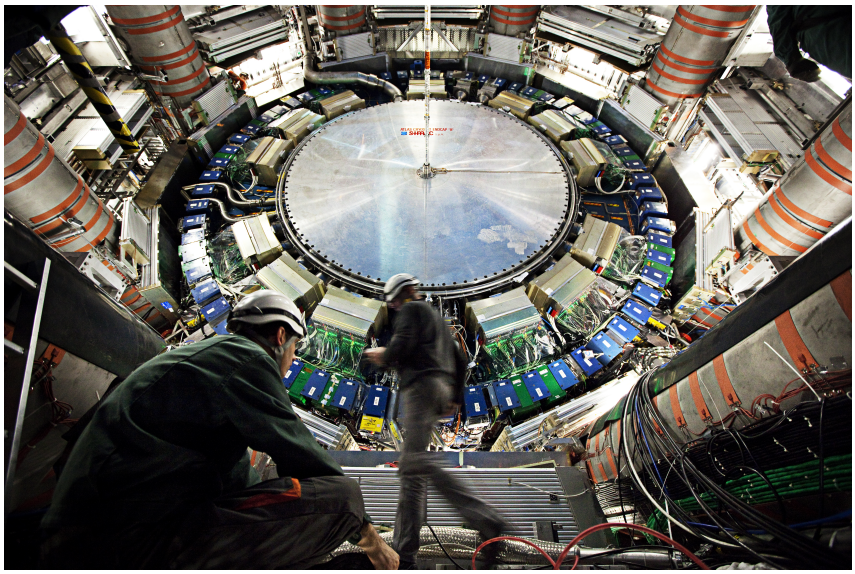


Figure 2.2: A picture of ATLAS taken in front of a calorimeter end-cap. Picture from [101].

The detector is supported by a collaboration of 6000 members and 3000 scientific authors. This impressive number of physicists and engineers indicates the complexity of the detector, the difficulty of operating the experiment, and the high diversity of physics research conducted with ATLAS results.

As one can see in figure 2.3, ATLAS consists of multiple sub-detectors that play complementary roles in detecting and identifying the diverse particles created through proton-proton collisions. These systems are organized in layers concentrically around the IP to ensure symmetric responses along ϕ and η. Combined, these sub-detectors provide a snapshot of each recorded event and measure many important properties of its particles, such as their energy, direction in space, electric charge, particle nature, and other

properties of single particles or systems of particles. The rest of the section describes, in a nutshell, the main ATLAS sub-systems.

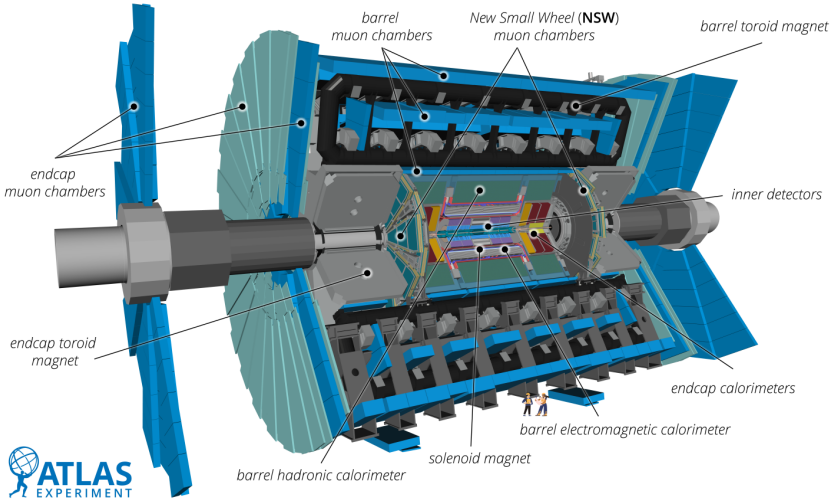


Figure 2.3: Schematics representation of ATLAS, each main sub-system is labeled [102]. The diameter of the detector is about 25 meters.

2.2.1 The Tracking system

The ATLAS tracking system is named inner detector (ID) as it is the closest to the collision point. It is designed to reconstruct the trajectories of charged particles, measure their momenta, and localize the originating vertices of captured particles. The ID is positioned inside a strong magnetic 2 T axial field generated by a solenoid system. Thus, one can use the particle-measured trajectories to infer their charge. The ID is also used to find the origin of multiple signals that occur in other sub-detectors. Additionally, this detector plays a crucial role when an important number of particles is produced in a collision by isolating particles through reconstructed track matching.

The inner detector consists of three main sub-detectors: the Pixel Detector, the Semiconductor Tracker (SCT), and the Transition Radiation Tracker (TRT). These sub-detectors provide hits to reconstruct charged particle trajectories up to 1 meter from the collision point in the transverse plane. Figure 2.4 illustrates a cut-out image of the inner detector to show all sub-detectors positioning. A description of each sub-system's dimensions is presented in section 2.2.5 in the context of long-lived particles. The coverage of the ATLAS Inner Detector in pseudorapidity extends up to $|\eta| < 2.5$ for the Pixel Detector and SCT. At the same time, the TRT provides coverage up to $|\eta| < 2.0$, ensuring comprehensive tracking in the center and end-cap regions with better particle identification capabilities in the central barrel region.

Pixel Detector The Pixel Detector [104] [105] is the innermost part of the tracking system, providing high-resolution measurements close to the interaction point. It is based on silicon pixel technology, which is capable of withstanding the high radiation environment near the beam line. The Pixel Detector consists of four layers that lead to a total of

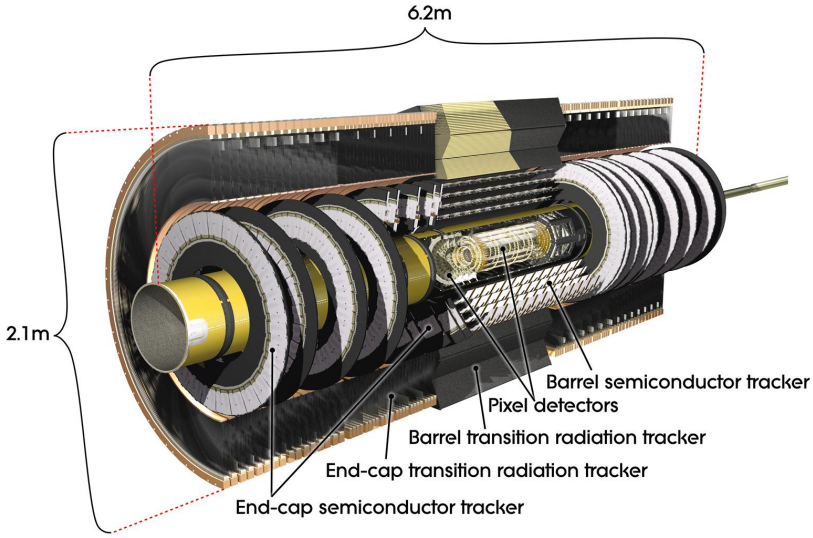


Figure 2.4: Schematics of the inner detector, each sub-system is labeled [103]. The maximum detector dimensions in the transverse plane and beam axis are written.

92 million pixels. Among the layers, the Insertable B-Layer (IBL) was introduced for Run 2. It is the closest to the beam pipe and improves the precision and robustness of track reconstruction. This layer offers the highest pixel resolution ($50 \times 250 \mu m^2$) and allows a space point resolution of $10 \times 60 \mu m^2$. Combined with the other pixel layers, the Pixel Detector provides a highly precise reconstruction of the track origin and helps identify the position of primary vertices.

Semiconductor Tracker (SCT) The SCT [106] [107] surrounds the Pixel Detector and consists of silicon strip detectors. It provides precise tracking over a larger volume and complements the Pixel Detector by offering additional measurement points. The SCT includes four two-sided barrel layers and two end-caps, each with nine disks. It has a total of 4088 modules, with a resolution of 17 µm along the transverse plane for the barrel region. With the SCT being positioned further away from the interaction point, the particle density is less important, resulting in a lower demand for high-pixel spatial resolution, thus allowing for the use of strip detectors instead of smaller pixels. An upgrade of such silicon pixel detectors is presented in the current chapter.

Transition Radiation Tracker (TRT) The TRT [108] is the outermost part of the tracking system. It consists of gas-filled straw tubes and provides tracking through gas ionization from particles passing by. The TRT contains approximately 298,000 straws, with an average resolution of 130 µm. It extends track reconstruction radially outwards to a radius of 1082 mm and provides only information on the transverse plane. Although it is a tracker, it can also provide identification through transition radiation measurements.

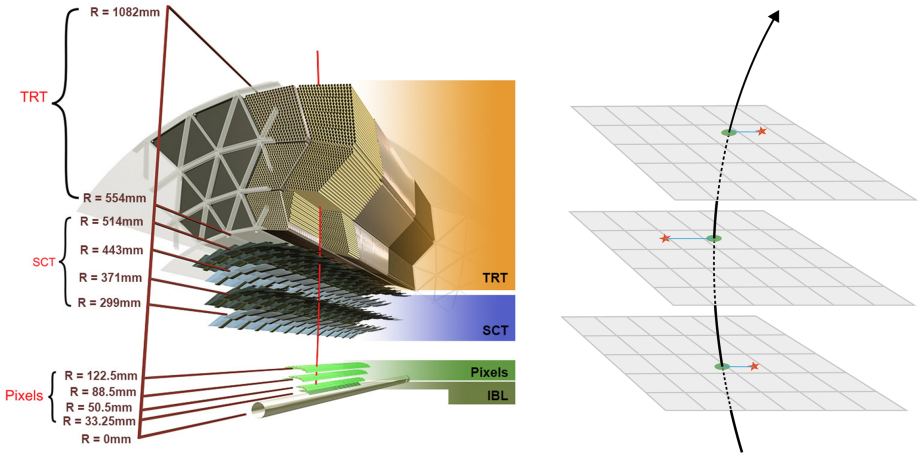


Figure 2.5: Schematic representation of ATLAS tracking system(left) including Pixels, SCT and TRT. A representation on the right indicates track reconstruction of a charged particle crossing the sub-detector planes. Red stars indicate each detector hit, while the fitted track is depicted with a black arrow. Green dots highlight the intersections of the track with each surface, and blue lines illustrate the track-to-hit residuals for each layer. From [109]

2.2.2 The Calorimeter system

When particles have passed the ID, they leave energy in the calorimeter system through EM and strong nuclear interactions, which effectively stop them. This is further described in 5.1. Only muons, that interact less through bremsstrahlung, penetrate the calorimeters and are captured in a dedicated system afterwards. The total lost energy in the calorimeters is assessed through charge and light collections resulting from incoming particle ionization. The different amounts of energy deposited through EM and nuclear interaction are used to determine a particle's nature. Additionally, the shape of the energy deposit yields information on the shower development and further improves particle identification. Note that before the EM calorimeter, there is a pre-sampler detector, which measures the energy of the pre-shower. This pre-shower is caused by particles interacting with the detector material before they enter the calorimeter system. This sub-detector corrects for energy lost in inactive material in the inner detector and improves the shower energy reconstruction.

The shower development in the calorimeters, due to particle absorption, contains a lot of information regarding its nature. The interactions related to different particles result in different shower shapes. This is a main topic of discussion in Chapters 4 and 5 as the shower shape information is used to distinguish multiple particles. The calorimeter system is divided into two main parts: the Electromagnetic Calorimeter and the Hadronic Calorimeter.

The difference between electromagnetic and hadronic shower developments inside the calorimeters is crucial for establishing analysis techniques for long-lived-axion-like particle searches. This is further explained in another chapter at 5.1.

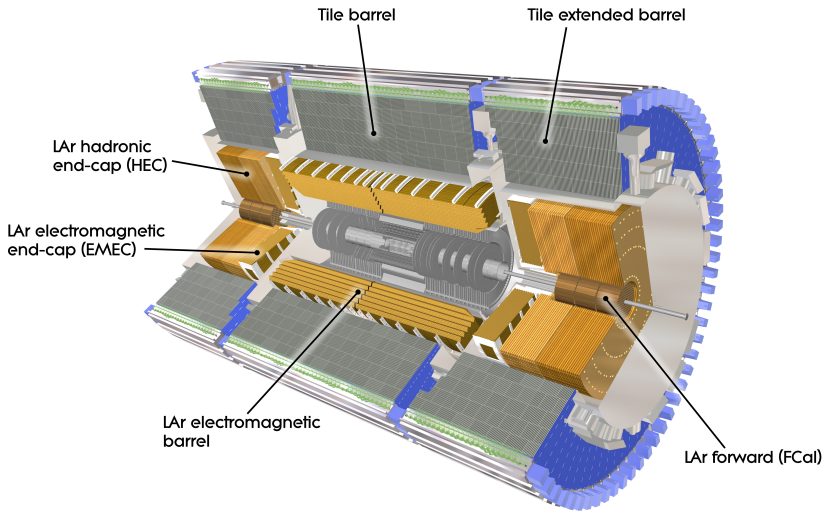


Figure 2.6: Schematics of ATLAS EM and hadronic calorimeter systems in barrel and end-cap regions. From [111]

Building new analysis strategies using the calorimeters is essential for long-lived particle (LLP) searches. In fact, LLPs are often investigated in ATLAS by searching for reconstructed displaced vertices [110] in the tracker system, which indicates a displacement between a particle production at the collision point and its decay. Naturally, this implies that such searches are limited to LLPs decaying in the inner detector, which spans up to 1.4 meters in the transverse plane. Thus, by using the EM and Hadronic calorimeters, the detection sensitivity of larger lifetime LLPs can be enhanced.

Electromagnetic Calorimeter - LAr The Electromagnetic Calorimeter [112], named LAr calorimeter due to its usage of liquid argon, is essential to capture and measure the energy of EM showers originating from electrons, photons, as well as the electromagnetic component of jets. The detector is a sampling calorimeter that uses a dense absorber material to produce showers through EM interactions of passing particles and an active material where the shower creates a signal through ionization followed by charge collection. Lead is used as an absorber, while the liquid argon is the sampling material. It uses electrodes disposed in an accordion geometry to measure the electronic pulses of the argon ionization in the high-voltage electric field, which gives a direct measurement of the deposited energy.
This detector is divided into a barrel region and two end-caps, providing coverage up to $|\eta| = 3.2$ and ensuring complete azimuthal coverage without gaps.

Figure 2.7 illustrates a module of the EM calorimeter in the barrel. In this image, one can identify the three EM sampling layers often referred to as S1, S2, and S3 and referred to as EM1, EM2, and EM3 in Chapter 5. The EM calorimeter offers a longitudinal and lateral description of the shower development by measuring energy deposits along the three layers (longitudinal) and assessing its geometrical deposition within each layer

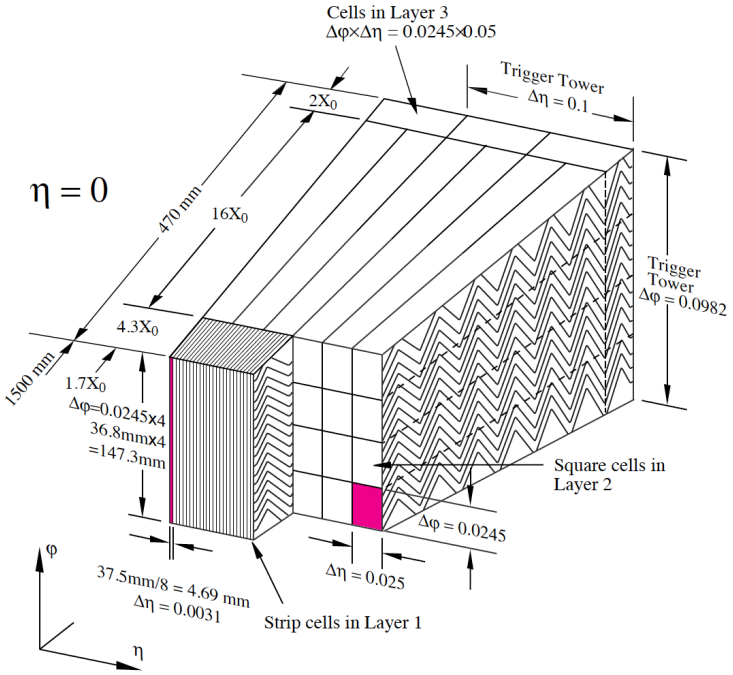


Figure 2.7: A module of the EM calorimeter displaying each layer depth. From the ATLAS experiment paper [100].

(lateral). Each layer plays a different role in the shower absorption, energy measurement, and particle identification.

The first layer is finely segmented in the η direction for separating from photons and is used for photon direction measurement. In fact, π^0 can decay into merged double photons that mimic the single photon signal. These are considered as background to eliminate when identifying photons. This standard strategy of identification strongly impacts the search for ALP decaying into two photons, which leads to new strategies discussed in this work 5. The second layer collects most of the shower energy as it is the deepest among the three. Figure 2.7 shows that this second layer represents about 70 % of the EM calorimeter depth, making up 16 radiation lengths (χ^0); this is more described in 5.1. The difference in depths between the three layers has an important impact on the longitudinal shower development; this is used in the case of long-lived ALPs to gain sensitivity to the ALP decay position within the calorimeters (see Chapter 5). Additionally, this layer has a granularity of $\Delta\eta \times \Delta\phi = 0.025 \times 0.025$ for $|\eta| < 2.5$, and it is used for finding the particle position. It is used together with the first layer for photon pointing. The last layer corrects for leakage behind the electromagnetic calorimeter. The impact of each layer's specificities is further described in a chapter dedicated to new photon identification strategies (Chapter 5)

The LAr calorimeter provides an excellent energy resolution for e/γ particles of: $\frac{\sigma(E)}{E} = \frac{10\%}{\sqrt{E}} \oplus \frac{0.4}{E} \oplus 0.7\%$ [113]. This energy resolution equation consists of a stochastic term $\frac{10\%}{\sqrt{E}}$, which reflects the fluctuations in energy deposition due to the random nature of particle interactions; a noise term $\frac{0.2}{E}$, accounting for electronic noise; and a constant term 0.7%, significant at high energies. The first term is often dominant, while the second

is negligible at the considered energies.

Additionally, this sampling calorimeter provides timing measurement of charge collections at each channel. By considering displaced ALPs decaying in photons, the final photons should create a delayed signal in the EM calorimeter compared to prompt photons. In fact, the massive ALP propagates at a lower speed. Timing measurements could potentially be used to identify events with late shower developments associated with LLPs. The channel timing resolution depends on the energy as illustrated in figure 2.8. At an energy range similar to the one of the photons investigated in the ALP search, this resolution is about 0.5 ns. This value remains below the ns, which is the expected order of delay for 10 GeV ALPs with a 20 GeV momentum decaying midway in the inner detector. This delay would increase with the decay position and mass of the ALP. However, the calibration of the channel responses probably adds a complication as current algorithms might consider the delayed signal as overlapping bunch crosses. This is particularly true for the EM calorimeter, which has a signal pulse that lasts for multiple bunch crosses [113].

New timing-based strategies, as conducted in CMS [114], could be developed for LLP searches, but they will not considered in this search.

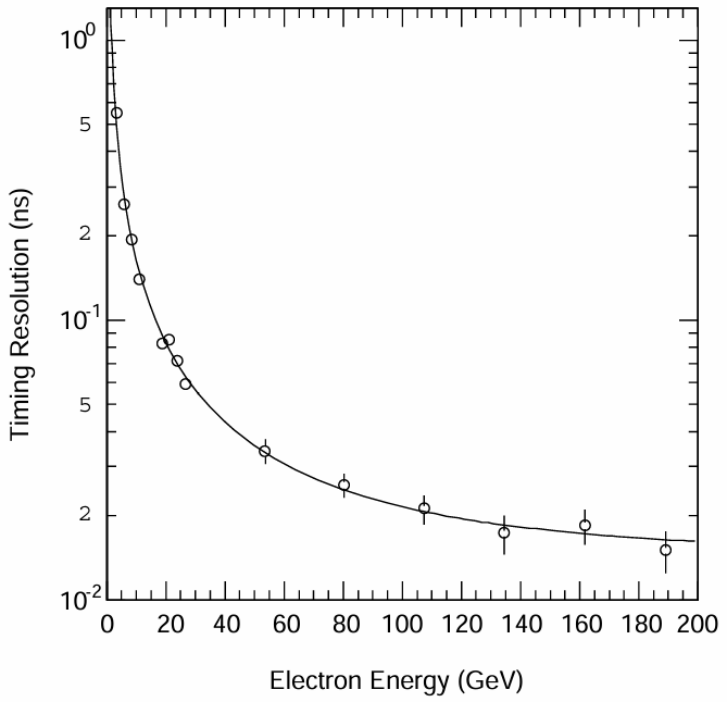


Figure 2.8: Timing resolution of single electronic channels of the LAr calorimeter [113].

Hadronic Calorimeter - Tile Calorimeter The Hadronic Calorimeter [115] [116], made of iron and plastic scintillating tiles, absorbs hadrons through strong nuclear interactions. The iron is the main absorber, and the scintillating tiles are the sampling material that generates photons (transition radiations) produced by a fraction of particles that pass the iron absorbers. This light is directed to photo-multiplier tubes with

wavelength-shifting optical fibers to generate a signal. The fibers absorb the scintillation light and re-emit it at a longer wavelength, which is better suited for efficient transmission and detection.

This detector was built to capture the hadrons present in jets that penetrate the EM layer and interact mainly with the strong nuclear force as well as the EM fraction of jets that were not absorbed in the EM calorimeter. On average, about one-third of a jet's energy is deposited in the EM calorimeters, mainly induced by π^0 components of the hadronic shower. At the same time, the rest is captured in the Hadronic calorimeters.

The calorimeter is divided into a barrel and two extended barrels, covering the pseudorapidity range up to $|\eta| = 1.7$. It is composed of three main layers presenting a lower cell granularity compared to the EM calorimeter. In this region of ATLAS, the shower shapes are less relevant to measure as e/γ particles are already absorbed inside the EM calorimeter.
The Tile detector consists of approximately 5182 cells, with a less accurate energy resolution of $\frac{\sigma(E)}{E} = \frac{55\%}{\sqrt{E}} + 3\%$ [117] [116] (the 1/E noise term is negligible). The tile calorimeter cell timing resolution also under-performs when compared to the EM calorimeter; this is illustrated in figure 2.9.

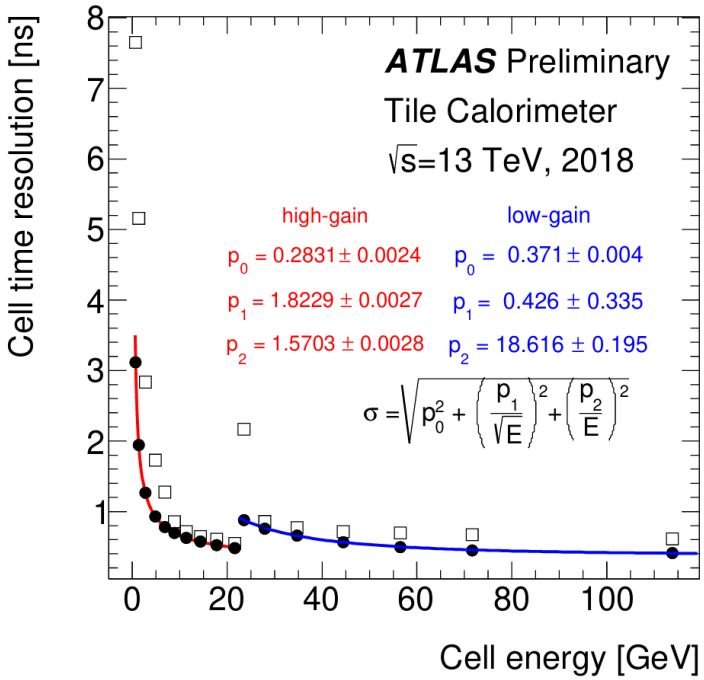


Figure 2.9: Timing resolution of a single cell of the Tile calorimeter [118] with respect to the deposited energy.

Additionally, the hadronic end-cap calorimeter (HEC) covers the $1.5 < |\eta| < 3.2$ region. The HEC uses liquid argon combined with copper as the absorber and contributes to the overall jet reconstruction and understanding of hadronic interactions in the forward regions of the detector, which is important for investigating vector boson fusion searches

[76].
Furthermore, the Forward Calorimeter (FCAL) covers the high η region and plays a crucial role in measuring missing transverse energy (ET) by ensuring no energy is overlooked in these areas.

2.2.3 The Muon detector

The Muon Spectrometer [119] surrounds the calorimeters and is designed to detect muons, which are highly penetrating particles since they interact very weakly. The muon system functions within a second magnetic field generated by a much bigger toroidal magnet. In this region, the muons are bent so that the dedicated sub-detectors can measure their charge and momentum. This detector provides stand-alone muon identification used for triggering events and reconstructing particles.
The Muon Spectrometer includes Monitored Drift Tubes (MDTs), Cathode Strip Chambers (CSCs), Resistive Plate Chambers (RPCs), and Thin Gap Chambers (TGCs), covering the pseudorapidity range up to = 2.7. This detector will not be discussed further in this work, but references [120] [119] provide more details.

2.2.4 Forward detectors

In addition to the systems presented above, the forward regions of ATLAS host different, more specific sub-systems. These are utilized for additional physics measurements [121], analyses with forward emissions event topologies, and monitoring purposes. The forward detectors include ALFA [122], ZDC [123], LUCID [124], MBTS [125], BCM [126] and more recently AFP [127]. These will not be discussed in this work.

2.2.5 Long-lived particles can decay in different sub-systems

The ATLAS detector was built to capture and distinguish multiple physics objects generated at the collision point, as described in the following sections. However, the main search considered in this work involves long-lived particles. This implies that the originating point of particles of interest is not the standard collision point but a displaced vertex. Considering this hypothetical phenomenology, one understands that the subsystem layout, as well as the particle identification, is unfit. For instance, final-state charged particles could be created from an LLP decay after the inner detector, leaving no tracks to be used in the particle identification and reconstruction of its properties. A discussion on the possible event topologies associated with LLPs is discussed in Chapter 4.
Within this work, a particular focus is put on the detector's reaction to a long-lived ALP decaying into photons in the barrel calorimeters. The following table introduces the relevant distances to the interaction point in the transverse plane of the sub-detectors. This distance is often referred to as L_{xy} (xy is the ATLAS transverse plane) or R.

Table 2.1: Distances R of ATLAS barrel sub-detector to the beam axis

Detector	R **in mm**
Pixels	50
SCT	300
TRT	550
Inner detector end	1080
Pre Sampler	1400
EM1	1500
EM2	1591
EM3	1927
HCal1	2280
HCal2	2580
HCal3	3465
Barrel calorimeter end	4000
Muons system	4500
Muons system end	10000

2.3 Data acquisition and analysis workflow

2.3.1 Hardware-based and software triggers

The ATLAS data acquisition system [128] uses a combination of hardware-based and software-based triggers to reduce the event rate from 40 MHz (collision) to 3 kHz (stored data). The trigger system selects events of interest for future analysis, ensuring efficient use of storage and computational resources. Different trigger levels are used to progressively refine the selection criteria, balancing the need for comprehensive data with the limitations of storage, processing power, and electronics bandwidth. The Level 1 (L1) trigger operates at the hardware level, using custom electronics to make fast decisions based on coarse detector information. The High-Level Trigger (HLT) further refines the selection using software algorithms. The available triggers reflect the planned physics analyses to be conducted. For instance, to optimize the signal-to-noise ratio of $h \to \gamma\gamma$ searches, a pre-selection of events is done by choosing the dedicated samples that pass di-photon triggers. Each trigger has associated efficiencies for selecting the target events and fake rates for selecting the wrong ones. This is due to either the complexity of a given event topology or due to detector and algorithm-related inefficiencies.
The topic of triggers and their sensitivity is discussed in the thesis. However, a specific point about electron trigger selection is provided in Chapter 5.

2.3.2 Reconstruction and analysis model

To perform searches, the selected events are processed through reconstruction algorithms that occur at multiple stages, generating different file formats. For a given analysis, a dedicated derivation file from the original data set is specifically constructed to incorporate all reconstructed physics objects and their properties relevant to the process under investigation. The reconstruction and analysis model in ATLAS involves identifying and

reconstructing various physics objects such as jets, photons, electrons, muons, and taus. The algorithms that perform the reconstruction algorithms utilize responses from different combinations of sub-detectors to build a coherent picture of the event. These reconstructed objects follow calibration procedures that compensate for the differences in energy relaxation of each type of particle. For instance, there is a clear difference between pions and e/γ in the way they deposit their energy in non-compensating calorimeter technologies as used in ATLAS. Moreover, both the trigger and reconstruction algorithms have inherent inefficiencies, and certain physics processes can produce objects that closely resemble the signal being studied. These factors introduce challenges that affect particle reconstruction efficiencies.

Data formats The data formats files in ATLAS progress from RAW detector response to final simplified ntuples containing high-level physics objects. Intermediate steps present files such as HITS and ESD. These files and their role in the full data stream are presented below.

- **RAW:** The initial data recorded by the detector contains unprocessed information directly from the detector electronics.
- **HITS:** Contains the output of the detector simulation, representing energy deposits in the sensitive detector elements. Mainly oriented for calorimeter simulation.
- **RDO (Raw Data Objects):** Digitized data derived from HITS, simulating the actual detector readout.
- **ESD (Event Summary Data):** Contains detailed reconstruction information, including full event data used for further processing and analysis, as well as low-level detector information.
- **AOD (Analysis Object Data):** A reduced format derived from ESD, focusing on high-level physics objects like tracks, jets, and vertices, optimized for analysis.
- **DAOD (Derived Analysis Object Data):** Customized AOD datasets tailored for specific analyses, containing only the necessary information for particular physics studies.
- **Ntuples:** Final data format used for user-level analysis, typically containing a flat structure of variables that are easy to manipulate in statistical analysis tools.

Standard ATLAS searches, including LLP searches, are indeed made by using custom DAOD that include relevant variables. For the exotic events created by LLPs, such derivations include very different lower-level information than standard analyses (this is discussed in Chapter 4). However, novel techniques for identifying photon pairs were investigated for the long-lived ALP search studies made during this work. These studies required access to low-level information that is removed from general-purpose AODs. Thus, low-level files such as ESD, which are usually only used as an intermediate step of the data stream, had to be accessed.

2.3.3 Reconstructed objects

A recap of the main ATLAS reconstructed physics objects is presented here. Figure 2.10 perfectly illustrates how each particle type yields very different detector responses, which are exploited for identification purposes.

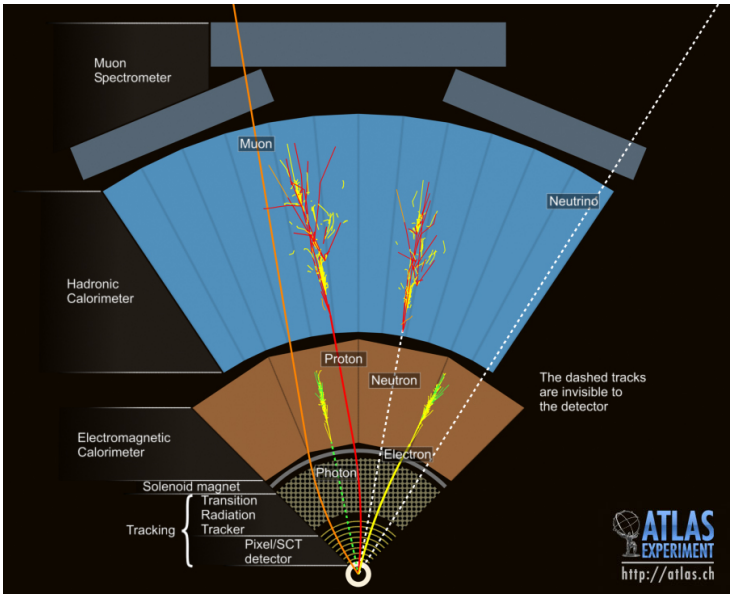


Figure 2.10: Different particles captured by ATLAS sub-systems. From [129]

Pile-up and Its Effects In the ATLAS detector, pile-up refers to multiple proton-proton interactions occurring in the same or nearby bunch crossings. These can be categorized as in-time pile-up, where multiple interactions occur in the same bunch crossing (which is around 50 in current Run 3 conditions), and out-of-time pile-up, where signals from previous or subsequent crossings overlap due to the long response time of detectors like the Liquid Argon (LAr) calorimeter. The LAr calorimeter, in particular, retains an electric pulse for over 16 bunch crossings, affecting the reconstruction of jets and other objects by introducing signals from multiple events into a single event. This is also relevant for muon detection in the Muon system, though to a lesser extent. Both types of pile-up impact particle reconstruction and can complicate long-lived particle (LLP) searches by distorting the timing and energy measurements.

Vertex and Track Reconstruction In ATLAS, the complex environment generated by high pile-up conditions necessitates precise reconstruction of vertices and tracks to distinguish the many particles. The detector distinguishes multiple proton-proton interaction vertices within each event, identifying the primary vertex associated with the highest-energy interaction as critical for accurate event characterization. Techniques such as adaptive vertex fitting are employed to resolve the primary from numerous secondary vertices. The primary vertex reconstruction highly depends on the pixel detector. For track reconstruction, using the full inner detector, the array of tracks generated by overlapping hits is managed using pattern recognition algorithms. These efforts are essential

to ensure each track is accurately linked to its corresponding vertex, significantly reducing the complications pile-up introduces to both data integrity and subsequent physics analysis.

Jets Jets are reconstructed using algorithms that cluster energy deposits in the calorimeters and tracks in the tracking system. The main jet-building algorithms from clusters and tracks are K_t, Cambridge/Aachen, and Anti-k_t. A review of each main algorithm is detailed in [130]. The Anti-k_t is often preferred in the ATLAS collaboration due to its natural interpretation and its robustness when facing soft jet pollution from pile-up [131]. The pile-up jets are produced through other interactions of protons in the same bunch. These algorithms are often configured with distance parameters that define the jet cone sizes in (η, ϕ). Thus, commonly building small-R jets ($R = 0.4$) and large-R jets ($R = 1.0$) that feature different properties and different particle content. The jet reconstruction algorithms are further discussed in Chapter 4 in the context of long-lived particles.

Photons and Electrons Photons and electrons are identified using the electromagnetic calorimeter and the tracking system. Photons do not render tracks as they are charge-less, apart from photons that convert into e^+e^- pairs in the inner detector. Their identification relies only on shower shape variables in the electromagnetic calorimeter, while electron identification benefits from tracking information. However, converted photons that decay into a pair of electron/positron tracks can also be used. The shower shape variables built from the LAr calorimeter response show high discrimination for recognizing electrons, photons, and jets. However, as will be discussed in the thesis, the shower-shape variables are not adapted to long-lived particles or close-by particles and, therefore, show important identification inefficiencies in such cases.

Identifying electrons or photons with respect to jets is a major topic of this thesis and is deeply detailed in Chapter 5.

Muons Muons are to be detected using the muon spectrometer and additional calibration information from the tracking system and the tile calorimeter. Their identification is achieved through pattern recognition in the muon chambers and matching with tracks in the inner detector. However, low-momentum muons create less activity in the spectrometers. They might rely more on the fraction of energy deposited in the calorimeters, thus lowering their reconstruction capacities in such energy ranges.

Taus Taus are identified through their decay products, which can be either hadronic jets or leptons, using a combination of tracking and calorimeter data. Tau identification algorithms exploit the narrow jet shape and the presence of secondary vertices in the ID from tau decays.

B-tagged Jets B-jets originate from b-hadron fragmentation and are crucial for many physics analyses, such as top quark property measurements and new physics searches. B-hadrons have longer lifetimes and greater mass than charmed mesons and light quarks, with a typical lifetime of 1.5 ps ($c\tau \approx 450\mu m$). A b-hadron with $p_T = 50$ GeV travels about 3 mm before decaying. This results in b-jets having measurable Secondary Vertex

and high decay product multiplicity, making them distinguishable from c-jets and light jets.

Jet b-tagging uses hadronic jets, associated tracks, and primary vertices. These jets are usually narrower due to the heavy mass boost; thus, small-R jets or variable-R (VR) track jets are used. Tracks are associated with jets based on their angular distribution ΔR(track, jet). With $\Delta R = \sqrt{\Delta\eta^2 + \Delta\phi^2}$ cuts that vary with jet p_T, since jets are expected to be narrower for higher p_T jets.

These flavour-tagging techniques are very important for searches involving heavy particles, such as electroweak resonances or SUSY particles that decay into SM particles. Such processes can produce emissions of top or b quarks. Chapter 6 presents a reproduction of an ATLAS SUSY search on a recasting framework that relies significantly on b-tagging. Multiple different algorithms present different working points that are difficult to reproduce in non-ATLAS-internal frameworks. However, Chapter 6 demonstrates that the efficiencies of b-tagging can drastically impact the results of a given search.

2.4 ATLAS upgrades

The ATLAS detector's stable performance over the years has required upgrades in both the software and hardware of its sub-systems. These modifications are motivated by different reasons, but the main upgrades are mostly motivated by the LHC operation conditions. In fact, between LHC runs, the accelerator is upgraded to provide higher energy collisions and a larger instantaneous luminosity. This implies that the experiments must be ready for such changes by improving all relevant sub-systems to ensure compatibility with different data-taking conditions. During LS2, the ATLAS detector underwent various maintenance activities, repairs, and smaller upgrades to ensure its readiness for LHC Run 3 [132]. This includes readout system improvements, new trigger technologies, LAr calorimeter, forward detector upgrades, and a new muon detection system [133] [134].

The LHC plan for the next phase (Phase II) aims to augment the accelerator's luminosity significantly. This pushes ATLAS to make major sub-system improvements and more detector replacements to secure future data taking and ensure detector compatibility with the new collision rate [135]. This causes new challenges to address, such as pile-up rejection, particle track isolation, and general granularity issues that the current setup cannot face. Additionally, the current sub-detectors have suffered important degradation due to radiation during LHC Runs 1, 2, and 3; this is particularly important for detectors closest to the collision point. The ATLAS Phase II Upgrade encompasses a significant number of changes to boost its performance and data acquisition capabilities. A list of major upgrades and new detectors for Phase II is presented below :

- **Trigger and Data Acquisition System:** The system will be upgraded to feature a single-level trigger with a 1 MHz output instead of 100kHz presently.
- **Electronics Upgrades:** Planned improvements include on-detector and off-detector electronics for the LAr Calorimeter, Tile Calorimeter, and Muon Detectors. This will feature a 40 MHz continuous readout with finer segmentation for better trigger performance [113] [136]. The current setup utilizes 34k cells at level 1, while the

HL-LHC system will present the possibility of selecting cells from the full container of 187k cells.

- **High Granularity Timing Detector (HGTD):** A new detector will be introduced, enabling precision time reconstruction with an accuracy of 30 picoseconds using Low-Gain Avalanche Detectors (LGAD) in the forward region ($2.4 < |\eta < 4.2$). This will improve pile-up separation and provide more accurate bunch-by-bunch luminosity measurements [137].
- **New Muon Chambers:** New chambers will be added to the inner barrel region. These upgrades aim to improve trigger efficiency and momentum resolution and reduce the fake rate.
- **New Inner Tracking Detector (ITk):** A fully silicon-based tracker will be implemented, featuring at least nine layers and extending up to $|\eta| = 4$. The optimized design reduces material usage and offers finer segmentation, providing better tracking precision [138] up to much higher η coverage.
- **Additional Upgrades:** Further improvements include upgrades to luminosity detectors for achieving 1% precision and the inclusion of sub-systems for heavy ion physics.

The ATLAS qualification task conducted during this PhD to obtain authorship was conducted on one main detector upgrade for Phase II, the new inner tracker (ITk). This chapter aims to present this specific upgrade briefly.

2.5 The High Luminosity phase of the LHC

The current run of the LHC will be followed by a shutdown during which multiple upgrades to the accelerator and the experiments will be implemented. The plan is to transform the LHC into a high luminosity machine [139]. The particle accelerator's new phase will be called HL-LHC (High Luminosity - LHC) and is planned, at the time of this thesis, to start with Run 4 in 2030. As one sees in the plan (figure 3.2), the nominal instantaneous luminosity of $L = 1.0 \times 10^{34} cm^{-2} s^{-1}$ will be boosted by a factor of five or seven times while the collision energy $\sqrt{s}$ will remain at the same level as Run 3 around 14 TeV.

The scientific benefit of such an upgrade will be mainly statistical. A higher number of collisions will greatly impact searches and studies dominated today by statistical uncertainties. As an approximate point of reference, using current instantaneous luminosity at the LHC, it would take more than 15 years of data to reduce the statistical uncertainties of the full datasets by a factor of two. Additionally, rare phenomena such as those considered in this thesis will be proportionally more common in this larger dataset.
As a reminder, the number of created events from a given process through the proton collision scales linearly with luminosity ($N = \sigma \times L$). This directly implies that with a high luminosity, the sensitivity to low cross-section processes is enhanced.

Entering the HL-LHC phase, rare phenomena such as di-Higgs or Dark Matter production can be studied [141]. In fact, the di-higgs searches in the most sensitive channels

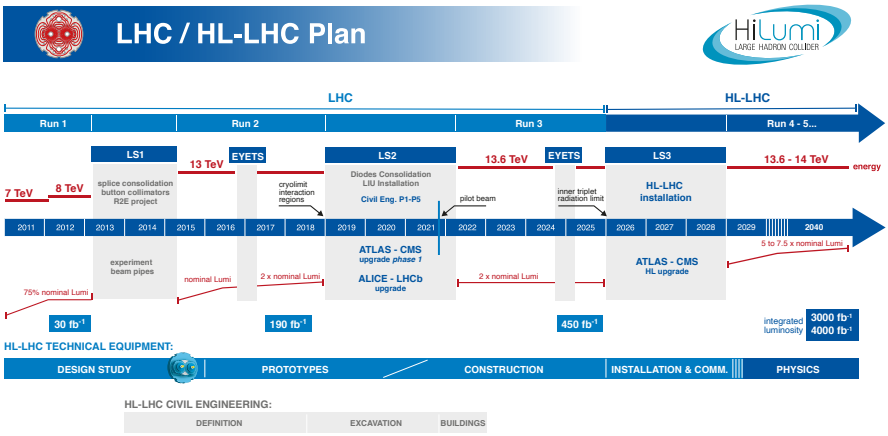


Figure 2.11: LHC evolution since Run 1 and plan for the high luminosity phase and future runs. From [140] in September 2024

($bb\gamma\gamma$,$bb\tau\tau$, $4b$) are currently limited to statistics [142]. Larger datasets can be used to constrain the possible values of the Higgs self-coupling and the two-Higgs-two-gauge-boson coupling. Important exclusion plot updates of multiple BSM analyses become achievable by lowering the result limits at the same confidence level. Standard model predictions will also be tested with more precision, further confirming the SM robustness or finding deviations that might indicate new physics. By the end of 2037, the objective is to collect an integrated luminosity 3 000 fb^{-1}, which is ten times the expected collected data of Run 3.

2.6 The need for a new tracker

This increase in luminosity comes with necessary modifications to the sub-detectors since there will be a higher event rate, number of collisions per bunch crossing $< \mu >$, radiation, and fluences. The average number $< \mu >$ will increase significantly from 25 to 200 [139] [138], and the total ionizing dose (integrated over time) to the innermost pixel layer will consequently increase from 160 Mrad to 1700 Mrad. The hardware must be robust to cope with a high radiation environment while keeping the trigger rates at least at the same values as for Phase 1 of the LHC with similar transverse momentum thresholds. As mentioned, a completely new inner tracker will be built. Tracking reconstruction precision will be very important in coping with the great number of pile-up events. It will be primordial to differentiate particles coming from different proton-proton primary vertices. However, it is a difficult task since the mean distance between primary vertices will be typically under the mm [138].

This new inner tracker (ITk) will be built fully using silicon semiconductors. The next section aims to explain the reasons behind this choice of detector system.

2.7 Silicon semiconductor detectors for ITk

In crystalline materials, the organization of electrons follows the guidelines of the Pauli exclusion principle, leading to the formation of energy bands. These bands are an extension of the energy levels that individual atoms exhibit when the number of atoms is large. Semiconductors possess two main bands: the valence band and the conduction band. Under low-temperature conditions, the valence band is fully occupied, while the conduction band remains vacant. Inversely, when the temperature rises, thermal energy allows some electrons to join the conduction band, thereby initiating conductivity from free electrons and holes. The energy required to form an electron-hole pair is called a band gap. Electrons within the conduction band and holes within the valence band exhibit behaviors similar to free particles.

Semiconductors can be doped with other elements. Adding specific impurities can alter their conductivity. N-type semiconductors are doped with elements that introduce extra electrons, creating an excess of negative charge carriers. In contrast, P-type semiconductors are doped with elements that create "holes" or vacancies in the crystal lattice, effectively creating an excess of positive charge carriers.
At the interface of an n-type and p-type semiconductor, disparities in Fermi levels create surplus carriers to diffuse into the adjacent material until thermal equilibrium aligns the Fermi levels across both materials. This region, devoid of charge carriers, constitutes the stable depletion zone.

The external voltage on the semiconductor allows for manipulation of the depletion zone's size. For particle detection applications, the objective is to maximize the depletion zone, within which the absence of free carriers facilitates the collection of charge carriers generated by ionizing particles to be detected, thus maximizing the hit efficiency. Nevertheless, the depletion zone can suffer from the high radiations it endures. In fact, radiation can displace silicon atoms in the structure, which leads to traps for charge carriers. Additionally, excessive radiation can worsen the charge collection efficiency over time and augment the leakage current of the device, which increases the intrinsic noise. To counter these issues, the operating temperature of silicon detectors is lowered to reduce the mobility of charge carriers, therefore limiting the leakage currents and the rate at which traps capture charge carriers. Moreover, to prevent runaway breakdown— a severe electrical breakdown caused by excessively high electric fields accelerating electrons to energies high enough to ionize other atoms in an avalanche— it is crucial to monitor the bias voltage. This control helps balance the maximization of the depletion zone against the risk of damaging the detector through uncontrolled current amplification.

Silicon detectors have superseded gas-based counterparts in tracking systems due to their superior position resolution and enhanced energy resolution. The advantages come from silicon's high density at room temperature and low mean ionization energy. Silicon has an energy band gap of 1.12 eV and a mean ionization energy of 3.6 eV. With a low radiation length X_0 of 9.37 cm, thin silicon detectors minimize multiple scatterings.

These properties facilitate the generation of substantial signals with minimal active thickness, ensuring good spatial resolution. When a charged particle crosses the silicon sensor bulk, it typically generates around 80 electron-hole pairs per micrometer. Reverse polarization of the sensor makes the charge carriers drift towards the electrodes within

the depleted region, inducing signals on the readout electrodes.

Silicon detectors form a pillar of modern High Energy Physics (HEP) experiments at colliders. The ITk detector will be built using silicon-based detectors with two main technologies: strip detectors and pixel detectors. This thesis work focuses on ITk pixel detectors [143], which will play a crucial role in primary vertex reconstructions as they will be incorporated in layers closest to the interaction point.

The dense particle fluence, reaching several 10^{11} particles per square centimeter per hour near the interaction point, implies significant challenges. This particle flux contributes to sensor and electronics damage. At high hadron fluences, prominent radiation damages lead to increased leakage current, altered operational voltage, and reduced signal amplitude. This, together with the necessary high bandwidth, is the main challenge ITk has to face. The distribution of modules layout of the detector is optimized to minimize radiation damage.

2.8 Pixel detectors

Pixel detectors are chosen to ensure the most precise measurement of a charged particle's position when passing through one module [144] [145]. These detectors are made of 2-dimensional arrays of single-pixel detectors, each single-pixel being independent. Minimizing the pixel size (or pitch) provides a more accurate hit-position measurement. Using more precise space points directly improves the reconstructed trajectory of a passing particle, notably when using several layers of pixel arrays, and will help distinguish between tracks and vertices coming from different p-p interactions. However, reducing pixel size also intensifies several challenges: it elevates the complexity of readout electronics due to an increased density of readout channels, enhances the thermal management demands due to higher power consumption, and complicates manufacturing processes, potentially increasing production costs and reducing yield. Additionally, smaller pixels can degrade the charge collection efficiency and create additional noises, such as cross-talk, further complicating the operational requirements of such high-precision detectors. These factors necessitate a careful balance in the design to optimize performance without compromising detector functionality and longevity.

Figure 2.12 shows the layout of a single-pixel detector, in which the active material in the bottom part is connected via a metal sphere to the front-end electronics on the top. This sketch illustrates the anode and cathode that collect the charges on the top and the bottom of the sensor. These are called planar sensors. This connection technique is called bump-bonding and allows the efficient link of a multiple-pixel sensor to multiple readout channels of the front-end chip. The charge collection on the cathode following an ionization from a passing particle in the sensor will induce a signal in the front-end (FE) electronics, which digitizes and sends it to the readout system.
The bump-bonding process (hybridization) requires highly precise machinery and is done through outside vendors after quality control of the sensor wafers by ITk and the wafer manufacturer.

Complementary, ITk will build 3D sensors that differ from the planar sensors. This different technology imposes the cathode and anode to penetrate perpendicularly to the

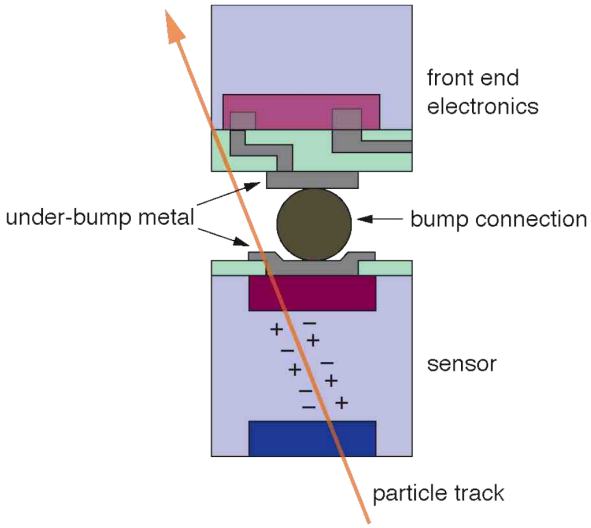


Figure 2.12: Illustration of a single pixel detector sensor. Particles ionize the active material (sensor), and the resulting pair charges drift towards the anode and cathode on the top and bottom. The collection of charges in the cathode is passed through the bump connection and creates a signal in the electronic chip. If the signal is above a given threshold, the acquisition system will record a hit. Taken from [144]

active material. The charges drift towards these columns. The benefits of 3D pixels with respect to planar pixels are presented in the following section.

2.9 The ITk layout

The next ATLAS inner tracker will be divided into two main substructures [138]: the pixel (innermost) and strip detector. Figure 2.13 provides a sketch of ITk's layout. Both systems are differentiated in two different colors.

The sensors within each part are arranged in a skeleton shaped like a cylinder around the beam axis. The inner part will host pixel detectors, and the outer part will strip detectors. The pixel system is further divided into five layers: L0 to L4. The layers L0 and L1 form the inner system of the ITk pixel, while L2, L3, and L4 form the outer barrel and outer end-caps. L0, being the closest layer to the beam axis and less than 50 mm away, is the layer that will endure the highest fluence during Run 4. This fluence is around 10 $e^{16} n_{eq} cm^{-2}$, which is one order of magnitude superior to the outer pixel layers. 3D Pixel sensors will be used in L0 to guarantee better robustness when facing semiconductor degradation over time. In fact, their vertical electrode design shortens the charge collection path, allowing for faster collection and reducing the risk of charge trapping from radiation damage. Consequently, the further layers L1 to L4, which face less fluences, will be built out of planar sensors. These layers will hold on ITk's quad pixel modules with a pixel size of 50x50 μm^2 and a thickness of 150μm (outer system) and 100μm for L1 (to reduce the material budget in the denser region). The Laboratoire de Physique Nucléaire et des Hautes Énergies (LPNHE), where I conducted my PhD research, is involved in the production of quad modules for the outer pixel system (L2-

L4). These quad modules, which consist of planar sensors with four electronic chips, are the main focus of this work.

ITk's outer part, 400-1000 mm in R, is composed of 4 pixel strip layers for the barrel area. Additionally, 6 pixel strip layers for the forward region are positioned at 90deg to the beam z axis.
In the inner part, the vertical modules corresponding to high η values are named ring modules.

An interesting aspect of ITk's layout is the inclination of pixel sensors with respect to η in each layer. Modules are parallel to z for the barrel region and perpendicular for the forward with inclination optimization in transition zones. This inclination provides three major benefits to the tracker's performance :

- The full coverage of the η range is achievable using less silicon surface.
- Incoming particles cross smaller amounts of material at large η. This improves transverse momentum resolution when $|\eta| > 2.7$, especially for low-momentum particles.
- More hits perpendicular to the sensor surface in the first layer at higher η provide less uncertainty of the track reconstruction close to the interaction point and yield a better reconstruction of primary vertices.

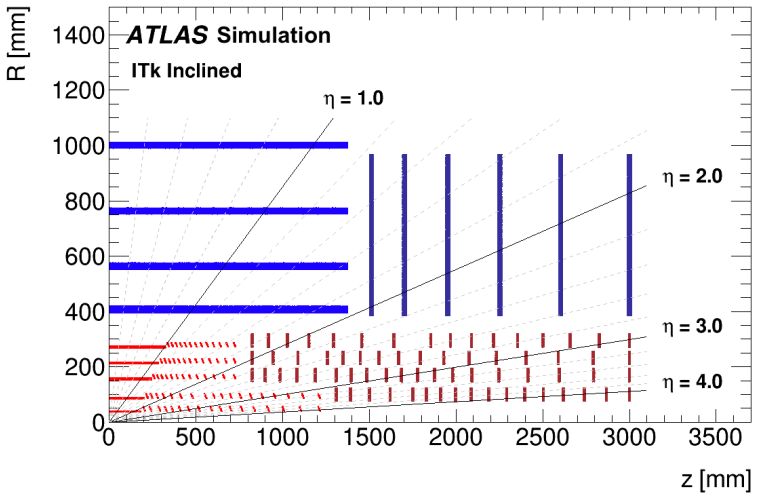


Figure 2.13: ITk layout in one quadrant and only showing the active detector elements. Strip detectors are shown in blue, and pixel detectors are shown in red.

Figure 2.14 provides a focused view of the inner ITk detector. The five layers of pixel quad modules L0, L1, L2, L3, and L4 are respectively positioned at 40 mm, 85 mm, 155 mm, 213 mm, and 271 mm in radial distance from the beam axis.
One sees that depending on the layers, the pixel module's inclination differs significantly. The length of layers, the module's thickness, the inclination, and the separation between layers all impact heavily the track reconstruction optimization and budget material reduction.

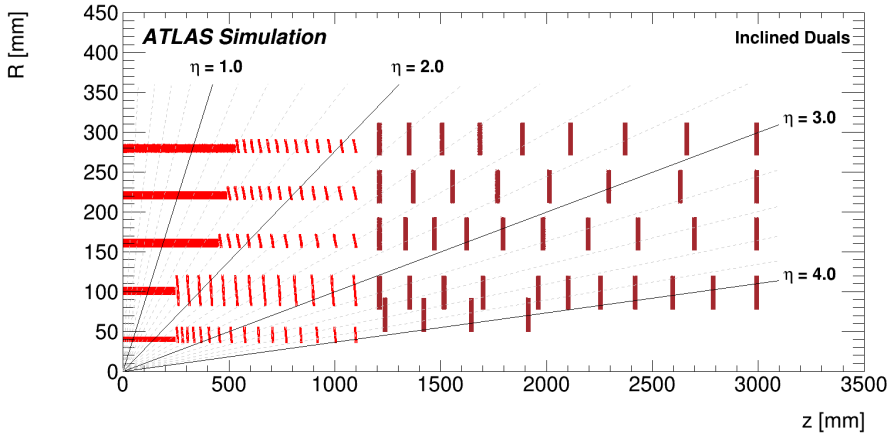


Figure 2.14: Inner part of the ITk detector. It is only composed of pixel modules. Barrel layers L0-L4 are shown in red, and all end-cap rings are darker. The position of inclined pixels is visible.

2.10 Quad and Triplet modules

As mentioned, two technologies are used for the sensors: 3D and planar. 3D sensors have n^+-type and p-type columns in p-type substrate; planar sensors are n^+-in-p type.
They will be used in different parts of the detector: 3D sensors will be chosen for the inner layer because they are more radiation-hard and require lower bias voltage (lower power dissipation); planar sensors will be used for the outer layers, with the layer L1 (closest to the beam) using thinner sensors (100 µm instead of 150 µm). The thin modules of L1 provide less material budget and lower power dissipation. However, the downsides are the risks and complications of processing such thin substrates and, consequently, the higher production cost. The pixel pitch of the central part (barrel) of the innermost layer (L0) is 25 $\times$ 100, as opposed to 50 $\times$ 50 μm^2 for the rest. Table 2.2 summarises the active thickness, position, pixel pitch, and overall sensor size of different types of sensors in the pixel detector and the types of modules into which they are planned to be assembled.

Module Type	Thickness μm	Position	Pixel pitch μm^2	Sensor dimensions cm^2
Planar - Quads	150 100	L2-4; R2-4 L1; R1	50 x 50	4 x 4
3D - Triplets	150	R0-0.5 L0	50 x 50 25 x 100	2 x 2

Table 2.2: Specifics of different ITk pixel modules.

2.11 Hybrid modules and readout

The ITk planar pixel detectors are built from sensor tiles that are bump-bonded pixel-by-pixel to the front-end (FE) readout electronics. The FE chips are based on 65 nm CMOS

technology. The combined sensor and FE chip assembly is then mounted onto a flexible printed circuit board, referred to as a "flex." This flex board provides the necessary connections to external peripherals for module signal readout. It contains circuits to separately power the readout electronics and apply bias voltage, which expands the depletion zone in the sensor. The complete assembly of the flex, sensor, and FE chips is called a hybrid module. These hybrid modules can be directly connected to power sources and external computers using specific pigtails, enabling testing and operation. Figure 2.15 illustrates the cross-section of a hybrid quad module; connections between the hybrid module's FEs and the flex are made through wire-bonds.

The pixel data, including induced current and timing information, are digitized and organized by the readout chip in a 2D matrix, with each pixel represented by a specific column and row. The flex communicates with external connections through a PCIe link using dedicated software called Yet Another Rapid Readout (YARR). This data acquisition (DAQ) system controls and reads data from these hybrid modules, utilizing an FPGA-based architecture. Initially developed for current ATLAS Pixel detector readout chips, YARR has been upgraded to accommodate the increased bandwidth requirements of the HL-LHC, increasing from 160 Mb/s to 5 Gb/s.

YARR not only handles data readout but also configures and fine-tunes pixel parameters such as signal gain.

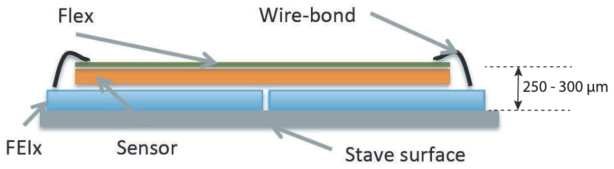


Figure 2.15: Hybrid Quad module layout. The flex is glued to the sensor, which is bump-bonded to four front-end chips. Very small wires connect the front-end readout pads to the flex. FEIx refers to one of the four FE chips of a quad module.

Chapter 3 will explore the detailed use of YARR, the quality testing procedures, and detection efficiency calculations based on test-beam data for these hybrid modules.

2.12 Summary

This chapter has presented the role of the LHC. In fact, it enables a wide range of particle physics experiments through the use of complex detectors, each consisting of sub-systems optimized for detecting specific particle features resulting from proton-proton collisions. The combination of signal responses across the multiple sub-systems allows one to identify particle types and measure their characteristics in each event. Nevertheless, challenges arise from the complex topology of p-p collisions that create in-time and out-of-time pile-ups, as well as detector-related difficulties related to noise or acceptance. As briefly discussed, the original purpose of each sub-system for object reconstruction in one event must be rethought for LLPs as one could expect final state particles of interest that do not come from the collision point.
As a general-purpose detector, ATLAS plays a critical role in experimental particle physics, relying on a large international collaboration to maintain, operate, and upgrade

these sub-systems. The performance of the sub-detectors is vital for efficient particle identification at the trigger level and for the accurate reconstruction of particle properties. This, in turn, directly impacts the quality of data used for various physics analyses.

Over time, radiation damage to the detector components and evolving beam conditions necessitate frequent upgrades and modifications. These upgrades ensure that the detector continues to perform optimally in increasingly harsher event topologies. The ITk upgrade is a key component of this ongoing evolution, especially given the LHC's planned increase in collision rates for Run 4. The tracker will be especially important, requiring enhanced radiation resistance and improved track reconstruction to reach similar resolutions compared to current standards in harsher conditions (as illustrated in figure 2.16). The ITk's innovative design, which includes both strip and pixel detectors, is optimized to meet these challenges.

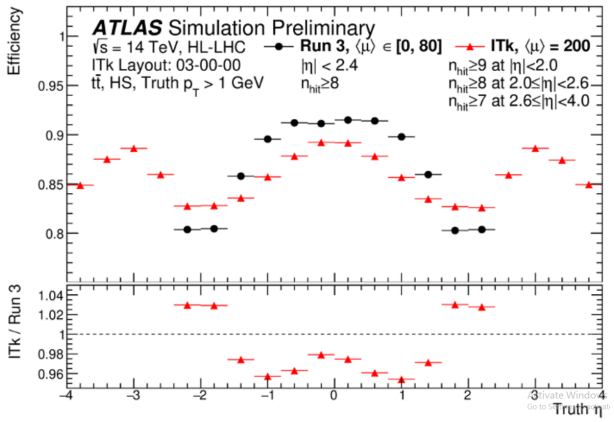


Figure 2.16: Tracking efficiency of the Run 3 and ITk hardware in their respective pile-up (μ) environments and the same collision energy [146]. The required number of hits for different eta ranges is labeled.

The following chapter will focus deeper into the qualification task for ITk pixel sensors in layers L1-L4, including testing, characterization, and performance evaluations, which are critical steps in ensuring the readiness of the upgraded detector for future data-taking.

Chapter 3

Contributions to the ITk project

This chapter presents an overview of different ITk-related activities conducted by the ITk Paris cluster including contributions of the present thesis. This includes module assembly, sensor and FE electrical tests, pixel-tuning procedures, and sensor performance assessments at test-beam.

Three groups form the ITk Paris cluster: the *Laboratoire de Physique Nucléaire et des Hautes Énergies* (LPNHE), the *Laboratoire de Physique des 2 Infinis Irene Joliot-Curie* (IJCLab), and the *Institut de Recherche sur les lois Fondamentales de l'Univers* (Irfu). This cluster is involved in the quality control, characterization, and production of quad-pixel modules, specifically targeting the ITk outer barrel.

To complete the qualification task (QT) for my ATLAS authorship, test-beam (TB) studies were performed for the ITk pixel detectors. This process required several weeks of TB shifts, which included bench setup, debugging, data collection, and quality control. Corryvreckan, the 4D track reconstruction software [147], played a major role in TB data analysis. These studies played a crucial role in characterizing sensor responses. Additionally, a preliminary study was performed to ensure results consistency by standardizing analysis parameters.

Complementary, this thesis contributed to various quality control procedures for sensors and FE chips at the laboratory. Especially, algorithms aiming at automatizing test procedures were developed including power supplies and climate chambers remote control.

3.1 Overview of hardware activities

To complement the information provided in Chapter 2, in ITk each silicon sensor is interconnected to one (single-chip cards (SSC)) or four (Quad modules) front-end readout chips to form a so-called "hybrid module" (or bare module). The hybrid module assembly is outsourced to industries such as HPK [148], FBK [149], and SINTEF [150]. Once received at the lab, each hybrid module is tested before being glued on and connected to a FLEX circuit board using micro-wires. At this stage, such an ITk module is ready to collect data and to be tested for integration.

A picture of an assembled Quad module ready for testing is shown in Figure 3.1. One

can see the four different FE chips as well as the wire bonds connecting the FE pads to the FLEX.

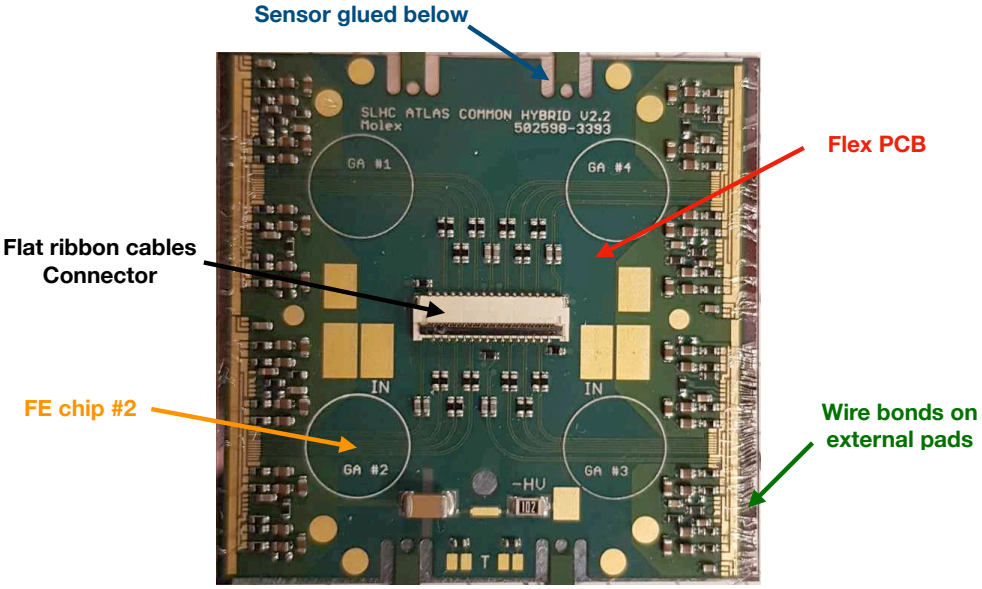


Figure 3.1: A picture of a Quad module after wire bonding as seen from the FLEX side. The module is about 4x4 cm^2. The FE chips are labeled GA1 to GA4. The flat ribbon connectors allow to connect the module to the PCI-e board controlled by the YARR software.

LPNHE is involved in the gluing and wire-bonding of modules and their quality control (QC). The robustness of the full assembly is demonstrated through thermal cycling and long-term stability tests.

The chronological order of the main assembling and testing steps at the lab are:

- High-precision individual component metrology: dimensions, alignments, and weight of both the bare module and the FLEX PCB are measured using optical comparators.
- Sensor electrical measurements: current-voltage sensor characteristics (IV curves) are produced to assess its leakage current against the bias voltage on its depletion zone.
- Assembly of the bare module on the FLEX PCB: specific tools are used to glue the two components with high geometric precision.
- Assembled module metrology: thickness, weight, and flatness of the module are measured with bare module-FLEX alignment to assess wire-bonding readiness.
- Module wire bonding: a high-precision machine is used to position and solder up to O(600) wires (Quad module) connecting the FLEX input and FEs output pads.

- Electrical tests: the verification of the proper operation of the different readout chip reading channels is conducted by probing specific pads with multi-meters.
- Trimming: initial configuration of FE electronics power regulators.
- Outsourcing of the micro-wire protection: a thin layer of parylene is deposited by an industrial partner on the connections.
- Module configuration: each pixel response is tuned by adjusting its digital-to-analog converters, allowing the identification of disconnected pixels.
- Performance characterization: reliability tests after thermal stresses and correct startup at cold temperatures are performed.
- Module detection efficiency measurement: each module's hit rates are tested under radioactive sources, or X-ray generators are done

Relevant testing procedures for multiple steps are found in [151–153].

After these operations, radiation tests are performed on few modules at CERN at the IRRAD facility. Their detection efficiency is checked before and after irradiation at CERN and DESY test-beams.

3.2 Production

Before entering the production phase of ITk modules, the Paris cluster has been involved in research and development of pixel modules of the RD53 collaboration [154] which is an ATLAS and CMS joint collaboration built to develop the next generation of pixel detectors for the HL-LHC with high hit rates capacities and radiation tolerance. Two SCC prototypes were successively produced, so-called RD53a [155] and RD53b [156], and served to develop ITk Quad modules.

The pre-production phase resulted in the ITkPixV1 chip Quad modules. Around 200 chips used for planar quad modules were assembled and tested by the Parisian cluster. This constitutes about 10% of the total planned module production for the group. This pre-production phase has enabled the assembly sites to develop infrastructure, test procedures, and expertise for production. This resulted in the design of upgraded assembly tools to simplify the procedure, enhance its precision and avoid misalignemnts between the FLEX and the bare module. Indeed, a misalignment between the FLEX and the module implies a difficult wire-bonding phase with error corrections.

The production has started in September 2024 and is expected to last for two years; the Parisian cluster will construct and test 2100 modules destined for the outer barrel. This represents approximately 33% of the total production of modules for the ITk's outer barrel. The 2100-module count includes additional modules (43%) to account for losses related to the intrinsic quality of bare components and modules that fail quality control during construction, loading, and integration operations.

After production, the modules are sent to loading sites where they will be mounted onto the specific mechanical structures that will be inserted into ITk's pixel barrel main structure.

The QT-related work on ITk was done mostly on RD53 SCCs as well as pre-production quad modules.

3.3 Modules Assembly

In this section, we discuss the module assembly and insist on the importance of alignment.

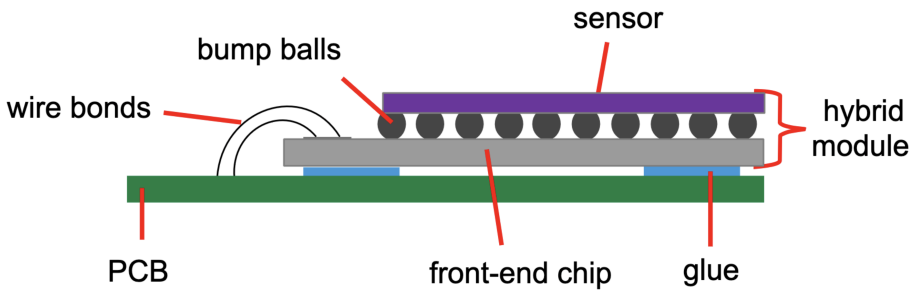


Figure 3.2: Crossectional view of an assembled module consisting of a hybrid module glued and wire bonded to the PCB.

3.3.1 Gluing

The gluing procedure is done using a dedicated tool known as a gluing "rig" or "jig". This object is divided into two main aluminum plates that host each bare part. The two halves of the gluing tool are made to embed on each other only one way. This gluing rig presents precise placement of columns and screws tailored for the bare hybrid module and bare PCB. The positioning of both bare pieces is constrained to embed them in the support. The support also encapsulates a suction system using an external pump to create a thin vacuum layer, which forces the flex to remain in place once it is correctly positioned. A fixed quantity of glue is deposited onto the flex, and the gluing rig compresses both parts. The applied pressure is calibrated to achieve the aimed module thickness. The glue used is an Araldite epoxy adhesive, and it was chosen to withstand the thermal and radiation stresses that the ITk modules will experience. The two components stay in contact for multiple hours until the glue hardens completely.

3.3.2 Wire bonding

Once the module is glued, it is prepared for the wire bonding step. It is placed on the wire bonding machine, and the wire soldering protocol is configured for the module type. However, metrology measurements conducted after gluing, such as determining the actual height, amount of glue used, and alignment of the flex relative to the sensor, may indicate the need for adjustments to the bonding scheme. These measurements are used to fine-tune wire bonding parameters, correcting for slight shifts or rotations

from the expected position. The bonding program is then adapted for each module to account for these variations or require delicate manual intervention. This type of situation is time-consuming and slows down the full assembly chain. Therefore, it is important to minimize such events by conducting proper procedures at the gluing step to ensure a correct alignment. A concept-proof tool was developed to show how one can use a raspberry pi 4 and a camera to verify the FLEX positioning on the gluing jig during the gluing step. Such a tool would measure the angle between reference points of the jig and the border of the FLEX PCB to validate the positioning.

3.4 Electrical tests

Several electrical tests are conducted in the quality assurance procedures. Both the sensor and the FE chip have separate tests. The sensor takes a high voltage (HV) input to deplete the active region and presents leakage currents of the μA order. The FE chips need a lower voltage and present a high current consumption to run (order of 5A) due to the high number of individual reading channels.

The initial module power-up is conducted in a clean room as certain voltages must be measured by direct contact on pads. For this step, a data acquisition (DAQ) card is required to communicate with the module and determine the fine adjustments of the embedded analog-to-digital converters (trimming). Once it is done, modules remain encapsulated in the carrying cases and leave the clean room for a series of electrical tests.

In a temperature-controlled environment (such as a cold box or climate chamber), a module undergoes a series of tests repeated at different temperatures. The tests are made at -15, 20, and 30°C. LPNHE's climate chamber, which is used for these steps, is capable of hosting multiple modules simultaneously. It can reach temperatures from -55°C to +60°C (during long thermal cycles) and presents multiple integrated sensors used to monitor important parameters such as humidity and dew point to avoid damaging the modules. These tests encompass measuring the current-voltage (I-V) curve of the sensor, evaluating the VI curve of the ASIC power supply regulation system (labeled SLDO and explained below), and performing data acquisition using an ionizing radiation source (radioactive or X-ray source). Thermal cycling is also conducted to assess the module's robustness under thermal stress.

As part of the QT project, a significant portion of work was put into evaluating IV curves and testing SLDO correct startup at different temperatures on prototype and preproduction modules, including both SCCs and quad modules.

3.4.1 I-V Curves

For each module, an I-V curve is computed from the sensor's leakage current for various voltages. The sensor's leakage current is measured step by step for different bias voltages (order of 1V per second). The resulting curve allows one to determine the operational range and the breakdown point of the sensor. The breakdown point of the sensor is the voltage at which the sensor experiences a rapid increase in current flow, potentially damaging it due to excessive bias voltage. In silicon particle detector sensors, this breakdown occurs because a high voltage generates a strong electric field across the silicon lattice.

This field accelerates free charge carriers to such high speeds that they can ionize the medium, creating additional charge carriers in an avalanche effect.
A similar breakdown trend is observed throughout the different modules but not always at the same exact values (see figure 3.3). The I-V curve is measured using a Kethley 2400, which supplies the bias voltage to the sensor and reads the current at room temperature in a light-tight environment. By increasing the bias voltage, the sensor's depletion zone gets larger up to a stable full depletion. After reaching full depletion, the increase in bias voltage will eventually cause the breakdown, showing a sudden increase in leakage current. This leakage current depends on several parameters, such as the size, thickness of the sensor, or the temperature. During these tests, the FE electronics are not powered.

The quality validation criteria are defined for the different types of modules. Planar $150\mu m$ sensors must have an absolute breakdown voltage point greater than $V_{depl} = +70V$, and on the other hand, the 3D sensors should not exceed $V_{depl} = +30V$.

These tests are of particular interest or irradiated modules. IV curves conducted on irradiated modules are made to asses how robust they are and to understand how the operational range is shifted in bias voltage. For these irradiated modules, the test is conducted at lower temperatures ($-50C°$). In fact, the total absorbed fluence that a module has suffered increases this leakage current significantly, thus requiring a lower temperature to limit it.

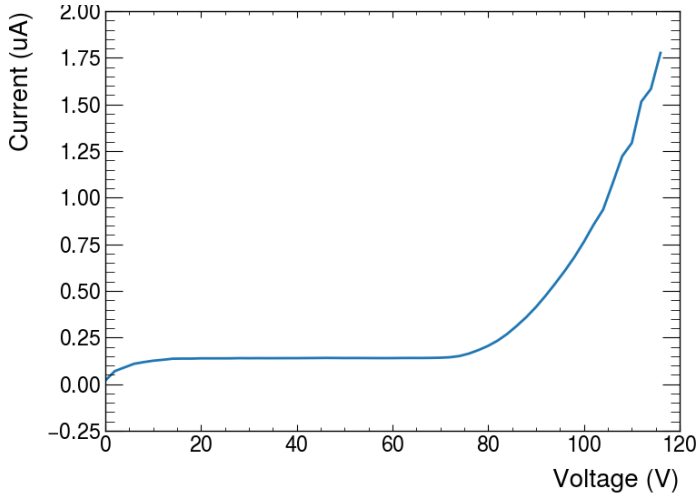


Figure 3.3: An IV curve of a planar module's sensor taken at room temperature. The breakdown point is visible at 80V, which means the depletion zone is already fully depleted prior and further increase in voltage is not necessary for particle detection as it only causes the current to jump.

3.4.2 SLDO qualification

The Shunt Low Dropout (SLDO) is a power regulation system designed to provide stable and efficient voltage regulation to the front-end (FE) chips. The SLDO operates by shunting excess current away from the chips, maintaining a stable output voltage even under fluctuating power demands, and allowing regulation even with minimal input-to-output

voltage differences. This system generates both analog and digital voltages of the FE chips.
The SLDO system should "startup" at a given current value (about 1.2 A), at which point the FE voltage reaches the operating value. These values vary for different modules.

The SLDO system of FE chips must be operational at low and room temperatures. Thus, ITk modules are installed in a climate chamber or cooling box to apply the procedure that verifies the chips' power regulation system.

This test is conducted independently of the HV applied on the sensor since it concerns only the FE chips. One begins with a room-temperature assessment to verify functionality under typical operating conditions. Afterward, a cold test is repeated at $-35°C$. The SLDO startup procedure involves setting a voltage limit (2V) on the input V_{in}, powering up the chip by applying 1.2A/FE (Quad modules have 4 FE chips), measuring the resulting voltage, and then obtaining a VI curve by ramping down the LV PSU (power supply unit) in current steps. An example of the obtained VI curve is in figure 3.4. In this example, one can see the expected transition at which all the chips start successfully. The V_{in} plateau at high currents reflects the operating point of the chip.

To verify if the chip also starts at cold temperatures, one needs to turn it on with a sufficient current and measure the voltage at -35°C. If V_{in} is in a $\pm 0.01V$ range from the operating value measured at room temperature, 1.1V for figure 3.4 example, the FE chips have successfully started. If the SLDO fails to start at -35°C, the temperature is incrementally increased. A grade is given to each module depending on the temperature point at which it managed to start up correctly. In fact, the ITk pixel modules should work at low temperatures since irradiated modules are required to run at lower temperatures to limit the sensors leakage current. Additionally, the high currents of Quad modules directly imply high heat production, which is countered by starting the chip at lower temperatures.

A script using an MQTT interface was developed to remotely control both the PSUs (Keithley 2410) and the climate chamber for this test. This script ensures that the procedure can be run remotely if the module is set up in the climate chamber. Such a script also allows the automatization of this type of procedure and optimization of the quality control chain.

3.5 Pixel calibration

One can control, through YARR, multiple DAC (digital-analog converters) parameters of individual pixels on each FE chip [157]. This allows the calibration of the module's signal threshold for registering a hit as well as managing noisy pixels with a pixel masking procedure. One can configure pixel parameters to modify individual pixel responses for a given absorbed charge. The disparity in bump-bonds connecting the pixels anodes to the FE chips across the pixel layer requires such individual calibrations to guarantee a homogeneous response.
YARR offers guidelines on how to approach this homogeneous response by performing scans across the pixel matrix with different adjustment levels. The full procedure is described below, and it is referred to as "tuning" the module.

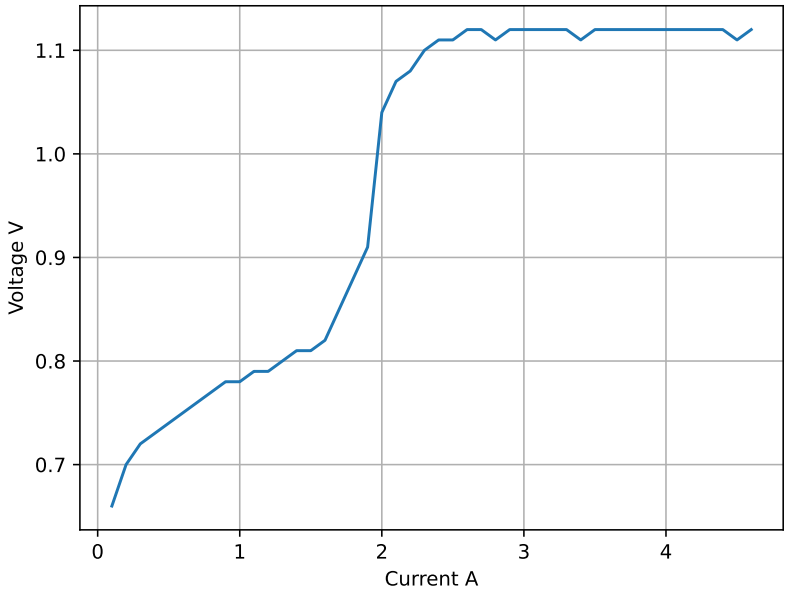


Figure 3.4: A VI curve of a digital module (no sensor installed) taken at room temperature.

3.5.1 Yarr tuning

The tuning of a module is done at the laboratory. All the steps are made in a light-shut environment at $20°C$ ($-50°C$ for irradiated modules). A climate chamber or a cold box is used during these steps to guarantee such an environment. Once tuned, a module might need further re-tuning. For instance, during the test-beam data-taking periods, module tunings must be redone since the change in environment can have an impact. However, the previous (original) tuned parameters are saved in a configuration file and are used as a base for such re-tuning.

The rest of this section briefly describes various tuning steps performed with YARR.

Digital Scan

During this step, digital hits are introduced, mimicking the output of the FE discriminators. Using such digital hits one can assess malfunctions at the end of the readout chain by investigating whether the number of hits is different from the actual number of injections. Based on the result, the pixels experiencing malfunction are deactivated within the module.

Analog Scan

The following step includes actual charge injections of a chosen intensity N times over all pixels. The analog scan evaluates the readout chip's performance. Dead pixels will show a 0 occupancy result, while noisy pixels will surpass the signal threshold more frequently than expected. Typically, the analog scan is conducted at least twice: once before and once after threshold adjustment as part of a calibration sequence.

Threshold tuning

This step involves adjusting each pixel to ensure that only signals above a certain level are registered, avoiding unnecessary noise-triggered readouts. A typical threshold target for a sensor of 100-150 μm thickness is 1000 electrons charges. In cases of irradiated sensors, a higher threshold may be necessary due to increased noise levels. This process aims to render stable hit detection and correct charge and Time-over-Threshold (ToT) measurements across the entire chip. It is conducted through a multi-scanning procedure, for which a pre-determined charge is injected each time. Hits are recorded for charge values above the threshold, resulting in a digital answer of the discriminator. This procedure aims at having a homogeneous response of 50% firing rate across the pixel matrix at the determined charge target. The threshold tuning is monitored and accepted when the occupancy distributions of pixels are Gaussian-centered at 50%.

To achieve an optimal result, multiple runs of tuning are conducted using three different YARR pixel scans: `Global` general adjustment where a common threshold is tuned for all pixels, `Pixel` level adjustment where each threshold is changed, `Fine Pixel` changes of individual thresholds with finer modifications. These adjustments are directly made using the pixels DACs. In fact, ITk modules present a TDAC (Threshold DAC) for every pixel channel that can be accessed and controlled by YARR. Figure 3.5 shows the evolution of occupancy of all chip pixels during a tuning procedure. One can see that the number of pixels triggering too much or not enough (respectively occupancy 0 and 100) drops down significantly while the number of pixels recording 50% increases at each step. Figure 3.6 illustrates the resulting distribution of pixel detection thresholds after one full tuning cycle.

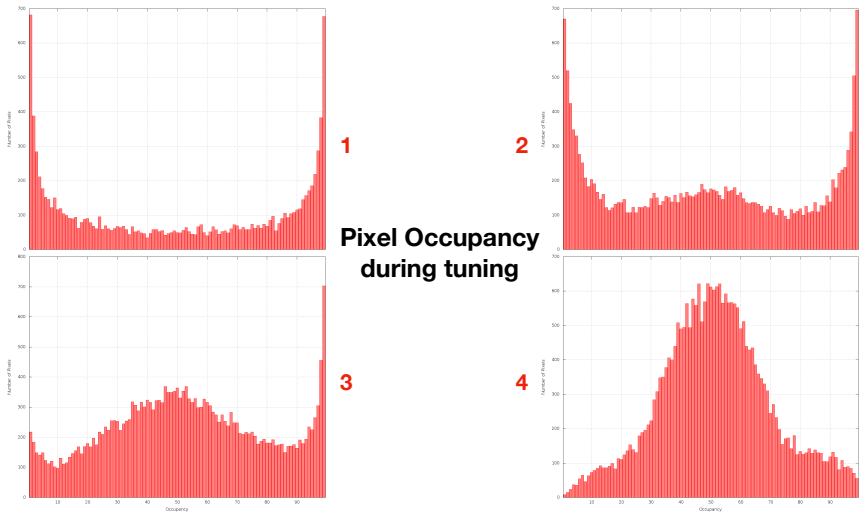


Figure 3.5: The occupancy distribution during 4 steps of pixel threshold tuning. The x-axis is the occupancy in percentage, and the y-axis is the number of pixels. Realized on an RD53A SCC

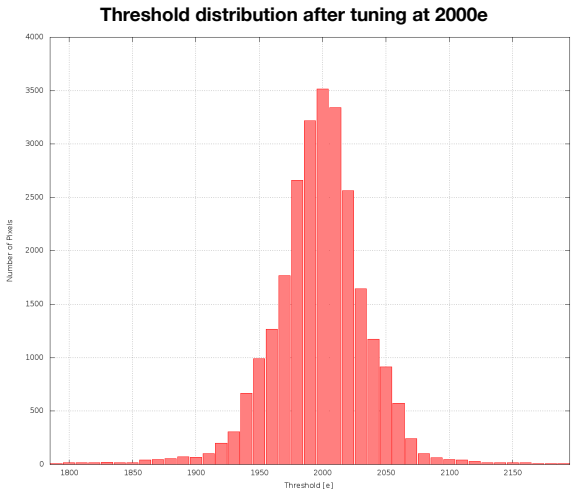


Figure 3.6: A resulting distribution pixel thresholds after tuning. Realized on an RD53A SCC with a target threshold of 2000 electron charges.

Noise Scan and masking

This scan is conducted post-tuning. At this step, random triggers are sent to the chip, and the number of hits from each pixel is recorded. Pixels exhibiting a higher-than-expected rate of hits, likely due to intrinsic noise in specific channels, are subsequently turned off during data acquisition using the individual pixel DAC.

3.6 Testbeam characterization :

Once an ITk module passes the qualification criterion in the laboratory, its particle detection efficiency is assessed. In fact, ITk modules are required to have a particle-hit detection efficiency superior to 98% (97% for irradiated ones). A selection of modules can be tested under X-ray tubes or radioactive sources. Such a simple experimental setup can be composed of a source and two scintillators (see figure 3.7) surrounding the module. Triggering is done in coincidence with the scintillator's PMTs (photo-multiplier tubes). This simple setup can provide a general measurement of the sensor's detection capacities.

Nevertheless, a more precise measurement requires a high number of statistics and a significantly better-controlled environment (focused source of high-energy particles) to reconstruct particle tracks and verify hit positions on ITk modules where an intersection is expected.
To study the detection efficiencies of ITk pixel modules in such conditions, several modules are sent to test beam facilities. These modules come directly from various ITk institutes after passing the QA procedures. Test-beam campaigns are organized throughout the year to properly measure the pixel sensors' detection efficiency of those multiple modules in various operation conditions. Test-beam campaigns are also an opportunity to test and further develop the readout system and acquisition software. Results presented in this chapter were obtained from data acquired in 8 campaigns of 2022. This was during the prototyping and the early pre-production phase.

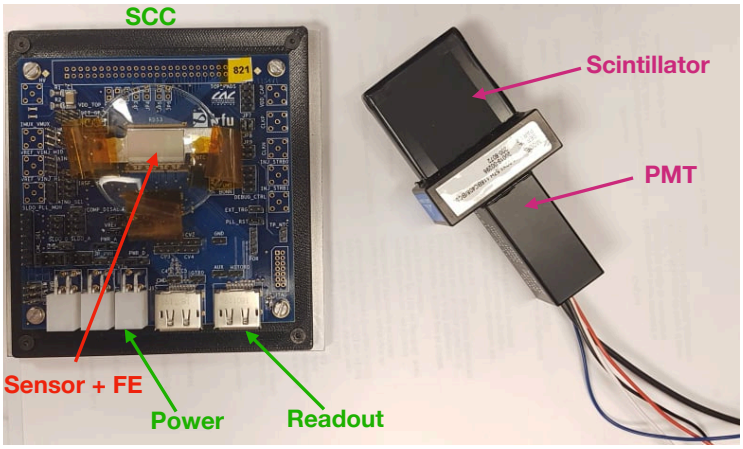


Figure 3.7: A picture of an SCC hosting a hybrid module wire-bonded to the chip next to a standard small crystal scintillator and photomultiplier tube assembly.

3.6.1 Test beam facilities

ITk's test-beam campaigns mostly occur with CERN's SPS in the north area test-beam site. Other sites have also been actively used in the past, such as CERN's east area, which receives protons from the PS or at DESY facilities. Figure 3.8 illustrates CERN's complex and highlights the SPS and PS experimental beam areas. The particle type and energy of these three different beams are in table 3.1

Location	Particle Type and Energy
DESY	Electrons / Positrons @ 5.8 GeV
CERN East area PS	Protons @ 25 GeV
CERN North area SPS	Protons @ 400 GeV

Table 3.1: Particle Accelerator Facilities used for ITK test-beam campaigns.

The results discussed in this chapter will only consider data taken using the SPS beam. The North Area facility is used for various R&D purposes on a multitude of experiments in HEP, particle astrophysics, and others. It houses diverse experimental facilities and beamlines, offering a range of possible studies and experiments. Figure 3.9 shows how a target station splits the SPS beam into multiple beamlines. These beamlines are designed to match specific experimental requirements and can offer different types of particles at different energies. ITk test-beam campaigns utilize the designated target station T4, specifically through the H6 line, such as other non-ATLAS pixel detector projects for the HL-LHC [158] [159]. In this beamline, ITk modules encounter a 120 GeV pion beam positioned perpendicular to the sensor and aimed at the center. Data is acquired and analyzed afterwards to evaluate the device's performance.

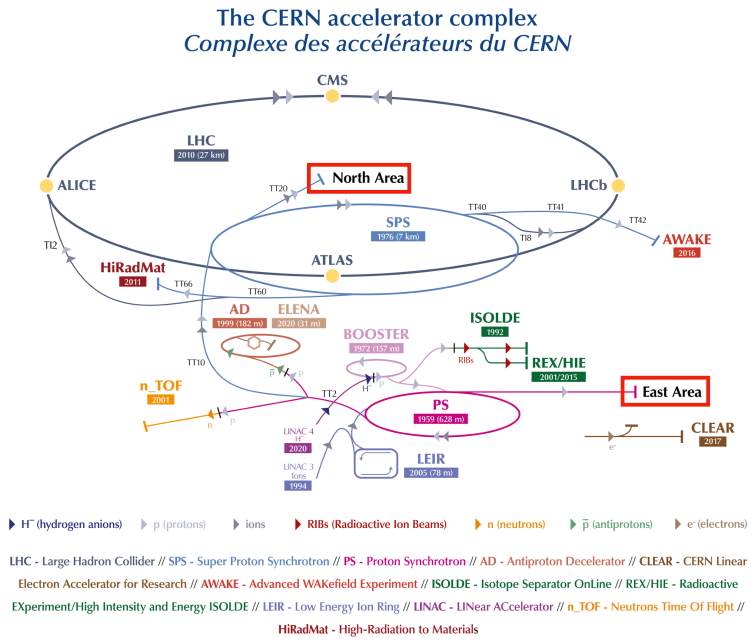


Figure 3.8: The CERN accelerator complex. The north and east test-beam areas are highlighted in red. Modified from [160].

3.6.2 Test beam main activities of 2022

The 2022 ITk pixel test-beam campaigns focused on characterizing the detection efficiency of multiple types of modules both Single Chip Cards (SCC) and Quads planar sensors. A list of tested module types is shown below.

- SCCs with RD53A/B FEs and 3D pixel sensors (50x50 μm^2)
- Irradiated SCCs:
  - Uniformly irradiation on sensor: 1×10^{16} neq/cm^2
  - Non-uniformly irradiation on sensor: 1.7×10^{16} neq/cm^2
- Prototype Quad: ITkPixV1 (RD53B) FE and planar pixels (50x50 μm^2)
- Preproduction Quad sensors : ITkPixV1 FE and planar pixels (50x50 μm^2)

Multiple aspects of the module's detection efficiency were tested. The impact of temperature, the sensor bias voltage, the module target threshold with different tuned configurations, the angle of the plane with respect to the beam, and the test detection efficiency degradation after module irradiation. This agenda required multiple data-taking sessions of 1-2 weeks with varying bench step-ups.

Additionally, from testing the modules, these sessions allowed to adrees software-related challenges. In fact, issues concerning the data acquisition and the simultaneous control of multiple modules were present as the ITk pixel group had just transitioned to the YARR software. The 2022 test-beam campaigns also encompassed software development for linking the data acquisition software EUDAQ [161] to the YARR readout system.

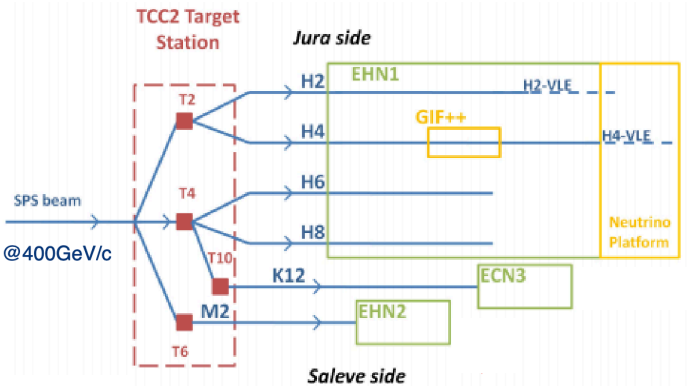


Figure 3.9: Target station TCC2 in the North Area.

Overall, the test beam activities during 2022 were crucial to developing a stable workflow but came with important challenges.

3.6.3 Challenges and opportunities

The main challenges of 2022 ITk's test-beam campaigns during the prototyping phase were:

- Ensuring stable communication with multiple modules simultaneously using one (or two) YARR PCIE cards;
- Controlling the environment to investigate the impact of a set of parameters;
- Verifying the stability of modules over long data-taking periods;
- Improving the track reconstruction workflow;
- Developing correct links and data formats between YARR and EUDAQ;
- Investigating the impact of irradiation.

This period also included the first test beams on prototype Quad modules. Since quad modules were not ready for testing before, all previous campaigns focused on SCCs. Thus leading to the first test-beam results of Quad modules with the ITkPixV1 FE chips.

3.7 Experimental setup at CERN:

At the test-beam facilities, the particle beam passes through a test bench composed of multiple detector planes. These include a telescope for track building, a timing reference detector, the Devices Under Test (DUT), which are the ITk modules, and scintillators for triggering. The timing reference is a FEi4 pixel detector [162], which serves as a crucial

component for the event building scheme. It provides precise timing information synchronized with the triggered events, facilitating accurate data acquisition. Additionally, it is used in the trigger logic unit as part of the necessary coincidence planes. In each triggered event, all signals from each plane's pixels are registered using the EUDAQ data acquisition software [161], which references each connected FE chip separately. Modifications are implemented through a Yarr-Eudaq plugin so that the four individual chips of a Quad module are merged correctly. With extra manipulations of EUDAQ, the YARR configuration of the ITk modules, which encapsulates all the chips post-tuning configuration, is added to the *.raw* event files; this offers the possibility of verifying the module's tuning configuration when analyzing the data but has not yet been automatically implemented in the analysis software.

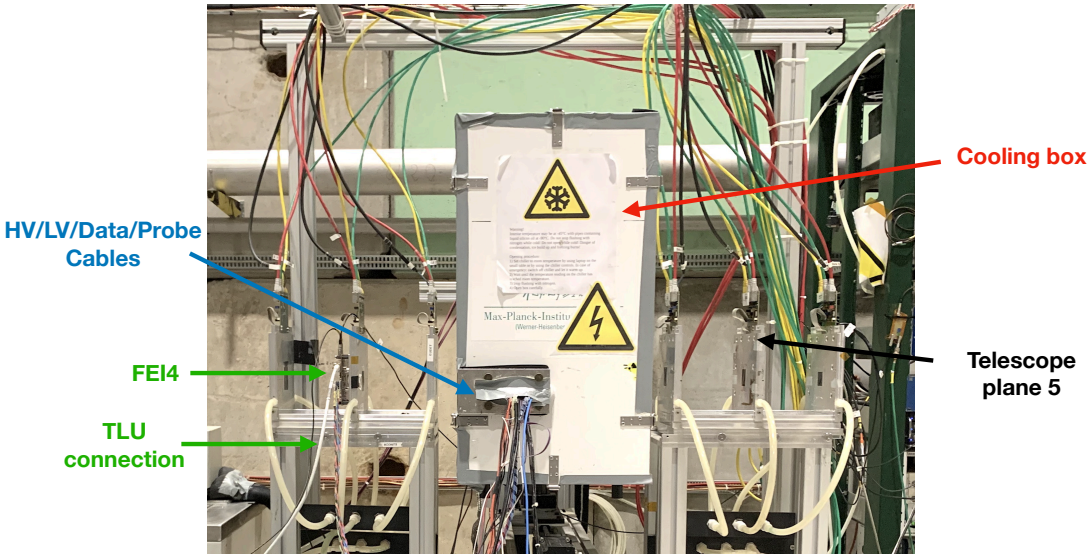


Figure 3.10: Picture of the test bench at CERN north area facilities. An arbitrary telescope plane is highlighted but the 6 planes are visible. The distance between the first and last telescope planes (1 and 6) is about 1.1 meters.

The telescope planes are MIMOSA26 [163] detectors, renowned for their high spatial resolution owing to a pixel pitch smaller than 20 μm. Such a high resolution offers precise hit positions on each plane. The particle tracks are reconstructed using the 6 Mimosa26 planes, ensuring high confidence in the reconstructed tracks and a correct computation of the expected hit position on the DUTs. Figure 3.11 illustrates the positioning of each detector plane in the test bench. Of course, the DUTs are placed in the center to ensure that the telescope-reconstructed tracks intersect them.

During data acquisition, controlling the temperature of the DUTs is of the utmost importance. Specific temperature sensors and humidity probes are taped onto the DUT cooling box support. All environmental sensors are read in a common platform, provid-

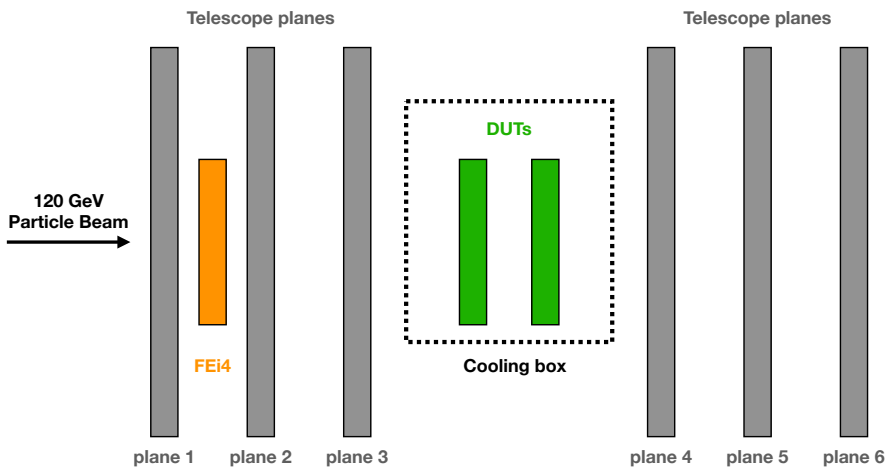


Figure 3.11: Scheme of the test bench. Six planes are used in the telescope to build tracks, an FEi4 detector is used for timing, and the DUTs are kept at a controlled temperature inside a cooling box. The total size of the bench is around 1.1 meters along the beam axis.

ing monitoring of the dew point to ensure the module's safety. Due to a high current powering 4 individual chips, Quad modules tend to create a significant amount of heat, thus requiring perfomant cooling solutions. Additionally, irradiated modules also require lower temperatures to run due to the damage suffered.

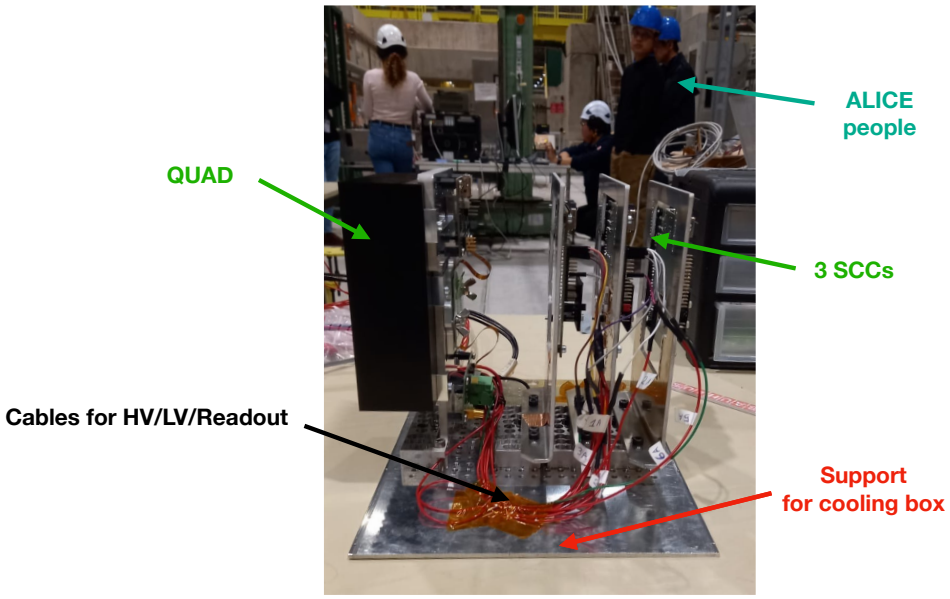


Figure 3.12: Picture of DUTs mounted onto support before insertion inside the cold box. Additional probes would be taped on the support surface for environment monitoring.

All DUTs are kept inside an isolated cooling box. Nevertheless, a hole is necessary to pass all low-voltage, high-voltage, data, and probe cables. Still, it is tightly sealed to ensure a minimum amount of exchanges with the exterior. A refrigeration chiller system composed of a tank and a pumping system is used to control the temperature inside the cooling box through liquid cooling and ventilation. This liquid is a specific silicon oil mixture that does not solidify until temperatures reach O(-100)°C. The chiller is set to a temperature of -80°C, which allows the DUTs to run at temperatures around -50 °C. Maintaining this temperature stable by remote controlling the chiller is essential during the full operation and could become an important limitation as water contamination in the tank could lead to solidification and render lesser cooling performances. Such situations required manual interventions, interrupted the data-taking sessions and would bias the data analysis if not reported.

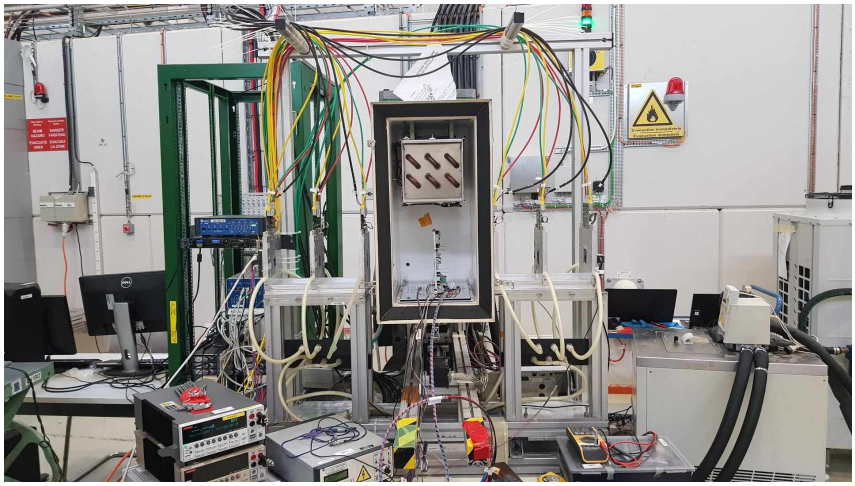


Figure 3.13: Picture of the test bench with an open cooling box. A single DUT is installed. The chiller tank and the tubes conducting the silicon oil are visible on the bottom right. Taken at PS test-beam facilities CERN

3.8 Testbeam data reconstruction

After data-taking the *.raw* event files built with EUDAQ are used for track reconstruction and efficiency computation in Corryvreckan [147]. A typical test-beam data analysis flow, using Corryvreckan, is illustrated in figure 3.14. The rest of this section will present the test-beam analysis strategy in more detail.

3.8.1 Corryvreckan and data analysis workflow

Corryvreckan is the software framework used for test-beam data analysis in the ITk pixel community. It stands out as a versatile and highly adaptable software solution characterized by its modular architecture. Each module is used for different purposes and steps in the full data analysis sequence, such as calculating efficiencies, finding the correct alignment of the different planes, or loading data from an EUDAQ raw file. It is tailored

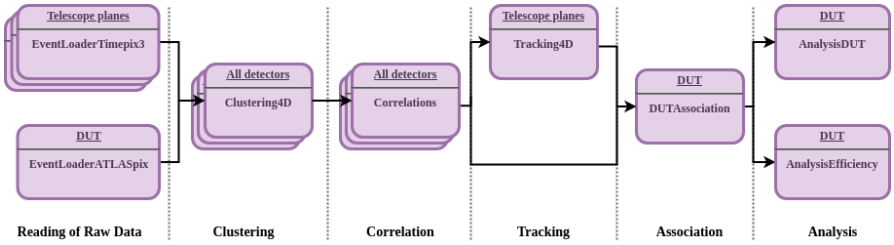


Figure 3.14: Example of a data reconstruction flow using multiple Corryvreckan modules [145]

for the test beam and laboratory environments and allows for seamless integration of detectors with diverse readout schemes, either with or without trigger information. It also makes good use of the hit timing information for some analysis modules, such as the plane clustering and tracking steps as it facilitates the correlation of data from multiple devices by leveraging timestamps.

This section provides a brief overview of the key steps of ITk's standard data reconstruction workflow in Corryvreckan.

Geometry file creation

For each data batch, the incorporation of the associated geometry files is essential, as they encompass critical information on detector setup and plane disposition on the test bench. These files contain measurements of DUTs and telescope plane positions and rotations in an internal (x,y,z) coordinate system, where z is the beam axis. The measurements are initially conducted during the test bench setup process to ensure accurate alignment and orientation of planes. Generally, from one campaign to another, the telescope planes do not move as they are fixed into a structure. However, the cooling box positions and the DUTs within it can change significantly. These position modifications are reported and inserted for each data-batch geometry file so that Corryvreckan can correctly compute tracks in 3D. These files include additional details such as the plane numbering scheme in the EUDAQ system, the type of detector, the pixel specifications including number and pixel size, as well as the designated role of each plane (DUT, reference, auxiliary, telescope plane) which indicates to Corryvreckan what planes are to be used at each step.

Mask creation

The module `MaskCreator` allows the creation of masking files for each plane of the telescope and the DUTs. In fact, with correct masking, one discards noisy pixels and avoids biases in track reconstruction. This masking process involves identifying and excluding

those noisy pixels based on their firing rates in the acquired data. Specifically, the method employed is `"frequency"`, which consists of calculating the global mean hit rate (f) and excluding pixels with a firing rate exceeding the threshold defined by `frequency_cut` $\times f$. The user in Corryvreckan determines this frequency cut, and it is usually set to [30-50] by the ITk pixel group at the time of this work. Additionally, pixels that never fire are also masked as dead pixels.

As mentioned in this chapter, another pixel mask has been obtained during the tuning procedure of ITk modules. This first mask is more relevant as it is obtained in the laboratory and not using data points under a high-energy beam. In fact, the mask created in Corryvreckan is very efficient in disabling very noisy pixels or pixel clusters of the various telescope planes but offers a mask dependent on beam conditions. This isn't an optimal solution for the tested ITk modules. The work conducted for this QT also included the initiative to develop a script that extracts and reformats this mask obtained in the laboratory from the Yarr configuration file associated with each EUDAQ *.raw* file. This allowed the comparison of both masking techniques for the DUTs efficiency measurements and resulted in an updated analysis workflow. However, the results presented in this chapter were obtained using the standard Corryvreckan mask, as it was the defined workflow at the time of this work. The appendix 3.A.3 presents the preliminary performance difference investigation between the two masking procedures.

Pre-alignment

As the geometry file implementation of the plane positions consists of manual measurements, further finer alignments are required, which are conducted in the reconstruction software. The alignment process consists of two sequential steps: pre-alignment and alignment. The pre-alignment adjusts each plane's (telescope, FEi4, and DUT) positions in the (x,y) transverse plane. In this process, a reference plane is defined, and hit-cluster correlations are computed between the reference and all other planes. These correlations are computed separately in x and y for all events. Event by event, the maximum correlation position in both axes for a given plane is used to adjust its position in the geometry file. The objective is to position all planes with respect to the reference plane so that the correlation of cluster positions is maximal at the same (x,y) values. In fact, as the beam axis is perpendicular to all planes, the hit positions in the transverse plane should be the same.
To better exemplify, if a correlation between a given plane and the reference peaks at $-X\mu m$ in the y-axis, the plane's y coordinate is shifted by $+X\mu m$ in the geometry file. This allows for the first adjustment of all plane positions in one step, followed by a finer iterative alignment.

Telescope alignment

This Corryvreckan alignment procedure only affects the telescope planes to allow proper track reconstruction. During telescope alignment, the `AlignmentTrackChi2` module refines the pre-alignment on the same events and incorporates plane rotations. In fact, during the manual setup and dimension measurements, slight rotations might remain unspotted. This alignment step deduces such small rotations that could bias the track

reconstruction.

In comparison with the pre-alignment using cluster correlations, the telescope alignment is conducted by reconstructing tracks using the General Broken Line model [164] as track representation. The plane geometries are adjusted by the distance between the reconstructed track intersection position and the cluster position on each plane. These distances, called residuals, are represented in the equations below. The procedure's objective is to minimize residuals in both axes. A threshold parameter `"spatial_cut_abs"` is determined as a spatial criterion used for the association of the cluster to the reconstructed track. If the residuals of a certain plane are above this threshold, an adjustment is made to the plane geometries.

$$x_{\text{residual}} = x_{\text{track intercept}} - x_{\text{associated cluster}} \tag{3.1}$$

$$y_{\text{residual}} = y_{\text{track intercept}} - y_{\text{associated cluster}} \tag{3.2}$$

The telescope's alignment is run multiple times with a gradual decrease of `"spatial_cut_abs"` for each run until good alignment is achieved. This is determined when the residual distributions reach a narrow Gaussian centered at 0 μm with a standard deviation inferior to the intrinsic pixel resolution $\sigma_{\text{resolution}}$, which is given by:

$$\sigma_{\text{resolution}} = \frac{\text{pixel pitch}}{\sqrt{12}}$$

This term is standard in pixel detectors as it represents the theoretical limit of spatial resolution assuming uniform charge distribution across the pixel pitch.

Figure 3.15 shows an example of final residual distributions after telescope alignment. Achieving this residual distribution is primordial as it provides a higher confidence in the reconstructed tracks.

Figure 3.15: Residuals of a telescope plane in the X and Y coordinates after a full alignment procedure. The standard deviation is below the intrinsic pixel resolution.

DUT alignment

After the telescope is aligned, the DUTs follow the same adjustments. The `FileReader` module reads reconstructed telescope tracks from the last step and uses them in the same way. Clusters on the DUTs are assigned to the reconstructed telescope tracks, and residuals are calculated. Similar to the telescope alignment, the geometry update is repeated until residuals are optimal by gradually decreasing the spatial cuts. When DUTs are finally aligned in Corryvreckan's geometry system, one could use them for track reconstruction as well. The FEi4 detector used for timing reference can also be aligned during this step.

Final track reconstruction

After a full alignment, the same reconstruction algorithms are employed, but the spatial requirements are set to a tighter point. Notably, an extra plane is used to build these final tracks that will be used for the analysis. This extra plane can be one of the ITk DUT modules or the FEi4 (if there are not multiple DUTs). It is referred to as "reference DUT" so as not to confuse it with the alignment reference plane. This plane is integrated into the tracking process as an additional telescope plane, ensuring only tracks with a hit on this DUT plane are accepted. This further improves the confidence in the reconstructed tracks. These final tracks are significantly more accurate and reliable; they will be used as reference tracks for the analysis and efficiency benchmarking of ITk modules.

Analysis

This final step aims to measure the DUT detection efficiency based on final reconstructed reference tracks. In the analysis, the DUT (SCC or Quad module) hits are matched with the reference tracks by calculating the transverse plane residuals and comparing them to a threshold for hit matching.

During this step, the spatial resolution used for track-hit association is recomputed. Both the reference DUT and telescope resolution are taken into account as they are used for the track reconstruction. The new resolution is the quadratic sum of both the telescope planes and the reference DUT resolutions.

$$\sigma_{\text{resolution}} = \sqrt{\sigma^2_{\text{telescope}} + \sigma^2_{\text{reference DUT}}} \tag{3.3}$$

$$\tag{3.4}$$

If the finalized alignment is correct, the track intersection position and the hit position on the DUT should be within a pixel's distance. Figure 3.16 presents such a distribution for an ITk SCC module; one clearly sees that the distance between the hit position and the track intersection position stays within a pixel pitch $50 * 50 \mu m^2$, with a maximum in the pixel's center.

Several parameters, such as the threshold distance to accept a match between tracks and clusters and other track preselection criteria, were not yet optimized by the time of the QT. In fact, as Corryvreckan was also a new software within the ITk pixel group, a fixed workflow describing precisely how to configure the analysis module was under development. The appendix of the current chapter shows a study of such parameters and their impact on the measured efficiency that benefited the ITK test beam analysis workflow developemnt.

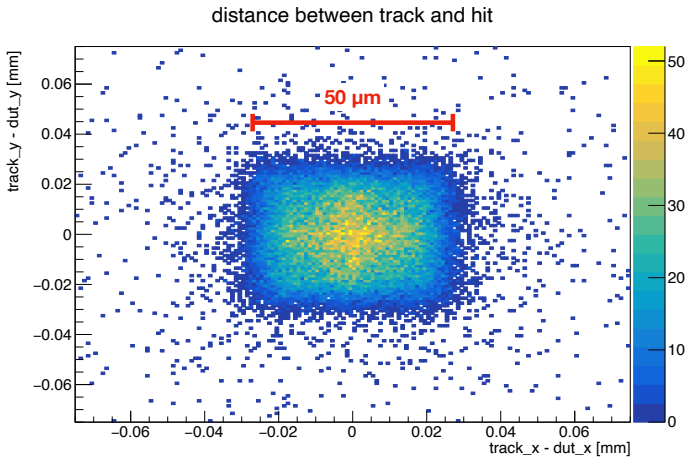


Figure 3.16: Distribution of distance between hit position and track position on the x,y plane. The main bulk is kept inside a $50 * 50\mu m^2$ area. Obtained with a fully depleted RD53B SCC.

The `DUTAssociation` and `AnalysisDUT` Corryvreckan modules are deployed on the final reference tracks to compute the residuals, and thresholds are defined for track pre-selection and for accepting or rejecting DUT matches.

The number of tracks with accepted clusters directly gives the measure of hit detection efficiency (ϵ). It is simply defined as the probability of detecting a particle passing through the sensor. The following equation gives its computation :

$$\epsilon = \frac{\text{Number of associated cluster tracks}}{\text{Number of associated + non associated cluster tracks}} \tag{3.5}$$

The efficiency uncertainty is also computed in Corryvreckan. However, it is purely statistical as it is determined using the ROOT TEfficiency method, which applies a Clopper-Pearson confidence interval [165] with a 1σ level. This uncertainty is not enough to clearly assess the error margin of our measurements because other sources are not considered. These, for instance, can be related to hardware intrinsic noise, leading to fake tracks/hits, or biases due to the arbitrary Corryvreckan configuration of the track pre-selection and matching criteria. These errors had not yet been quantitatively taken into account by the ITk group at the time of this work.

Through the study presented in the appendix 3.A, it was understood that such error sources were dominated by the software implementation, which is still in development, and the flexibility of the workflow with regard to man parameters as it was not established yet. The preliminary quantitative assessment of these parameters' impact conducted during the QT, showed possible errors of the order of 1% in efficiency by the time of this work. This additional source dominated the statistical uncertainty provided by Corryvreckan

but remained small enough to assess ITk pixel sensor performances.

Finally, the performance results can be presented as a `chipEfficiencyMap`. It is a 2D map of the sensor showing the pixel matrix hit detection efficiency. Figure 3.18 from the result section illustrates such a map for an RD53B SCC. This map allows one to see the individual pixel performances, but the global efficiency of the detector (not including masked pixels) is calculated as the average of the individual pixel efficiencies. This value is used to benchmark each module, which will be shown in the next section.

On top of these efficiency results, one can compute the in-pixel efficiency distribution. In fact, the Mimosa26 telescope used in ITk's test benches features a higher spatial resolution than the DUTs pixel pitch. This allows for precise positioning of the reconstructed track within a given DUT pixel. One can benefit from the high track resolution and build a `pixelEfficiencyMap`. This map represents the efficiency of detection concerning the track position inside the pixels. It is produced via an overlap of all the pixels of the sensor to get the average distribution of in-pixel efficiency. This provides an estimate of the detection efficiency's dependence on where the track intercepts the pixel (close to the center, edge, or corner of the pixel). Figure 3.19 from the result section 3.9.1 shows and further explains such a distribution on a 3D pixel SCC.

The Corryvreckan modular framework offers a straightforward workflow for all important steps of test-beam data reconstruction. The alignment, track reconstruction, and efficiency computation algorithms allow high parametrization and flexibility. Adjusting these variables and running the corresponding steps multiple times can result in excellent alignment of all relevant planes, which allows tight track reconstruction for a correct analysis of ITk pixel sensor performances.

3.9 Results

In this section, a few results concerning different modules from the 2022 test-beam campaigns will be presented. The 2022 campaigns tested various modules, including irradiated ones. However, this section will discuss unirradiated RD53 single-chip cards using 3D pixels and the first analyses on Quad modules. It is at this step that analyzers can understand the performance of the detectors and identify defects. As a reminder, ITk pixel modules are required to have a detection efficiency superior to 98% and 97% for uniradiated and irradiated modules, respectively.

The current section will focus on the ITk module performances under optimal operating conditions, although other investigations were made to test the detector dependence on the operating conditions, such as the configured threshold for hit registration and the sensor bias voltage. These are presented in the appendix 3.B.

3.9.1 Single Chip Card

A reference SCC was tested throughout the multiple campaigns. It presents a smaller surface compared to the quad modules and is composed of 3D pixels with a pixel pitch of

50x50 μm^2. This SCC integrates an RD53b FE chip as an electronic readout, which was also implemented on the ITkPixV1 Quad modules.

For this SCC, multiple different tunings were done using the Yarr procedures mentioned in 3.5.1 to beam-test the detector under different configurations. The following results are from data taken in room temperature conditions (17.4 °C) with a sensor bias voltage of 10V for full depletion, and the pixels are tuned to a charge detection threshold of 1000e, which is lower than the expected 2000e working points for the ITk operation (value at the time of this work). In these results, the FEi4 plane is used as the reference DUT to build the final reference tracks used for analysis.

Chip efficiency

The global efficiency computed using a total of 59 765 reference tracks passing through the DUT yields a value of $98.916 \pm 0.043\%$ (only statistic uncertainties). This value passes the detection efficiency requirement criterion for ITk pixel modules in these conditions. Additionally, by looking at the single pixel efficiency histogram illustrated in figure 3.17, one sees that the quasi totality of pixels efficiency is superior to 99% with a low number of unmasked pixels having an efficiency below 90%. These defective pixels bias the global value of the detector and show the need for improving the masking strategies. The efficiency calculation strategy at the time of this work kept these pixels in the final results as it used the standard Corryvreckan mask. However, current discussions aim to write different masking algorithms that take such pixels into consideration.

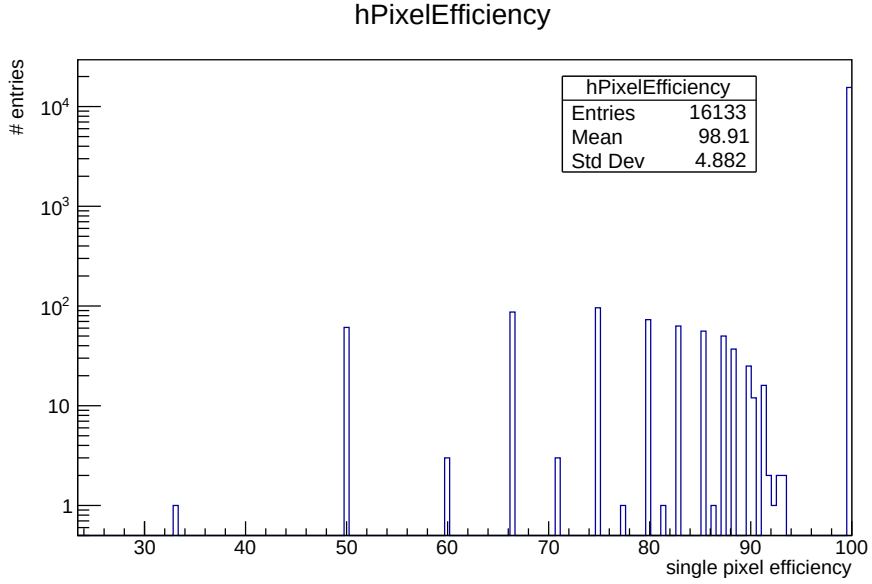


Figure 3.17: Distribution of single pixel efficiencies of an RD53 reference SCC used throughout the TB campaigns. Only showing the efficiency of unmasked pixels.

Efficiency map

Figure 3.18 shows both the raw 2D hit map of the SCC under the beam and the associated chip efficiency map obtained with the reconstructed tracks. They reveal a very homogeneous efficiency distribution throughout the unmasked pixels in the beam area. As one can see, the beam does not cover the sensor's total surface; this depends on the beam conditions when the TB data was taken. All pixel hits measured outside of the beam region originate from noisy pixels that will be masked or come from special physical effects such as delta rays or other unwanted emissions along the different planes that create a signal in the SCC sensor. One sees that the reconstructed tracks, onto which the sensor is evaluated, overlap as expected with the beam area. This demonstrates that the many noisy hits are unrelated with stable particle tracks. A hard cut is visible on the right side of the beam region, after which no tracks are reconstructed. This line corresponds to the FEi4 sensor dimensions, which are smaller than the SCC ones. Any track not passing through the FEi4 plane is not reconstructed since the FEi4 is used as reference DUT for the reference tracks used in the analysis.

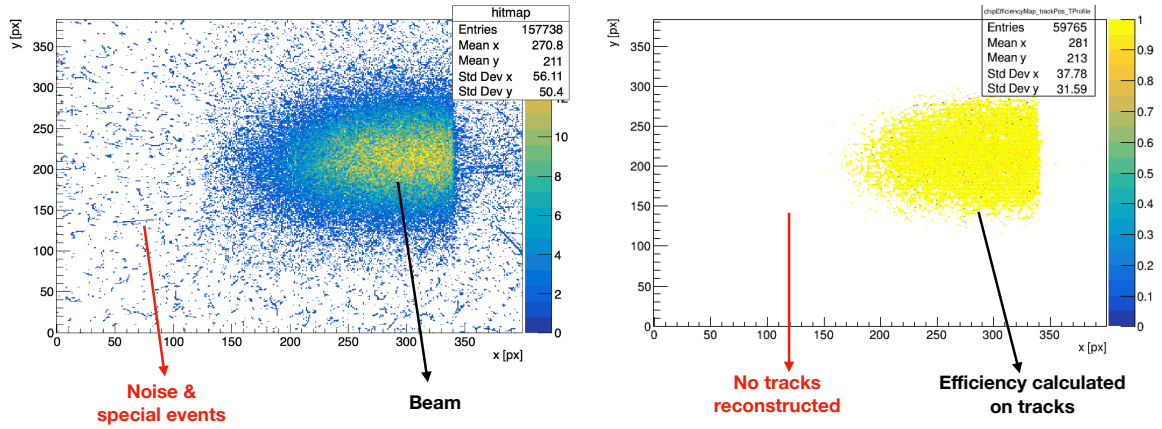


Figure 3.18: Left: Raw hitmap off all pixels on the sensor plane. Right: the associated chip efficiency map. A clear difference between the beam-induced signal and the background is visible on the reconstructed track region on the right figure. These results are obtained on an RD53B SCC.

In pixel efficiency distribution

Thanks to the high resolution of the telescope planes, one can also compute the in-pixel efficiency distribution. The obtained distribution is illustrated in figure 3.19. The length of both the x and y axes correspond to the pixel dimensions, and the coordinates are local pixel plane coordinates. It becomes clear that the tracks going through the corners of pixels suffer a significant drop in efficiency. This phenomenon is expected as this SCC is made with 3D pixel technology. The charge-collecting cathode goes through the pixel-active material in the form of a column. These columns occupy the four corners of each pixel, which worsens the detection efficiency by creating less sensitive zones. This effect remains minimal when one evaluates the overall detection efficiency of the pixel and is not be present on Quad modules as they use planar pixels.

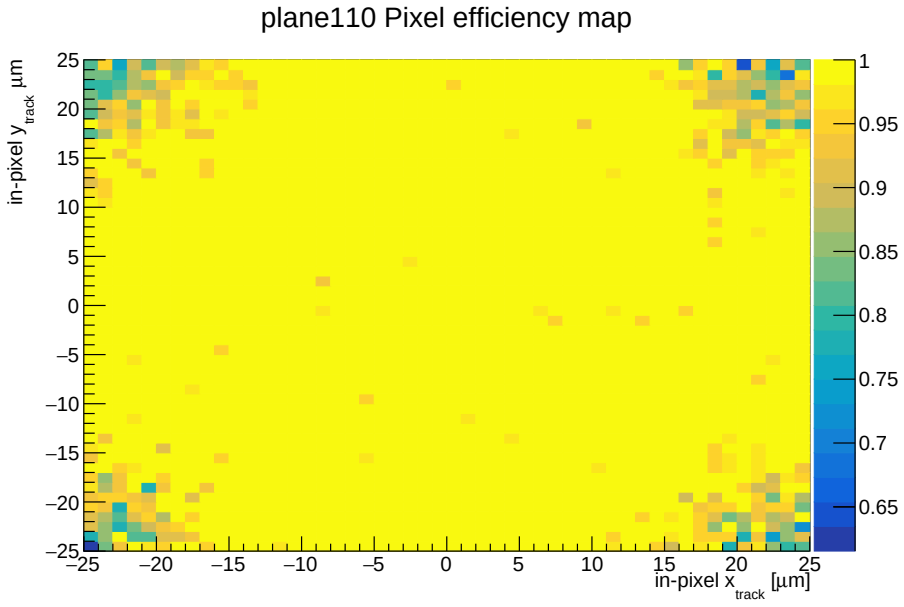


Figure 3.19: A 2D histogram of in-pixels average efficiency. The x and y coordinates are local.

3.9.2 Prototype Quad

A prototype Quad planar sensor was tested during several campaigns. On top of measuring its global detection efficiency, a particular interest was focused on the inter-chip region. Indeed, at the frontier between the 4 FE chips, the analog signal is more difficult to collect, and a special design of pixels has been done in this zone to measure this signal efficiently. This creates technical difficulties in the connection between the sensor and the FE electronics, whose performance requires evaluation in detail. Effectively the bump-bonding scheme between the FE and the sensor is modified in the inter-chip. This renders different-sized pixels in this particular region with 25x100 μm^2 dimensions to allow connection with the FE borders. Understanding the reliability of the inter-chip pixels was essential to develop ITk Quad modules further and prepare its production.

The results shown in this section were obtained from a prototype ITkPix Quad operated with a sensor bias voltage of -100V and a pixel charge detection threshold tuned to 2000e. Note that this choice of configuration implies a fully depleted sensor for the Quad and a detection threshold similar to the expected operating conditions.

The total global efficiency of detection was measured on 200k triggered events and resulted with low value: **96.54 +/- 0.06%**. This result did not fit the expected requirements for this configuration and was explained by an important defect in the inte-chip region.

Inter-chip region

The available prototype Quad module during the TB campaigns exhibited a manufacturing defect. Figure 3.20 illustrates its 2D efficiency map. It shows that the inter-chip region

presented a critical malfunction, most likely linked to bump-bonding miss-connections, leading to pixels with a null efficiency. The global detection efficiency was largely impacted by those pixels.

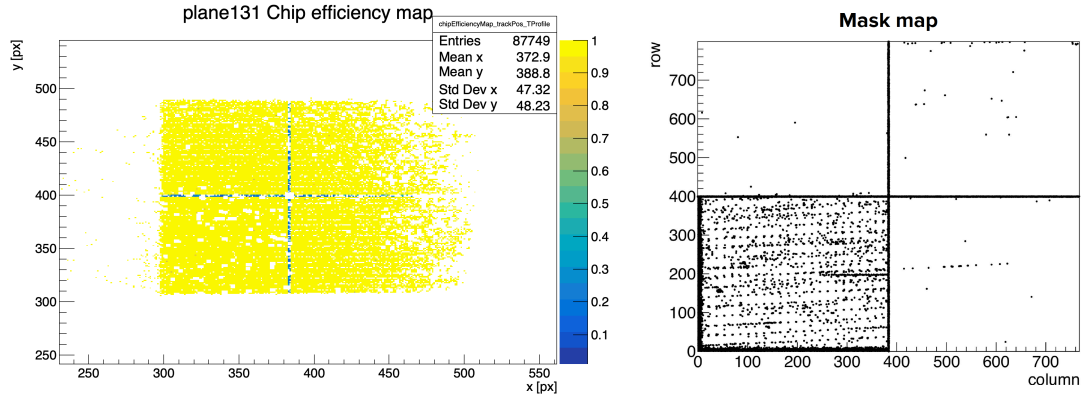


Figure 3.20: Left: The chip efficiency map of the prototype Quad module (plane 131). Right: Yarr pixel masking map.

To measure the proper detector efficiency, the columns and rows of the inter-chip region were manually masked. This resulted in a much better global detection efficiency of **99.950 +/- 0.001%** that validates the prototype Quad sensor. This reveals again significant matters with the masking strategy applied within Corryvreckan which failed to mask these pixels automatically.

3.9.3 Pre-production Quad

A second Quad module, with an ITkPixV1 chip and a pre-production version sensor, became available for testing in the last testbeam campaign of 2022. The first data analysis showed a high detection efficiency of **99.545 +/- 0.008%**. This unit did not present production defects on the inter-chip region. Figure 3.21 illustrates the 2D efficiency map of the pre-production Quad sensor. One sees that the efficiency distribution is homogeneous across the pixel matrix, with detection efficiencies close to 1. This offered the possibility of studying the inter-chip pixels of different sizes in more detail in the following campaigns.
Later test beams have demonstrated that the inter-chip pixels on the pre-production sensor do not suffer any performance differences compared to the "regular-sized" pixels, although the signal collection and readout are different due to a different bump-bonding pattern. This validated the four individual FE chip combination techniques for the production phase of planar Quad modules destined for ITk barrel layers.

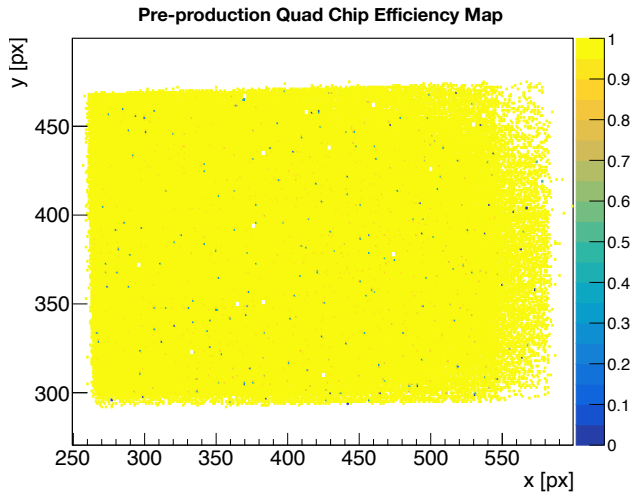


Figure 3.21: The chip efficiency map of the pre-production Quad module.

3.10 Conclusion

The ITk project, encompassing both hardware and software challenges, has various operational facets ranging from the production of planar Quad modules to sensor quality tests and pixel tuning manipulations. The qualification task project, aimed at validating my ATLAS authorship, has provided opportunities to study different important aspects of the ITk modules and the precision at which we could qualify their performances. This includes working on the production chain of planar Quad modules, conducting electrical and sensor quality control tests, performing pixel tuning manipulations, and, notably, working on the pixel's TB campaigns.

Particularly, the TB campaigns conducted in 2022 have not only measured the sensors' high detection efficiency but have also provided a critical stress test for various modules and the DAQ system. Through these efforts, important advancements have been made, with findings integrated into YARR or RD53 documentation, contributing to ongoing improvements in detector technology.

While these campaigns have demonstrated an impressive detection efficiency of approximately 99% that passes ITk requirements, they have also highlighted significant challenges in data acquisition and analysis consistency. To address these issues, I proposed the implementation of a standardized workflow. This workflow will allow better control of the efficiency measurements across various TB campaigns by using consistent parameter sets for track selection, efficiency analysis algorithms, alignment procedures, and more. This will enhance the scientific methodology of the TB group, ensuring uniformity among analysts and leading to a clearer interpretation of results.

Following this project's findings, a better methodology was implemented within the group, which minimized this type of occurrence and ensured more robust results. However, as the main software pieces are still under development, updates to the workflow are necessary.

In addressing the discrepancies in data-taking and reconstruction, it is imperative to capitalize on the full potential of Test Beam campaigns. This will involve not only routine enhancements to the workflow but also ensuring adequate resource allocation—such as module availability and dedicated personnel for analysis tasks. Continued efforts in these areas are essential to advance the ITk detector's research and development, ultimately optimizing the scientific output and operational efficacy of future campaigns.

3.A Data analysis consistency issues

In this appendix, the limits of ITk's TB reconstruction workflow, by the time of the current work, with Corryvreckan are tested. Specifically, this section focuses on the consistency of efficiency results of analyzed test beam data. This was an important preliminary study that explained the consistency issues of the previous workflow and led to a stable reconstruction and analysis workflow in Corryvreckan.

The multiple modules tailored to various tasks, such as correlation or track reconstruction, include a significant number of configurable parameters. An important workflow issue spans from the variability in parameter settings across different users in the test beam reconstruction group. This results in significant discrepancies in some analysis results (order of 1-2% absolute detection efficiency difference). Understanding and quantifying the impact of the main analysis parameters has been a major aspect of the qualification task project.

During the qualification task period, the TB reconstruction data tasks were very personally oriented; each analyst would take a given set of data to test specific features of the modules that were of interest. However, this was never done in a stable software environment between all analysts. Each analyst had its own software version and setup. Notably, analysts had different YARR to EUDAQ conversion plugins, which would minorly modify the labeling of pixel coordinates in the EUDAQ raw file planes.

In fact, when encountering difficulties, TB analysts frequently adjust parameters in Corryvreckan. However, due to variations in individual parameter sets, the resulting reconstructed efficiencies become incomparable. A strict Corryvreckan workflow should be implemented, and a set of options and parameters should be decided and adapted for each test-beam data batch.

This section presents several key parameters from important steps in Corryvreckan and their impact on the analysis outcomes. The investigated parameters are from the modules Track Reconstruction, Efficiency Analysis, DUTAssociation, Masking, and Final Alignment.

3.A.1 min_hits_on_track

This parameter is used during track reconstruction. It is the minimum number of associated clusters needed to create a track, equivalent to the minimum number of planes required for each track. The value is usually set to be the same as the number of telescope planes plus the reference FEi4. Depending on the setup and the performance of some planes, the user sometimes lowers this value. The impact is very significant, as one can see in table 3.2. Nevertheless, this is not an important issue since one usually sets up the value correctly.

If the number of required hits is too low, a large number of fake tracks are reconstructed, significantly lowering the computed efficiency.

3.A.2 chi2ndof_cut

Every reconstructed track has an associated χ^2/ndof score. This value comes from the track reconstruction fit algorithm on hit positions and corresponds to the global dist

Value	Efficiency	Details
6	**3.25%**	67k events correspond to 2M tracks (30 tracks/event) 66050 clusters associated with 65948 tracks Total accepted tracks: 1196196 Efficiency measured with 38840 matching tracks
7	**97.98%**	67k events correspond to 41k tracks (0.612 tracks / event) 38825 clusters associated with 38776 tracks Total accepted tracks: 24573 Efficiency measured with 24076 matching tracks

Table 3.2: Comparison of Efficiency Results for Different Values of min_hits_on_track. Results were taken from the same SCC in fixed conditions.

representing the track's "quality". Indeed, this value increases with the distances between tracks and real hit positions.
During the efficiency analysis, this value is used as an acceptance criterion for telescope tracks and provides the major track rejection criterion. It has a value by default, but analyzers often tweak it when the number of selected tracks is too low. Doing this type of tweaking creates essential differences in the analysis process and strongly biases the final result.

	χ^2/**ndof**				
	40	**10**	**5**	**3**	**1**
Efficiency	96.90%	96.90%	97.15%	97.73%	98.58%
# rejected tracks	4486	4486	5468	6443	17841

Table 3.3: Final global detection efficiency results of an SCC for different track quality criterion.

From table 3.3, there is a clear visible correlation between the computed efficiency and the track χ^2/ndof score (as long as there are enough tracks after rejection). This free parameter is essential for the final detection efficiency result. Indeed, if one selects only the best-reconstructed tracks, the efficiency rises automatically. If this value remains different from one analyzer to another, from one data batch to another, it will create major biases resulting in non-comparable detection efficiencies between runs, analyzers, modules, etc..

Fixing this variable is of the utmost importance to establish a consistent analysis workflow. Bias-related uncertainties incorporating this parameter should be effectively implemented when presenting the result of the obtained detection efficiency.

3.A.3 Masking

Every reconstruction workflow starts with the masking step. However, the chosen batch of data and the number of events considered to create the mask can differ among multiple users. Different batches can yield different masking because of temperature differences, beam condition changes, etc ..

A test was conducted by running the same analysis script utilizing identical analysis configuration files, raw data files, and alignments but differing in their mask settings. The mask files for the same module at the same TB campaign were taken from three analysts. This yielded different results within a narrow range: **96.71**% , **97.67**% and **97.37**%; demonstrating inconsistencies within a 1% margin. Further pointing out the fact that the statistical uncertainties remain very minimal compared to the biases introduced by arbitrary workflow choices.

The Corryvreckan masking procedure described earlier is used for all planes: telescope, reference, and DUTs. This masking technique differs significantly from the YARR masking procedure based on its internal noise scan. While the YARR masking and tuning are done at the laboratory at room temperature, the Corryvreckan mask is done with TB data under beam conditions. It was observed that the resulting mask change was caused by YARR masking much fewer pixels. The two methods are radically different because of the beam presence, which can be questionable. This difference leads to a very high number of pixels considered "noisy" by Corryvreckan.
A script was developed to import the mask from the chip's YARR configuration file and rewrite it in the Corryvreckan format. This enables one to use the YARR mask instead for all different alignment, reconstruction, and analysis steps.

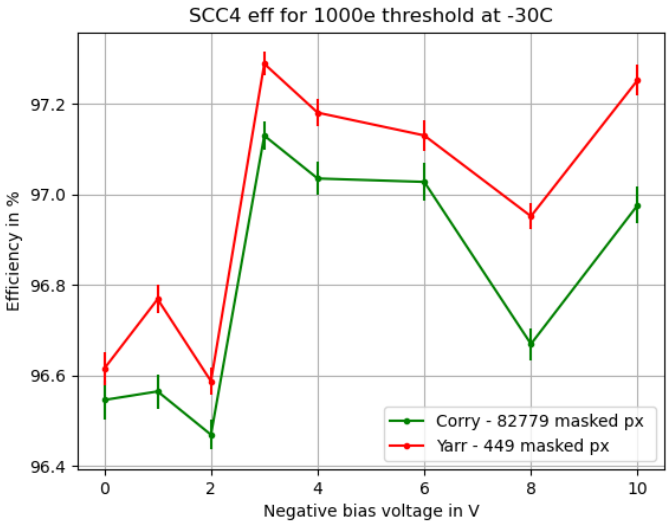


Figure 3.22: Efficiency of a SCC at different voltages using both masking techniques

Figure 3.22 depicts the impact of the chosen pixel mask. Corryvreckan has masked about 200 times more pixels than the Yarr method. Overall, the efficiency decreases when using the standard Corry mask, but the curve shape remains quite chaotic compared to what is expected. By default, the analyzers utilize the Corryvreckan method as it is a straightforward implementation inside of the workflow. Nevertheless, establishing a new tool to extract masks from YARR configuration files offers more possibilities.

The mask is a considerable parameter, and all analyzers looking at the same data or wanting to compare results must use the same mask. It has been shown that the masking method impacts the computed efficiency and that the data batch used to build

the Corryvreckan mask also influences the results. Understanding which mask should be used for optimal analysis and providing a common mask for each plane on a given data batch is crucial to secure result consistency.

3.A.4 Other parameters

In addition to the parameters associated with Corryvreckan procedures presented above, other parameters have shown lesser impacts, such as a loose criterion for validating an alignment that rendered slightly different geometry files, leading to different final results.

Additionally, impacts on the error can be caused due to software stability. Corryvreckan, Eudaq, and Yarr are software under development. Multiple versions of each software and plugin that link Yarr to Eudaq were available and would change from one campaign to another. Results obtained in different periods would also change slightly and add an extra effect on the error. By the time the work was done, there was no default version of these software and plugins to be used for TB analysis. This could lead to each analyst working with different versions depending on when they joined the reconstruction efforts. This also contributed to the detection of efficiency discrepancies, as presented below.

Testing an equal analysis set of parameters (variables, masks, geometry files, input files) has shown differences between two users installations:

Running the same script led to different results :
96.68 ± 0.07 % and **97.66 ± 0.06** %

Discovering this type of variation was crucial to addressing workflow stability and ensuring compatible measurements below the 1% level in future developments. The software performance was nevertheless precise enough to qualify the tested prototype and pre-production modules and to see improvements between various versions.

3.A.5 A new workflow

Systematic studies assessing the impact of analysis parameters in Corryvreckan have revealed significant implications for detection efficiency. It was confirmed that the observed variations are not due to intrinsic randomness. In fact, repeated trials on the same software setup and machine have consistently yielded identical results, emphasizing the feasibility of standardizing a workflow to ensure comparability across analyses.

To enhance the integrity of results and facilitate effective cross-checks among team members, a set of default parameters was established for each major step of an analysis following this preliminary study. This new Corryvreckan workflow significantly benefits the methodology of the ITk-pixel test beam group, leading to more reliable results.

Additionally, a clear protocol for modifying parameters when necessary should be implemented. Certain data-taking situations, such as variations in beam conditions or telescope plane malfunctions, can require manual adjustments of parameters, such as the

spatial acceptance of hits for track building.

The construction of this workflow focussed on a tight selection of reconstructed tracks to ensure only the most relevant tracks are used for computing efficiencies. Furthermore, the criteria for fixing parameters is adapted based on the type of module under test and their respective pixel pitches.

This stricter workflow also enables new analysts, particularly those without prior Corryvreckan experience, to contribute effectively to the project.

Moreover, a quantitative assessment of the combined effects of these parameter impacts on the results should be conducted. The findings should then be systematically incorporated into the bias uncertainties in results, thereby enhancing the scientific rigor and reliability of ITk test beam campaigns.

3.B Detection efficiency dependence on operating parameters

The test-beam is also an opportunity to assess quantitatively the detector efficiency dependence on various operating conditions. Various parameters should have a considerable impact, but this section will focus on the tuned threshold configuration for hit registration of the modules as well as the applied bias voltage on the sensor. The objective is to confirm that the module sensor and FE chips are behaving as expected and that the manually set configurations are effective.

The sensor charge collection capacities depend on the applied high voltage. At low operating HV, the sensor will not present a full depletion zone. This lowers the number electron-hole pairs created one a passing particle interacts as well as the drift speed for charge collection. This effectively lowers the amount of electrical signal sent to the FE for a given energy deposit. Additionally, the detection efficiency depends as well on the FE analog-to-digital signal thresholds, as high thresholds result in a lower signal efficiency due to the low energy deposits.

By fixing the environment and ensuring a stable, controlled system, the test beam can be used to test these parameters' impact on the final analyzed efficiency with step-by-step parameter scans.

Maintaining all other parameters stable can be challenging, particularly during test beam operations. The chiller at disposition typically fills up with ice after water contamination, leading to an increase in temperature within the cool box. This instability can be important with a rise of 10 degrees over a couple of days. Additionally, the beam can change its cross-section shape due to different SPS operations. Also, software bugs in the YARR-EUDAQ framework tend to lose correlations between the Telescope planes and the DUTs after a certain period during data-taking making some datasets lighter compared to others as events that lost correlations cannot be used. This later error is still not completely understood today, necessitating further investigation into the Yarr FPGA firmware.

The combination of all those factors creates challenges when trying to have seamless parameter scan procedures. A quantitative assessment of errors related to those is still to be studied.

Prior to conducting these parameter scans, the expected efficiency dependencies of threshold and bias voltage are already qualitatively understood. The threshold scan is expected to yield an approximately linear decrease in detection efficiency toward higher thresholds while the efficiency is anticipated to increase with bias voltage to eventually reach a plateau when the sensor cannot deplete further.

Figure 3.24 and 3.23 show the results of such parameter scans on an RD53b SCC. The plots were produced using 1 million events per parameter value for the efficiency computation. The first-order expected behavior of the sensor and chip is visible. The observed important efficiency drop at 8V and 2V in figure 3.24 could be caused by a change in temperature or beam conditions during its associated runs. Nevertheless, important questions on uncertainties are still raised by their shape; as mentioned before, the

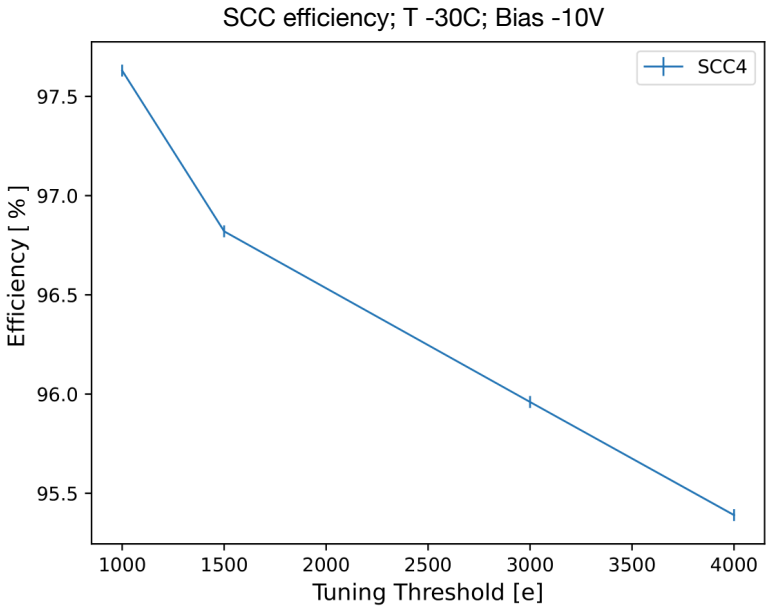


Figure 3.23: Threshold parameter scan of an SCC and impact on detection efficiency.

computed uncertainties are purely statistical and are underestimated.

During this work, the utilization of YARR and Corryvreckan for the ITk pixel modules was very recent. This lack of expertise with YARR and Corryvreckan led to major difficulties and bugs during TB data acquisition that required a lot of development effort from the group. The main consequence was that no strict workflow was established by that time. Therefore, it was crucial to conduct a study on the impact of different parameters along the multiple reconstruction and analysis steps. This study showed the ITK TB group the importance of the issue, which had not been investigated yet. Additionally, this also allowed the group to understand differences in final efficiencies obtained by different analyzers on the same modules and same runs. The challenge of comprehending these variations raised significant concerns about the reliability of ITks TB reconstruction framework and led to the development of a strict workflow. A thorough analysis of Corryvreckan's data analysis configuration and its influence on the final results is presented in the appendix 3.A.

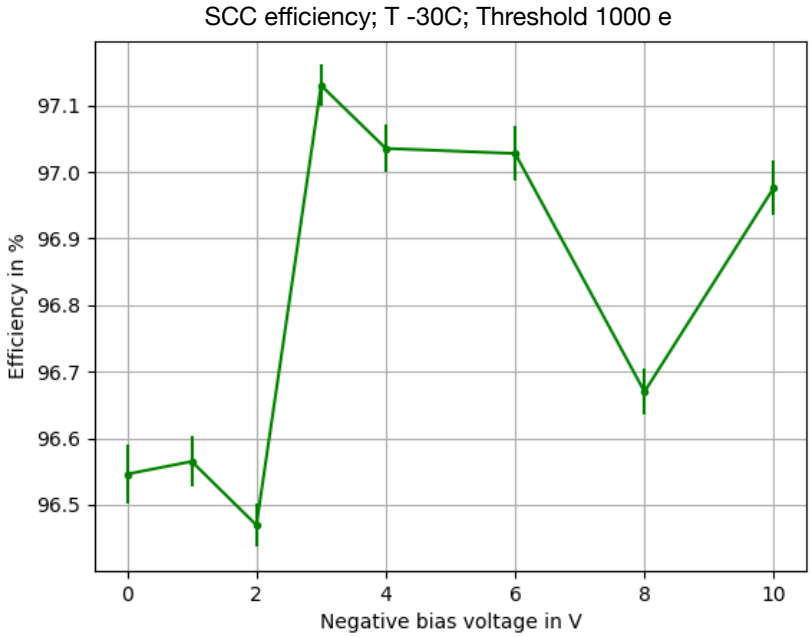


Figure 3.24: Bias voltage parameter scan of an SCC and impact on detection efficiency.

Chapter 4

ATLAS long-lived ALP search

According to BSM models 1, axion-like particles (ALPs) could be produced at particle colliders through resonances or the Higgs portal in ATLAS and CMS. The ALP EFT approach (1.7) is considered in this part to address phenomenology in a theoretical agnostic way with Wilson coefficients allowing decays into different SM particles. This gives the possibility to search for complementary signatures such as jets in forward regions [166], di-photon resonances [83], 4 photons searches [84], light-by-light scattering [167] and other exotic event topologies [81].
Additionally, certain combinations of EFT parameters can create ALPs with small widths, leading to long-lived particles (LLP) [79, 94]. Such LLP decays are searched through unusual signature analyses and displaced vertices (DV) searches [110]. However, current ATLAS DV reconstruction techniques are limited to LLP decays in the tracker and become unusable at displacements above 0.5 meters in the x-y plane.

This chapter discusses the production mechanisms of ALPs, their decay modes, and the implications of long-lived ALPs (LL-ALPs), with a special interest in ALP decays happening in the calorimeters. It will also discuss the challenges of particle reconstruction for LL-ALP di-photon decays and the need to develop new approaches to enhance ATLAS's sensitivity.

4.1 ALP at high energy colliders

This section will describe ALP phenomenologies at colliders with the EFT description of section 1.7.

4.1.1 Production mechanisms

ALPs can be produced at high-energy colliders through several mechanisms :

- **Resonant Production**:
  Multiple resonant processes could create ALPs in a wide mass spectrum, including gluon fusion $gg \to a$ and photon fusion $\gamma\gamma \to a$ at the LHC or in e^+e^- collisions $e^+e^- \to a$. Vector boson fusion (VBF) processes are also considered if the ALP

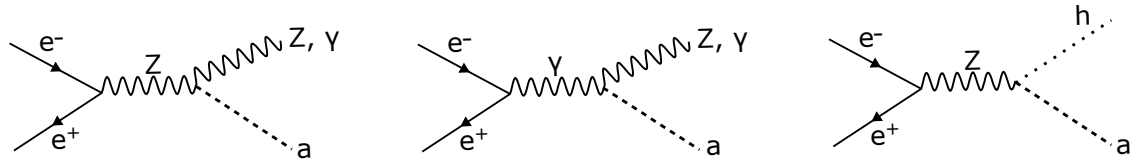


Figure 4.1: Tree level diagrams contribution to the production of ALPs + X at e^+e^- colliders.

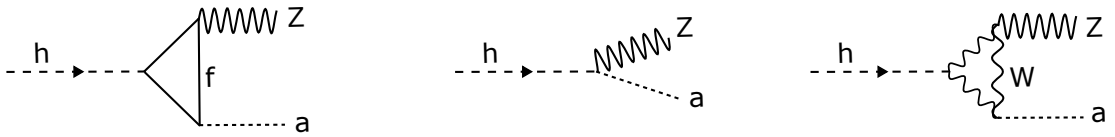


Figure 4.2: Multiple diagrams contributing to $h \to Za$ production processes at the LHC.

couples to heavy gauge bosons, however these are suppressed by the $\frac{m_a}{\Lambda} << 1$ limit, which reflects the EFT nature of the model.

- **Associated Production with other particles**:
  It is an important mechanism at e^+e^- colliders. ALPs could be produced alongside gauge bosons, Higgs, or jets. Such processes yield a well-defined SM particle emission, which can be used for pre-selecting events. Processes like $e^+e^- \to \gamma a$ or $e + e- \to Za$ are of interest [168].

- **Decay of Heavy SM Particles**:
  ALPs could be produced via on-shell exotic decays of Higgs and Z bosons. Relevant decay channels include $h \to Za$, $h \to aa$ and $Z \to \gamma a$. For the Higgs decays, branching ratios could be quite large due to suppressed SM decay widths [93] [79]. These offer a signal with a precise invariant mass of the final state particle system, that can be used for event selection. Additionally, $h \to Za$ and $Z \to \gamma a$ allow a preselection trigger due to an extra particle. This is the main production mechanism discussed in the thesis.

- **Production in Hadron Decays**:
  ALPs can be produced in hadronic decays, such as B meson decays, via flavor-changing neutral currents [169].

4.1.2 Decay channels

ALPs can decay through various channels depending on their mass and couplings:

- **Leptonic Decays**:
  ALPs can decay into lepton pairs ($a \to \ell^+\ell^-$), where ℓ denotes a lepton. This decay mode is relevant for ALPs with masses above twice the lepton mass and allows DV searches (considering LLP) through the leptons displaced tracks.

- **Photon Decays**:
  ALPs can decay into photon pairs ($a \to \gamma\gamma$) through effective couplings to the EM tensor. For low-mass ALPs ($m_a < 2m_e$, this is the dominant decay mode. For standard DV searches, one must look at converted photons. However, collimated and non-pointing photons can be expected, creating a new opportunity for ALP searches. This decay mode will be discussed in the current thesis.

- **Hadronic Decays**:
  Higher mass ALPs can decay into hadrons with processes such as $a \to gg$ or $a \to q\bar{q}$. Additionally, one can consider the hadronic decay of a tau pair.

Long-Lived ALPs

LL-ALPs arise from the EFT if their masses or couplings to SM fields are small. Thus, LL-ALPS searches are more sensitive to a complementary parameter space region than prompt searches. However, the ATLAS analyses dataflow includes particle identification algorithms that suffer from the displacement of LLP decay products. New detector concepts like MATHUSLA, FASER, and Codex-B are being designed to search for such particles [97]. Notably, they aim at detecting ALPs decaying into photons at long distances, $O(100)$ meters, from the collision point. Nevertheless, as ATLAS is a sizable detector (50,25) meters, new identification strategies can be implemented to capture LLPs in existing and upcoming data.
Dedicated long-lived particle experiments and LHC/HL-LHC analyses are crucial for exploring the ALP parameter space and promise important updates on ALP constraints.

4.2 Photon Channel

ALP decay ($a \to \gamma\gamma$) 4.3 offers a clean experimental signature due to the EM shower reconstruction in the LAr calorimeter. Capturing this decay depends heavily on the ALP mass, boost, and life-time. In fact, the reconstruction efficiency of photons is very sensitive to the photon's vertex position [170] and their geometrical distribution.

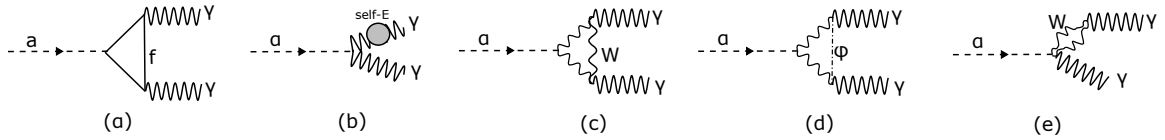


Figure 4.3: Diagrams contributing to the decay $a \to \gamma\gamma$. Fermion loops are considered (a), as well as internal charged W bosons (c,e) and associated Goldstone fields (d). (b) introduces the self-energy coupling.

4.2.1 Two-Body Geometrical Distribution

In the ALP rest frame, the photons are back-to-back (opening angle of 180 degrees) with an energy of $E^*_\gamma = \frac{m_a}{2}$. However, in the laboratory, the opening angle and energies of the two photons depend also on the ALP momentum. The angle between the two photons decreases with the ALP boost, leading to collimated photons at large momenta. Additionally, low-mass ALPs decay into soft photons, implying they get collimated easily. While high mass ALPs need a higher momentum to collimate the decay photons. For these reasons, the geometrical distribution of the photons directly depends on m_a and P_a.

The close-by pairs of photons are referred to as "merged" in contrast to "resolved" photons. $\Delta R = \sqrt{\Delta\eta^2 + \Delta\phi^2} = 0.4$ is the opening angle in (η, ϕ) under which photons are considered merged as it is the standard cone size for jet reconstruction [131]. Considering prompt ALPs via $h \to Za$, this limit is associated with $m_a = 2$ GeV.

Life-time impact on photon separation:

The opening angle of the two photons becomes insufficient to describe the photons' proximity in the calorimeter when a displacement is involved. Indeed, a photon pair can be very wide due to a large ALP mass and a low boost, but if the decay happens close to the calorimeter, such a wide angle might still result in two photons absorbed in the same calorimeter zone and count as a merged category.

This serves as an example of how analysis paradigms become irrelevant if one takes into account macroscopic displacements and shows how many aspects of ATLAS depend on prompt decays. Identifying all such features is critical to open ATLAS sensitivity to LLPs.

4.2.2 Challenges of a di-photon decay

Merged photons pose challenges compared to resolved ones for their identification. If their separation is smaller than the detector's and/or identification algorithm's angular resolution, the photons are reconstructed as a single object. In fact, the photon isolation uses measurements of transverse energy within a cone around the photon cluster ($ETcone$) which is parameterized in ΔR (in the EM calorimeter's (η, ϕ) plane). The isolation underperforms for photons registered in the same cone. Even if such a shower passes photon identification criteria, it might be reconstructed as a single photon. This effect reduces the correct classification of ALP di-photon decays. Additionally, such photon overlaps can appear broader than a usual single shower, and are rejected as background. Such properties have been used to reject high momentum $pi^0 \to \gamma\gamma$ as they are "fake photons". One tends to use looser photon identification criteria for low mass ALP (<2 GeV) analyses. It reduces the amount of rejected signals but raises the background. LL-ALPs suffer more from this effect as large masses can still yield merged photons when the decay is close to the calorimeter.

Furthermore, the two-body clusters exhibit a natural asymmetry in energy deposition compared to single bodies. The 2 photons in one cluster present a preferred axis

of energy deposition, the line connecting them, which renders an asymmetric calorimeter response. Figure 4.4 illustrates this. This asymmetry is not exploited by reconstruction algorithms, which often assume symmetrical energy deposition characteristics of single objects. Using this effect, new algorithms could probe these collimated photons with higher efficiency when the isolation fails. This would allow the differentiation of single photons from merged photons and directly improve the signal-t-background ratio of ALP searches. This principle is further developed in the next chapter.

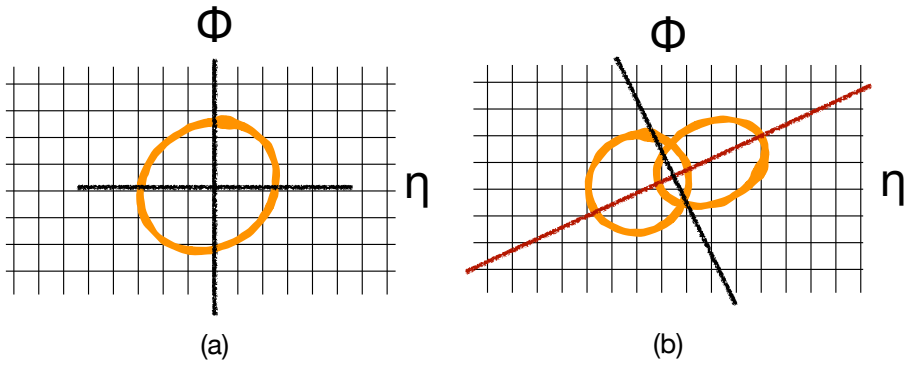


Figure 4.4: Representation of single (a) and double body (b) cluster in a calorimeter transversal cut. A red line is drawn to represent the preferred axis for energy distribution in (b).

4.2.3 Challenges of a displaced di-photon decay

Displaced decays add another layer of complexity as photons could be generated anywhere in the detector along the ALP trajectory. The displacement can cause non-collimated photons to get absorbed in the same cluster. Additionally, if their opening angle is large enough, the photons do not point back to the primary vertex like prompt photons (an illustration of this is presented in figure 4.9).The photon trajectory points to its DV instead of the collision point. The shower development inside the calorimeter is "tilted" as it does not remain along the usual (η, ϕ) cone. This emphasizes shower asymmetry and can yield broad energy deposits in the EM layers. This differs significantly from what is considered in the identification algorithms.

Challenges for LL-ALP identification The combination of displacement and collimation makes it particularly challenging to identify such events. Only ALPs decaying promptly with wide-open photon emissions are compatible with the current photon reconstruction. Figure 4.5 illustrates the displacement impact on the loose photon reconstruction efficiency on simulated samples of $h \to Za \to l^+l^-\gamma\gamma$ (samples described in section 4.5). The distance traveled by the ALP before decaying renders the identification photons increasingly less efficient and becomes null in the calorimeter range (1.5 meters).

Additionally, the figure shows that high-mass ALPs have a higher reconstruction efficiency at low displacements since the produced photons are resolved. In fact, prompt photons originating from 9 GeV ALP decays are resolved and present a reconstruction efficiency of around 0.9, while those originating from 0.4 GeV ALPs are merged present an efficiency of around 0.3. However, when displacement in the ID is considered, the merged photon reconstruction efficiency is stable while the resolved one drops significantly. After L_{xy}=1000 mm, the reconstruction efficiency of merged photons becomes superior. This is due to the non-pointing nature of displaced photons with large opening angles. If photons are very collimated, their trajectory would still point to the collision point. This is graphically illustrated in a later truth-matching section 4.6.2.

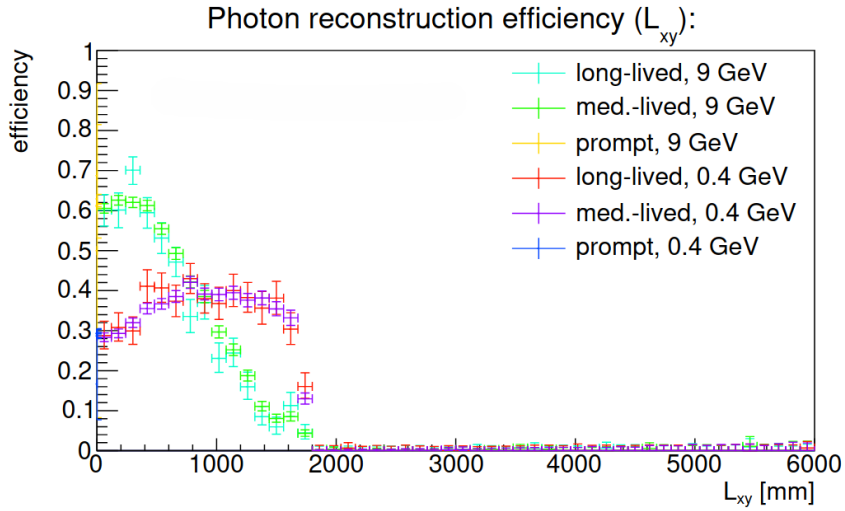


Figure 4.5: Photon reconstruction efficiency of ALP decay products for 2 mass points (0.4, 9) GeV and 3 life-times (prompt, medium, long) - samples described in 4.5. Note that the two masses are above and below the merged threshold (2 GeV) of prompt ALPs. The Lxy axis is the distance traveled by the ALP in the x-y plane. The reconstruction efficiency is computed by truth-matching the reconstructed loose photons to the truth-simulated particles.

This lack of performance is an opportunity to expand the current ATLAS software arsenal for analysis for boosted regimes and LLP searches. Advanced techniques using machine learning with low-level calorimeter data trained to recognize this type of signature could represent a significant upgrade. However, these techniques suffer from a high dimensionality problem due to the detector's granularity. Technical solutions to these encountered difficulties in tagging unusual signatures left by long-lived ALPs are presented below. An analysis considering both prompt and displaced ALPs produced in $h \to aa \to \gamma\gamma$ processes was conducted in ATLAS on run 2 data [84]. However, the published paper focuses more on prompt cases as the extra LLP challenges posed major difficulties.

4.2.4 Two strategies

Different strategies are needed for this unusual topology.

New shower-description and tagging

Photons are identified using shower-shape variables (presented in the next Chapter) that fail to stress the features presented above. Creating a new set of variables to describe the shower will benefit displaced ALP searches. These should include a correct focus on the center of the energy deposition to fight against photon collimation and have a good reading of the asymmetry. Such variables must be built from cell-level data, which presents technical difficulties explained through this thesis. They should be optimized and used within dedicated tagging algorithms that can be ML-based (Machine-Learning) to make maximal use of highly non-linear correlations.

With such variables, new triggers for displaced or collimated photon pairs can improve the selection of relevant events, which would benefit many LLP searches. The studies provided in this thesis open new possibilities for such shower-shape variables. Developing and employing sophisticated algorithms with working points associated with LLPs is one of the key objectives of this PhD project, as presented in the next Chapter.

Detector Upgrades

Upgrading the detector components can be a crucial improvement in opening ATLAS LLP sensitivity, but it will not be the main topic of discussion here. Below are a couple of examples of upgrades and their benefits for LLP searches.

The new timing detector HGTD [137], together with ITk, will both present very fine segmentations to help in separating close-by objects. Additionally, ITk can allow one to find displaced vertices in a larger zone than current hardware.

Furthermore, the HGTD will also improve the timing measurements of energy clusters - outside of the barrel. Timing information can be very discriminative for LLPs. Displaced particles are expected to produce "late" signals with respect to other processes. One can compute the time-flight difference between a prompt photon and an ALP to reach a given position where the ALP would decay. If one considers a 9GeV ALP with a 20GeV momentum decaying 2m away from the interaction point, this time difference is about 3 ns. If one considers lower masses and higher momenta, the timing shift can become much harder to detect. Such information could be utilized to trigger events and reconstruct displaced vertices. HGTD will offer a timing resolution of 30 ps [137], which will greatly benefit LLP searches outside of the barrel by allowing new time-based tagging techniques.

Conclusion

The ALP photon decay presents both opportunities and challenges. While the clean signature of two photons is appealing, the issues of collimation and displacement complicate the reconstruction process. Nevertheless, as is demonstrated later in this chapter, this type of phenomenology expects a very small contribution from SM background. Building software tools capable of reading these exotic shower shapes renders a high discovery/rejection potential that can strongly constrain the parameter space associated with a long life-time. Addressing these new challenges requires a combination of calorimetry studies, advanced algorithms, and dedicated triggers. This ensures that experiments like

ATLAS can effectively search for and identify LL-ALPs with high sensitivity.

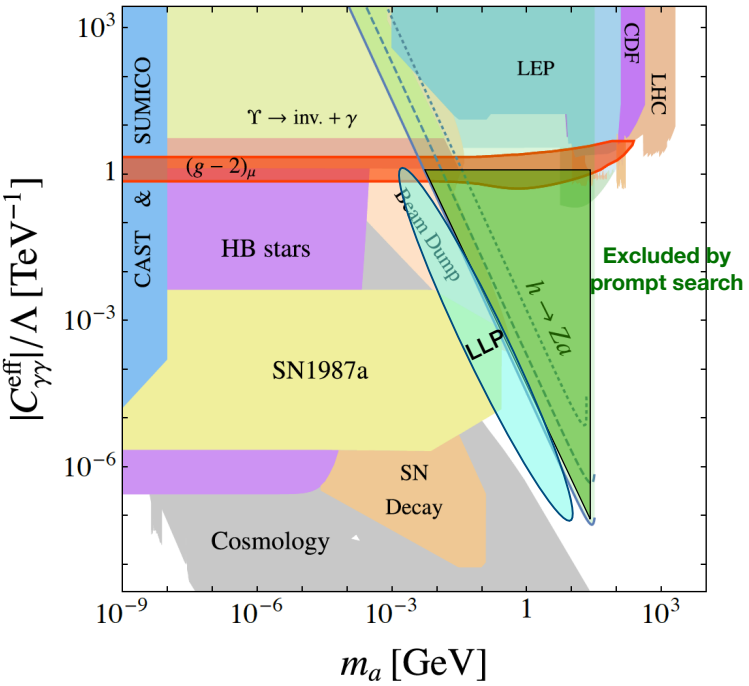


Figure 4.6: The ALP parameter space of photon decays. Presenting the LLP and prompt regions associated with $h \to Za$. Adapted from [79].

4.3 LLPs in ATLAS

Displaced decays from LLPs present unique opportunities for detection due to their distinctive signatures. Allowing ALP searches to extend to long life-times models opens the parameter-space region that ATLAS can probe. In fact, LL-ALPs present lower masses and couplings than prompt ALPs. Figure 4.6 illustrates an approximate parameter space region associated with LL-ALPs produced in a $h \to Za$ process and decaying to photons. This shows how searching for longer life-times complements the prompt analyses. In fact, an ALTAS Run2 search [83] for the same signal excluded prompt ALPs within the green region and calls for new analysis strategies targeting displaced ALPs. This region requires new paradigms and specific identification tools to cope with LLP-related challenges presented throughout the chapter. Additionally, figure 4.6 also indicates that the specific LLP region is unexplored and represents a gap between different experiments. This strongly motivates searches for LLPs in ALP models.

This section explores the general signatures of LLPs and dives into the specifics of displaced decays.

4.3.1 General LLP Signatures

LLPs can decay into a variety of final states, leading to a range of experimental signatures. These signatures differ significantly from those of promptly decaying particles. Consequently, they require specialized detection techniques. The SM background of

such events is usually highly suppressed [171], the main pollution coming from long-lived hadrons (K_l) and being mostly important only for low $c\tau$ decays. Figure 4.7 illustrates the rich diversity of very specific event topologies one can expect from decaying LLPs. The primary signatures of LLPs include displaced vertices, missing energy, and unusual energy deposition patterns.

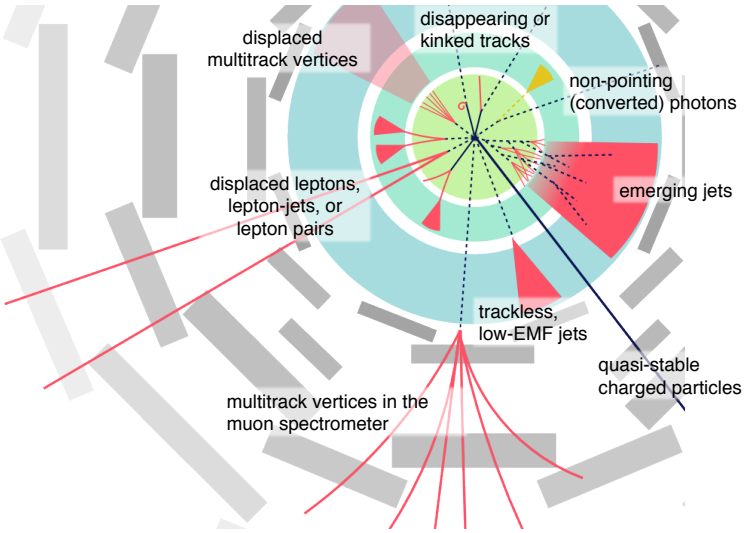


Figure 4.7: Schematic of various LLP signatures at LHC experiments. Represented on an ATLAS-like detector.

- **Displaced Vertices (DVs):** One of the hallmark signatures of LLPs is the presence of displaced vertices, where decay products originate at a significant distance from the primary interaction point. However, for secondary vertices $> 10mm$, standard tracking starts dropping in the vertex reconstruction efficiency. New tracker-based algorithms are developed to locate and rebuild disappearing tracks to find these DV. Figure 4.8 illustrates this purpose for the search of long-lived $\tilde{\chi}_1^0$. New internal developments using Graph-Neural-Netowrks show promising results for DV reconstruction.
  However, current DV techniques require tracker information, so they can usually not be used for photon decays (only if a photon is converted to $e + e-$) and cannot work for decays happening in the calorimeter.

- **Missing Transverse Energy (MET):** LLP can result in significant MET if the decay products include neutrinos or if the decay occurs outside the detector. As mentioned in Chapter 1.5.2, these signatures are mostly investigated through Mono-X searches and are very similar to DM candidates, as they also escape the detector.

- **Unusual Energy Deposition Patterns:** The decay products of LLPs can produce unconventional energy deposition patterns in the calorimeter, creating displaced jets or non-pointing photons [172]. Most ALP ATLAS and CMS searches did not consider life-times yielding decays inside the calorimeters due to the extra layer of reconstruction difficulty. However, such greatly displaced photon pairs would create a highly exotic calorimeter response. This phenomenology is investigated in the next section.

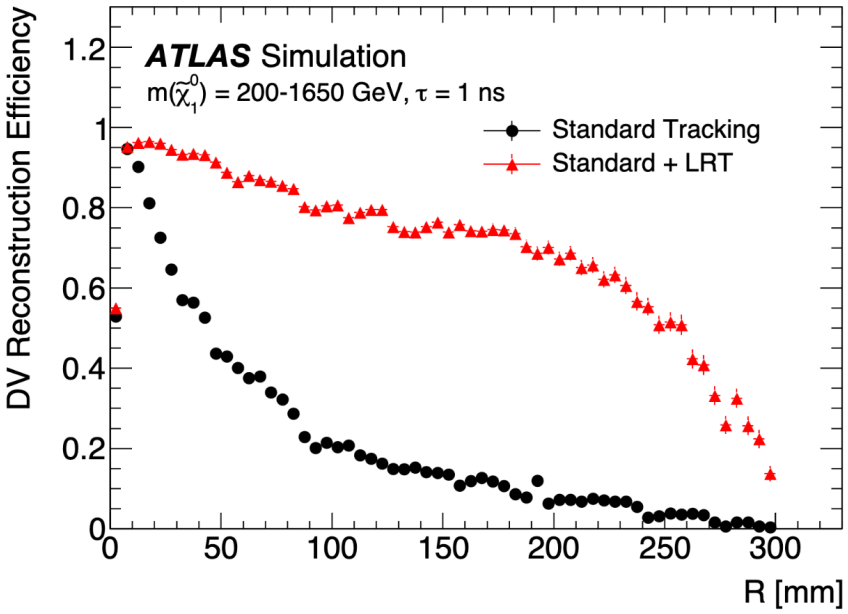


Figure 4.8: DV reconstruction efficiencies for ATLAS standard and modified track reconstruction algorithms. The modified algorithm is large-radius tracking and is tailored for LLP cases [110].

4.3.2 Decays in Calorimeters

If its life-time allows it, LLPs can decay directly inside the calorimeters. This type of event offers very complex challenges since its detection relies on sub-detectors that are not designed for such situations. Additionally, many reconstruction algorithms, such as the ones for photons or electrons, drop to a near 0 efficiency when decays occur after the tracker region. However, the shower shapes created in those events radically differ from the SM background and offer opportunities to reconstruct LLPs and measure their properties. It is a complex problem to solve, but only a few events can guarantee a discovery.

ATLAS calorimeters were constructed to stop and measure the energy of particles produced at the collision point. Considering the case where a photon pair is produced in the hadronic calorimeter, the resulting shower shape will be EM-like, but the EM part of the calorimeter will detect no signal. If such events occur, the photon identification will fail as it relies heavily on the EM calorimeter. This type of possible scenario modifies completely the way calorimeters should be used to reconstruct LLPs properly. Figure 4.9 depicts how such a specific event can manifest itself in the ATLAS detector. In addition, this figure illustrates key possible event topologies due to the long-lived nature of the ALP, including (double) photon conversions inside the tracker, which create different signatures that have not been investigated in this work. Figure 4.9 also highlights special calorimeter responses like non-pointing photons, asymmetrical energy deposits, collimated photons, and strongly absorbed photons in the hadronic calorimeter.

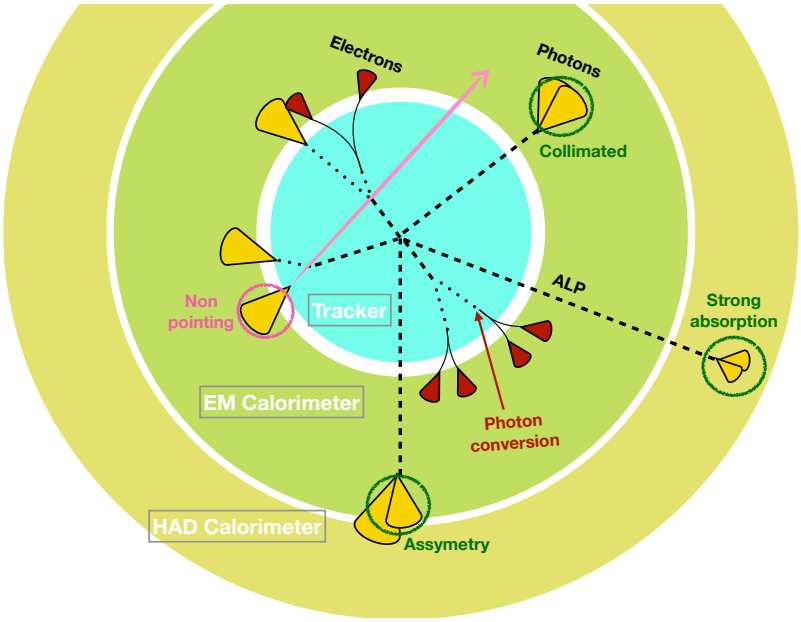


Figure 4.9: Diversity of photon decays from an LL-ALP in an ATLAS-like detector.

As mentioned, very displaced ALPs can create situations where energy may only be deposited in the last layers of the calorimeters, creating a distinctive signal that is easily distinguishable from background noise. Selecting events with no energy deposited in the early calorimeter layers but with high absorption in the later EM calorimeter or Hadronic calorimeter can significantly contribute to the LL-ALP search. ML tools trained on samples that include ALPs decaying in the calorimeters can easily learn and exploit this unusual signature. Additionally, EM-like showers appearing in the hadronic calorimeter are indicative of these exotic decays, contrasting with the typical QCD shower profiles expected in these detectors.

Furthermore, the significant displacement of the decays in the calorimeter results in a higher timing shift relative to the underlying events. This large difference facilitates timing-based discrimination approaches. In fact, it is harder to identify (with timing measurements) LLPs decaying in the tracker compared to in the calorimeter.

The features associated with the two-body cluster of merged photons are emphasized for decays inside the calorimeter. The further away the decay occurs from the interaction point, the more pronounced the expected unusual signatures become. By looking at figure 4.9, one can see that ALPs with rather long life-times result in much more stressed non-pointing effects. Additionally, for a given photon-pair opening angle, longer decay lengths yield more close-by photons compared to shorter ones. Indeed, the distance remaining between the decay position and the calorimeter allows the photons to separate from one another. This implies that photons produced by calorimeter-level decays create narrower showers with an extra level of difficulty concerning photon isolation, particularly for low-mass ALPs.

This more concentrated energy deposit creates a higher difficulty in discrimination concerning single photons. A perfect overlap of two photons provides a shower shape

that is extremely difficult to discriminate from single photons. The only difference, for such perfect overlaps, remains in the shower depth inside a calorimeter layer in the R axis. Two perfect-overlapped photons with an energy $\frac{E}{2}$ will not penetrate as deep as a single photon with energy E; this is illustrated in figure 4.10. This type of measurement could be done using the LAr EM calorimeter by looking at the charge collection time. Internal calibration studies (on single e/γ) have demonstrated that the charge collection time in a cell depends on the energy deposited. A high-energy photon creates a signal across the depth of a given layer; thus, the full charge collection takes longer. However, if one considers overlapped photons at the same total energy, they produce a shallower shower, therefore, a quicker charge collection. This information shows a high potential for discrimination. Nevertheless, technical difficulties are present as you need to extract this very specific low-level information, and the time precision might not fit the requirements. This type of technique will not be investigated further in this thesis but could potentially be the focus of future work.

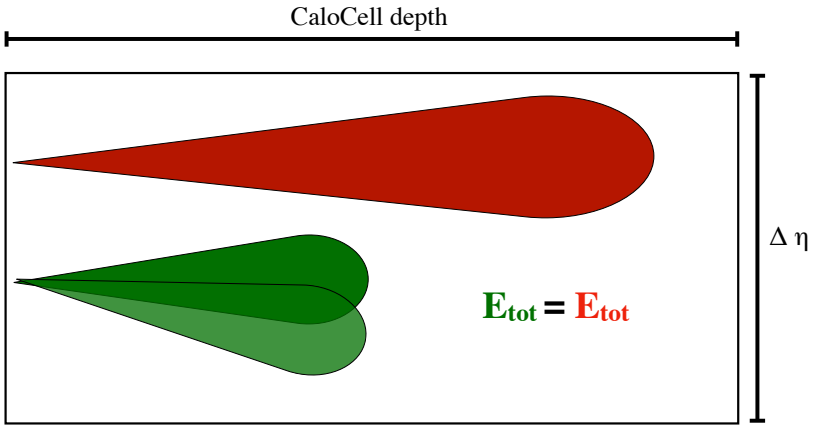


Figure 4.10: Illustration of how same energy single-photons and photon pairs are absorbed with different depths in an EM Calorimeter cell. The depth is in the R axis, perpendicular to $\vec{z}$.

While the depth measurement might be too technically challenging, measuring the expected energy deposit asymmetries with different shower shape descriptions can be done; this is described in Chapter 5. Still, the accentuated collimated effects due to calorimeter-level decays complicates this process. The number of cells separating the two bodies directly impacts the precision of asymmetry measurement (see previous figure 4.4). Thus, high granularity layers will play a significant role in this matter.

This discussion demonstrates that to tag LL-ALPs decaying in the calorimeter, it is crucial to capture the essence of the double body structure as it will provide discrimination to single photons. It is clear that for calorimeter decays, the special signatures discussed so far are greatly emphasized but have become technically more difficult to probe. Variables expressing these features provide high discrimination potential if used with new ML-based taggers.

The multitude of exotic signatures that can occur in a displaced $a \to \gamma\gamma$ decay offers many opportunities for LL-ALP ATLAS analyses. These event topologies are so unique, particularly for calorimeter-range decays, that the standard model background is immensely suppressed. Although technical challenges are important, different new algorithms implemented in the ATLAS reconstruction and analysis workflow can make it possible to identify these rare events. These new algorithms must find solutions to counter the complexity of shower shapes and the inefficiencies of current reconstruction techniques.

It should be noted that the analysis presented in this chapter focuses on the barrel region and its extension, excluding the forward calorimeters. This decision is based on the overall more complex structure and higher granularity of the barrel calorimeter layers. These factors provide opportunities to develop new experimental techniques for identifying the unusual showers under consideration. Additionally, as will be presented in this chapter, the ALP η distribution predominantly peaks at 0, with negligible occurrences in the high-$|\eta|$ regions for $h \to Za$ production, which is the main target of a first analysis.

4.4 ALP phenomenology studies

A first study was conducted in this PhD to construct the region of the ALP's parameter-space compatible with a decay inside ATLAS calorimeters and compute the expected number of events for such a signal in run 3. This was done in the context of preparing a calorimeter-based analysis of Higgs exotic decays into ALPs ($h \to Z + a$; $a \to \gamma\gamma$). More precisely, the aim was to find the combinations of mass (m_a), effective coupling to photons ($C_{\gamma\gamma}$), and energy scale (Λ) for which the ALP has a life-time that leads to decay inside the ATLAS calorimeters. In the second step, the goal was to provide the number of signal events by fixing the relevant cross-sections and branching fractions in an optimistic scenario.

4.4.1 ALP decay in ATLAS

This section describes the important parameters to consider when computing the ALP decay kinematics inside ATLAS.

Higgs boosted

The signal under investigation is considered a Higgs boson exotic decay. Consequently, Higgs production kinetic distributions have to be taken into account to construct the associated ALP distributions for a given set of parameters (m_a; $C_{\gamma\gamma}$; Λ). Taking into account the scalar nature of the Higgs boson and its $h \to Za$ decay allows one to compute the associated ALP kinematic distributions.
The production mechanism of the ALP has a significant influence on the final state distributions; it is important to set a clear production process and consider all associated implications. For instance, by considering the $h \to Za$ decay one should consider the upper mass limit of $m_h - m_Z$, which differs from the $h \to aa$ productions.
After considering the kinetic impact of the Higgs boson distribution on needs to consider the ALP life-time.

ALP life-time

From the effective field theory (EFT) (detailed in section 1.7 of Chapter 1), a relation between the decay rate to 2 gammas and $(m_a, \Lambda, C_{\gamma\gamma})$ can be derived :

$$\Gamma_{a\to\gamma\gamma} = 4\pi\alpha^2 m_a^3 \frac{C_{\gamma\gamma}^2}{\Lambda^2} \tag{4.1}$$

For simplicity we re-define the axion decay constant as : $f_a = \frac{\Lambda}{\sqrt{4\pi}\alpha C_{\gamma\gamma}}$.
By doing so, the parameter space is reduced to a plane spanned by m_a and f_a. The partial width of the ALP can then be rewritten as :

$$\Gamma_{a\to\gamma\gamma} = \frac{m_a^3}{f_a^2} \tag{4.2}$$

The intrinsic life-time of the ALP is given, in natural units, by the inverse of the width: $\tau = \frac{1}{\Gamma_{tot}}$. If one considers the photon decay as the dominating process, the total width can be approximated $\Gamma_{tot} \approx \Gamma_{\gamma\gamma}$. Therefore, the life-time computations are reduced to :

$$\tau = \frac{f_a^2}{m_a^3} \tag{4.3}$$

One directly recognizes an expected relation, indeed low masses and low couplings contribute to more stable ALPs.

This life-time is an intrinsic property of the ALP that is considered to be in its center of mass frame. To compute life-times in the laboratory frame (ATLAS), one must consider time dilatation induced by the high speed of ALPs produced in high-energy collisions. For that, τ is multiplied by the ALP's Lorentz factor $\gamma_a = \frac{E_a}{m_a}$ in the lab frame; resulting in :

$$\tau_{lab} = \gamma_a \tau \tag{4.4}$$

Decay time

However, the intrinsic life-time of ALP does not directly give a definite decay position. It is used to build the probability distribution of survival time from which one can extract the possible time of flights for a given ALP with a given boost.
The time of flight of the ALP before decaying into two photons is a stochastic quantity that follows an exponential distribution guided by the decay constant $\lambda = 1/\tau_{lab}$. The probability density function (pdf) is:

$$p_{decay}(t) = \lambda e^{-\lambda t} \tag{4.5}$$

The anti-derivative of the density function yields the probability that the ALP has survived at a given time:

$$P_{decay}(t) = \int p_{decay}(t)dt = 1 - e^{-\lambda t} \tag{4.6}$$

For a given value of γ_a, the decay time distribution of the ALPs would follow a single pdf. However, the problem is more complex since each event presents different kinematics for the Higgs boson thus a different ALP boost γ_a. Therefore, for a fixed intrinsic life-time in the center of mass frame, different time dilatations leading to a different time of flight distributions are to be considered in the lab frame. The real decay time distribution inside ATLAS is a convolution of multiple distributions that depend on each event's kinematics.

Energy distribution

As just explained, the expected energy distribution of the ALP for each parameter-space point must be determined to find the observable decay length distribution. In the $h \to Za$ production process, the ALP energy distribution is directly correlated to the Higgs one. This also depends on the production diagrams of the Higgs boson, which will be covered later. From the 4-momentum conservation law in the decay, the ALP energy in the ATLAS frame is :

$$E_a = \frac{m_h^2 + m_a^2 - m_z^2}{2m_h} + \frac{1}{2m_h}|\vec{P}_a||\vec{P}_h|\cos(\theta) \tag{4.7}$$

where θ is the angle between the Higgs ($\vec{P}_h$) and the ALP ($\vec{P}_a$) 3D momenta. The second term of the equation vanishes in the Higgs center of mass frame:

$$E_a^\star = \frac{m_h^2 + m_a^2 - m_z^2}{2m_h} \tag{4.8}$$

Using this equation, the ALP energy for each event in the Higgs center of mass can be computed.

From the Higgs kinematics distributions, accessible from simulated samples, a Lorentz boost is applied to get the ALP distribution in the lab frame. Using this strategy, one can compute the expected kinematic behavior of ALPs inside ATLAS for a given production process and parameter space point without having to use event generators.

Another option consists of using the additive property of rapidity ($\nu_{AC} = \nu_{AB} + \nu_{BC}$) and then linking it to the ALP's β and γ values to change from the Higgs center of the mass frame to the lab:

$$\beta_i = \tanh(\nu_i) \quad ; \quad \gamma_i = \cosh(\nu_i) \tag{4.9}$$

Decay Length inside ATLAS

After fixing the ALPs free parameters, the energy distribution of the ALP in the lab frame (boost from Higgs decay) yields the γ_{ALP}^{lab} and β_{ALP}^{lab} values. Using equations 4.4 and 4.5, the ALP's decay time distribution is retrieved. The decay length distribution is easily obtained by including the speed of the particle in the lab frame.

$$D = \beta_a^{lab} \cdot c \cdot t_{decay}^{lab} \tag{4.10}$$

4.4.2 Calorimeter geometries

To study ALPs that can decay in the calorimeters, one must identify clear geometrical arrangements of these sub-detectors. By collecting geometrical information from the relevant technical design reports [100] [112] one can find the important z and R (i.e the distance to the beam axis z) positions of the different sections of the electromagnetic and hadronic calorimeters in the ATLAS frame. Their segmentation along η is also retrieved. The figures used to infer the general geometrical description of the calorimeters are 4.11, 5.11 (in Chapter 5), 4.12 and 4.13.

Decay in the EM Barrel

PS	EM1	EM2	EM3
1400	1500	1591	1927

Table 4.1: Distance in mm between the collision point and each layer of the EM calorimeter on the transverse plane (for η=0)

For the ALP to decay inside the EM barrel, it should have a decay length L_0 in the range [1500 - 1970] mm at $\eta = 0$. Opening the η spectrum, the decay length has to increase. Equation 4.11 defines the ALP's trajectory angle with respect to $\vec{z}$ as a function of η. The EM barrel decay-length acceptance range is written for any η as in equation 4.12.

$$\theta = 2 \times arctan(e^{-\eta}) \tag{4.11}$$

$$L_\eta = L_0 \times sin(\theta)^{-1} \tag{4.12}$$

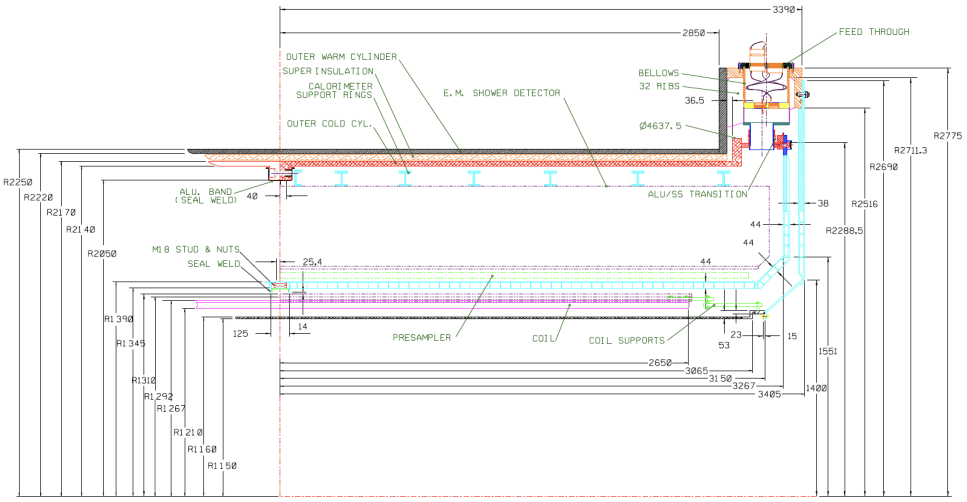


Figure 4.11: Side view of the LAr calorimeter. Relevant distances in the R axis are illustrated as depicted in the LAr calorimeter technical design report [112].

The EM barrel has a full acceptance for $|\eta| < 1.375$, which corresponds to a maximum angle of $\theta = 28.38°$.
To decay inside the EM barrel, the ALP must have a **decay length of 1400 mm at the minimum and cannot exceed 4140 mm**.

Decays in TileCal

Similarly, figure 4.13 shows that at $\eta = 0$, the range of decay lengths within the TileCal in mm (L_0) is within [2280 - 3865]. TileCal has an acceptance of $|\eta| < 1$ for the main

barrel and of $|\eta| \in [0.8, 1.7]$ for the extended barrel. The same method can be followed for the EM barrel. At maximum η, the ALP can only decay in the first layer of the TileCal since the higher layers stay out of its trajectory, as it is clear from figure 4.13.
Using equation 4.12, it concludes that for decays inside the TileCal, the ALP's decay length must be between 2280 mm and 7300 mm.

Decay inside the barrel

Including both central calorimeters (not taking into account the EM pre-sampler), one gets the limits in table 4.2.

	EM Barrel	HAD Barrel	**Calorimeter Barrel**
min decay length	1400	2280	**1400**
max decay length	4140	7300	**7300**

Table 4.2: Minimum and maximum distance in mm between the collision point and the barrel calorimeter; considered on all η values within acceptance.

Decay inside the end cap

Combining information from figure 4.12 and endcap inner and outer wheels in [100], one can find the dimensions along the $\vec{z}$ axis and the dependencies with η of both EM and Hadronic EndCaps. The EM End Cap has an acceptance in the range $[\eta = 1.37; \eta = 3.2]$, is placed 3.45 m away from the interaction point, and is 576 mm thick. The Hadronic end cap has a smaller acceptance (as can be seen in figure 4.12) of $[\eta = 1.5; \eta = 3.2]$ and is placed right behind the EM end cap. It stops at 6.70m from the interaction point.

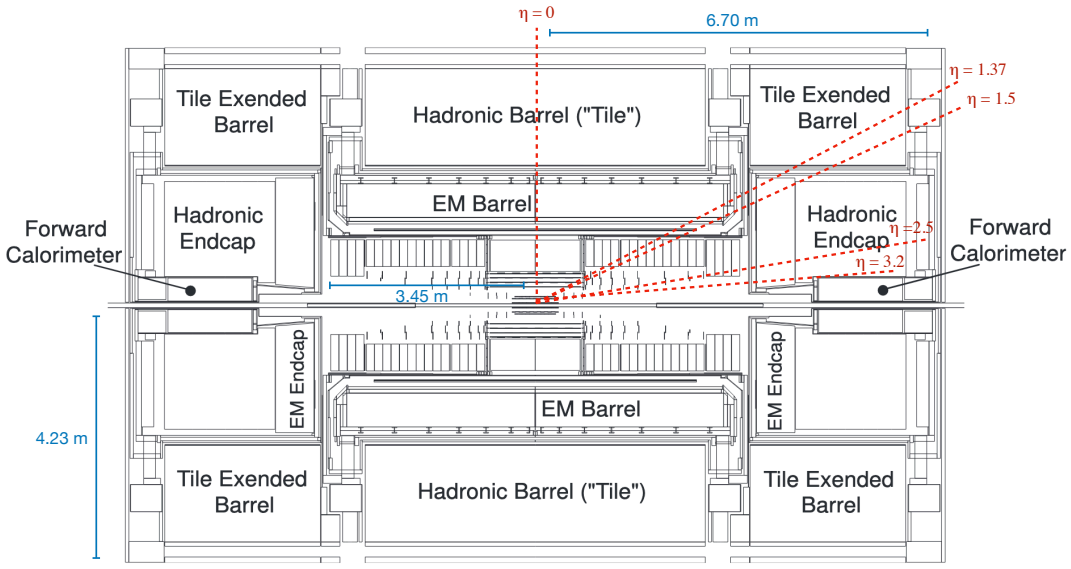


Figure 4.12: Side view of ATLAS calorimeters with relevant dimensions and important eta segmentation.

To calculate the maximum and minimum decay lengths with respect to η, the following equation is used :

$$L_\eta = L_\infty \times \cos(\theta)^{-1} \tag{4.13}$$

where L_∞ is the length along $\vec{z}$ ($\eta = \infty$). Results are found in table 4.3.

	EM End Cap	HAD End Cap	**Calorimeter End Cap**
min decay length	3460	4050	**3460**
max decay length	4570	7045	**7045**

Table 4.3: Minimum and maximum decay lengths in mm between the collision point and the end cap calorimeters, including the full η range within acceptance.

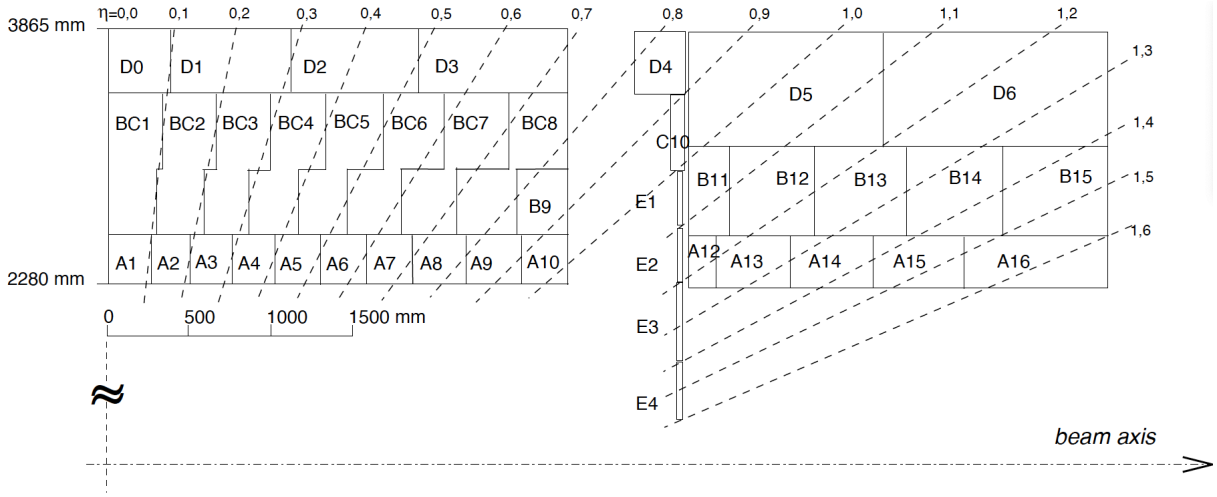


Figure 4.13: ATLAS TileCal segmentation in η. The left side is the barrel, and the extended barrel is on the right side. From the ATLAS experiment paper [100].

4.4.3 A new Python tool to predict ALP production

Previous internal studies of LL-ALPs were conducted using a full generation of $h \to Za$ signal samples. In such a case, the kinematics and decay positions of the ALP were studied in order to access truthful information. However, this standard way of assessing the ALP's relevant distributions is time-consuming since it demands the production of MC samples for each parameter space point. By building a simple Python tool with ROOT and utilizing all important equations exposed earlier, one can find similar results more flexibly. The workflow of this important phenomenology tool is presented below.

The tool requires as input Higgs kinematic distributions. For this reason, 10k events of MC-simulated Higgs bosons were used. The simulation considers Higgs bosons produced via a gluon fusion mechanism (like in figure 4.18 of a later section) at NNLO, in pp collisions at $\sqrt{s} = 13TeV$.

Main steps of the project

For each event, the following steps are performed :

1. **Calculate τ_{ALP} using chosen parameters (mass m_a, $C_{\gamma\gamma}$, Λ):**
   By using equations 4.1 and 4.3.

2. **Calculate E^*_{ALP} in the Higgs center of mass frame:**
   As in equation 4.8 and implementing a Breit-Wigner distribution from which m_Z is sampled for each event.

3. **Randomly choose a value of ϕ^* and θ^* (according to the spin configuration of the decay):**

   In the center of mass frame (c.o.m.f) of the spin 0 mother particle, the decay is isotropic, therefore :

   - The azimuthal angle ϕ is uniformly distributed with a probability given by :

   $$P(\phi) = \frac{1}{2\pi}, \quad \phi \in [0, 2\pi]$$

   - While the polar angle θ is distributed such that $\sin(\theta)$ is uniform:

   $$P(\theta) = \frac{1}{2}\sin(\theta), \quad \theta \in [0, \pi]$$

   In fact, for a spin 0 particle :

   $$\frac{d\sigma}{d\Omega} = \text{cst} \Rightarrow \frac{d\sigma}{d\phi d(\cos\theta)} = \text{cst} \Rightarrow \frac{d\sigma}{d\phi d\theta} \propto \sin(\theta) \tag{4.14}$$

4. **Build the ALP's 4-vector in the Higgs c.o.m.f. :**

   $$\widetilde{P}^*_a(E^\star_{\text{a}}, p^\star_{T_{\text{a}}}, \theta^\star, \phi^\star) = \begin{pmatrix} E^\star_{\text{a}} \\ p^\star_{x_{\text{a}}} \\ p^\star_{y_{\text{a}}} \\ p^\star_{z_{\text{a}}} \end{pmatrix}$$

   where $\star$ refers to the Higgs boson c.o.m.f.

5. **Retrieve the 4-vector from the Higgs truth container in the ATLAS frame:**

   $$\widetilde{P}_h = \begin{pmatrix} E_{\text{h}} \\ p_{x_{\text{h}}} \\ p_{y_{\text{h}}} \\ p_{z_{\text{h}}} \end{pmatrix}$$

6. **Boost the ALP to the lab frame with the TLorentz ROOT functions**

   $$\widetilde{P}_{\text{a}} = \text{Boost}(\widetilde{P}^*_{\text{a}}, \widetilde{P}_{\text{h}}) = \Lambda^\mu{}_\nu \widetilde{P}^*_{\text{a}}$$

7. **Find τ_{ALP} in the lab frame using the Lorentz factor of the ALP**
   As it is explained in equation 4.4.

8. **Randomly select a value from the associated probability density function:**
   As described by equation 4.5 using the scipy.stats python library [173].

9. **Compute the decay length.**
   By using equation 4.10.

10. **Retrieve the boosted η and ϕ in the ATLAS (lab) frame through the ALP TLorentz vector.**

11. **Confirm or reject if each ALP decays inside the calorimeter.**
    Done by referring to tables 4.3 and 4.2 sliced in 4 eta ranges. Covering the barrel, the TileCal extended barrel, and the end caps.

12. **Finally, compute the fraction of events that are expected to decay in the calorimeters for a given set of model parameters.**

The resulting distributions were compared to the previously obtained ATLAS MC simulation on benchmark parameter space points and showed deviations below 1%. This software tool saves computation time and resources since no full event generation is required.

Running coupling

The electromagnetic coupling constant α is indeed a running constant, meaning its value changes with the energy scale at which it is measured. At low energies, α is approximately 1/137, or about 0.0073. However, at higher energies, such as those reached in particle colliders like the LHC, the effective value of α increases. This is described in equation 4.15.

$$\alpha(Q) \approx \frac{\alpha(m_e)}{1 - \frac{\alpha(m_e)}{3\pi} \ln\left(\frac{Q^2}{m_e^2}\right)} \tag{4.15}$$

The choice of the coupling value must be accurate to better represent the experimental conditions ($\sqrt{s} = 13$ TeV).

4.4.4 Parameter-Space scan

With the tool validated, a thorough scan of parameter combinations was performed. Masses were fixed in the range $[10^{-3}, 30]$ GeV. The mass conservation law fixes the maximum limit in the $h \to Za$ decay. The $\frac{C_{\gamma\gamma}}{\Lambda}$ ratio was scanned in the range described in figure 4.6 (i.e $[10^{-10}, 10^{3}]$).

Criteria to accept parameter-space points

For each (m_a,f_a) point, the fraction of ALPs decaying inside one of 4 (η, R) calorimeter regions, defined in table 4.4, and inside the tracker is computed. The 4 regions are only a global approximation of the calorimeter's main structures' geometrical positions. For

decays in the forward calorimeters, the region is defined as $(\eta, \vec{z})$. The distance along the z-axis is more pertinent in such cases.

Region	η intervals	Distance (mm)
cal_range1	$\eta < 1.25$	[1500, 3865] : $\vec{R}$
cal_range2	$1.25 \leq \eta < 1.375$	[1500, 3345] : $\vec{R}$
cal_range3	$1.375 \leq \eta < 1.5$	[2280, 2900] : $\vec{R}$
cal_range4	$1.5 \leq \eta < 3.2$	[3450, 6700] : $\vec{z}$

Table 4.4: Distance ranges for different η regions. cal_range4 refers to the forward region; therefore, the distance is considered along the $\vec{z}$ axis.

To confirm or reject a given parameter-space point, a loose threshold on the fraction of events in the calorimeter is applied. The required percentage of events to decay inside the calorimeters is set to 0.01%.
Figure 4.14 depicts the resulting decay length distribution for a given combination of model parameters. Both the decay fraction inside the calorimeter and the tracker are indicated, and this parameter-space point is accepted.

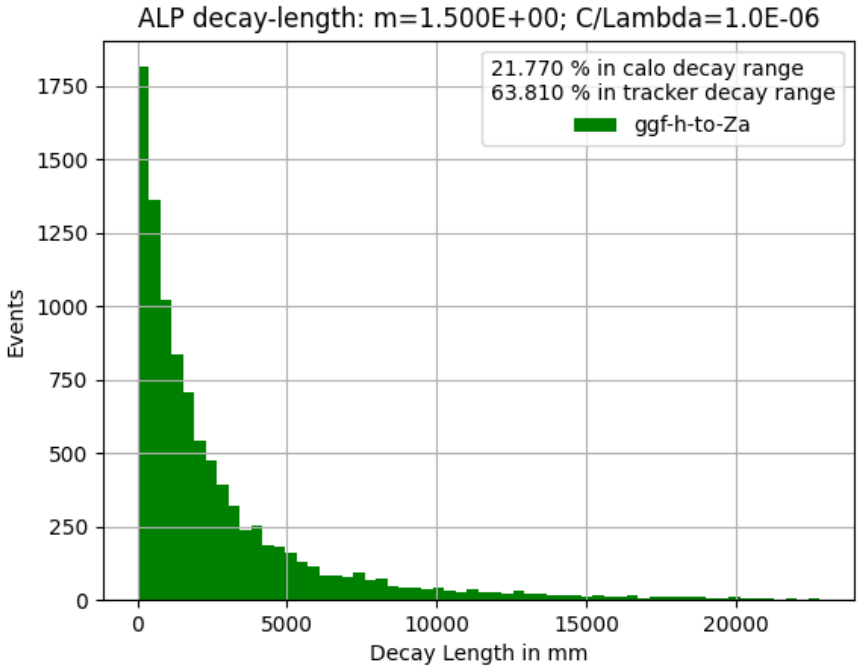


Figure 4.14: ALP computed decay length distribution for $m_a = 1.5$ GeV and $f_a = 10^{-6}$.

To validate this new simple tool, a comparison was made with the previous $h \to Za$ MC simulations on the same $(m_a, C_{\gamma\gamma}, \Lambda)$ points. Table 4.5 shows different masses and their associated life-times at a fixed value of f_a obtained via the new tool. Table 4.6 compares the results with the Monte Carlo simulations at the same parameter-space points. Showing an average relative difference of only 1.4%, this table validates the

Python script by demonstrating that the numbers computed using the fast computation tool are very close to those obtained from the official full-scale MC simulations.

m_a (GeV)	$c\tau$ (mm)	τ (s)
0.1	2.94×10^{-1}	9.84×10^{-13}
0.2	3.69×10^{-2}	1.23×10^{-13}
0.5	2.36×10^{-3}	7.87×10^{-15}
0.7	8.60×10^{-4}	2.87×10^{-15}
1.0	2.95×10^{-4}	9.84×10^{-16}
2.0	3.69×10^{-5}	1.23×10^{-16}
4.0	4.60×10^{-6}	1.54×10^{-17}
6.0	1.37×10^{-6}	4.55×10^{-18}
9.0	4.05×10^{-7}	1.35×10^{-18}

Table 4.5: Values of $c\tau$ and τ for different masses of ALPs for $f_a = 10^{-4}$.

ma (GeV)	Γ_{tool} (GeV)	Γ_{MC} (GeV)
0.1	6.69×10^{-17}	6.60×10^{-17}
0.2	5.35×10^{-16}	5.28×10^{-16}
0.5	8.36×10^{-15}	8.25×10^{-15}
0.7	2.30×10^{-14}	2.26×10^{-14}
1.0	6.69×10^{-14}	6.60×10^{-14}
2.0	5.35×10^{-13}	5.28×10^{-13}
4.0	4.28×10^{-12}	4.22×10^{-12}
6.0	1.45×10^{-11}	1.43×10^{-11}
9.0	4.88×10^{-11}	4.81×10^{-11}

Table 4.6: Evolution of ALP decay widths computed via the quick phenomenology tool and the MC simulation for different masses m_a but fixed $\Lambda = 10^4$ GeV and $C_{\gamma\gamma} = 1$.

4.4.5 Compatible parameter-space

The computed parameter space region compatible with decays inside ATLAS is represented in figure 4.15. As expected the region follows the the main prompt $h \to$ Z a region with lower masses. The blank space observable between the calorimeter region and the prompt includes the low-displaced ALPs that do not reach the calorimeter. The lower border of the calorimeter region corresponds to ALPs with too long life-times.

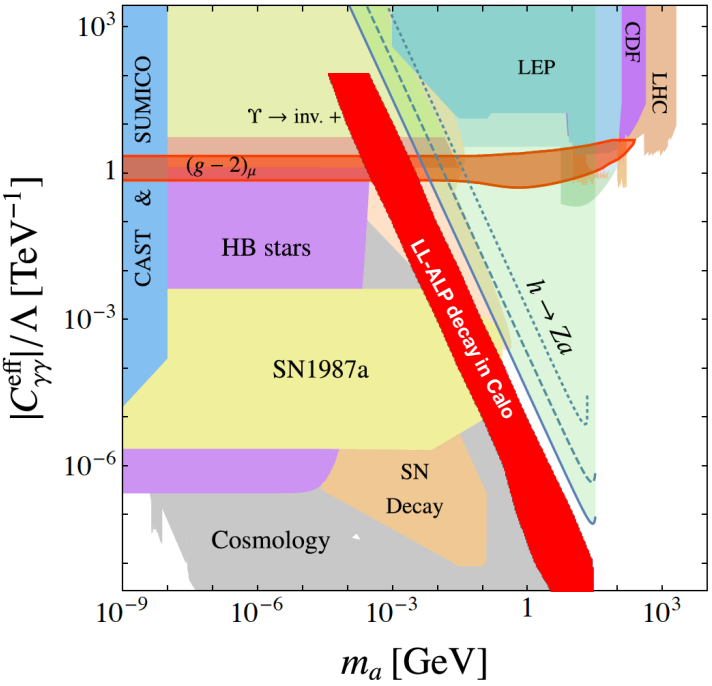


Figure 4.15: Resulting parameter space for ALP decays inside the Calorimeters. The region compatible with $h \to Za$ ALP decays in the calorimeter is highlighted in red. The limits are computed as described in 4.4.4. The prompt ALP decay region corresponding to the same process is highlighted in light green. Adapted from [79].

Note that a blank region is present between the prompt and in-calorimeter decay regions. This region includes LL-ALPs that decay within the tracker radius.

4.4.6 Run3 expected number of events

To better estimate the number of events expected in run 3, optimistic model assumptions were made and should be considered as a reference.

The following assumptions and cuts were made for the parameter-space covering region for ALPs decaying into two photons:

- $\text{Br}(a \to \gamma\gamma) = 1$ and $C_{Zh} = 1$ for simplicity of reinterpretation.
- $\Lambda = 10^4$ GeV; to guarantee compatibility with experimental limits and enhance the expected number of events, as explained in appendix 4.A.
- $C_{\gamma\gamma} \leq 10$; to guarantee compatibility with experimental limits, as explained in appendix 4.A.
- $\frac{C_{\gamma\gamma}}{\Lambda} < 10^{-3}$, inferred from the two previous points
- $\sigma_{pp\to h\to Za} = 10^3$ fb, expected production cross section for $\Lambda = 10^4$. See figure 4.16.
- $L_{\text{Run 3}} = 300$ fb^{-1}. Integrated luminosity over the full data-taking period.

The total run 3 number of events is given by equation 4.16.

$$N_{a\to\gamma\gamma} = \mathcal{L}_{\text{Run 3}} \cdot \sigma(pp \to h \to Za) \cdot \mathcal{B}(a \to \gamma\gamma) \tag{4.16}$$

After injecting the fixed parameters, one computes the total number of expected events:

$$N_{a\to\gamma\gamma} = 3 \cdot 10^5 \text{ during Run 3}$$

Figure 4.17 depicts parameter space associated to run3 in-calorimeter decays of the investigated signal. The $C_{\gamma\gamma}$ and Λ limits described above are incorporated. The borders are defined as containing 0.05% of events in the calorimeter range. The number of expected events at the borders is around 150, while the center of the region could potentially go up to 10^4 events. The central region corresponds to the points having a maximum number of ALPs decaying inside the calorimeters. This value is around 25%.

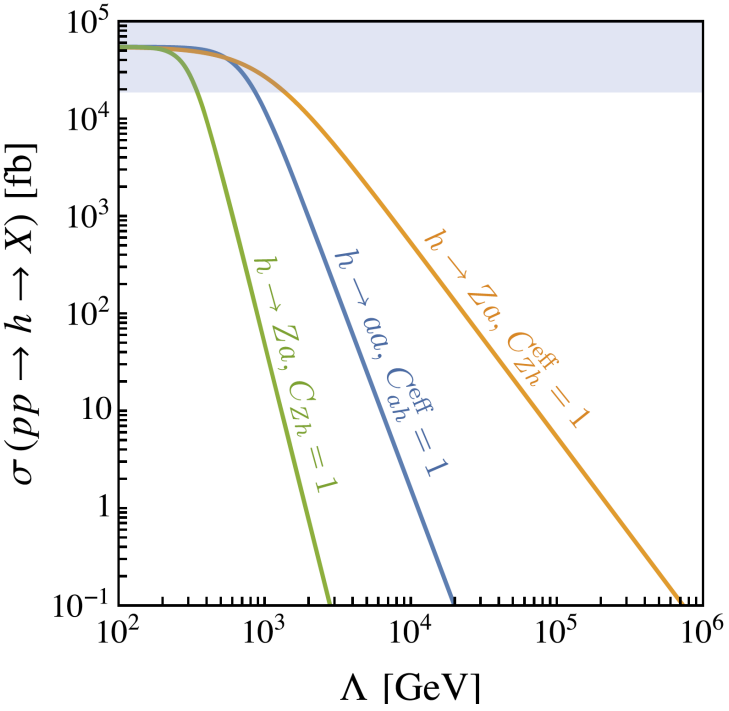


Figure 4.16: Production cross sections of ALPs produced in the decays of Higgs and Z bosons at the LHC for the energy scale Λ [79].

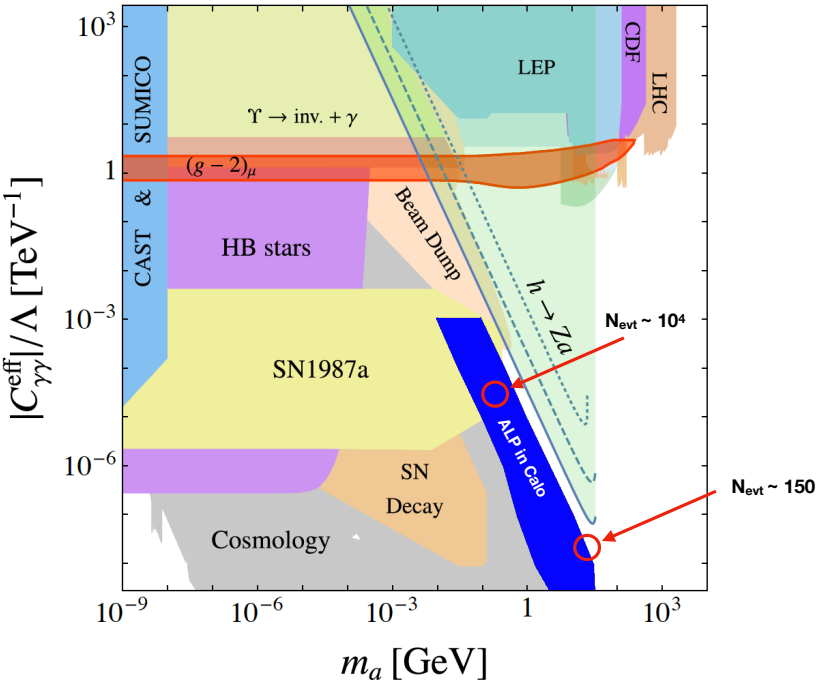


Figure 4.17: Resulting parameter space potentially leading to a discovery of LL-ALPs, decaying in calorimeters, in run 3 with a realistic f_a cut. The arrows show several events for run3 at the limit (minimum) and center (maximum) of the region of interest for in-calorimeter decays. Adapted from [79].

This result is promising as it is the best-case scenario. If the energy scale Λ was higher or if the branching ratio $\mathrm{Br}(a \to \gamma\gamma)$ was lower, the number of expected events would decrease. However, the topology of the calorimeter response to such events is so incredibly unique that a handful of events could be enough to allow signal discovery. This leaves great flexibility concerning these unknown parameters.

This phenomenological study was important to grasp how large the parameter-space region of the planned analysis is and how it compares to other experiments. The result confirms that this type of event in ATLAS represents an important region to constrain. However, to probe them, a precise analysis strategy must be implemented. This analysis needs to cover decays inside the calorimeters with new tagging algorithms using low-level calorimeter data. The work conducted in this thesis also led to the creation of a dedicated analysis group with a plan to complete the analysis in 2025/2026 on the run 3 data. This analysis will cover both $h \to aa$ and $h \to Za$ processes for life-times compatible with decays inside the tracker and the calorimeters and masses between 0.1 and 50 Gev.

4.5 Full Simulation Datasets

To prepare an effective analysis of ALPs decaying into photon pairs in the calorimeters, extensive studies on the actual reconstruction of those events must be performed. Consequently, LL-ALP signal datasets were built to represent this very special phenomenology in realistic ATLAS conditions to properly evaluate signals and backgrounds.

Preliminary studies for this analysis were realized on official signal MC productions.

4.5.1 MonteCarlo simulations

For the displaced ALP signal, MC simulations imitating run 3 conditions were produced. These newer run 3 simulations take into account the higher energy collision of $\sqrt{s} = 13.6$ TeV as well as a more accurate pile-up profile. As a first step, the signal $h \to Za \to \gamma\gamma$ in run 3 conditions was produced in large amounts for different benchmark points of the signal model. The choice of parameters $m_a, \Lambda, C_{\gamma\gamma}$ was guided by parameter-space studies, as presented above. Different production methods for the Higgs boson were taken into account. The used event generators and shower development simulators are Powheg(v.05-05), Pythia8(v.308), and EvtGen(v.2.1.1) configured for AZNLO (approximate next to leading order) corrections. The full simulation of the detector and the subsequent particle reconstructions were made using the latest versions of internal software.

The Higgs boson kinematic distribution is sensitive to its production mechanism. It is important to take into account this parameter when producing the required signal samples. The main diagrams involved in the Higgs boson production at the LHC are represented in figure 4.18. Two processes mainly contribute to the production cross-section. These are the gluon-fusion and vector-boson-fusion mechanisms. The MC simulated samples were made for both leading processes to account for the impact they should have on ALP distribution.

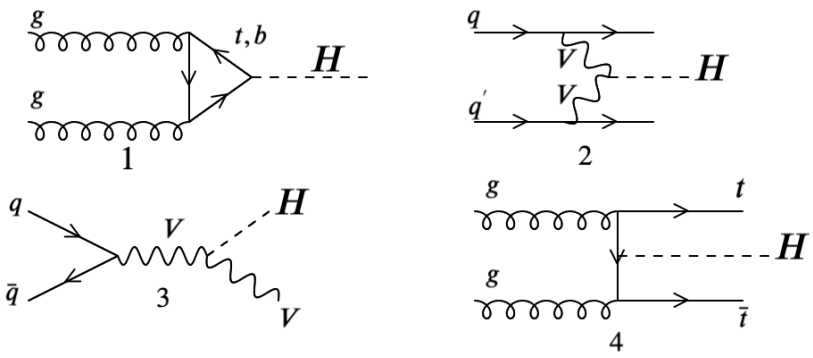


Figure 4.18: Feynman diagrams main processes for Higgs production in pp collisions at the LHC. 1: gluon-gluon fusion mechanisms; 2: Vector boson fusion, V stands for W or Z bosons; 3: Higgs-strahlung of an off-shell vector boson; 4: production in association with top quarks

Three mass points were chosen to build benchmark models presenting different challenges. The values were chosen to cover the full mass spectrum and cover different photon opening angle ranges: **0.4, 2, and 9 GeV**. The differences in opening angles should have an important impact on the resulting signatures. Validation plots, presented in figure 4.19, show very merged photon pairs for 0.4 GeV ALP decays and much wider angles for 9 GeV ones.

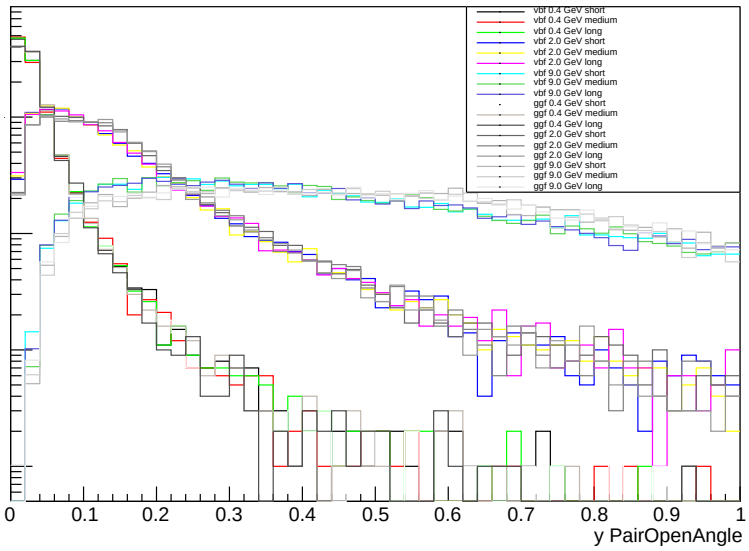


Figure 4.19: Histogram of photons' ΔR opening angle from the ALP decay. Multiple ALP masses, life-times, and Higgs production processes are present, but configurations are regrouped in three main distributions led by the ALP masses (0.2, 4, and 9 GeV).

For each mass point, different life-times were fixed: a short life-time (prompt), an optimal life-time for decay in the calorimeters, and a long life-time. The objective is to investigate the sensitivity of the detector to the displacement. For this reason, these multiple life-times were chosen to access a wide range of decay positions, including prompt cases. In addition, different intrinsic life-times yield different flight-time distributions due to the exponential decay. For instance, if one considers very long life-times, the distribution of decay positions remains flat across the detector due to its relatively short dimensions compared to the typical flight time. Figure 5.12 of Chapter 5 illustrates this purpose.
The optimal life-time is computed to maximize decays in calorimeters for fixed theoretical parameters. After selecting the optimal life-time for decays in the calorimeter (τ_{best}) for a given mass, the long and short life-times were defined as: $\tau_{long} = 10 \cdot \tau_{best}$, $\tau_{short} = \frac{\tau_{best}}{10}$. These are manually forced into the simulations.

Table 4.7 presents the computed τ_{best} values for different ALP masses.

The total amount of simulated samples for each mass and life-time combination are given in table 4.8. The samples were simulated for gluon-fusion-produced Higgs and the vector-boson-fusion process.

m_a (GeV)	$c\tau_{\text{best}}$ (mm)	m_a (GeV)	$c\tau_{\text{best}}$ (mm)
0.4	27	7.0	507
0.7	45	9.0	643
1.0	65	12.0	843
2.0	131	15.0	985
2.5	179	20.0	999
3.0	179	25.0	1004
4.0	249	28.0	1000
5.0	350	30.0	1009
6.0	365	33.0	987

Table 4.7: Optimal life-times for calorimeter decays for different ALP masses.

m_a (GeV)	Lifetime (τ)	Number of Events
0.4	τ_{short}	1M
	τ_{medium}	1M
	τ_{long}	500k
2.0	τ_{short}	1M
	τ_{medium}	1M
	τ_{long}	500k
9.0	τ_{short}	1M
	τ_{medium}	1M
	τ_{long}	500k

Table 4.8: Number of simulated events for different ALP masses and lifetimes; for a given Higgs boson production process.

In total, the MC simulation signal samples contain a large amount of events. The samples include mass points that yield different opening angle ranges, as seen in figure 4.19 at different life-times. The prompt sample can also be used to study the extension of di-photon resonance searches to low ALP masses. Also, the prompt ALPs are a necessary data set to calibrate taggers that discriminate single-γ from $\gamma\gamma$ showers by exploiting the double body structure as described earlier in the chapter.

These simulated samples are crucial to prepare all necessary studies to design the displaced $a \to \gamma\gamma$ analysis. Only a few parameter-space points were chosen as a first step, but a tighter grid of points will be fully simulated in the future. Building new simulations at different points can also be performed via reweighing approaches [15]. Current samples are being utilized for simple cutflow studies, ALP photon-jet consistency studies, and calorimeter-based performance investigations that will be discussed in Chapter 5. Machine learning taggers utilizing calorimeter information and shower single vs double-showers topologies are under development. A large number of simulated samples are available, which is crucial for the supervised training processes of such ML tools.

The wide range of events with different decay lengths and masses was necessary to define new calorimeter shower-description variables for the ALP search. The aim was

to understand how to better use the calorimeter signal dependence on parameters such as the displacement or the mass of the ALP. For this reason, having access to various samples was a mandatory technical step.

In parallel with these official MC productions, a Geant4 ParticleGun event generator-based tool used in conjunction with the above-described ALP kinematics script is under development. The objective of this software is to generate the double photon decay of the ALP at precise locations. Using this, one can artificially augment the number of events decaying in a naturally low-populated region. For instance, in figure 4.20, one can see that a low number of ALP events is present in high values of η. Augmenting the population of this region could be important in the future for training taggers dedicated to the forward regions.

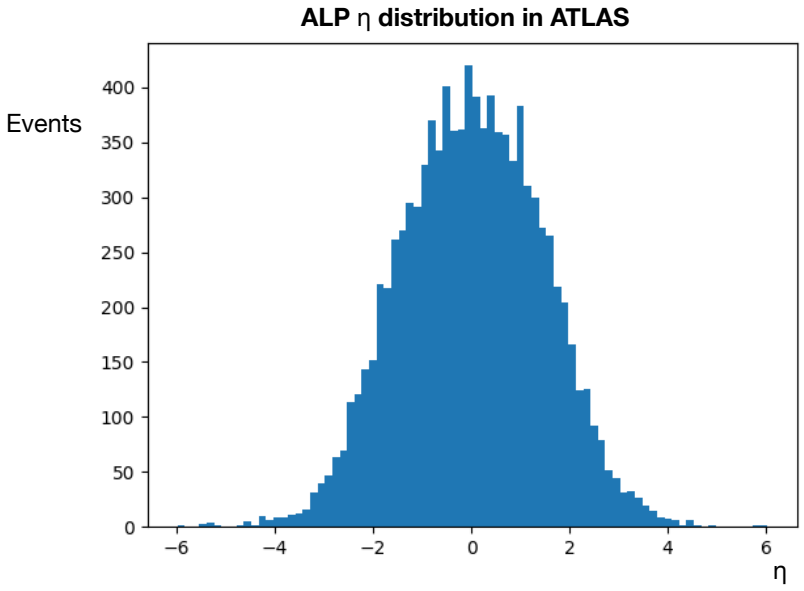


Figure 4.20: ALP η distribution in ATLAS, produced from a gluon-fused Higgs boson decay in association with a Z boson. Computed via the fast computation Python tool described in the current chapter.

4.5.2 ATLAS data

Early run 3 data was processed using a custom derivation framework to build the necessary variables for the LL-ALP analysis. Derivation DAOD files are a part of the ATLAS analysis model presented in Chapter 2. This is a modification of the main LLP derivation used by ATLAS's LLP community. The standard LLP derivation includes many important variables for displaced vertex searches. Extra low-level calorimeter information was the most important addition to this derivation. This includes the CaloTopo (which contain topological calorimeter clusters [174]) related containers as well as the CaloRings shower description variables (presented in Chapter 5). This extra piece of information is

crucial to developing optimal taggers capable of assessing the main features of the very unusual shower shapes predicted by these LLPs.

For decays happening inside the calorimeters, standard algorithms cannot use a combination of tracker and calorimeter variables. This significantly reduces the number of useful standard variables and indicates the need for other low-level calorimeter-only information. Low-level detector information is removed regularly from the usual physics analysis ATLAS data formats. In fact, for file-size reasons, a large amount of low-level information is removed in the reduced file format used to perform analyses. Nevertheless, LLP searches require many newer techniques. This often requires access to lower-level information to build new high-level variables or to be used directly. Current standard derivation files for LLP searches on data occupy around 90kb/evt. This value is double what is counted on the general derivation files for many standard physics searches. However, the added pieces of information to the custom LLP derivation meant for the LL-ALP analysis raised the bar. The overall low-level additions augment the files to 160kb/evt, however through efficient file thinning it is currently around 110 kb/evt.
Addressing this type of issue is typical of LLP analyses since many modifications to the usual ATLAS workflow are required. Establishing the useful tools and new variables to be implemented in the analysis format files to allow a search on the full ATLAS dataset must be done in the first step. Determining what can be removed from the files is necessary to have a persistent derivation. Once such studies are complete, large amounts of data can be processed with only the information needed.
Both data from Run 3 and Run 2 are planned to be used for the search of LL-ALPs in the photon channel.

Important work is being conducted to add the CaloRing variables under development, presented in Chapter 5, to the ATLAS standard reconstruction workflow. This would allow access to alternative shower-shape descriptions, which can immensely benefit many LLP searches, taggers of close-by physical objects, and could be used for better π^0 reconstruction for instance.

4.6 A3LP

The studies presented in this chapter lead to the creation of a new analysis project within ATLAS. This group named A3LP for axion-like-long-lived-particles, which I coordinated as analysis contact with another ATLAS colleague during my PhD, presents an important workforce combining multiple institutes, which opens many R&D possibilities on ML, calorimeter studies, software utilities, and other general ALP/LLP studies. The main objective is to build dedicated specialized taggers to probe displaced axions decaying into photon pairs in run 3 and run 2 ATLAS data. Building these taggers requires extensive studies combining ML algorithms with low and high-level calorimeter-based variables.

4.6.1 Analysis Strategy

The current early analysis strategy is to study $h \to Za$ processes in early run 3 data. Utilizing the Z l^+l^- decay, one can optimize the selection of events. For instance, by

selecting events containing a double lepton system ll with an invariant mass close to $m_Z = 91$ GeV, many events can be rejected, further improving the signal-to-background ratio of the analysis. The first analysis will focus on low-mass ALPs, implying merged photon pairs. The life-times under consideration include mostly large values of displacements and calorimeter-level decays.
Multiple ML-tagger tools are under development utilizing topo-cluster containing cell energy information [174] or CaloRings [175] (see Chapter 5 for a detailed description). This includes multi-layer perceptrons (MLP), convolutional neural networks (CNN), and graph neural networks (GNN). These Neural-Network classifying algorithms will be optimized to enhance signal acceptance and background rejection rates.

As a second step, the gathered knowledge and the developed taggers will open the search to $h \to aa$ processes beyond the analyses performed by ATLAS [84] that show important selection inefficiencies for calorimeter-range ALP decays. Utilizing a tagger for event pre-selection since such events do not present a Z boson. A second full analysis is planned with the combination of production processes and data from both run 2 and run 3.

4.6.2 Jet based analysis

Using the photon objects built by ATLAS e/γ reconstruction provides a total loss of sensitivity. This remains the case even if one selects a loose working point. To counter this efficiency loss, the analysis will not use photon-objects. The purpose is to eliminate any pre-selection of showers based on standard shower-shape criteria. As explained in the next chapter 5.1, the jet reconstruction algorithms encapsulate a great portion of all energy deposits around all main clusters, this includes of course single photons and collimated photon pairs. In fact, photons that fail to pass the photon identification criteria stay in reconstructed jet collections. Basing the analysis on reconstructed jets instead of reconstructed photons offers a way to solve the sensitivity loss effect. The jets can be considered as super-loose photons.
By constructing the analysis this way, new tailored identification criteria must be developed for the photon pairs using jet objects as starting points.

Additionally, this causes the overall background to include single-photons and QCD jets, which make up a significant portion of LHC production. The QCD jets and single photons must also be tested under the new reconstruction and ID criteria. Nevertheless, the very unusual nature of the signal under investigation yields a signature hard to mimic by QCD jets, improving its rejection.

Furthermore, selecting this approach implies conducting studies on photon-jets reconstruction with respect to QCD-jets, which are presented below.

Jet Algorithms for optimal candidates selection

All jets under investigation are consistently constructed using the anti-k_t algorithm [131], which provides a robust jet topology that is well understood from a theoretical point of view.

- **Topological (Topo) Jets:** These jets are formed from topological clusters [174] of calorimeter cells. The cells are grouped based on their energy deposition patterns and demand a high signal-to-noise ratio. The topo jets capture the essential of the deposited energy.
- **Particle Flow (PFlow) Jets:** PFlow jets implement a hybrid collection of low-level objects, combining information from the calorimeters and the tracking detectors to reconstruct particle showers. This leads to improved jet energy resolution and reconstruction efficiency by matching the tracks to the topo clusters [176].
- The reconstructed jets are often considered at the EM scale due to calibration procedures. The $\frac{e}{\pi}$ ratio, which measures the calorimeter response to electromagnetic showers (from electrons or photons) versus hadronic showers (from pions), is used to ensure accurate energy measurements. This ratio helps in correcting for the different calorimeter responses, improving the precision of jet reconstruction. Therefore, the types of jets are labeled AntiKt4EMTopo and AntiKt4EMPFlow jets.

Although PFlow jets generally provide better overall performance and are often recommended for analyses, their effectiveness unfortunately diminishes in searches for long-lived particles (LLPs). This limitation arises because LLPs can decay after passing through the calorimeter or decay late within the tracker, which can bias the track reconstruction, one of the crucial variables for PFlow algorithms. Therefore, for LLP searches, Topo jets are preferred as they rely only on calorimetric data and are less susceptible to biases from displaced particle decays. This approach is a common practice in ATLAS LLP searches. In the case of $a \to \gamma\gamma$, this choice is even more natural since tracking can only provide partial information about converted photons. This discussion point once again exemplifies the common issues LLP searches face in the standard prompt-driven ATLAS framework.

Selecting Jets at Truth Level for LLPs

To study the jets resulting from ALP decays, one needs to match the reconstructed jets to the ALP decay products via truth information from the simulated samples (*i.e.* the truth particles 4vectors). This process is called truth matching.

The exact knowledge of which particle is responsible for which energy deposit is not accessible at the truth level since it would imply having sizable truth containers in the MC data. Consequently, truth matching is done by associating a reconstructed jet with a simulated particle based on their proximity in the (η, ϕ) coordinates. Typically, one measures the angle $\Delta R = \sqrt{\Delta\eta^2 + \Delta\phi^2}$ between the jet and the truth particle of interest and defines a cut (0.2) below which the match is validated. This standard approach is represented in figure 4.21 in the $a \to \gamma\gamma$ case.

Truth-matching techniques are generally used in many analyses when dealing with overlapped objects that need to be identified or to map the decay products of a given particle to reconstructed objects. This intuitive approach for matching particles is common ground on many searches and not a main topic of discussion or development. Concerning the ALP search, one would compute the ΔR distances between the reconstructed jets and the photons produced from the ALP decay. However, this interpretation of particle (η, ϕ) orientation in ATLAS does not remain relevant when one considers displacements.

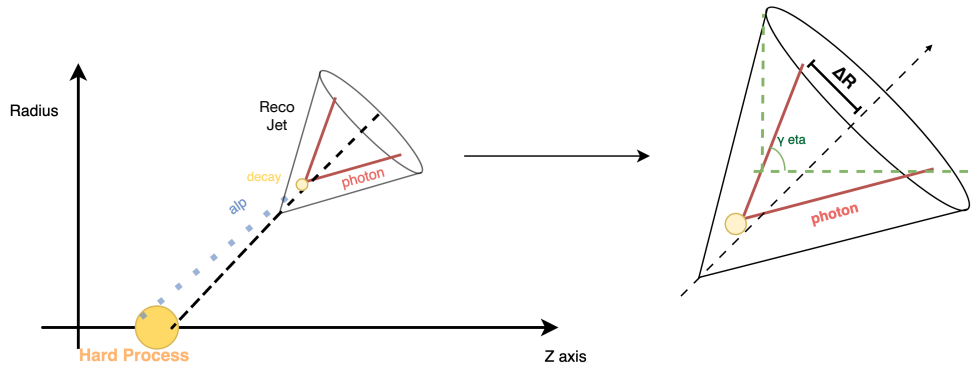


Figure 4.21: Schematic view of the truth matching made between the photon and the reconstructed jet in a merged case.

In fact, due to the different geometrical situations, different origins of particles should be considered, whereas reconstructed objects point to the primary vertex. This is further described below.

Challenges with LLPs decaying into photons.

Truth matching faces difficulties due to the unique geometrical situation of displaced decays.
Reconstructed jets are oriented towards the collision point, whereas photons from LLP decays can be massively non-pointing. This discrepancy leads to significant differences in ΔR values, making standard truth-matching procedures inadequate. Figure 4.22 illustrates the actual angular difference in a displaced case where the photon pair is reconstructed in one jet. This is visible by projecting the photon axis on the primary vertex. Standard truth-matching would fail because the ΔR separation is too important even though the photon is absorbed in the jet-associated cluster. This effect is increasingly significant when the displacement is important and enhanced by the angular opening between the two photons, which results from the ALP mass and momentum.

Matching with the ALP.

The possibility of matching the reconstructed jet directly with the mother particle is a viable solution.
In fact, by matching the pointing jet with the ALP, one suppresses the difficulties encountered with the non-pointing photons. However, this method can only be used in cases where both photons are quite merged and reconstructed in a single jet. This is the case for the current investigated signal in the LL-ALP analysis, but future work might include resolved cases that would need a new approach.

Overall, the results of jet matching indicate a higher matching rate when using ALPs instead of daughter photons (see table 4.9). Additionally, as seen in figure 4.23, this

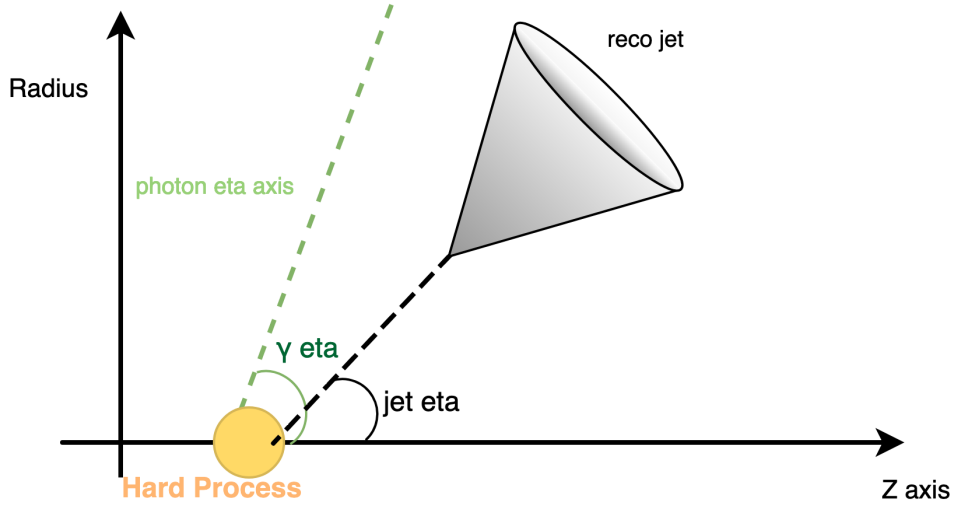


Figure 4.22: The angular separation in η between the photon axis and the jet axis for a displaced case. The photon axis is projected to the collision point to illustrate the large difference. This difference is above the threshold for truth matching; however, the photon is inside the jet cone. This demonstrates that only angles cannot be used for truth-matching LLPs.

matching method remains reliable over the full spectrum of displacements, including large displacement values where standard truth matching fails. Figure 4.23 also depicts the effect of mass. Starting at a certain mass, the opening angle between the two photons is large enough so that each photon is reconstructed in a separate jet. This is important at low displacements since the two photons have enough time to drift apart. At high displacements and for a high mass, the matching rate remains high. As mentioned previously, if the photon-pair angle is wide open and decay happens in the calorimeter, both photons are absorbed in the same cluster, resulting in a single jet being reconstructed.

Photon match ϵ (ΔR: 0.1)	**ALP match ϵ (ΔR: 0.1)**	**ALP match ϵ (ΔR: 0.2)**
67.46 $\pm$0.82%	71.88 $\pm$0.85%	76.1 $\pm$0.87%

Table 4.9: Truth matching Topo jets for different ΔR values obtained from 10k sample of a 2 GeV mass ALP decaying into two photons. Note that ALPs decaying outside of ATLAS are included in the inefficiencies.

Truth matching for displaced resolved photons

If the two photons are resolved, the jet-ALP match cannot work, as the two photons will not land in the same jet. This is not a main concern for the current project but should be considered for the next studies. New ideas for matching in these cases require much more complex truth-matching algorithms since the ΔR between the two objects of interest will often be very big. Augmenting the ΔR threshold is no viable solution since it will create many pollution effects due to nearby particles. To allow matching in such cases and make sure efficiencies remain consistent no matter the decay position, one should get

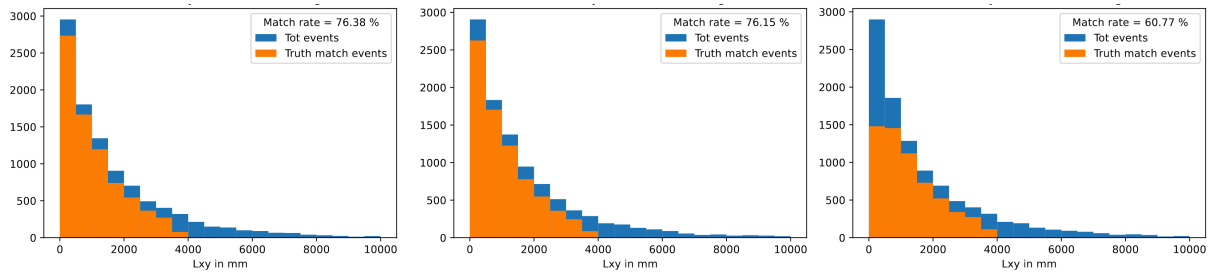


Figure 4.23: Matching rate of ALPs with topo jets for different bins of displacements. L_{xy} refers to the displacement in the (x, y) plane. Left: 0.4 GeV ALPs. Middle: 2 GeV ALPs (threshold between merged and resolved). Right: 9 GeV ALPs.

the (x,y,z) position of the main cluster associated with each jet and verify if the decay products of the ALP would intersect this point. This can be done using the 4-vector of the truth photons and building a virtual trajectory based on the (p_x, p_y, p_z). Then, a fit between the track and cluster position can be made. The resulting $\frac{\chi^2}{N_{dof}}$, which measures the fit's quality, can be used to select or reject a match between a reconstructed jet and the ALP decay products using a predefined cut.

This section is not of great importance regarding LL-ALP physics but gives a great example of all the technical and experimental difficulties one encounters when searching for LLPs. In fact, while truth-matching strategies are very well established and used in many scenarios, they immensely fail when important displacements are considered. Such not very significant steps on a full analysis project scale can demand a lot of discussion and different solutions proposals to be correctly set for the displaced $a \to \gamma\gamma$ search and other LLP analyses. The discussion on truth matching for displaced resolved photons perfectly illustrates the level of detail and complexity of new techniques that are required for addressing this very interesting phenomenology.

This further stresses the challenges faced during this project but creates development opportunities for new algorithms and strategies that can become a great addition to the ATLAS analyses framework.

Photon-jets calibration can help ALP searches

By default, in ATLAS analyses, an overlap removal procedure is performed to avoid double counting between jets and photons.
Photons are kept, and jets matching those photons are removed. For this reason, reconstructed jets are not used for photon signal searches since the dedicated photon objects offer much better identification and tailored calibrations. Working with jets instead implies possible calibration issues that one needs to check so as not to cause signal inefficiencies.

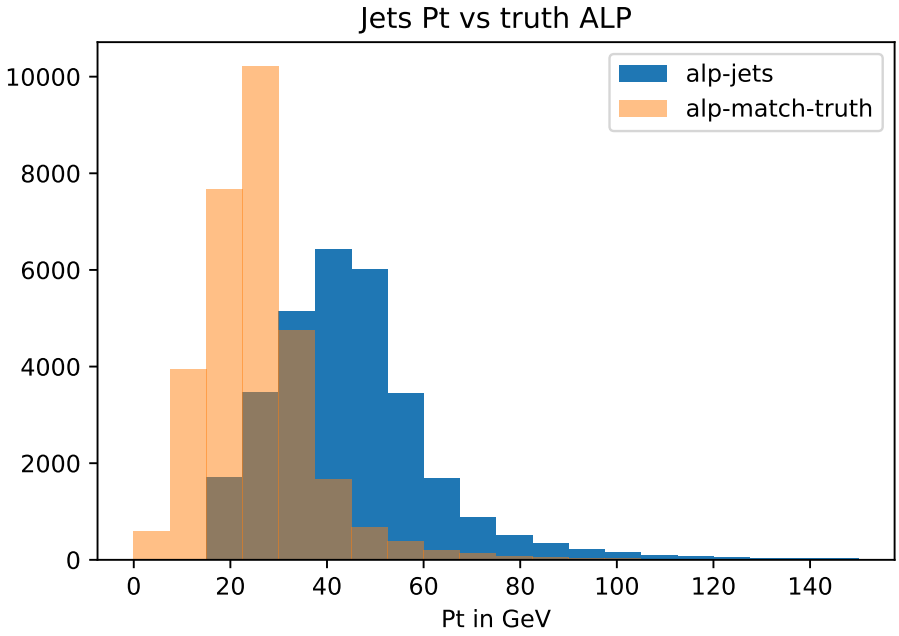


Figure 4.24: Pt distribution of the ALP and the associated reconstructed jets.

Studying these photon-jets calibrations, it was observed that the reconstructed jets have an energy value much higher than what is expected from the truth ALP variables. Looking at figure 4.24, one sees this effect in the Pt distributions. The absolute difference between the jet Pt and the ALP truth Pt is presented in Figure 4.25. A systematic calibration issue attributes an overestimation of $\approx$ 20 GeV of the jet transverse momentum for ALP-produced jets, as illustrated in figure 4.25 while QCD jets remain well calibrated. The same was observed with EMPFlow jets but with a lower overestimation of around 10 GeV.

To ensure that this difference does not come from mismatching the jets, correlations between the alp-matched jets and the leading jets were produced.

It was understood that this feature is typical of e/γ particles, which cannot be calibrated as QCD jets. QCD jets present a high fraction of pions, which make lower energy deposits in the calorimeter compared to e/γ particles. This is a specific difference between hadronic and EM showers and is covered in the next chapter at 5.1. This is taken into account when calibrating the jets. Therefore, the photon-jets show a biased value of Pt, which pushes the full distribution to higher reconstructed values.

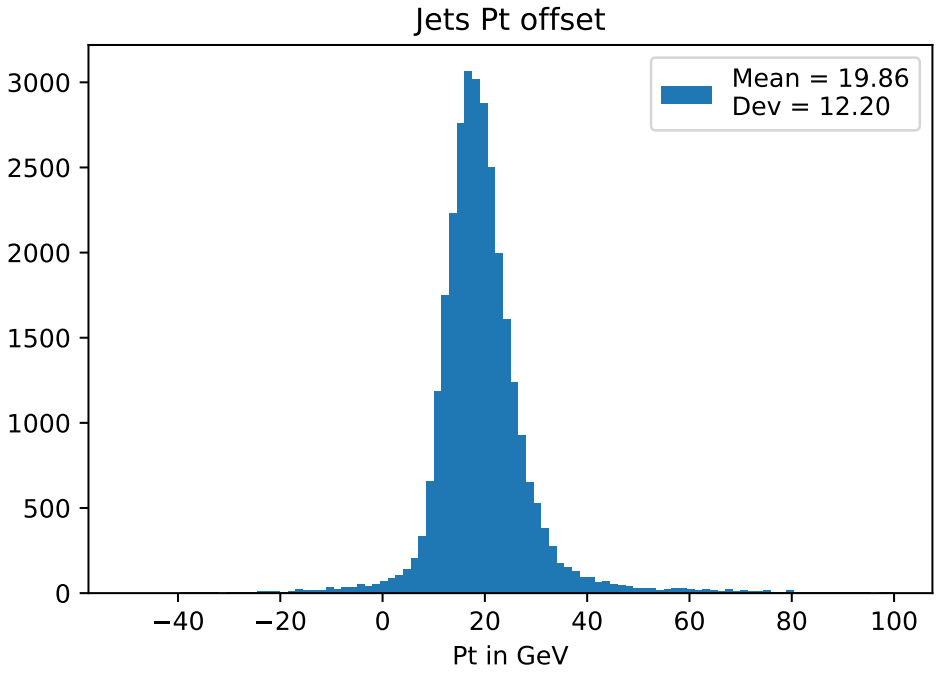


Figure 4.25: Pt absolute difference between the reconstructed topo jet and the associated truth ALP.

It is important to be aware of this effect throughout the analysis. Paradoxically, having an overestimation can be beneficial. The low expected values of the ALP Pt, typically ranging between 10 and 40 GeV, as one can see in figure 4.24, should imply that a given number of associated jets would be under the Pt threshold for reconstruction. Indeed, many jet reconstruction algorithms put a minimum Pt threshold of 20 GeV; thus, many ALPs would not meet the criterion. Yet, after an overshoot of the photon-jets Pt value, the ALPs that shouldn't pass the Pt threshold end up passing them. Fortunately, this means that the sensitivity to low Pt ALPs is automatically augmented. Otherwise, one would need to manually lower the Pt limit for reconstructing EMTopo jets. This would, by itself, raise more background contributions from pileups as well.

The current goal of the analysis team is to develop taggers based on calorimeter cells and clusters. Therefore, the reconstructed alp-matching jets are mostly used as a directional seed to isolate the relevant regions of interest in the calorimeter layers. Having a precise energy reconstruction on the jet object is not of primary importance. The most important point regarding jet objects is in maximizing the reconstruction efficiency of ALPs and maximizing the rate of truth-matching. This overestimation of the Pt and its impact could be studied deeper to estimate how the sensitivity of the analysis is raised. One can expect a sizable contribution since the Pt spectrum usually follows a power law.

4.7 Conclusion and prospects

Searches for ALPs in collider experiments have been conducted through multiple analyses probing different signatures. The EFT parametrization allows to address in a single theoretical framework a high multiplicity of production mechanisms and possible decay modes. This significantly increases the quantity of possible signatures generated by ALPs that ATLAS could capture. Some models allow for longer life-times, which bring exotic experimental signatures that need to be looked for to tackle new physics beyond the SM.

LLPs are present in many BSM theories and present unique signatures with respect to SM background. For the LL-ALP case, photon-pair productions inside ATLAS calorimeters are expected to yield very unusual shower developments that are difficult to mimic from SM processes. This also implies poor identification efficiency with up-to-date algorithms that still do not consider macroscopic displacements. Indeed, such a geometrical situation must come with new ways of using the detectors and new analysis strategies.

A special interest is given to LL-ALPs decaying into photons inside the calorimeters. This is well-motivated as it covers an important gap in the parameter space, which is unexplorable by other experiments. A dedicated analysis group has been created within the ATLAS collaboration to perform this task. Current ML taggers are being developed, and studies regarding calorimetry are in progress to optimize the tagger's input variables and maximize discrimination, as it will be discussed in the next Chapter 5.

A complete analysis of early run 3 data is planned, using the finalized ML taggers on jets to probe $h \to Za \to \gamma\gamma$ events with long displacements covering the calorimeter ranges. This analysis will be followed by a broader one that considers another production mechanism and dives into data collected during run 2. These analyses will implement several ideas tested in this thesis.

An interesting prospect concerning the developed ML taggers is to create dedicated LLP triggers. Such an evolution would greatly benefit the ATLAS LLP community by upgrading the detector sensitivity to displaced signals. Reviewing current methods is of the utmost importance for the future of LLP searches. Building tools capable of looking for these events remains a significant challenge and differs radically from what is currently done. Nevertheless, constraining LLP phenomenology is primordial for a better understanding of new physics beyond the Standard Model.

4.A Analysis of Parameter Choices

4.A.1 Energy Scale Λ and Coupling $C_{\gamma\gamma}$

The energy scale Λ and the coupling $C_{\gamma\gamma}$ are critical parameters of the EFT. As exposed in section 4.4.6, realistic limits were fixed when computing the expected number of ALPs produced in run 3. The reasons for choosing this EFT parameter value limit for the ALP are to avoid experimental constraints and maintain theoretical consistency.

Energy Scale Λ

The energy scale Λ represents the characteristic scale at which new physics effects become relevant. This BSM theory can arise through new resonances that mediate interactions involving the ALP. Λ is tied to the mass of these resonances.

For a coupling constant g_*, the mass m of the new resonances can be expressed as:

$$m = g_* \cdot \frac{\Lambda}{16\pi^2}$$

Explanation:

1. **Strong Coupling and New Resonances:** For very strong coupling scenarios, we can have $g_* \sim 10$. Therefore, the mass of new resonances becomes:

$$m \sim 10 \cdot \frac{\Lambda}{16\pi^2}$$

2. **Experimental Constraints:** Experimental data from the LHC and precision tests exclude new electroweak resonances for masses below a few hundred GeV [177]. For safety, let's consider the lower limit for new resonances to be around 500 GeV:

$$m > 500\,\text{GeV}$$

Substituting m and solving for Λ:

$$500\,\text{GeV} < 10 \cdot \frac{\Lambda}{16\pi^2}$$

$$\Lambda > \frac{500 \cdot 16 \cdot \pi^2}{10}\,\text{GeV}$$

$$\Lambda \geq 10\,\text{TeV}$$

Therefore, to ensure new resonance masses are above the experimental limits, Λ is chosen to be at least 10 TeV.

Coupling $C_{\gamma\gamma}$

To avoid running into constraints from collider experiments and precision tests, $C_{\gamma\gamma}$ should not be too large. Having $C_{\gamma\gamma} \gg 10$ would imply significant contributions from new heavy particles, which would be experimentally detectable. Therefore, $C_{\gamma\gamma}$ is typically constrained to be of the order of 10.

Final Choices:

- $\Lambda = 10\,\text{TeV}$: Ensures new resonance masses are above the experimental exclusion limits. It is optimistic in terms of the expected number of events, as seen in figure 4.16.
- $C_{\gamma\gamma} \leq 10$: Keeps the coupling strength within experimentally acceptable limits without introducing too many new detectable particles.

This ensures that new resonances are heavy enough to evade current experimental limits and that the coupling strength remains within a natural range.

Chapter 5

The Caloring approach

The ATLAS photon identification strategy is the main bottleneck of the LL-ALP search presented in the previous chapter. Ensuring a correct identification for each particle type and reconstruction of its properties is a critical task for the performance of all searches, and the current data flow offers a panel of working points that satisfies different analysis requirements. However, BSM analyses with extremely unusual event topologies are often required to use the loosest identification working points, which augments the amount of background. Consequently, alternative strategies are developed in parallel to the standard pipeline to counter the limitations of existing algorithms. This Chapter will discuss the difficulties of experimenting with alternative techniques in a private data-flow and how Caloring variables can replace the shower-shape description used for photon identification in the context of a $h \to Za \to ll\gamma\gamma$ search.

Additionally, an extension of Calorings is investigated to measure cluster asymmetries and separate merged photons from the background. A first ML-based classifier is deployed to discriminate between single bodies and merged bodies using those.

Calorings are variables constructed on low-level calorimeter information [175] [178], and were developed for trigger purposes. These variables have shown strong discrimination to separate e/γ from QCD jets and are used in the photon and electron high-level trigger. Calorings also contain different information on shower development compared to the standard shower-shape variables used for e/γ reconstruction. These variables will be described later in the chapter after a reminder of the standard photon identification approach.

5.1 Review on Jets and e/γ Showers in ATLAS

Understanding the fundamental differences between jets and electromagnetic showers in ATLAS is crucial for interpreting the calorimeter-based results presented in this chapter. This section provides a brief recap of key concepts that will aid in understanding the subsequent discussions.

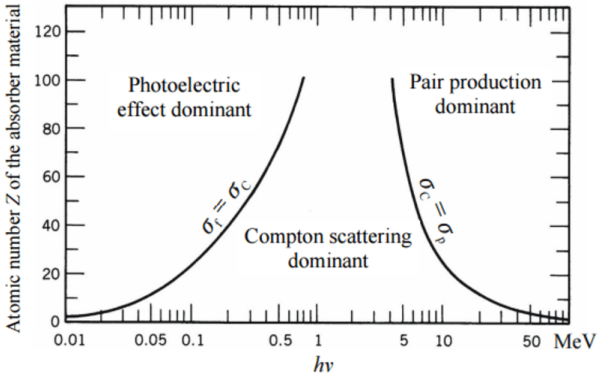


Figure 5.1: Three major types of photon interactions with matter as a function of their energy and the atomic number [179].

5.1.1 Hadrons and e/γ interact through different forces

Different fundamental interactions with matter, guiding the jets and e/γ shower developments, yield different shower shapes. Jets are products of QCD processes and are composed of hadrons, whereas e/γ particles are governed by EM interactions.

In the ATLAS calorimeters, these different interactions lead to distinct energy deposition patterns. Electromagnetic particles such as electrons and photons interact with the calorimeter material primarily through bremsstrahlung, ionization, and pair creation. Electrons mainly lose energy in the calorimeter with bremsstrahlung (photon emissions). Photons lose energy in the calorimeter in a very similar way since they create pairs of electrons that then interact also with bremsstrahlung. Figure 5.1 shows the main processes by which a photon loses energy in matter. Thus, the showers produced by these two particles are very similar. However, the charged electrons leave tracks, so it is simple to differentiate between both particles.

Hadrons within jets can also interact via bremsstrahlung if they are charged. Nevertheless, the bremsstrahlung effect is heavily suppressed by the particle mass. This means that hadrons, which are significantly heavier than electrons, do not deposit a large amount of energy in the same way as e/γ particles. This is why charged hadrons, like protons, leave deposits that are more similar to neutrons than charged electrons. These heavy, stable hadrons easily penetrate the EM calorimeter and then undergo nuclear interactions with the hadronic calorimeter material.

This difference in matter-particle interactions drives the resulting energy deposition patterns inside the EM and Hadronic calorimeter. However, as described later in this section, jets also contain hadrons that decay into e/γ particles. Those decay products are then absorbed in the calorimeter in the same way as other e/γ particles but can differ in geometrical distribution due to the high dimension of jets.

This relation between bremsstrahlung and particle mass is also what allows muons to penetrate the calorimeters easily. In fact, as they are heavy, they do not interact with bremsstrahlung and do not strongly interact with nucleons; thus, they penetrate both calorimeters without leaving much energy.

5.1.2 Radiation and Interaction Lengths

Two key concepts to understanding the calorimetric response to different particles are the radiation length (X_0) and nuclear interaction length (λ_{int}). The radiation length represents the mean distance (in a given material) over which an electron loses $1/e$ of its energy via bremsstrahlung. It is a measure of a material's ability to absorb EM particles. In ATLAS, the EM calorimeter (ECal) is designed with a strong X_0 to effectively absorb electrons and photons; for instance, lead, which has a radiation length of 0.56 cm, is used as an absorber in the LAr EM calorimeter.

On the contrary, the nuclear interaction length indicates the mean free path for hadronic inelastic nuclear interactions in a given material. The hadronic calorimeter is designed with a strong λ_{int} to absorb hadrons effectively. It is built with steel tiles (in the central region) as an absorber, which has an interaction length of 16 cm.

5.1.3 Electromagnetic and Hadronic Shower Development

The different nature of particle-matter interactions of jets and e/γ objects yield different shower developments and different results in energy depositions.

EM showers are much narrower and cleaner due to processes like bremsstrahlung and pair creation, leading to localized energy deposits within the ECal. These showers are compact and almost fully absorbed by the ECal.

On the other hand, jets produce hadronic showers that are more complex and widespread due to the multiple hadronization processes. The high multiplicity of particles and the presence of unstable heavy hadrons within a jet can yield many soft emissions and decay into lighter particles. This results in an overall larger shower cone and wider energy deposits in the calorimeters.

Additionally, some hadrons within a jet can decay into EM particles, such as e^+e^- pairs and photons, which contribute to the EM component of the shower. All jets have an EM-fraction due to the multitude of particles that compose a jet; a fraction of them, like π^0 and other neutral mesons, can decay into photon pairs that suffer from the ECal radiation length and get absorbed. At the same time, stable hadrons pass through ECal without depositing energy since they need to undergo nuclear interaction.

While e/γ objects mostly leave energy in the ECal, jets deposit energy in both calorimeters. The EM-fraction of jets leaves an energy deposit in the ECal. However, it geometrically differs from the ones produced by e/γ objects.

This is a key component of shower-development differences in the two ATLAS calorimeters. Jet and shower simulations are optimized and revised to reflect these complexities in the physics process and detector responses [180].

5.1.4 Reminder of Jet and e/γ Reconstruction

Jet reconstruction in ATLAS typically employs algorithms like Anti-k_t [131], which clusters particles based on their transverse momentum. These particles are reconstructed by matching calorimeter clusters with high enough energies combined with tracks (if available) before being reconstructed into jets. The calorimeters absorb many particles created at collision and get reconstructed in jets. This includes e/γ objects. It is in the second step that identification algorithms, which rely on geometrical energy deposition cuts across the calorimeter layers, are applied to distinguish QCD jets from other EM particles. These identification algorithms are further detailed in the present chapter.

5.1.5 ALP into Two Merged Photons Search

The objective of this chapter is to explore the discrimination between merged photons, which appear as classic gamma showers, QCD jets, and single photons.

Discriminating between jets and EM objects relies on their very different shower shapes. However, distinguishing merged photons from single photons is more complex as it must rely on probing the double body structure of the EM shower. This can be quite limited by the usual photon identification algorithms. This chapter investigates the detector's sensitivity in identifying overlapping photon showers using novel calorimeter shower descriptions called Calorings. This new shower description could heavily benefit the search of $a \to \gamma\gamma$ since, for low masses, the two photons are expected to be in a merged regime.

Additionally, the identification of long-lived ALPs introduces other challenges, such as non-pointing effects and other complications discussed in Chapter 4. The Caloring description of showers also looks into these challenges, aiming to improve the identification capabilities for LL-ALPs decaying into double photon signatures.

5.2 Standard electron and photon identification

This section explains photon and electron reconstruction, focusing particularly on the pseudorapidity range corresponding to the calorimeter barrel.

Photon and electron detection involve combining data from the EM calorimeter (ECAL) and the inner tracking detector (ID), while HCAL is used as a veto to reject jets. In the ECAL, EM showers result in clusters that are distinguished as photons or electrons based on the presence of a track in the ID. This simple picture is complexified by the fact that photons occasionally convert into electron-positron pairs within the ID, the probability of which varies based on the material traversed [181].

The process begins with creating "seed clusters" using a sliding-window algorithm [182] on the ECAL layers to detect local energy maxima. These clusters are then matched with tracks from the ID to identify them as electrons, converted photons, or unconverted photons. Specific track-cluster matching criteria are used to ensure accuracy, taking into

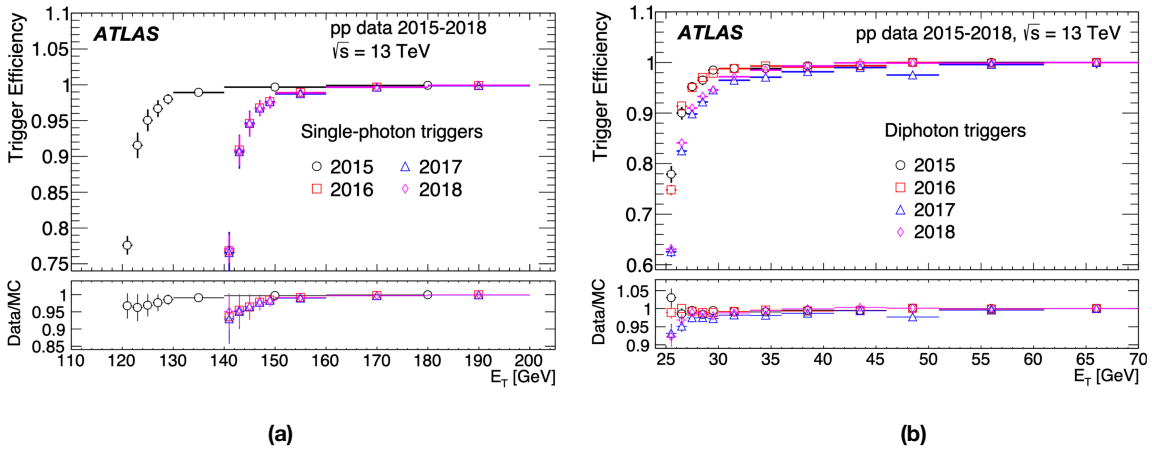


Figure 5.2: Run2 single (a) and di-photon (b) trigger efficiencies versus transverse energy. From the ATLAS performance paper [183]

account factors like track quality and the geometrical relationship between the track and the cluster.

Photon conversions are found through pairs of oppositely charged tracks that are coming from a common origin. This origin can be determined from single tracks if the second track energy is too low or suffers from reconstruction inefficiencies. Photon conversion reconstruction efficiency is maximized through various selection criteria and kinematic fitting techniques to detect both dual-track and single-track conversions, improving overall photon identification accuracy.

Ultimately, clusters are classified as electrons or photons based on further criteria involving the track's properties, energy matching, and specific electromagnetic interaction signatures as explained in section 5.1.

Overall, the detection efficiency is high and approaches 98% for photons with significant transverse momentum. Trigger efficiencies of di-photon and single photon during run2 are presented in figure 5.2. While single-photon triggers target events with a high momentum photon, the di-photon triggers identify softer photons to enable invariant mass reconstruction of decaying particles. This would be the case of an ALP decaying in the photon channel. Various ATLAS development efforts are being conducted to improve the identification of low-energy photons. As one can see, the di-photon trigger severely suffers inefficiencies for photons reaching 25 GeV.

5.2.1 Shower-Shape Variables

Distinguishing genuine prompt photons from hadronic jets, which often contain significant electromagnetic components from neutral meson decays such as $\pi^0 \to \gamma\gamma$, is crucial. To achieve this, ATLAS uses a range of discriminating variables derived from the geometrical structure of energy deposited in the ECal. These variables exploit the differences in

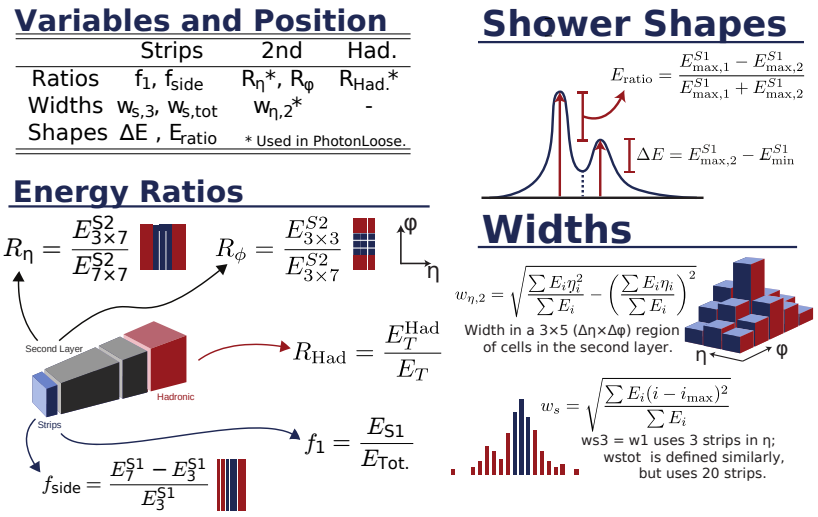


Figure 5.3: Geometrical sketch of the standard shower-shape variables used for electron and photon identification against jets in ATLAS. [184]

electromagnetic shower geometric profiles between isolated photons/electrons and QCD jets, providing high sensitivity for effective particle identification. They are referred to as e/γ shower shape (SS) variables. These are schematically pictured in figure 5.3.

e/γ Shower Shapes

The following Shower Shapes (SS) exploit the high granularity of ECal to discriminate between electromagnetic and hadronic showers:

- **Hadronic Leakage (R_{had})**:
  - **Definition:** The ratio of the total transverse energy deposited in the hadronic calorimeter (E_{had}) to the total transverse energy of the photon candidate (E_T).
  - **Purpose:** This variable quantifies the energy leakage into the hadronic calorimeter, which is typically higher for hadronic jets than for isolated photons. The ECal is about 25 X_0 but only 1 λ_{int}. However, very hard photons could penetrate the HCal.
- **Second Layer (S2) Variables**:
  These variables are primoridal as S2 is the most absorbent layer
  - **η Energy Ratio (R_η):**

$$R_\eta = \frac{E_{S2}^{3\times7}}{E_{S2}^{7\times7}},$$

    where $E_{S2}^{3\times7}$ and $E_{S2}^{7\times7}$ are the energies in 3×7 and 7×7 cell rectangles (in $\eta\times\phi$) in the second layer of ECAL, centered around the cluster seed. Represented in figure 5.3.

- ϕ **Energy Ratio (R_ϕ):** Similar to R_η, but evaluated along the ϕ direction, reflecting the bending of charged particles in the magnetic field and their resultant energy spread. Beyond a much larger value for jets, this variable is very efficient in discriminating between converted and unconverted photons.
- **Lateral Width ($w_{\eta 2}$):**

$$w_{\eta 2} = \sqrt{\frac{\sum E_i \eta_i^2}{\sum E_i} - \left(\frac{\sum E_i \eta_i}{\sum E_i}\right)^2}$$

where E_i is energy sum of cells collected in a considered 3×5 cell rectangle in (η, ϕ). It provides a measure of the lateral span along η.

- **Front Layer Variables**:
The front layer refers to the frist layer (S1).
  - **Front Lateral Width (w_{s3}):**

$$w_{s3} = \sqrt{\frac{\sum E_i (i - i_{max})^2}{\sum E_i}},$$

measures the shower width along η in the front layer (S1), using two strip cells around the maximal energy deposit. It provides a sizable discrimination between single EM objects and π^0 decay to photons.
  - **Front Lateral Width (total) ($w_{s,\mathbf{tot}}$):**
similar to w_{s3} to but uses the very precise granularity of the S1 by considering all cells in a window $\Delta\eta \times \Delta\phi = 0.0625 \times 0.2$.
  - **Front Second Maximum Difference (ΔE):**

$$\Delta E = E_{S1}^{\text{2nd max}} - E_{S1}^{\text{min}},$$

is the difference between the second maximal cell strip energy and the minimal energy found between the two highest energy cell strips in the layer.
  - **Front Maxima Relative Ratio ($E_{\mathbf{ratio}}$):**

$$E_{\text{ratio}} = \frac{E_{S1}^{\text{1st max}} - E_{S1}^{\text{2nd max}}}{E_{S1}^{\text{1st max}} + E_{S1}^{\text{2nd max}}}$$

measures the relative difference in energy between the two most energetic strip cells. It provides an important discrimination to π^0 photon decay, which is composed of an overlap of two EM showers (particularly if it has a high energy).
  - **Front Side Energy Ratio ($F_{\mathbf{side}}$):**

$$F_{\text{side}} = \frac{E(\pm 3) - E(\pm 1)}{E(\pm 1)}$$

measures the tail structure of the shower development along η in a symmetrical way. $E(\pm X)$ represents the energy in the $\pm X$ strip cells around the maximum.

Selection Criteria

Two main sets of photon identification criteria are used as described in [183]:

- **Loose Selection:** Applies broadly to both converted and unconverted photons, focusing on shower shape and hadronic leakage, achieving high trigger efficiency and a photon identification efficiency of approximately 99% for $E_T > 25\,\text{GeV}$. It is used to define control samples to measure events with combinations of jets and photons and analysis considering a $\gamma\gamma$ decay.

- **Tight Selection:** Incorporates more stringent cuts on the middle and front layer variables to provide a high background rejection rate, especially against jets that include high EM fractions from decaying neutral mesons.

These discriminating variables and criteria significantly enhance the capability to reject QCD jets while accurately identifying photons and electrons. The multiplicity of variables allows for different selection criteria, which lead to a choice in compromise between efficiency and quality. Additionally, some variables discriminate more for electrons and others for photons, so specific criteria are defined to identify electrons and photons. Together with tracking information, this set of variables is optimized to identify and reconstruct photons and electrons while rejecting the very large QCD jet background.

5.2.2 Limits

As mentioned in Chapter 4, the usual photon reconstruction efficiency utilizing the SS variables underperforms when facing displaced signals and collimated photon pairs.
A very important reason lies in the fact that SS variables definitions assume a single pointing shower developing over the full EM calorimeter. As one can see in figure 5.3 and as described above, the SS variables severely lack asymmetry measurements while they naturally occur in dual showers. Apart from E_{ratio} and ΔE, the SS is built symmetrically by summing equidistant cell strips from the cluster seed. This forbids an assessment of asymmetry in the energy deposit. Events presenting non-pointing photons provide harder configurations since the geometrical situations can induce a non-homogeneous interaction profile in the calorimeter. Such events are important to be probed for the displaced ALP to photons analysis but would not pass loose reconstruction cuts. Additionally, the sizes of windows around an electron or photon candidate were thought for pointing particles; such aspects require "re-thinking" when encountering new geometrical situations from long-lived particles.

The lack of focus on the energy repartition in the cluster's center is an important limitation of SS. If one considers events where the two photons are not resolved (meaning that they are absorbed in the same cluster), the photon identification fails significantly. This is often the case in $\pi_0 \to \gamma\gamma$ decays, or more generally in any photon pair boosted decay with an angular separation $\Delta R < 0.1$ [185]. Furthermore, LLPs that create very displaced decays can still produce photon pairs that are absorbed in a single cluster, as explained in the previous Chapter.

The general limits of photon pair identification and reconstruction using the standard SS are also related to asymmetries that are not taken into account in 2 body decay configurations.

These important limitations call for new reconstruction strategies using other ways of describing shower developments in ATLAS calorimeters.

5.3 Caloring variables

The Calorings approach diverges from standard shower description techniques. These cell-based variables offer a lower-level detector description than SS variables, enabling greater flexibility for phenomenology studies. Cluster cell energies are summed using ring masks, as illustrated in figure 5.4. In essence, building a mask for a list of cells is similar to having a list of pixels input to image processing algorithms. The construction of ring masks provides valuable geometric information about the spatial configuration of the cells, much like how a convolutional layer operates in image processing to extract features. This approach also helps to reduce the dimensionality of the problem, making it more manageable while preserving the essential structure of the data.

This calorimeter reading technique was developed to answer issues regarding electron identification at trigger level [183]. It was shown that a Caloring-based approach considerably diminished the selection of fake-electron compared to techniques based on standard e/γ SS variables. Studies around this field have led to the development of various Caloring variable topologies, which are presented throughout this chapter and have constantly shown sensitivity to features of electrons and photons showers with respect to jets. Additionally, they have proven to work efficiently with ML tools that can exploit nonlinear correlations between rings. This is the case for electron selection at the HLT using the NeuralRinger algorithm [175] [178].

In the context of LLP searches, diphoton pairs could manifest in very diverse ways within the calorimeters (see 4.9 of the previous chapter). As a result, there is no typical shower shape for LLPs; rather, it is a continuum of configurations that require a comprehensive representation of the energy deposits in the calorimeters. Therefore, relying on standard electromagnetic shower shapes is insufficient, and new, more compact representations of the showers are necessary to make the analysis manageable. Using individual calorimeter cells in the cluster of interest is overly granular and suffers from multiple issues described in this section. However, the use of rings, initially designed for trigger purposes, offers an interesting alternative for all possible diphoton decay configurations as it is a more global representation of the energy cluster. Indeed, e/γ SS reveals a narrow range of precise features of prompt particles in comparison to rings. Since the LL-ALP search faces significant photon identification challenges using standard techniques, the Calorings are a potential basis for developing new identification strategies driven toward diphoton decay properties in new ML-based taggers.

Currently, multiple ATLAS developments for LLP searches use CaloTopo clusters instead of standard shower-shape variables to build new ID strategies, as they can be accessed in AOD files. By working on a Caloring approach, one considers a lower-level

method, allowing for complementary techniques. In fact, the current analysis group, to which I am an analysis contact, is developing both approaches in parallel. However, using Calorings instead of clusters implies specific challenges due to the absence of low-level detector information in analysis-level ATLAS files. These issues will be discussed in this chapter.

Additionally, the caloring algorithm is already available in ATHENA [186], the reconstruction ATLAS software framework, allowing the corresponding rings to be built and follow the data reconstruction stream up to analysis-level files (if custom flags are given). However, this implementation is based on the electrons and photons that have been identified at the moment. A solution to build rings around jets is required for this analysis because diphoton pairs are poorly identified as standard EM objects at the trigger level.

Working on such variables for an analysis, instead of an online trigger, leverages their full potential by allowing more complex algorithms and ML tools to use them since processing time is not an issue. The development of these new ID techniques could benefit many LLP searches and merged di-photon reconstructions that cannot rely on classical techniques. This is the case of π^0, whose rejection is still a challenge in ATLAS in the context of Higgs to diphoton searches. Although these particles are not LLPs, their two-body structure can greatly benefit from the new ring-based variables defined in this thesis.

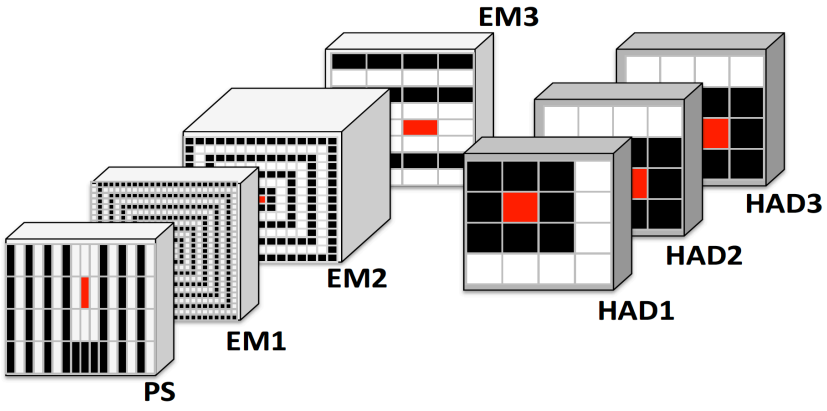


Figure 5.4: Sketch of Calorings longitudinal structure in multiple layers around a given region of interest (ROI) window. The change in granularity impacts heavily the number of rings.

The energy of cells is summed in concentric ring shapes around a cluster's barycenter or its hottest cell. These rings are built in a (0.4×0.4) window in (η, ϕ) for all layers : Pre-Sampler, EM1, EM2, EM3, Had1, Had2 and Had3.

Typically, for a given cluster, one expects 1000-1200 cells if all layers are included, but the rings result in 100 individual variables. Note that, from figure 5.4, the number of rings from one layer to another differs; this is due to the change of granularity between layers. Table 5.1 gives the number of rings per layer in a 0.4×0.4 window. Figure 5.5

illustrates how a window containing 49 cells is compacted into 8 rings. Additionally, this figure illustrates how the ring energy distribution is to be read.

Layer	**PS**	**EM1**	**EM2**	**EM3**	**H1**	**H2**	**H3**
Number of rings	8	64	8	8	4	4	4

Table 5.1: Layer and Number of Rings

These variables function well in ML approaches. In fact, multiple studies investigated the options of using low-level calorimeter data as inputs to neural networks [175]. A naive approach would consider inputting all cells of a given cluster (or window around a e/γ candidate) into a sizable network architecture. Such a network, if optimized, could benefit from the high precision of the layer's granularity and withdraw characteristic features of energy deposit structures. These features could directly reflect specific electron, photon, or jet signatures and would be effective for identification. However, the Caloring approach is a better solution due to the advantages of the compaction of cells into a ring. The reduction of the dimensionality allows for simpler NN architectures and input vectors that can run faster, which is important for triggering and allows for better optimization of hyperparameters. Additionally, by combining the cells in specific shapes, correlations between rings can arise and be explored more easily than when one considers all cells. Differences in correlations can relate to different shower development features by different particle types. ML tools with ring inputs can become performant, as we will see later in this thesis. Furthermore, this compaction allows for more robustness against noise in calorimeter cells. By combining multiple cells, the individual cell-level fluctuations are compensated due to their stochastic nature, yielding more stable structures. The rings also show lower Data to MC differences as these bigger structures suffer less from mismodeling intrinsic detector effects such as cross-talk compared to using individual cells. Through private communication with the EM ATLAS trigger team, it is understood that the ringer algorithm used at the HLT is regularly trained on both MC and Data formats without showing major differences; a paper is being prepared to document that work but is not yet public.

When combining the cells into a bigger structure, one can orient the variables to reflect specific shower features that are expected from the physics of interest. For instance, later in this chapter, asymmetric topologies will be discussed, as well as their impact on tagging double-body energy deposits. Thus, ML algorithms using these variables are also oriented to identify particles using these physics-driven features. Choosing this specific a mask in a ring shape essentially allows to capture more detail on the shower center (as one can see in figure 5.5), which is missing from standard SS, while being an intermediate level between using all cells and using high-level variables.

The fact that the Calorings are concentrated on the cluster's hottest cell and incrementally measure energy in wider rings has also proven sensitivity to dual particle showers. At the trigger level, current developments are ongoing to study the potential of rings to select both single and boosted electron pairs.

On the technical side, to build Calorings, one requires access to cell-level data files. This is done easily at the trigger level within the ATLAS data flow. However, offline

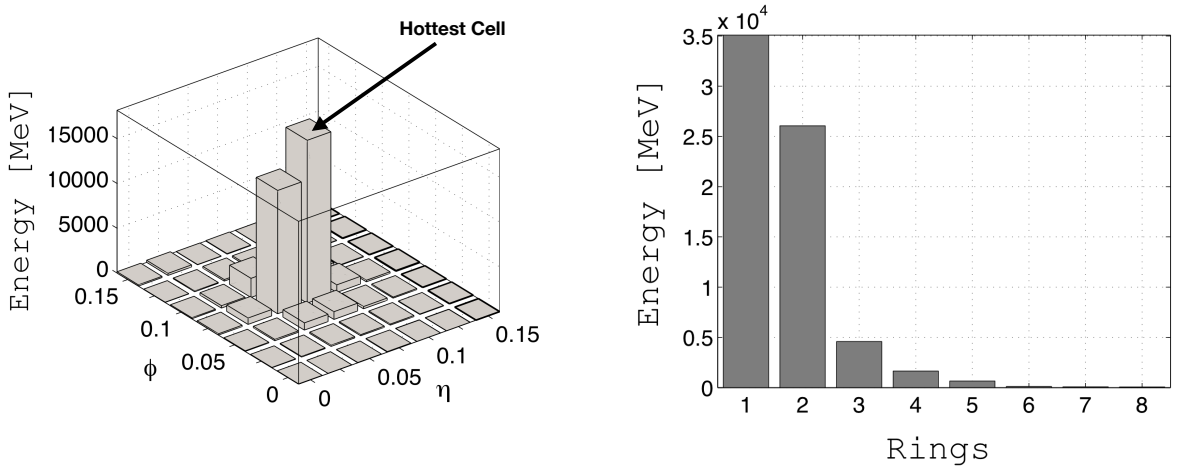


Figure 5.5: An illustration of how the calorimeter cell grid is compacted into a lower dimension ring energy profile. From [187].

analysis data streams lack the tools necessary to create and study Calorings. Their potential to be used in an ATLAS analysis as an alternative shower description is heavily impacted by the technical effort required. A special effort is needed to reprocess data files from raw data to build the rings and propagate them in the data stream up to the analysis data format. For this reason, calorings have never yet been used in an analysis context.

5.3.1 Ring construction procedure

A simple step-by-step procedure of how these variables are built is explained below :

- **Select Cluster**: a loop over all relevant clusters in the event is made
- **Select a given layer**: a loop over the different layers is made from PS to Had3
- **Fix the cluster's center**: either the hottest cell can be used or the energy barycenter of the cluster
- **Build a ROI**: a region of interest window of (0.4×0.4) is built around the center.
- **Loop on all cells in the given layer** :
  - calculate the distance of this cell in η and in ϕ to the center
  - normalizes the distances by the granularity of both axes; this yields distances in the number of cells
  - add the cell energy to the relevant ring number

A simple graphic representation of this process is illustrated in figure 5.6.

EventReader

Special tools have been built to produce these types of variables for offline studies of physics. In ATLAS software organization, accessing calorimeter cells must be done using a low-level data file format labeled ESD. This format embeds the raw information from all ATLAS subdetectors. These files can also be produced from MC simulations. ATLAS reconstruction algorithms are run on the base of ESD files to build higher-level objects ready to be used for physics. The resulting analysis-ready files lack all low-level containers, such as the calorimeter cells, except if a special reconstruction configuration is implemented.

The ATLAS Caloringer team developed a tool named EventReader [188], which enables studies on ESD files. This ATLAS software package was adapted for the displaced $a \to \gamma\gamma$ analysis with Calorings. More flexibility and functionalities were added to this tool to build new Caloring-based variables characterized by asymmetrical topologies. Parameterized options have been implemented to select reconstructed jets, photons, or truth particles as seeds for the ROI instead of clusters.

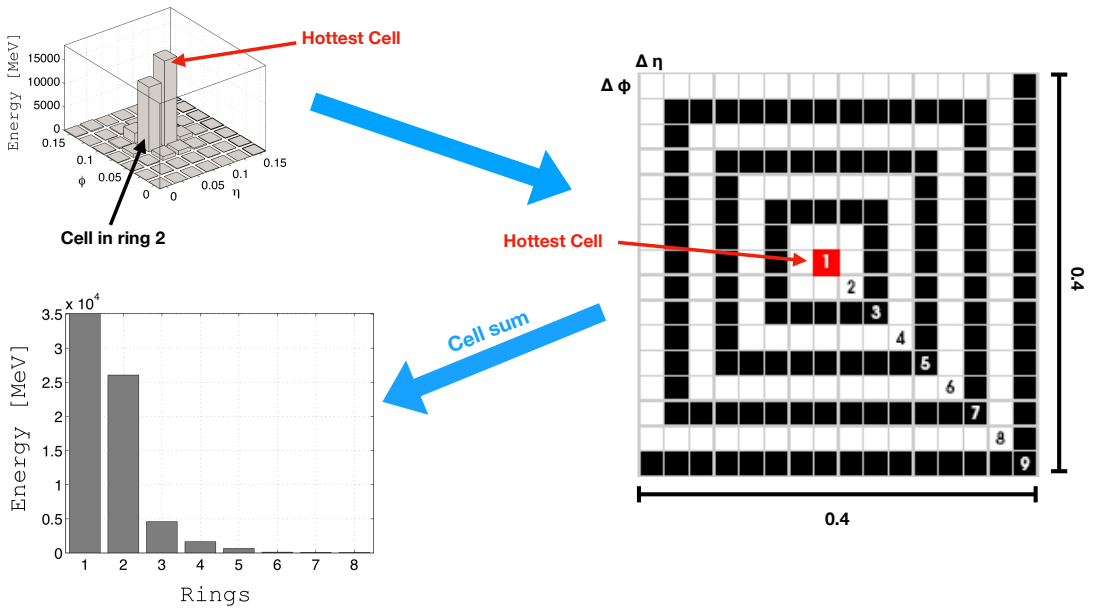


Figure 5.6: Schematics of how the cell grid is turned into rings with the correct number labeling. All cells are then summed into ring energy values.

5.3.2 Electron identification at HLT

ATLAS trigger system is divided into two main steps [189], the level one (L1) and the high-level trigger (HLT). The L1 system is implemented at the hardware level, while the HLT is software-based. Together, the trigger chain is capable of reducing the input rate from 40 MHz to 1 KHz on average. The HLT runs in parallel different steps using calorimeters, tracks, or a combination of both with dedicated algorithms for each type of particle identification or topological signatures. The flow of software guarantees a significant reduction of rate accompanied by a gain in precision in two steps.

For particle identification, the first step at HLT is named FastCalo. At this step, the purpose is to process detector signals, using only calorimeters, at high rates and classify between candidate electrons and fake electrons with a low fake acceptance efficiency. This step used to be done using cut-based selections on SS variables for electron identifications. Mainly using R_η, R_{Had} and E_{ratio} variables and track-based information which show relevant discriminating power for electrons.

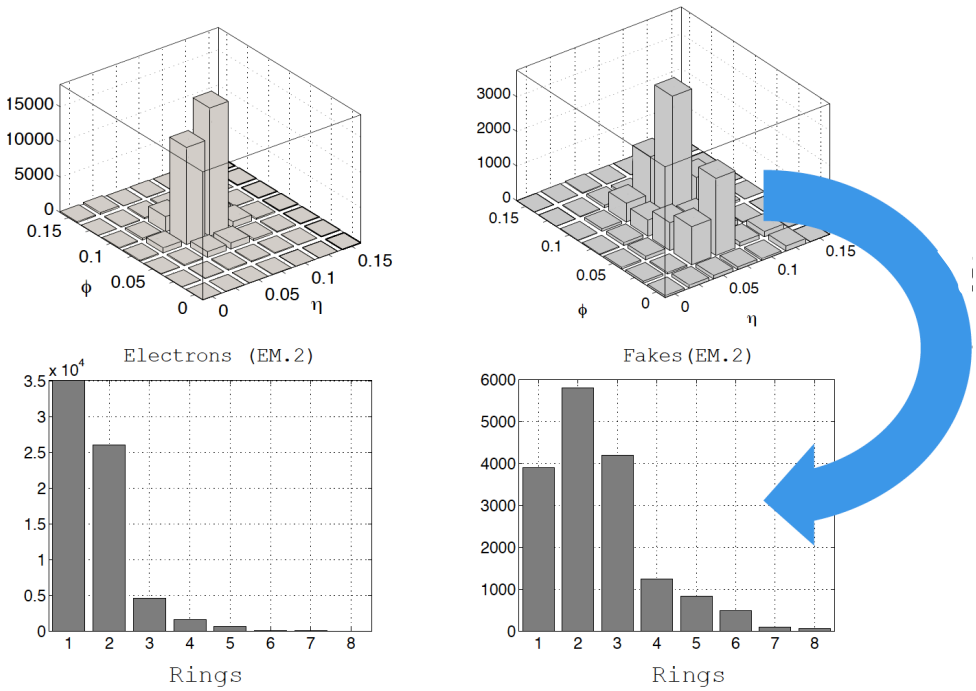


Figure 5.7: Differences in ring profiles for electrons and fakes.

However, since 2017, these cut selections have been replaced with a neural network approach using Calorings [175] [178]. This ML tool is decomposed into an ensemble of NN for different η and E_t regions. The input variables are only the 100 rings that take into account the full layers. Such an approach enables the algorithm to take advantage of non-linear correlations among the different input rings. It was shown that this technique is highly efficient. In fact, with the same trigger rate and trigger efficiency, the rejection power of jets was multiplied by $\approx 2 - 31001[175]dependingonthe(\eta,\ E_t)$ region.

Figure 5.7 illustrates how electrons and fake signals in a calorimeter layer are transformed into a ring profile to be used as discrimination variables.

This ML algorithm combined with rings is called NeuralRinger and has been verified to be a significant improvement. The current project aims to implement this algorithm in FPGAs to work at L1. Multiple ongoing studies use the NeuralRinger as a basis for electron pairs and photons. In addition, Calorings are also used to perform an improved calibration in the fastcalo step.

5.4 Using rings for LL-ALPs

The rings can provide information on the very central part of energy deposition, which improves sensitivity to collimated photons. Additionally, extensions of rings, introduced in the present chapter, allow asymmetry measurements, which are important in the context of LLP photon pair decay.

Studies introducing rings on displaced $a \to \gamma\gamma$ signals and QCD background jets in the context of the $h \to Za$ LLP search are presented below.

5.4.1 Building jet rings

The EventReader package was deployed on MC simulated samples of $h \to Za$ with $a \to \gamma\gamma$ (presented in Chapter 4.5). AntiKt4EMTopo jets are chosen as they can better reconstruct the displaced ALP decay products compared to EMPFlow jets. This is due to the lack of tracker information for late decaying ALPs.

Truth-matching was implemented (see 4.6.2 to identify the ALP-jets, and use them as seeds to build rings.

Background MC di-jet samples in similar run 3 conditions with the same pile-up profile and a Pt range [10-40] GeV are used as background.

5.4.2 QCD jets vs di-photons

Firstly, QCD jets and photons show very different shower developments due to the differences in interactions with matter. The important differences feature shower width, depth, energy ratio between EM layers, energy ratio between EM and hadronic calorimeters, and more... These differences in shower developments impact the energy profile of Calorings.

Ring profiles explanation: It is crucial to understand how to read ring profiles. These were shown in figures 5.5, 5.6 and 5.7. They provide an intuitive way of representing the energy distribution read through the ring masks. These prior examples only considered a single layer. However, the following results consider all layers. This is done by stacking up the layers of ring indexes. On the first result (figure 5.8), one observes the ring profiles of each layer arranged sequentially. The ring indexes are taken from table 5.1 and go from 0 (first ring of the presampler) to 99 (last ring of the 3rd HCal layer). The energy of each ring is often normalized to the total energy, thus allowing good comparisons between events with different particle momenta.

All ring energy peaks and other features that will be commented on must be understood in their respective layer. For instance, ratios of energy peaks inside EM1 rings refer to energy distribution features within the layer EM1. Meanwhile, ratios of peaks between different layers give a sense of longitudinal development. Additionally, this representation of energy distribution allows for a read on the shower width in (η, ϕ) as thin peaks imply focused energy deposits that are captured in fewer rings. In contrast, large peaks imply

showers that cover a wide number of rings.

Ring-profile of merged photons

To plot the expected ring energy distribution of merged photons, one selects a low-mass alp prompt decay.

Figure 5.8 shows the ring profile of a jet matching with an alp ($m_a = 0.4$ GeV) decaying close to the collision point ($L_{xy} < 0.1$ mm) with a relatively high boost ($P_t = 38$ GeV). While 38 GeV is not a high momentum value compared to collision energies, it remains high in the ALP momentum spectrum. A strict $|\eta| < 0.8$ cut is implemented to choose only ALPs directed to the central barrel. The barrel acceptance can go up to 1.4 η; but in this lower range, the dead material in front of the detector remains constant, and no cracks are present [113]. Choosing the barrel as a first step to study energy profiles limits effects linked to changes in the detector structure, which are complex in the end-cap region. The impact of looking at higher pseudorapidity regions on ring profiles will also be covered in the present chapter.

Figure 5.8 shows that the main absorption peak is in the second EM layer together with a small hadronic leakage. This distribution is expected since the second layer is the most absorbent (more than half the ECal radiation lengths). Figure 5.11 is a reminder of the different radiation lengths of the EM calorimeter.

A crucial feature is observed in this ring profile. Each layer shows a major peak accompanied by a secondary one. This means that, in each layer, a main energy deposit is absorbed close to the center while another is captured by a ring further away. This can be interpreted as a sensitivity to the double body structure of the shower or as a pile-up contribution. If the secondary peak is related to a photon the distance between the ring energy peaks reflects the photon's opening angle. Asymmetry measurements can be used to differentiate between the two scenarios. However, by studying multiple events, the hypothesis of sensitivity to the dual body is more likely than pile-up-related peaks.

Figure 5.8 is a single event. However, one can compute the average ring profile by taking multiple events. To better identify the dual-photon sensitivity in various events, an average rind profile, figure 5.9, was produced with a displacement limit of 100 mm.

This figure shows energy ratios between layers similar to those in the first plot.
However, the secondary peak is no longer clear. Nevertheless, it can be deduced from this profile. In fact, between events, the kinematic configuration of the ALP varies. This implies that the position of the secondary peak changes. Thus, when multiple events are included, the spectrum of secondary peak positions is integrated into a continuous tail that follows the main energy peak. This is visible in layer EM1 thanks to its high granularity. This tail distribution directly reflects the dual-photon decay of the ALP and gives a link to the photons' opening angle distribution, which is governed by the event kinematics.
Additionally, by averaging on multiple events, one compensates for event-related fluctua-

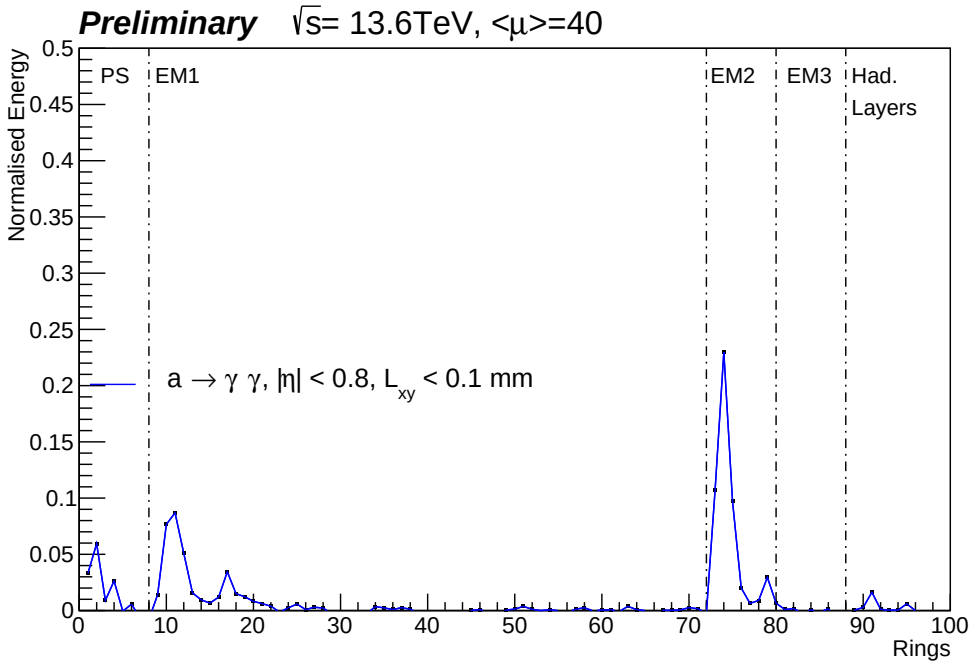


Figure 5.8: Energy profile of rings, for a prompt boosted merged photon decay of a 0.4 GeV ALP. A double peak structure is visible in the main absorbent layers. The x-axis represents the rings index according to table 5.1 as explained in section 5.4.2

tions, yielding a smoother energy profile

This sensitivity to the double bodies is an indication that Calorings could build a merged photon identification tool.

Ring-profile QCD jets

QCD jets yield very different energy ring profiles, with overall wider deposits and higher hadronic leakage, changing the ring energy ratios compared to photons at similar Pt values.

Figure 5.10 shows the average energy ring profile for background QCD jets. Important features of the energy spread in (η, ϕ) are noticeable in all layers through wide ring peaks. A clear saturation of EM rings is visible as these layers absorb the EM fraction of the jet (e/γ emissions, e^+e^- pair creations, π^0 decays ...).
The ratio between peaks of the EM and Had layers differs from that of merged photons. As the EM calorimeter presents only $1\lambda_{int}$ (nuclear interaction), the stable hadrons are mostly absorbed in the HCal .

The pre-sampler (PS) ring signals drastically change, allowing a high QCD background rejection with a few variables. This layer is designed to improve energy reconstruction by measuring the energy lost by particles/jets that interact with the material in front of the EM calorimeter. In jet processes, a fraction of the EM soft emissions and decaying

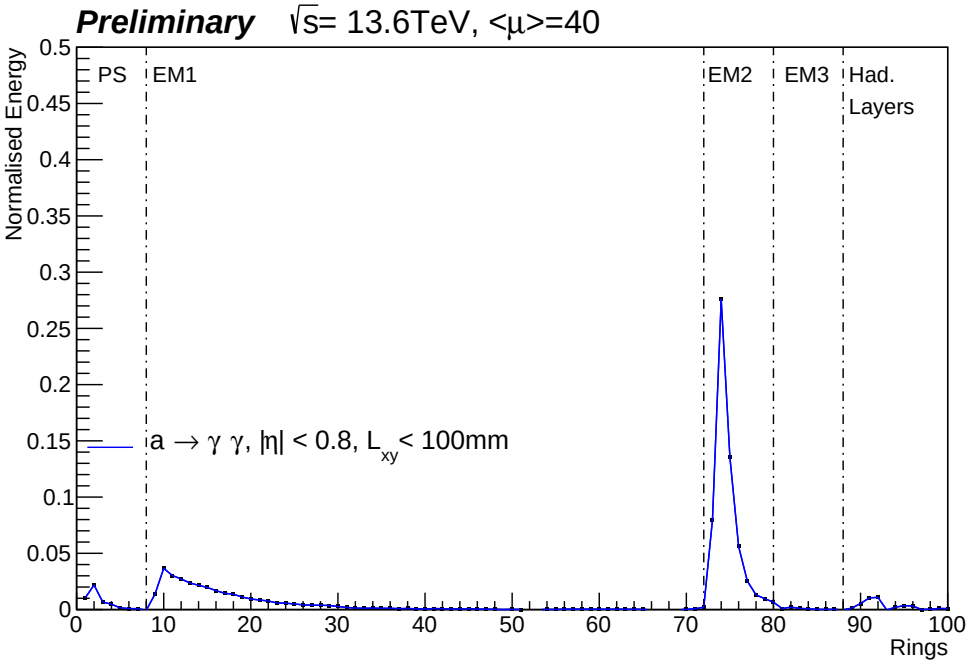


Figure 5.9: Average energy profile of rings, for low ($L_{xy} < 100$ mm) displaced 0.4 GeV ALPs. Tails are visible following main peaks, reflecting the spectrum of secondary peak positions. The x-axis represents the rings index according to table 5.1 as explained in section 5.4.2

particles happen before the calorimeter, which induces an important PS signal.

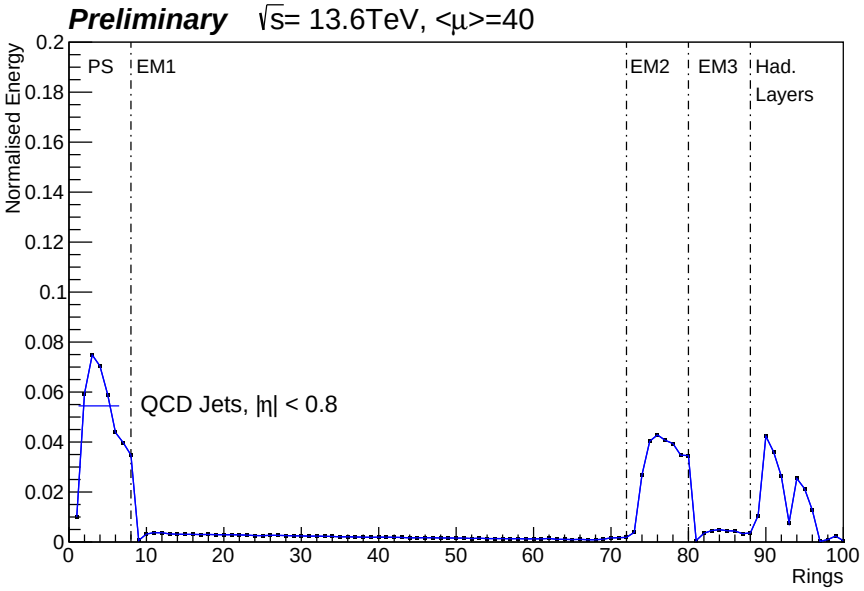


Figure 5.10: Average ring profiles of QCD jets created at the collision point. The x-axis represents the rings index according to table 5.1 as explained in section 5.4.2

Calorings capture the shower-development differences between QCD jets and photon jets. The longitudinal ring description of the shower and the PS contribution yield crucial information for discriminating these two types of showers. The number of energetic rings in a given layer gives a direct measure of the shower span, which further improves the discrimination.

These ring profiles illustrate their potential as an alternative shower-shape description.

5.4.3 Decay length sensitivity

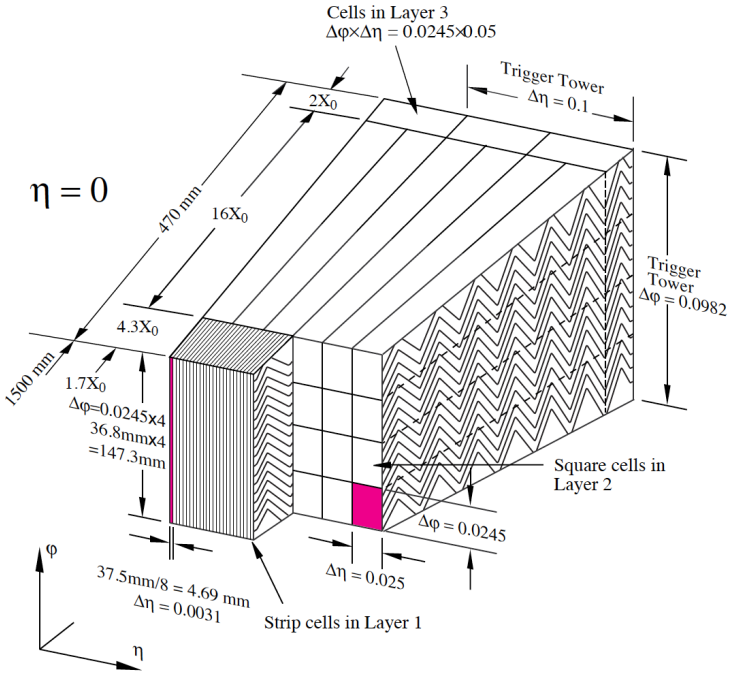


Figure 5.11: A module of the EM calorimeter displaying each layer depth. From the ATLAS experiment paper [100].

Although the rings show discriminating potential for QCD background rejection, these variables need a sensitivity to the decay position to build specific LLP taggers. Studies were conducted by dividing the ALPs into different displacement ranges and assessing the ring-related features in each case.

The simulated ALP events are divided into these decay position ranges: Tracker; EM calorimeter; Hadronic calorimeter and outside ATLAS.

Further slicing of the EM calorimeter subparts is conducted since the EM calorimeter. Each EM layer indeed presents a different response to the decay due to different granularities and radiation lengths (see figure 5.11). Table 5.2 gives the chosen L_{xy} cuts for each decay range.

Average ring profiles on each range were produced, and the main features are detailed below.

Range	Lxy **Min (mm)**	L_{xy} **Max (mm)**
Tracker	0	1400
EM	1400	2200
Hadronic	2200	3800
Long	3800	∞
Presampler	1400	1500
EM1	1500	1591
EM2	1591	1927
EM3	1927	1970

Table 5.2: ALP decay ranges minimum and maximum displacements. Considered for the barrel region.

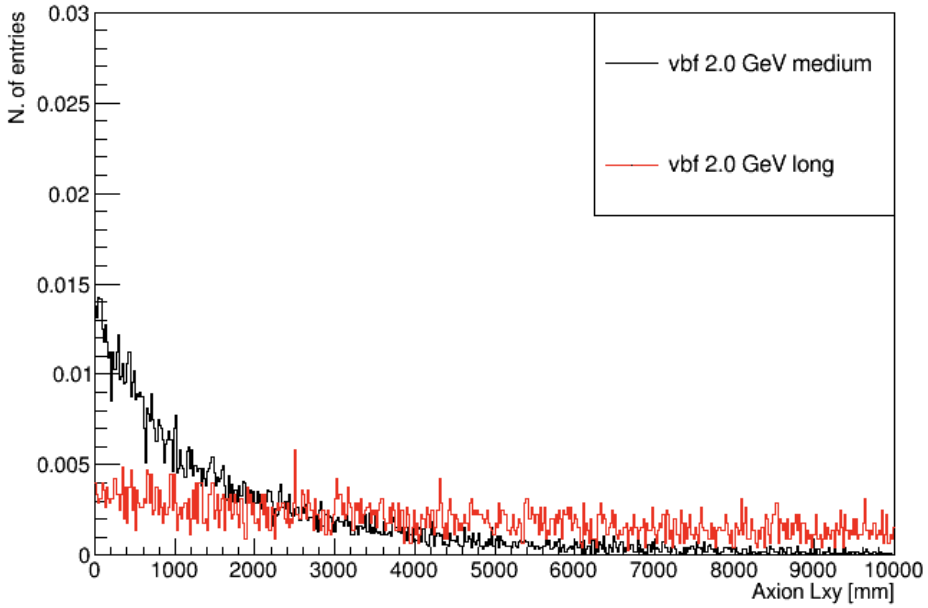


Figure 5.12: Transversal displacement distribution of an ALP ($m_a = 2$GeV) produced by a VBF-Higgs (boson-fusion) decay for two lifetimes: $c\tau_{med} = 131$ mm and $c\tau_{long} = 1.3$ m

Depending on the ALP intrinsic life-time, the populations of different ATLAS regions can differ. Figure 5.12 shows the decay position population variation between a long lifetime ALP compared to a lifetime maximizing decay in the calorimeter range.

Pre-calo decays

ALP decays happening inside the tracker yield calorimeter signals that are very similar to what is observed in figure 5.9. Whether the decay happens promptly or presents a significant displacement up to $L_{xy} = 1.4$m, the energy profile in rings remains similar. Nevertheless, this decay region can be investigated using techniques involving displaced vertices reconstructed with tracks when photons convert or with calorimeter pointing. It is important to note that depending on the lifetime, ALP decays closer to the interaction point and can be significantly more present than decays at higher displacements.

A calorimeter-based search could be implemented via the Calorings to understand the sensitivity to the decay position inside the tracker. However, this region was not the main focus during this PhD since other techniques and analyses have studied this [83] [84]. Tracker decays will be further investigated shortly, including resolved photon scenarios and photon conversions with improved di-photon identification.

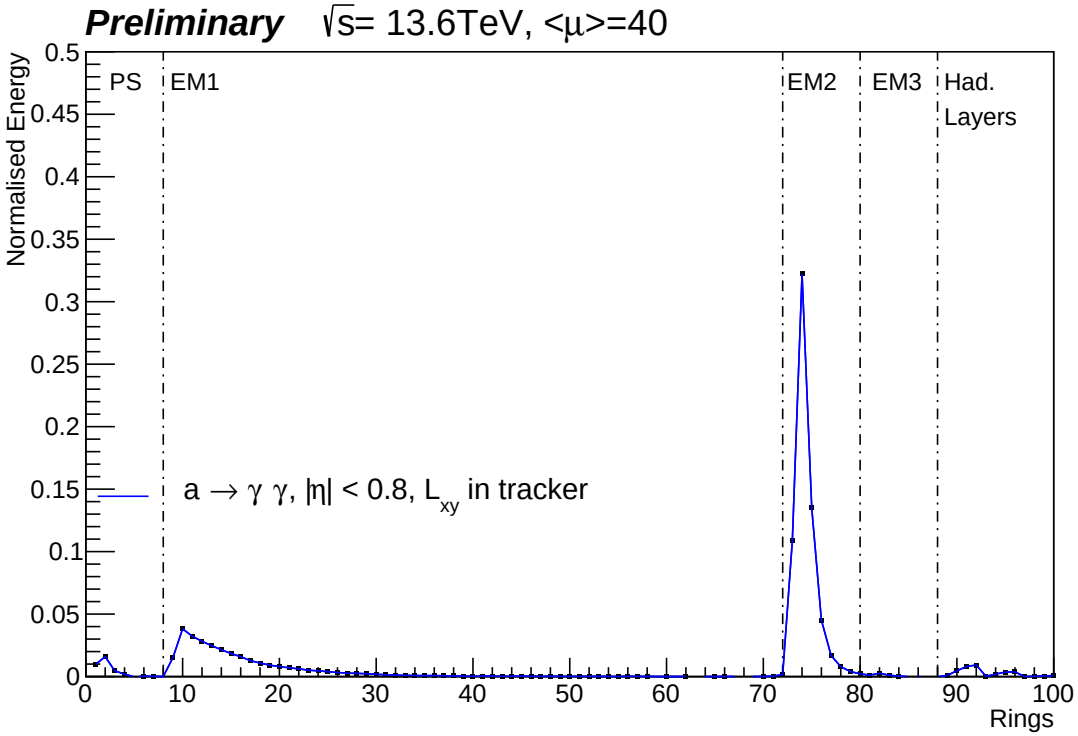


Figure 5.13: Average ring energy profile for 0.4 GeV ALP tracker decays into two photons. The x-axis represents the rings index according to table 5.1 as explained in section 5.4.2

The main features observed in pre-calo decays are related to the EM2 layer, as shown in ring profiles figure 5.13. The second layer contributes heavily to the full energy absorption, and a very small fraction of energy gets absorbed in the following layer, EM3, and the HCal. As expected, energy is still absorbed before layer two. The photons easily penetrate the presampler and leave a significant fraction of energy in the layer EM1. This layer has a very thin granularity and allows the probing of double-peak structures easily, as seen before.

Decays in EM calorimeters

When selecting jets matched with an ALP that decays in the EM calorimeter (including PS), a variety of energy profile features are observed. In fact, while in-tracker ALP decays produce photons that are stopped in EM2, later decays render higher signals in EM3 and in HCal. In figure 5.14, the resulting average ring profile of EM calorimeter decays is presented. The leakage post-EM2 is greatly enhanced compared to the in-tracker decays. However, the PS captures 0 energy, and EM1 shows close to no activity. This can easily

be understood by the fact that these layers are thin. Figure 5.11 shows that EM1 is only 4.3 X_0 radiation lengths. This directly implies that the probability of decaying within these specific layers is lower, making the shower development happen further away, as seen in the ring profile 5.14. Additionally, the first layer of the hadronic calorimeter is analogous to EM2 for in-tracker decays as it practically stops the ALP photons, a very small fraction of energy is captured past that.

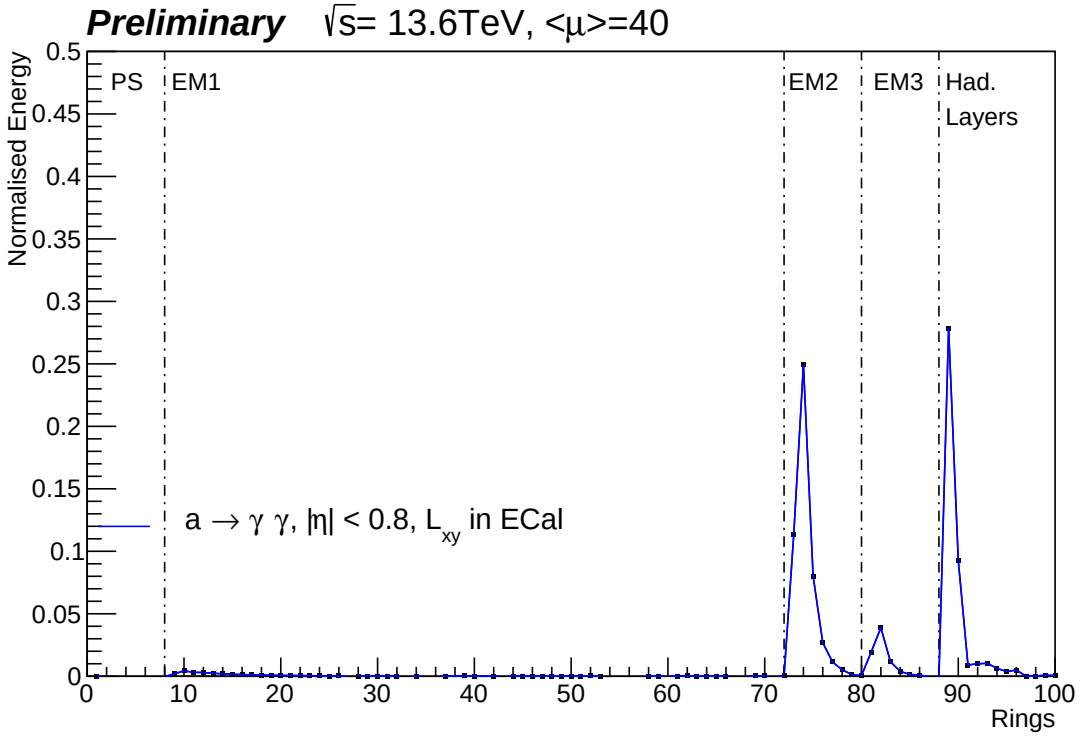


Figure 5.14: Average ring energy profile for 0.4 Gev ALP EM-calo decays into two photons. The x-axis represents the rings index according to table 5.1 as explained in section 5.4.2

Comparing this profile to tracker decays shown in figure 5.13 further marks EM1 and the PS as a very useful layer for retrieving the LL-ALP decay position. The energy fraction captured by these layers indicates if the photon pair was produced in-tracker or after. Moreover, the very thin peaks seen in the HCal are very QCD-unlike and differ from what is observed for QCD jets (figure 5.10). This type of thin shower in the hadronic layer is characteristic of focused energy deposits left by photons in this absorber.

Decays in the Hadronic calorimeter

Looking into longer flight-times, one gets ALPs decaying in the hadronic layers. The associated ring profile is shown in figure 5.15. The full shower is absorbed quickly by the hadronic layers. Additionally, as explained above, the thin peaks reflect the EM-interaction features of the photons. There is a triple peak structure that relates to the 3 hadronic layers. The second peak is dominant compared to the other two. This is caused by the fact that, in the barrel region, the second layer is the thicker one (see figure 4.13

of Chapter 4). Therefore, the probability of decaying inside the second layer is proportionally higher than that of Had1 and Had3.

It is important to note that the sensitivity to a double body is not obvious with the HCal. This is explained by the lower granularity of these layers. The merged photon pair is captured in the same rings.

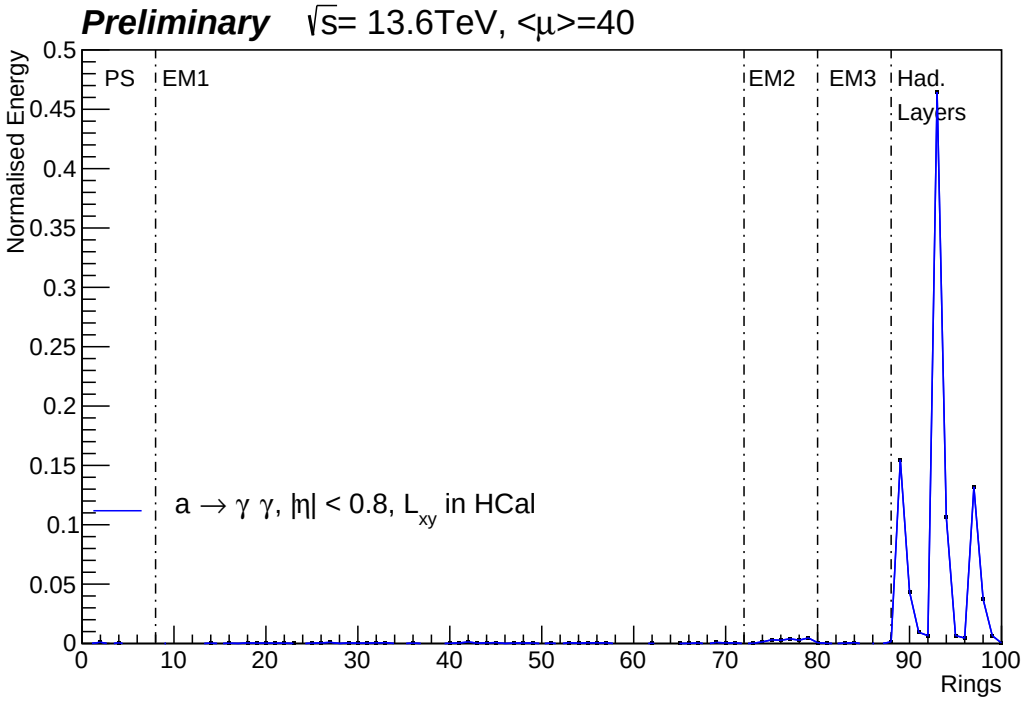


Figure 5.15: Average ring energy profile for 0.4 GeV ALP hadronic-calo decays into two photons. The x-axis represents the rings index according to table 5.1 as explained in section 5.4.2

The specific signature rendered by these very displaced ALPs decaying into photons is strongly suppressing the SM background. EM-like showers in the HCal that do not leave energy in any ECal layer can only be explained by a process where photons (or electrons) would be produced via an LLP decay. Tools capable of capturing this type of signature could severely constrain LLP models on ATLAS data. ATLAS analysis using so-called CalRatio techniques [190] [191] have investigated this type of signatures in search for LLPs. However, tagging efficiencies drop when one considers low-mass LLPs—further confirming that alternative particle identification strategies must be developed with new shower-shape description variables.

5.4.4 Sensitivity to EM layers

As seen for the different main decay ranges considered above, each EM layer shows a specific signature of the ALP decay depth. Figure 5.16 illustrates the ALP shower absorption in ring energy profiles depending on the EM-layer decay position. Thus giving a

finer description of its relation to the different radiation lengths of each layer.

The main features of each layer are described :

- Decays in the Presampler:
  - Layer with X_0 <1 and consequently no strong absorption
  - No energy is captured in the decay layer
  - Most energy absorbed in EM2
  - Signal produced in EM1 integrates the tail structure reflecting the double EM shower overlap
- Decays in layer EM1:
  - Thin layer: $4.3X_0$
  - No energy is captured in the decay layer
  - Ring peak in EM2 representing a greater fraction of total energy
  - This ring profile is very similar to the distribution produced by decays in the PS, but the EM1 ring energies offer good discrimination potential.
- Decays in layer EM2:
  - Thickest layer: $16X_0$
  - Significant portion of energy absorbed in decay layer
  - This decay position case is the one contributing the most to EM3 ring energies.
  - Energy decreases quickly in Had layers
  - Only layer decay position creates a major energy peak in more than one layer.
  - Noticeable peaks ratios between layers EM2, EM3, and Had1
- Decays in layer EM3:
  - Thinnest layer: $2X_0$
  - Close to 0 energy captured in the decay layer due to the low X_0
  - Energy is mainly absorbed in the first Had layer
  - Very narrow peak in Had 1
  - Maximum ring containing $\approx 80\%$ of total energy
  - This profile resembles HCal-level decays but contrasts with the fact that the 2nd and 3rd HCal layers remain almost empty
  - It is hard to distinguish ALP decays in EM3 from decays in HCal1.

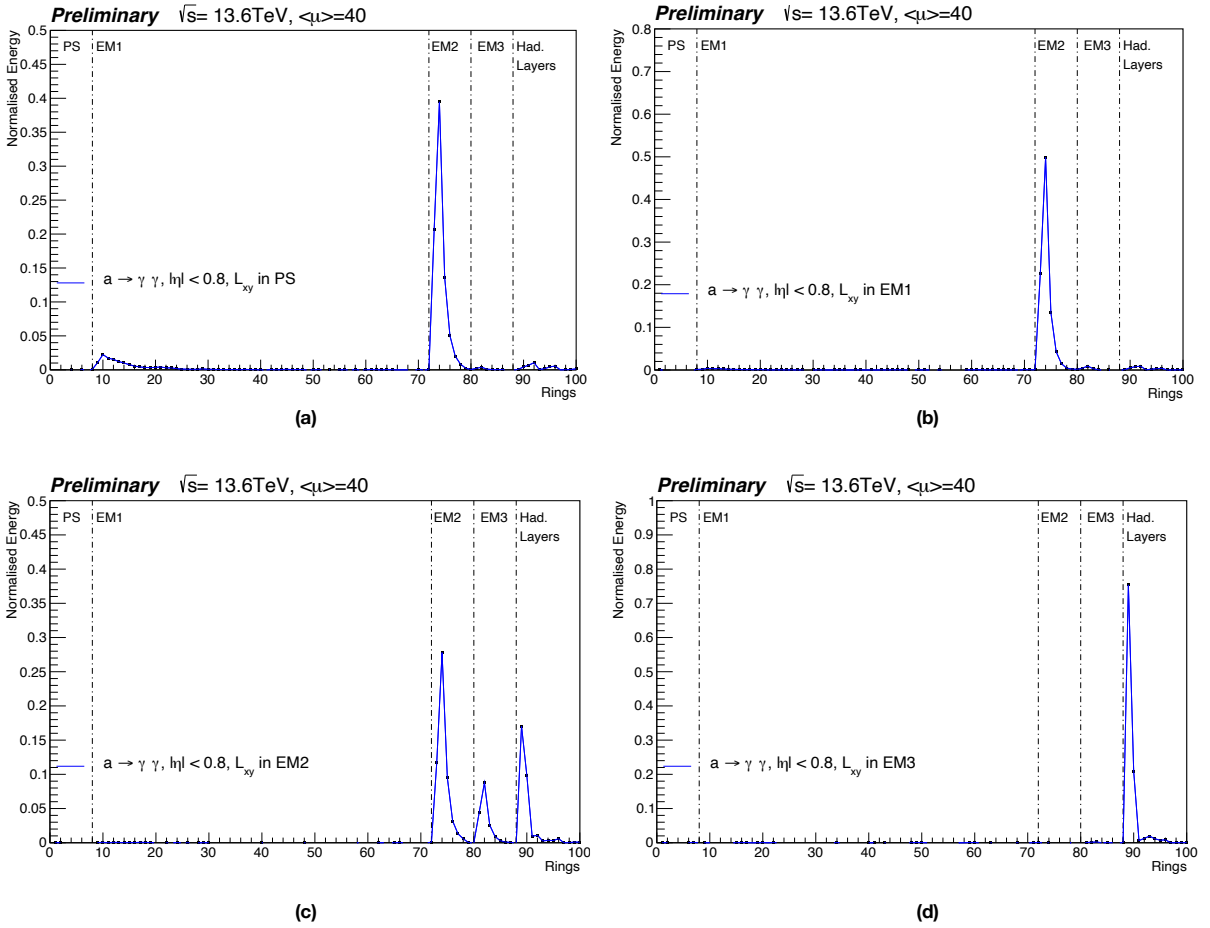


Figure 5.16: Average ring energy profiles for different 0.4 GeV ALP decay lengths associated with 4 layers of the EM calorimeter. Mind the fact that all vertical axes do not reach the same maximum for visualization's sake. (a): ALPs decaying in the Presampler. (b): ALPs decaying in the first sampling. (c): ALPs decaying in the second sampling. (d): ALPs decaying in the third sampling. The x-axis represents the rings index according to table 5.1 as explained in section 5.4.2

These observed features point to the fact that the analysis should use correlations between ring energies from different layers to infer the ALP decay position. These studies demonstrated a clear dependence between the ring energy distribution and the ALP decay position.

Decay position regression in calorimeters for LLPs

Regressing the particle decay position is the most powerful tool to identify LLPs against the SM background. Many analyses are conducted by searching for displaced vertices (DV) but these heavily rely on tracker information and can only concern charged particles. DV searches of photons can be conducted if photons convert into a e^+e^- to produce tracks. However, the track reconstruction of late-converted photons shows additional complications. Additionally, when one considers longer lifetimes, such techniques cannot

be used. This is the major limitation for regressing the DV of LLPs.

The Calorings description of the shower may offer a solution to surpass this. Ring energy profiles directly relate to the ALP decay position. From this information, the ALP decay position could be regressed. This regression approach can effectively extend the DV searches to neutral particles that do not produce tracks and extend the sensitivity to higher ranges of delayed LLP decays, including calorimeter decays. This pushes toward further development of Calorings in the context of LLPs to quantitatively evaluate new regression algorithms.

5.4.5 Extended barrel and end caps

The Caloring variables can also be constructed in other regions of the calorimeter. Using the extended barrel and the End Caps, one can expand the range of η for ALP decays. Considering the production mechanism under investigation for this analysis ($h \rightarrow Za$), the η distribution of ALPs peaks at 0. But the fraction of events in less central regions (above $\eta > 0.8$) is nonnegligible (see figure 4.20 from Chapter 4). Additionally, if one considers other models and production mechanisms, extending the search sensitivity to higher η is beneficial.

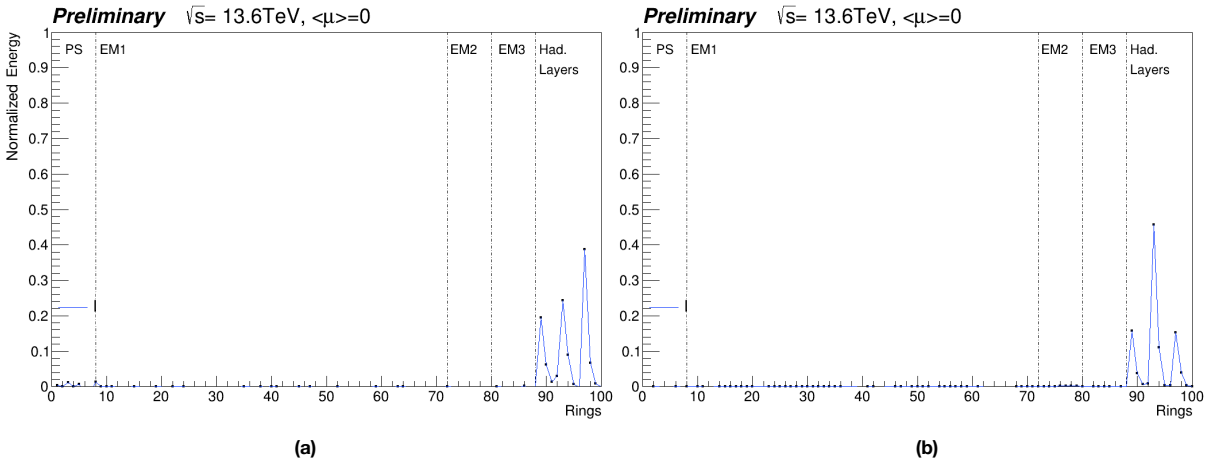


Figure 5.17: Average ring profiles for ALPs decaying at same displacement L_{xy} inside the hadronic calorimeter. (a) ALPs going towards the extended barrel and end caps (η [0.8 - 2]). (b) ALPs are directed to the main barrel. The x-axis represents the rings index according to table 5.1 as explained in section 5.4.2

Preliminary investigations of the η impact on the ring energy profile have been conducted. Figure 5.17 illustrates how the η direction of the ALP changes the ratio of peaks in the hadronic layers.
In fact, depending on the angle at which a particle enters the HCal, the material budget per layer can differ radically. Therefore, the expected shapes of energy deposition in ring profiles show an important response to the photon's direction productivity. This further

indicates that a ring-based tool could potentially retrieve with better precision the decay position of the ALP by considering both L_{xy} and η.

5.5 Asymmetric topologies

New Caloring variables have been developed to allow for shower asymmetry measurements. Two main structures have been added to the ATLAS reconstruction software Athena [186]. These are the Quarter-Rings and the Super-Strips. They follow the same construction strategy as standard rings but use different masks to combine cells.

Super-Strips

Superstrips are simple structures to describe shower asymmetry in a given axis (along η or ϕ). Figure gives a visual representation of Super-Strips 5.18. These variables are defined for each layer of the calorimeter.

Cell energies are summed in strip shapes following a given axis. Strip 0 includes the seed cell (hottest or barycenter) and the surrounding equidistant strips of cells, which are built and saved in different pair variables. Super-Strips allow one to compare the energy distribution on opposite sides of the central strip. For instance, one can compute the energy differences between strip $S\bar{S}_2$ and strip SS_2, which are both two cells away from the center, in η or ϕ, in the negative and positive regions. These can provide a direct measurement of axial-asymmetry within the energy deposit as in the following:

$$\text{Asym}_{S2} = \frac{S\bar{S}_2 - SS_2}{S\bar{S}_2 + SS_2} \tag{5.1}$$

Quarter-Rings

Quarter rings are based on the standard rings. For every ring, one builds 4 variables representing the 4 quadrants. They are labeled (++, +-, –, -+), and the positive and negative reflect the quadrant position in (η, ϕ) concerning the center. Only cells of a given ring in the same quadrant are summed up. This yields 4 times more variables, apart from the very central ring, which cannot be divided. Utilizing these variables, one can measure point-like asymmetries and compute excesses in a given quadrant of a given ring. Figure 5.18 gives a visual understanding of these variables.

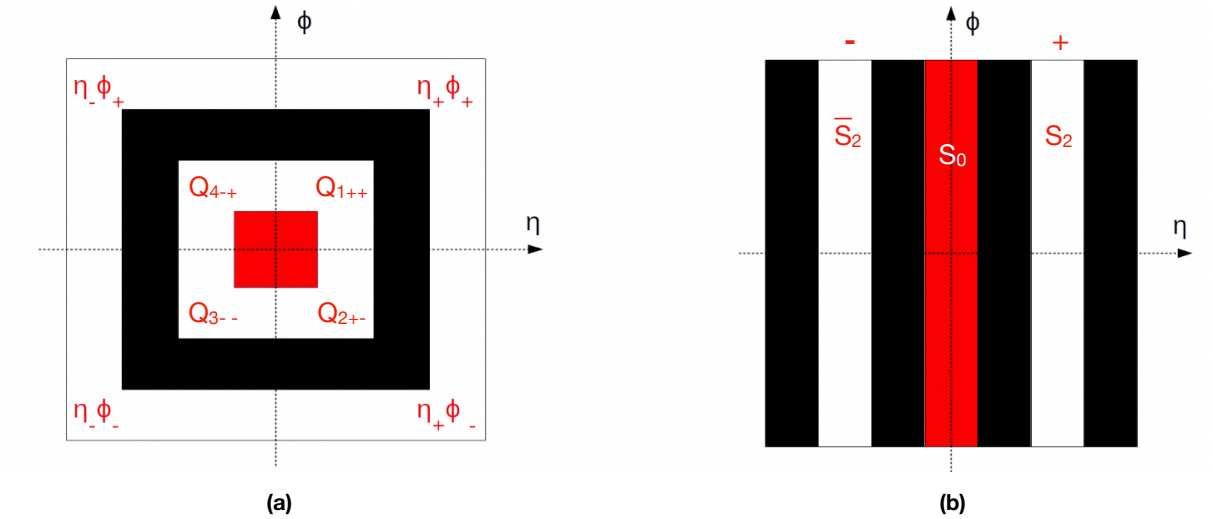


Figure 5.18: Schematics of different shower asymmetry sensitive variables using different topological structures. (a) Refers to Quarter-Rings. The 4 quadrants are labeled with a plus and minus scheme in all rings. (b) is Super-Strips built for the η axis.

Quad-Rings

To complement these asymmetric topologies, a new idea was investigated to measure shower development from different perspectives and maximize the sensitivity to the overlap of two showers. The Quad-Rings are constructed as standard rings but are offset from the shower center. One can understand this as measuring the same deposit from different points of view. Four seeds are chosen equidistant to the shower center - these are called corner seeds or corners - and are the center of 4 new ring sets. The collection of the 4 ring sets is called the Quad-Rings. One can compare energy differences of a given ring number between different Quad rings. If an energy deposit is homogenous, the ring profiles of each Quad-Ring are the same.

Figure 5.19 represents these variables. Supplementary, using these "shifted" rings, one can still observe all standard Caloring features mentioned in this chapter. The structure of standard rings is present in the Quad-Rings, however, they are displaced by a fixed index - reflecting the displacement of the corner seed with respect to the standard seed.

Following the illustration provided in figure 5.19, the Quad-Rings sets are labeled Top-Right (TR), Bottom-Left (BL), Bottom-Right (BR), and Top-Left (TL). They will be often referred to as TR/BL/BR/TL corner rings. Multiple offset values were tested to keep the rings in the 0.4×0.4 window in (η, ϕ), available from a software point of view in trigger level (which could become a potential port of the developed taggers) while maximizing the sensitivity to the photons opening angle. A diagonal offset of 3 cells was found to be a good compromise. A different choice of this window size at the offline level

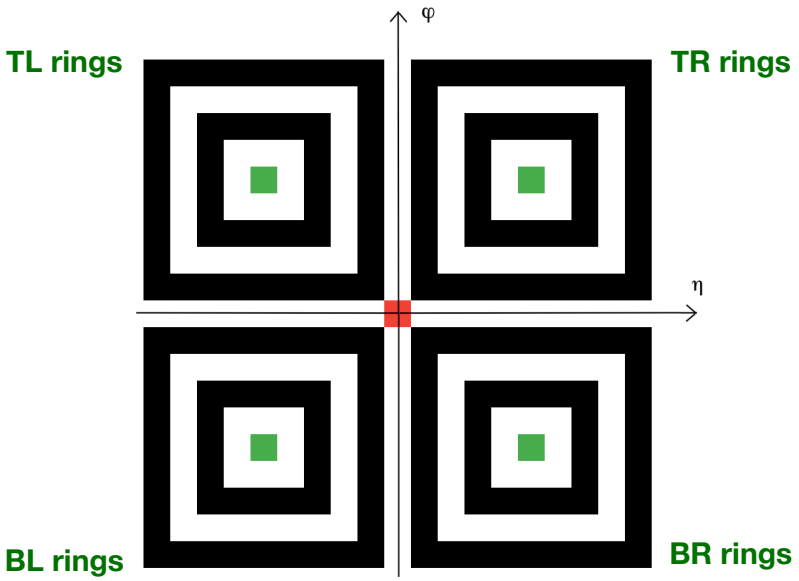


Figure 5.19: Schematics of Quad-Rings placement around the center. The red cell is the hottest in the energy deposit. While the green cells give the 4 new corner-seed positions to compute 4 new ring sets.

could be made. Nevertheless, it would cut a possible port of these variables to the trigger level, impeding the usage of Quad-Rings to select collimated photon pairs during data taking better.

Figure 5.20 shows a more precise description of 2 rings, TR2 and BL2 (2 refers to the displacement in cells) in the EM2 layer.

5.6 Asymmetries in double showers

Comparing the ring profiles of each corner allows us to assess the asymmetry level of the shower. Multiple comparisons can be made if one considers one-to-one rings due to the 4 independent ring sets. Asymmetry can be measured, for instance, by comparing the rings of the TL set and the BR similar to what is in equation 5.1. Each one of the combinations reveals the asymmetry along a given axis in the cluster. Estimating the asymmetry along multiple axes is fundamental to better increase the sensitivity to the two-body system and its mass-related opening angle (see figure 4.4 of the previous chapter).

Figure 5.21 shows all possible axes to measure energy distributions with the Quad-Rings.

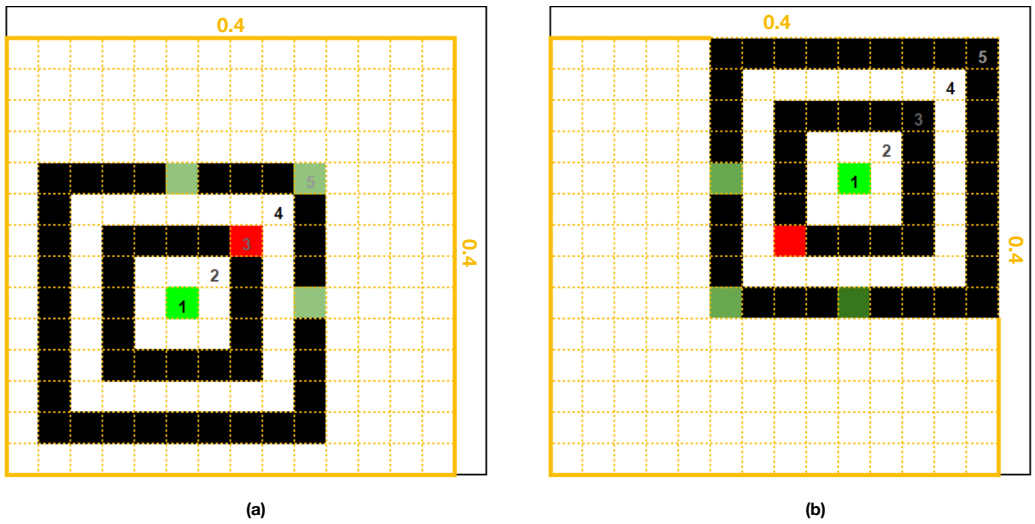


Figure 5.20: Schematics of TR and BL ring sets for a 2-cell displacement between the new seed (green) and the one used for standard rings (red) in the EM2 layer. The red cell indicates the usual center for rings, while the green cells indicate the 4 offset centers. (a) is the TR2 set, and (b) is the BL2 set.

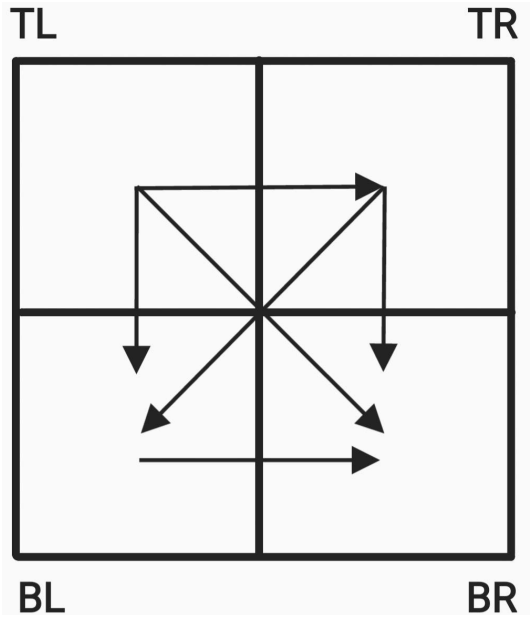


Figure 5.21: Illustration of all axes one can define with the TR, BL, BR, TL ring sets. Each axis can be used to compute ring energy distribution asymmetries [192].

5.6.1 Quad-Ring reliability

To ensure that the new Quad-Ring variables do not present any bias creating artifact asymmetries, a study was performed by taking QCD jets that yield homogeneous energy deposits around their axis.
In figure 5.22, the TR and BL average energy ring sets profile of prompt QCD jets are plotted, showing that the two profiles match. This demonstrates that the variables do not present any asymmetry by construction and that, for a homogeneous process, both corners show indistinguishable ring profiles.

This validation result ensures that any observed differences relate to asymmetrical energy deposits and directly gives physics-rich information about the nature of the shower development.

In contrast to standard ring profiles, which are normalized by the total energy, these Quad-Ring profiles will be plotted using the absolute energy. In fact, to compare energy excesses in one corner with respect to another, one must use the absolute energy of each corner ring set. Indeed, relative local energy distributions could remain similar in the two corners even though the total energy might be higher in one of the corners. Utilizing the absolute energy gives one more information to differentiate ring profiles located in different positions.

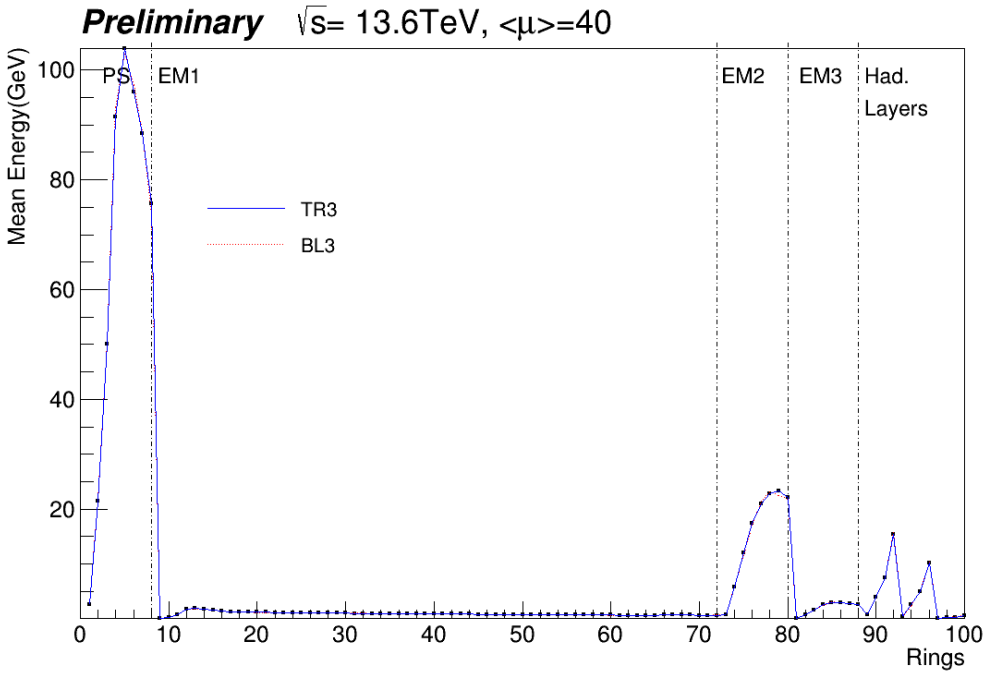


Figure 5.22: Average ring profile for QCD Jets for TR3 and BL3. The x-axis represents the rings index according to table 5.1 as explained in section 5.4.2

It is interesting to note that these displaced profiles present a similar distribution as in figure 5.10 but with a shift towards higher ring numbers due to the seed being dislocated from the center, thus showing the consistency of Quad-Ring variables.

5.6.2 Removing noise

Calorimeter cells present a constant noise level, which is stochastic by nature. When comparing ring energy values from two different corners, every small difference due to random noise can add up and strongly bias the overall asymmetry read. This is why these fluctuations must not be accounted for. To guarantee that measured asymmetries only reflect the energy deposited from the passing particles, noise rings must be taken out. For this, an aggressive approximation of the expected noise per ring was conducted.

The EM2 calorimeter cells present a noise of about 40 MeV, which is, to a very large extent, independent from one cell to another. Consequently, the noise present in a given ring is defined as the quadratic sum of its cell's content noise.

$$\sigma_{Ring} = \sqrt{\sigma_{cell}^2 \times N_{cells}} \tag{5.2}$$

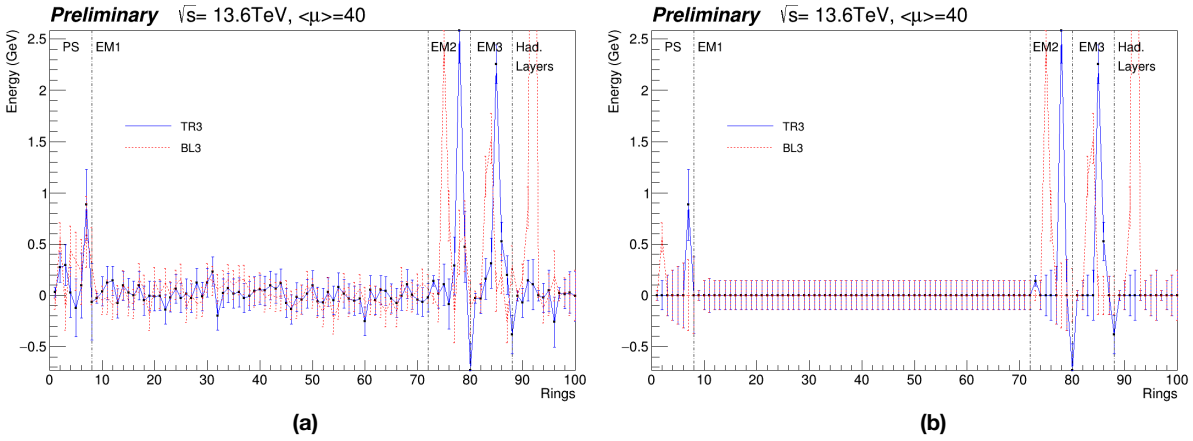


Figure 5.23: TR3 and BL3 ring profiles for a very asymmetric energy deposit. (a) without the noise removal procedure and (b) with removed noise. The x-axis represents the rings index according to table 5.1 as explained in section 5.4.2

By fixing σ_{cell} to 40 MeVd and computing the number of cells in each ring, an uncertainty value can be associated with each ring. Note that the number of cells per ring depends on how a given ring fits completely or partially in the 0.4×0.4 window; this was taken into account. Also, note that this uncertainty is conservative as it does not take into account possible noise cancellation effects in large structures due to the stochastic nature of individual cells' noise.
To remove the noise, all ring energy with an absolute activity below $2 \times \sigma_{Ring}$ are set to 0. Figure 5.23 shows the ring profiles of an asymmetric energy deposit from an ALP decay before and after noise removal. σ_{Ring} is used as an energy uncertainty on each ring. Note how the distribution of energy between the 2 corners differs significantly in the TR/BL axis, suggesting that the energy deposit is highly asymmetric.

With the noise removal, adding the ring energy differences between the two ring sets renders a value that reflects the particle-induced asymmetry.

During this project, all measures of asymmetry were conducted only on rings in layers EM1, EM2, and EM3. This region of the calorimeter is well understood in terms of noise level and offers the best granularity to build multiple complete rings. Thus providing the best case to assess the sensitivity of this approach on $a \to \gamma\gamma$ searches. However, future studies will include the Hadronic rings as well.

5.6.3 Asymmetry computation

Different strategies to measure the asymmetry within the Quad-Rings have been tested. A simple approach, utilizing the TR and BL ring sets, is explained below and shows how one can obtain very interesting measurements to tag the dual photon decays.

For each ring index, two values are retrieved :

- The maximum energy E_{max} between the two corners at this given ring index.
- The relative difference $\frac{\Delta E}{E_{tot}}$ between the two corners for the same ring index.

Equation 5.3 shows how the energy difference is computed for a ring index between the TR and BL sets :

$$\frac{\Delta E_i}{E_{tot_i}} = \frac{(TR_{3_i} - BL_{3_i})}{TR_{3_i} + BL_{3_i}} \tag{5.3}$$

where TR_3 (BL_3) represents the energy value of a given ring in the TR3 (BL3) set.

To emphasize the differences seen in high energy peaks, weights are associated with each $\frac{\Delta E_i}{E_{tot_i}}$. The objective is to build a normalized weight that directly reflects the energetic contribution of a ring in the full ring energy profile. Equation 5.4 shows a definition for such weights.

$$\omega_j = \frac{E_{\max_j}}{\sum_i E_{\max_i}} \tag{5.4}$$

where E_{max_j} refers to the maximum energy of ring index j (between TR and BL sets), and the denominator is the sum of all maximum values. This way, if a ring index contains a significant fraction of the energy distribution, it will have a consequent ω weight that amplifies its contribution to the asymmetry value of the shower.

For a given shower, the asymmetry is the weighted sum of all ring differences as in equation 5.5.

$$A = \sum_i \omega_i \cdot \left| \frac{\Delta E}{E_{tot}} \right|_i \tag{5.5}$$

where i concerns only the EM calorimeter ring index as mentioned in this section.

5.7 Results

This section presents asymmetry results on different shower categories that are of interest to the LL-ALP search. These are single QCD jets, single photons, and merged photons decaying from the ALP.

5.7.1 Asymmetry on event by event basis

To better understand how the asymmetry measure reflects differences in energy profiles, a specific ALP event is taken as an example.

The event configuration is : m_a= 9.0 GeV; Pt= 27 GeV; η= 0.6; L_{xy}= 1.2m
This reflects a typical largely displaced event that decays close to the end of the tracker. The large 9 GeV mass point creates a wide separation between the two photons, and the low Pt value does not significantly boost the photons. This type of situation should yield large asymmetries.

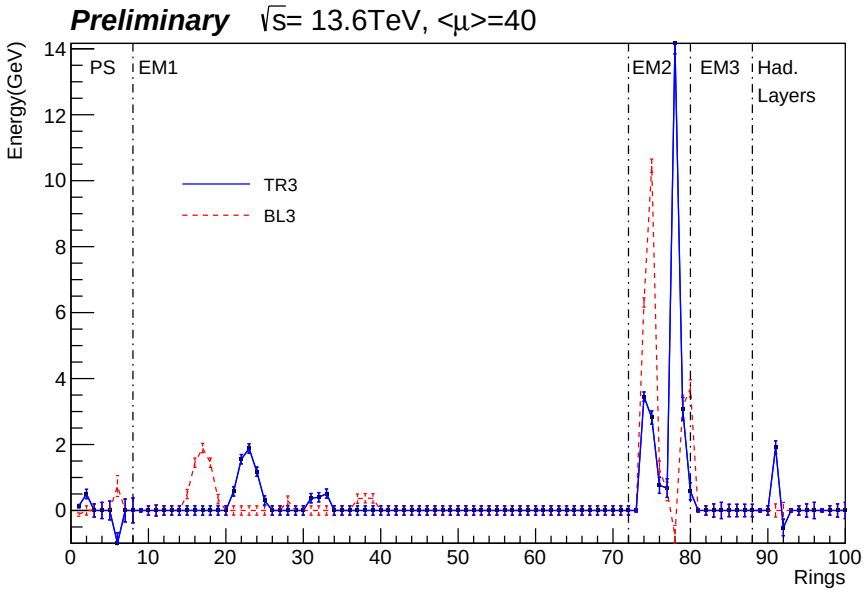


Figure 5.24: Ring profiles for TR3 and BL3 sets for the example ALP event. The x-axis represents the rings index according to table 5.1 as explained in section 5.4.2

Figure 5.24 illustrates important differences between the two ring profiles for both BL and TR corners of this given ALP shower. By focusing on the EM1 layer, one can see that the same energy deposition pattern has shifted toward lower values of BL3. This implies that the energy is not homogeneously distributed around the shower center and reflects the nature of the two-body system asymmetry.
Figure 5.25 shows the absolute energy difference ring by ring and gives an overall understanding of the total quantity of energy difference between the two corner positions that are used to compute the shower asymmetry value.

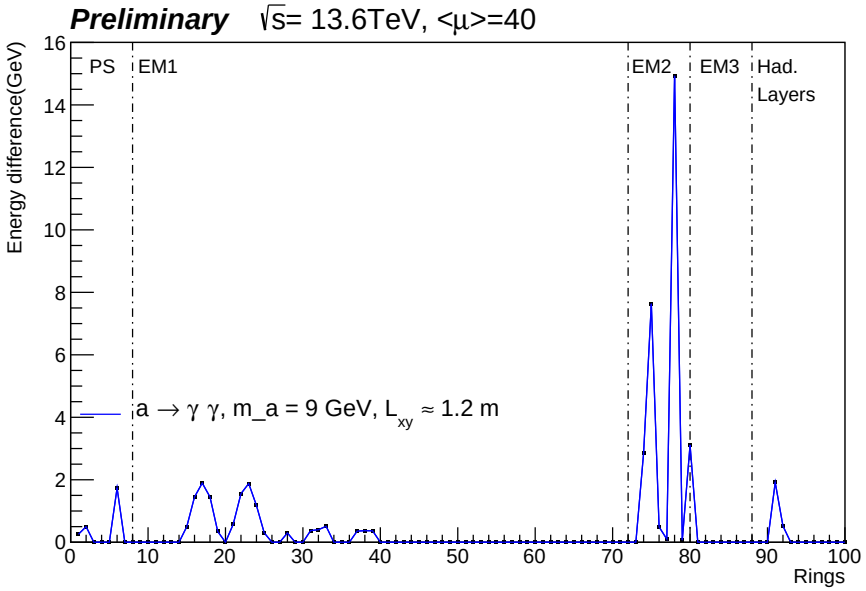


Figure 5.25: Absolute energy differences in Ring profiles. The x-axis represents the rings index according to table 5.1 as explained in section 5.4.2

Using equation 5.4, the weights associated with each ring index are computed. Figure 5.26 depicts these weights. One can see how the weights restrain or augment the contribution of each ring index. The PS ring number 6 energy is minimized with a low weight, reducing its impact on the sum from equation 5.5, while the weight of EM2 rings significantly raises its importance in the final result.

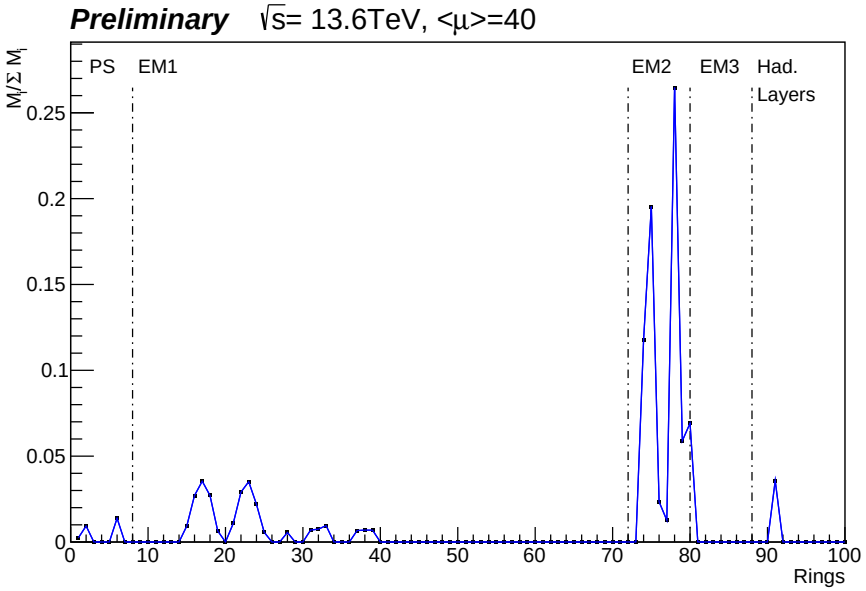


Figure 5.26: Associated weights to each ring energy difference based on equation 5.4. The x-axis represents the rings index according to table 5.1 as explained in section 5.4.2

Through this metric, the shower gets an **associated asymmetry value :** $A_{evt} = \mathbf{0.76}$

The objective of this metric is to classify and discriminate between the background jets and displaced photon pairs. Highly asymmetric clusters are expected to push A values to high values (close to 1), while prompt jets should generate clusters pointing to low values (0).

5.7.2 Jets and ALP discrepancies

Computing the A metric for each shower allows the creation of the asymmetry distributions related to each shower type. Figure 5.27 shows how QCD jets and ALPs (figures include the medium life-time point) behave differently concerning this Quad-Ring-based variable. ALPs tend to present higher A values compared to jets, which have an important peak at exactly one. This is an artifact of how the A metric is defined on events presenting a high energy ring with a 100% relative difference between the two corners.

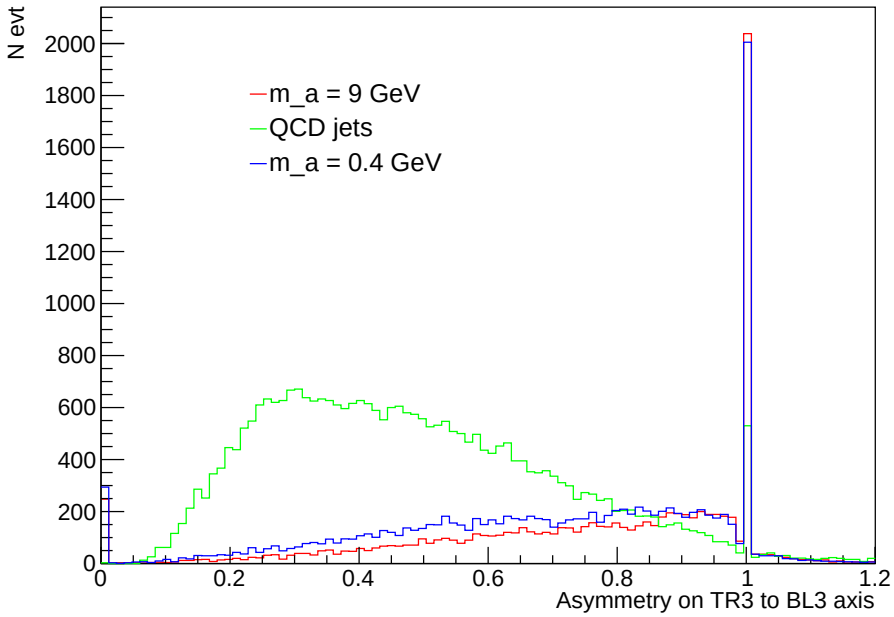


Figure 5.27: Asymmetry distribution between QCD jets and ALPs

A high number of showers present an important overlap between both categories. However, this first approach to an asymmetry metric is sub-optimal, and updates can improve the separation of both categories. For instance, when one modifies the normalization of the relative differences or redefines the ring weights, the resulting distributions change. Figure 5.28 shows how the separation of the different categories is impacted when such parameters are modified. In this alternative metric definition, the normalization was done by the average of TR and BL rings instead of the sum, and the weights definition was tweaked.

Nevertheless, it is important to clarify that the separation of distributions in figure 5.27 only depends on the asymmetry read along one axis while the problem is multi-dimensional. All axes should be considered, as they are highly complementary, to assess the real discrimination power. In fact, as a $\gamma\gamma$ shower yields a low A value along a given axis, it can be highly asymmetrical in another. This is demonstrated by plotting the same distributions considering two perpendicular axes in the next paragraph.

Additionally, the separation of both particle types using the combination of asymmetries along all possible axes of the Quad-Ring is presented in the ML section 5.7.4 and illustrates the real discriminative power of these new variables.

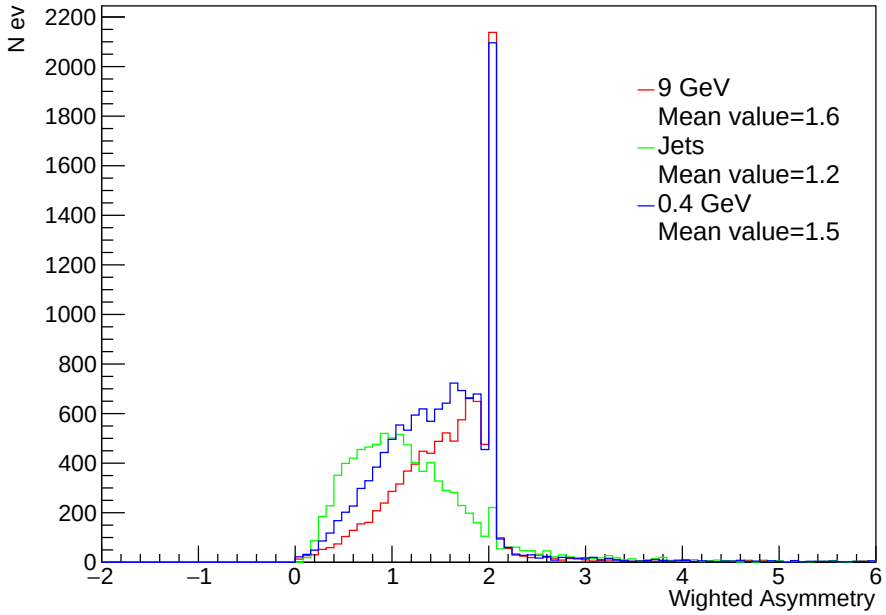


Figure 5.28: Asymmetry distribution between QCD jets and ALPs with metric using ring average normalization.

Asymmetry Mass dependence

The $a \to \gamma\gamma$ decay processes imply a relation between the shower asymmetry level and the ALP mass, thus the A variable (once optimized) could be used as a proxy to retrieve $m_{\gamma\gamma}$ in merged cases. The reconstruction of invariant mass is a powerful tool to select events in $h \to Za$ searches. In fact, selection cuts on $m_Z + m_{\gamma\gamma}$ have been applied on the prompt analysis [83], to select events with a system mass close to m_h. Additionally, in this analysis, $m_{\gamma\gamma}$ parametric fits are applied on data to look for excesses related to possible ALP decays. This allows to have a different approach than a cut-and-count analysis. However, invariant mass reconstruction algorithms require the photons to be resolved. This induced a lower worse signal efficiency and background rejection for ALP masses below 2 GeV.

Shower-asymmetry techniques introduced in this thesis provide a new class of estimators that could answer to such limitations. Together with background models extracted from background-enriched data-driven samples, this offers a way to analyze a selection of candidate signal events. This enables one to search for a quantizable excess of ALP events together with their best candidate mass provided by the asymmetry spectrum fit of the selected events. Furthermore, the Quad-Ring variables offer 6 axes onto which such an asymmetry spectrum can be fitted. Figure 5.29 illustrates how summing the A variable across all axes reveals a mass dependence on the ALP. A combined asymmetry spectrum fit would offer a more precise mass regression and would emphasize a potential ALP excess with respect to the SM background.

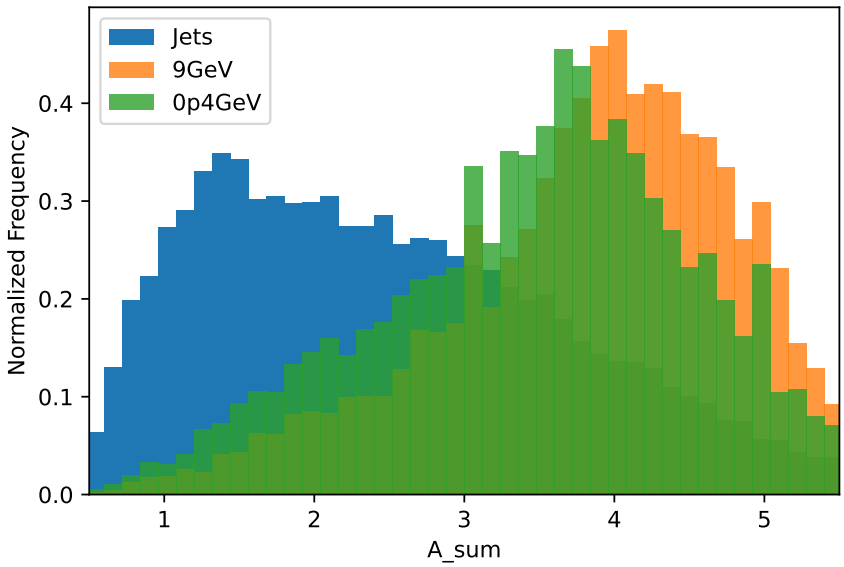


Figure 5.29: Sum of asymmetry distributions for QCD jets, 0.4 and 9 GeV ALPs.

It is important to note that this asymmetry value is still suboptimal and other Quad-Ring based methods can improve it. Such new methods could benefit different analyses with multi-body decays impacted by soft jet backgrounds. This would provide new sensitivities to many signatures that include close-by objects in the calorimeter. Such estimators, firstly focused on the LL-ALP, would be interesting to test in the context of large jets coming from the decay of a Higgs or a Z to a $b\bar{b}$ pair, for instance.

Two axis

2D asymmetry correlations between axes are presented in figure 5.30 for ALPs and in figure 5.31 for QCD jets and show major differences. In fact, the homogeneity of jet energy deposits yields similar correlations between all axes, while the merged photon clusters show a more complex behavior. This demonstrates that axes must be considered to account for the total shower asymmetry. This difference in correlation is a powerful feature to be exploited by classifiers using the asymmetry values as inputs for all axes.

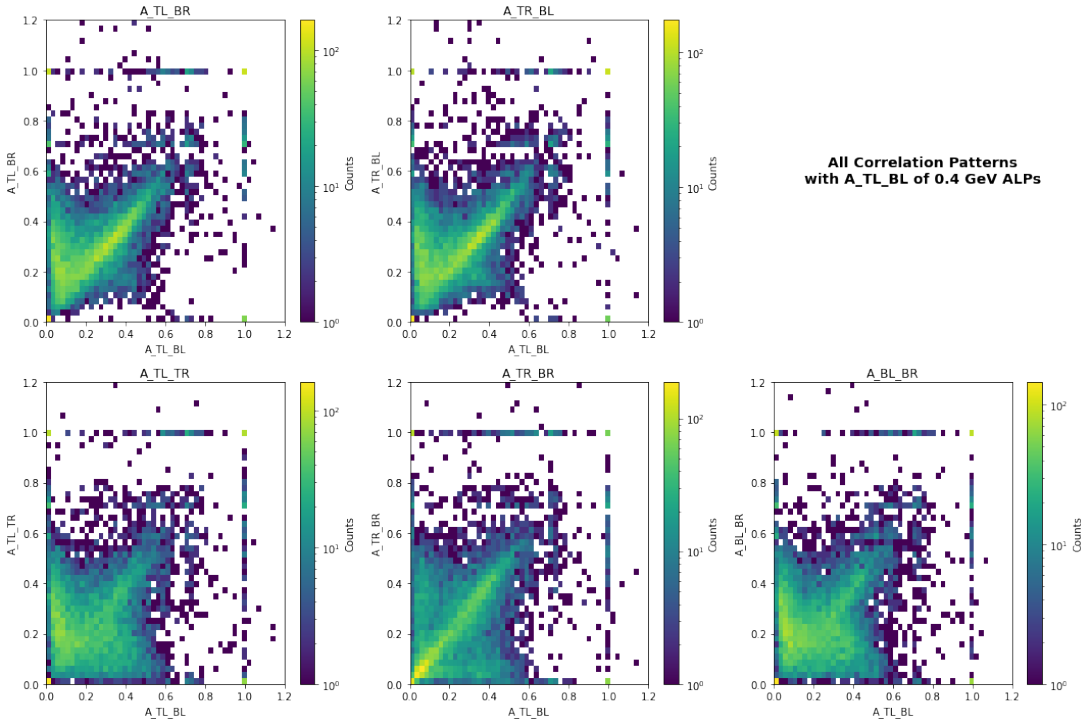


Figure 5.30: 2D histograms of correlations of the asymmetry axis TL-BL with the 5 other axes. Computed for 0.4 GeV ALPs with the medium lifetime (see 4.5). The different shapes of correlation reflect the two-body structure of the energy deposit.

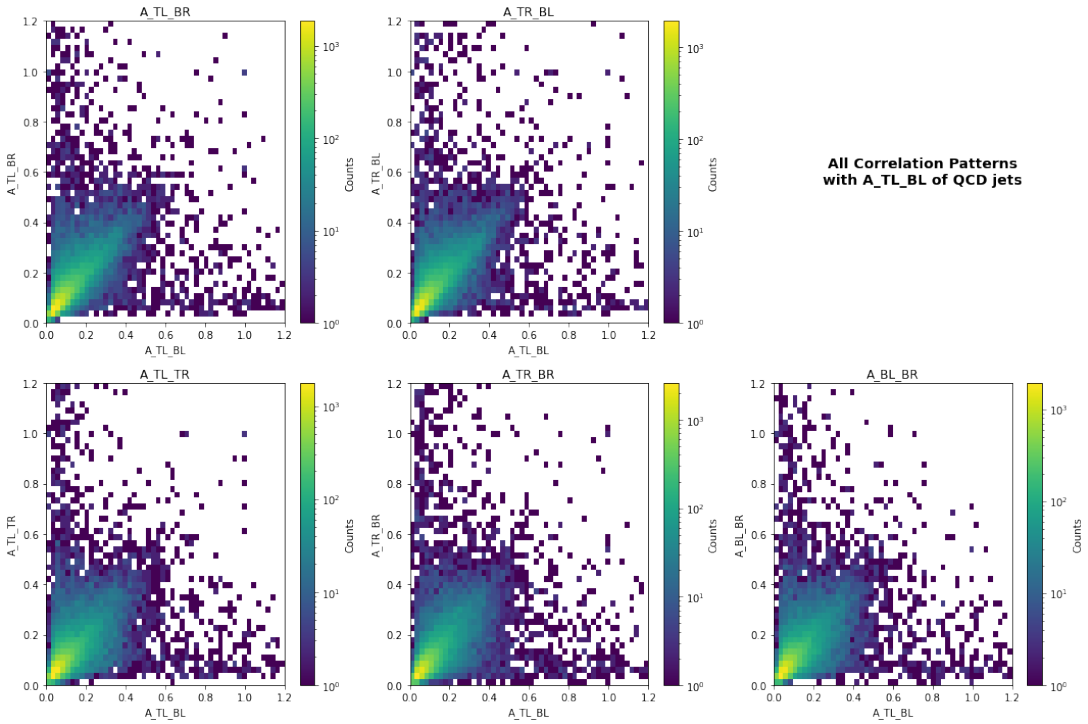


Figure 5.31: 2D histograms of correlations of the asymmetry axis TL-BL with the 5 other axes. Computed for QCD jets. The correlations remain similar no matter the combination of axes. This reflects the homogeneity of the energy deposit.

5.7.3 Limitations

Implementing metrics such as A_{evt} values and constructing high-level variables that reflect the most the Quad-Ring asymmetry sensitivities remains a complex task. Such high-level variables struggle to incorporate all the non-linear correlations between the possible axes or the correlations between rings, especially in different layers. Additionally, factors such as the normalization and the definition of weights could be more complex and maybe energy-dependent. For instance, the current definition of weights does not take into account that a given layer shows a higher absorption power than another. This has negative impacts; in fact, looking back to figure 5.26, one can see that the EM1 rings have low weights. The EM1 signal contains a great amount of information that the first definition of weights is using sub-optimally.
Investigating the ring noise levels would also significantly improve the measures of asymmetry. It is important to note that up until now, different pile-up profiles have not been investigated to verify how the pile-up jet pollution can bias the asymmetry assessment. To conduct such studies, different ESD files must be reproduced.

All these factors define a complex optimization problem. The chosen metric A is to be interpreted as a reference showing the potential of Quad-Rings to read asymmetrical energy deposits and to be used in tagging strategies. Other tools capable of extracting the important features from Quad-Rings could enhance the sensitivity of taggers to double-body showers. ML tools will play a role in defining the optimal asymmetry variable, as shown later.

5.7.4 ML tool

A first MultiLayer Perceptron (MLP) was built under Pytorch to classify between 9GeV ALP decays (with life-time maximizing decays in calorimeters - medium life-time 4.5) and prompt single QCD jets. The inputs are the 6 A values corresponding to the 6 axes of figure 5.21 along with the Pt of each jet or ALP. It is important to consider the momentum as the photon collimation effect is directly linked to the boost. The correlation differences between the input variables will be used by the MLP to classify the two shower types.

Recapitulation on MLP classifiers

An MLP is a type of neural network consisting of multiple layers of neurons: an input layer, one or more hidden layers, and an output layer. Each neuron in one layer is connected to every neuron in the neighbor layers, with weights assigned to each connection. MLPs use a process called backpropagation to adjust each weight according to its impact on the classification error. Thus allowing the network to learn from an input sample and improve its predictions. These ML models can capture complex correlations through their multiple layers, with very complex data structures to learn, requiring a larger network.

Model Description

This paragraph describes the first ML-model hyper-parameters, which have followed some optimization procedures; however, different MLP architectures are to be investigated to

understand how much information can be decorrelated from all asymmetry inputs.

7 Inputs : pT, A_{tr_bl}, A_{tr_br}, A_{tl_bl}, A_{tl_br}, A_{tr_tl}, A_{br_bl}.
Inputing the momentum value of each jet is a key concept to be utilized as higher energy particles create more focused showers. This directly impacts the overlap of the two photons in the ALP case.

Hidden Layer 1: This layer consists of 16 neurons with a TanH activation function. Its primary objective is to build and capture complex correlations between the input features, allowing the model to understand intricate patterns.

Hidden Layer 2: In this layer, there are 8 neurons, also utilizing the TanH activation function. The main purpose here is to condense the learned features into principal components, simplifying the representation of the problem while preserving essential information.

Output Layer: The output layer contains a single neuron that produces logits. There is no activation function applied at this stage, allowing the model to output raw values that will be passed to the loss function.

Loss Function: The model uses the BCEWithLogit loss function, which combines a sigmoid activation with Binary Cross Entropy (BCE). This approach is particularly effective for binary classification tasks, ensuring the model's outputs are probabilistic. The sigmoid function allows for the output distribution to be between 0 and 1, which are the target values for Jets and ALPs, respectively.

Optimizer: Adam, a popular optimization algorithm, is employed to adjust the weights during training. It combines the advantages of two other extensions of stochastic gradient descent (AdaGrad and RMSProp) and is well-suited for handling sparse gradients on noisy problems.

Weight Initialization: The weights for each layer are initialized using a uniform distribution, where the range is determined based on the number of input connections to each layer. This method helps in starting the training process with weights that are appropriately scaled, ensuring effective learning and faster convergence.

Training process

This simple ML classifier was trained on 40k QCD jet events as background and 10k ALP signal events selected with the same Pt range. Class weights were applied to face the statistical imbalance between both categories. This low number of events is due to the difficulty of integrating the alternative Caloring workflow into the ATLAS pipeline that would allow a large production. The learning rate value was fixed to 0.005 and the training was interrupted after 500 epochs of weight updates. Future ML developments for the ALP search will consider larger training datasets and hyperparameter tunning such as

the learning rate and the number of training epochs. Additionally, non-binary classifiers will be developed using datasets with three categories to include single photons.

Resulting discriminator

The MLP output distribution for the two categories was plotted using data points from the test set. To ensure an unbiased evaluation of the model, the test set and training set were built with no overlapping events. Figure 5.32 demonstrates how a simple neural network, utilizing asymmetry inputs, can effectively distinguish between the two types of events. This highlights the significant differences in energy deposits between single and double objects that can be used in ATLAS. One can guess that a selection cut around 0.6 will allow a high efficiency of ALP identification with a low fraction of background jets passing the cut.

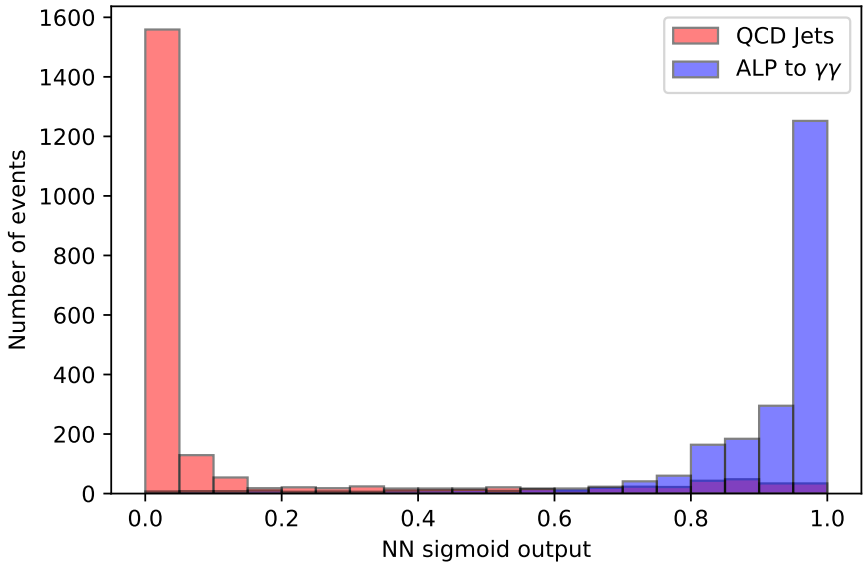


Figure 5.32: MLP classifier output distribution of ALP and QCD jet events. A clear and important separation between the two classes is visible. The raw output is processed in a sigmoid function to represent the prediction.

The table 5.3 shows the importance of each input. In fact, it was obtained by computing the average of the weights connected to each input neuron. It shows that the diagonal asymmetry axes (TR-BL and TL-BR) are the most impactful inputs regarding the prediction as they contain information on the double photon orientation in the calorimeter layers.

The performance of the developed machine learning tool can be assessed using the Receiver Operating Characteristic (ROC) curve. This curve offers a straightforward method for evaluating a classifier's efficiency by examining the balance between true positive rates (correct classification of ALP events) and false positive rates (incorrect classification of jets). These rates are determined by scanning different selection thresholds, producing a list of both rates. The effectiveness of the classifier is typically measured by the area under the ROC curve (AUC), with a larger area indicating better performance.

Input Variables	Weight
pT	3.0
A_{TR_BL}	6.1
A_{TL_BR}	9.1
A_{TL_BL}	1.9
A_{TL_TR}	1.9
A_{TR_BR}	1.8
A_{BL_BR}	2.7

Table 5.3: MLP final average weights connected to the input neurons.

Figure 5.33 shows the ROC curve for the presented MLP model. The $y = x$ line represents the performance of a random guess classifier. The farther the ROC curve deviates from this line, the more reliable the classifier is. The associated AUC is close to 1 (0.97), which confirms the overall strong performance of this simple model.

These preliminary results from a simple MLP demonstrate the potential of more advanced architectures reading Caloring-based variables. Improved classifiers that consider additional backgrounds and multiple ALP mass points could become highly effective taggers for the LL-ALP search.
Additionally, such tools could be directly applied to $h \to aa$ searches, where there is no strict pre-selection of events as in $h \to Za$ searches, due to the Z boson decay.

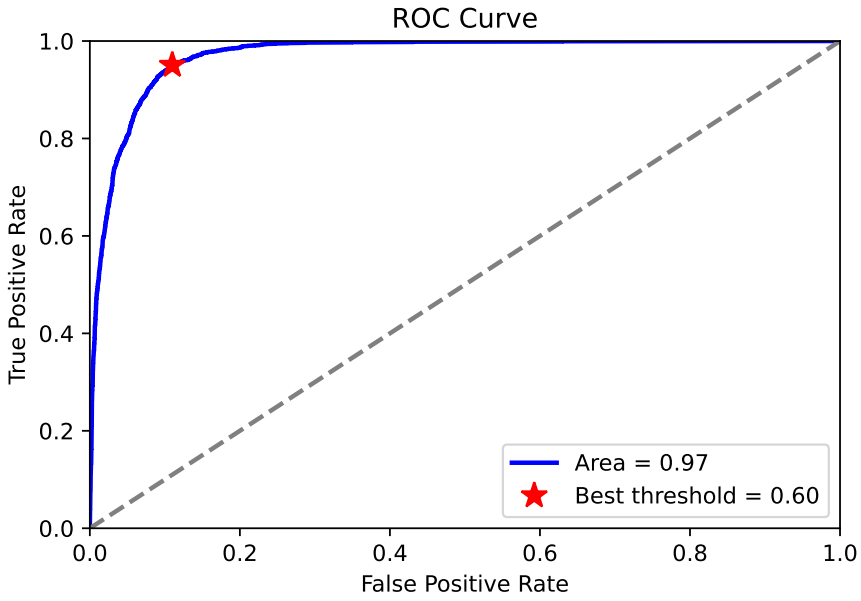


Figure 5.33: The ROC curve of the MLP classifier using asymmetry inputs. The dashed line illustrates the random guess performance. The best threshold is computed by maximizing the difference between signal and background efficiencies.

5.8 Conclusion and perspectives

Chapter 4 presented the reasons that force LLP searches to use radically different workflows. Commonly used tools, reconstruction algorithms, and trigger systems underperform when facing decay displacements. LLP strategies rely on lower-level variables and looser working points to build special selection criteria. However, these still rely on information available at the analysis-file level.

New ways of describing showers are needed for LLP searches, as classic shower shapes were built to represent features of non-displaced particles. The presented studies promote the Calorings used at the high-level trigger to the offline analysis level. These variables show promising results for the different challenges expected in the displaced $a \to \gamma\gamma$ analysis.

This project has demonstrated that Calorings-based variables show sensitivity to double body clusters and to the ALP decay position in the calorimeters. Their asymmetrical extensions (Quad-Rings) bring a new measurable quantity that can be utilized to further amplify the sensitivity to double body showers and might offer an invariant mass regression of merged photons. Important correlations have been established between the ring energy distribution and the decay position of an ALP inside the calorimeter. A possibility to regress the secondary vertex position of an LLP decaying in the calorimeter is now open for in-depth investigation. This is a considerable conclusion as current techniques to find displaced vertices are limited to LLP decaying into charged particles in the tracker. Being able to regress the decay position with Caloring-based techniques would significantly improve the sensitivity of DV searches to higher L_{xy}.
Essentially, this advancement in calorimeter utilization for shower description can greatly augment ATLAS sensitivity to many LLP signals.

Furthermore, the studies that were conducted show a good rejection of prompt QCD jets, and future tagger developments show the potential to be highly performant in detecting the very exotic showers expected by such ALP decays. Very preliminary studies, including single-photon backgrounds, are being conducted but are currently limited in statistics to bring any conclusion. This illustrates an important bottleneck in conducting such investigations in ATLAS. In fact, the ATLAS data flow used to perform the analysis remains very standardized. LLP searches often require larger derivation files as they add lower-level information to develop their strategies. However, building new variables from calorimeters requires access to much lower-level detector files containing cell-level information. To counter this, a private Athena package - EventReader - was developed, but it can only be used to build private samples using limited resources. Thus, this poses an additional complication for concept-proofing new variables.

Using Calorings at the offline level offers a lot of possibilities that can be exploited in complex ML tools. The asymmetry studies already show some classifying potential with simple asymmetry inputs and a small size NN, which could typically be investigated for merged-photons trigger projects. However, a larger NN could extract relevant complex features from the rings and could specialize in photon and QCD jet classification, dis-

placed signal identification, double body clusters identification, or even di-photon mass regression. All these tools can greatly impact the feasibility of LL-ALP searches in ATLAS if added to the ATLAS reconstruction pipeline.

Once such tools are implemented and validated, a potential new trigger algorithm could be defined to exploit dual body decay shower asymmetries. Recent CMS presentations from ICHEP 2024 [193] show how new triggers have been developed utilizing the hadronic calorimeter's segmentation and timing properties. These triggers are now being utilized for LLP run 3 analysis in CMS. A novel LLP trigger chain based on the new results obtained in this thesis would greatly benefit ATLAS LLP searches in the BSM physics plan for run 3 and at HL-LHC.

Chapter 6

Recasting an ML-based SUSY search

Recasting refers to the process of reinterpreting existing experimental results in the context of new theoretical models or hypotheses. It involves reproducing existing searches conducted on experimental data and comparing their results with simulated events generated from different theoretical scenarios. For instance, a given published ATLAS BSM search looking for a specific model can be recast by the phenomenology community by effectively replicating the results in a recasting framework. Of course, this is only possible when the material published in the main paper and auxiliary resources are sufficiently detailed. A recast analysis tries to reproduce as much as possible all aspects of the experimental search to be validated. Then, the results can be reinterpreted by inputting a new untested model. The ultimate purpose is to assess the compatibility of experimental data with various theoretical models. By applying recasting techniques, hypothesis testing can be conducted to see if new models are consistent with the observed results or if they are excluded. Furthermore, phenomenologists can modify or build new theories based on what the recasting process yields. Many existing tools are accessible for recasting LHC analysis in straightforward ways using simulated truth samples as inputs. These are described in this Chapter.

An important study conducted during the PhD involves the implementation of Machine Learning (ML) features into the recasting framework developed by the Laboratoire de Physique Théorique et des Hautes Énergies (LPTHE) for ATLAS and CMS BSM analysis. This work was carried out through an ANR (Agence Nationale de la Recherche) collaboration focused on multiple projects related to dark matter with long-lived particles (LLPs) in ATLAS searches, greatly involving phenomenologists from LPTHE.

In this chapter, we explore the various aspects of the project, explaining the significance and implications of recasting analyses. New results will be presented by incorporating ML features into the Madanalysis5 framework [194] [195], providing insights into its efficiency and potential implications for future investigations. This addition of ML functions is done through the ONNX inference tool. Furthermore, we address the importance and practicality of providing comprehensive auxiliary information essential for accurately reproducing all significant findings when a CMS/ATLAS analysis becomes publicly available. This includes ensuring correct legacy pseudo code, accurate descriptions of event selection criteria, and tagging efficiencies, among other aspects [196].

6.1 Recasting Frameworks

Various software tools and frameworks are available to facilitate the reproduction of experiment searches and allow the testing of multiple hypotheses. These tools are built to work with generated truth data and involve transfer functions in simplified detector simulations [197] [198] rather than replicating the complete reconstruction chain found in official ATLAS files. These techniques effectively implement efficiencies, which can be dependent on variables like transverse momentum (pt) or pseudorapidity (η), for tasks such as tagging b-jets or reconstructing photons. Official MC simulation production of experiments such as ATLAS relies on a precise emulation of the detector and the created signal. However, recasting frameworks rely on the utilization of more straightforward methods as a large amount of experiment information remains unpublished. FastSim, short for fast simulation, is a computational technique to approximate the behavior of the detectors quickly. Unlike detailed, resource-intensive full simulations using GEANT4 [199], it simplifies and accelerates the simulation process by using parameterized models and approximations. This allows for rapid testing and analysis of theoretical models against experimental data, facilitating more efficient studies in particle physics.

As ATLAS software, analysis frameworks define many physics-reconstructed particles/jets or truth-level objects as C++ classes. For example, in AOD (from ATLAS event data model [200]) files, one can find objects such as jets, truth particles, vertices, reconstructed photons or electrons for different reconstruction working points, and more.

Let's take the case of jet objects. They are typically defined as structures or classes that encapsulate various properties of physical jets. These properties may include:

- Kinematic variables: such as transverse momentum (pt), pseudorapidity (η), azimuthal angle (ϕ), and energy.
- Identification criteria: such as jet flavor (e.g., b-jet, c-jet), jet quality flags, and jet substructure variables.
- Associated objects: such as tracks and other particles clustered within the jet.
- Additional information: such as jet area, jet mass, and jet energy resolution.

These properties are computed based on inputs from particle-level-truth information (e.g., from MC simulations) or reconstructed data (e.g., from detector signal). The specifics of how jet objects are defined can vary depending on the software used and the specific analysis. The objective of recasting frameworks is to mirror the precise structures utilized in analysis frameworks to represent and manipulate jets and other objects efficiently.

Recasting frameworks, predominantly written in C++, are object-based and incorporate important main structures, functions, and objects. From 4 momentum vectors associated with particles and important vector transformation functions, any complex kinematic variable can be built. Objects such as jets, photons, and other particles have related structures. These structures can compute Lorentz boosts, access energy, invariant mass, spatial orientation (η, ϕ), and perform transform functions to simulate reconstruction inefficiencies. A robust recasting tool seamlessly integrates with intrinsic objects,

all essential parameters, and methods utilized in a conventional HEP analysis. Overall, they offer a compact and efficient means of imitating analyses on simulations using quick, modifiable scripts that can be reused multiple times to test various hypotheses and models.

Summary of Main Recasting Tools:

- **CheckMATE:** A tool that takes simulated event files in .hep or .hepmc formats for any model and determines whether the underlying model is "excluded" or "allowed" after performing a detector simulation and testing various implemented analyses. [201]

- **MadAnalysis5 :** A user-friendly framework for phenomenological investigations at particle colliders, featuring a growing collection of LHC analyses within its Public Analysis Database [202]. These analyses have been implemented in the MadAnalysis5 (MA5) framework for recasting, with detector simulation provided by Delphes3 [198] or SFS (simplified fast simulator) [197]. (Note: MadAnalysis5 will be the focus of this study.) [203]

- **Rivet:** Initially developed for validating Monte Carlo event generators, Rivet has evolved into a standard for documenting SM measurements. It now includes detector-smearing transform functions, making it suitable for recasting BSM searches as well. [204]

- **Gambit:** A global fitting code for generic BSM theories, Gambit includes modules for collider searches, flavor physics constraints, dark matter constraints, spectrum generation, decay rates, precision tests, and statistical algorithms. [205]

- **SimpleAnalysis (SA):** An analysis framework developed by the ATLAS Supersymmetry (SUSY) group/ It has been used to reinterpret ATLAS SUSY results since 2016 and is now available with a public version. The ATLAS SA (non-public) software provides extra features and access to internal information describing the efficiencies of many reconstruction working points and other effects. [206]

Furthermore, the typical protocol for utilizing these frameworks and reproducing analysis code is presented below. The list of key steps is :

- **Identifying key analysis parameters:** Utilizing shared auxiliary information and details from published papers, the first step involves understanding the precise cutflow the data undergoes. The primary definition of important high-level variables must be perfectly understood, and their value thresholds for signal rejection must be identified. The quality of this step heavily depends on the level of detail in the published material. Otherwise, exchanges with the analyzers are necessary.

- **Detector modeling:** The fast simulator of detectors offers high parametrization. For a given analysis recasting project, the particle reconstruction and flavor tagging efficiencies are investigated in performance papers to determine how they perform with respect to pT and η. This step is crucial as truth objects are approximated to reassemble the reconstructed objects used in the experimental analysis.

- **Reproducing Analysis procedure:** The analysis code is then reproduced in the recasting framework. If variables and functions remain internal to the experiment, approximations using available information are implemented. This is often the case for many-particle identification criteria that depend on multiple parameters that are opaque to the public.

- **Generating benchmark Samples:** BSM analysis is often interpreted within a paper following a given benchmark model. It is necessary to reproduce samples corresponding to the same model and evaluate the recast signal regions with respect to the expected ones. For this, the parameter-space points of the model chosen by the analyzers must be correctly defined.

- **Comparing Results:** Cutflows or other results obtained from the recast analysis are rigorously compared with those from the original experiment. All main histograms, exclusion limits, and curves from the analysis are reproduced on the same benchmark model.

- **Validation :** If the recast results closely align with the analysis ones on the same benchmark model, the recasting script is validated. This confirms its accuracy and reliability for reinterpretation projects.

- **Testing Alternative Models:** With a validated script, one can then proceed to test alternative models by altering the input samples, further exploring hypotheses and theoretical frameworks.

- **Constraining Models:** If the recast results of a given new model are not in agreement with experimental data, they can be excluded. This significantly aids in the elimination or refinement of many theories and is an essential tool to develop others.

The rest of this chapter will illustrate the application of this protocol within MadAnalysis 5 to recast a SUSY R-parity-violating analysis conducted on run 2 data from ATLAS [207]. The particularity of this analysis lies in its utilization of machine learning tools, which are often opaque for the phenomenology and the theory community and considered as a "black box". This poses a significant challenge for the future of particle physics, as such tools increasingly play a significant role in data analysis, capturing the intricate complexities of experimental data and reflecting essential aspects of BSM signatures that are otherwise difficult to discern. This issue shows the importance of ensuring compatibility between recasting tools and ML techniques, as well as the importance of analyzers in sharing ML-related material. Nevertheless, even with access to ML files from the original analysis, crucial information may remain undisclosed in publications, rendering recasting validation challenging. The importance of understanding data preparation and transformation before input into neural networks, as well as the interpretation of neural network outputs, can often be overlooked in papers. However, there is a growing trend among ML-based analyses to share auxiliary information, including Neural Network architectures and weights. This is often done using a specific ML file-sharing format such as ONNX [208], Pytorch [209], Petrify-BDT [210], or using custom XML from ROOT TMVA library [211]. The subsequent section will focus on the integration of machine

learning capabilities as a new feature within the MadAnalysis 5 framework, with a focus on its application to the already mentioned SUSY analysis.

6.2 Developing ML capabilities in MadAnalysis5

In recent years, many projects have been developed to address the challenges associated with interoperability and portability of deep learning models across different platforms and languages. These projects led to efficient file formats and their related interfaces that can save and deploy pre-trained models. Such tools are perfect for the recasting framework since a completely implemented ML library is not necessary. In fact, since reproducing and retraining models is nearly impossible, the essential functionality for a recasting framework is to load the exact trained models used in the original analyses rather than attempting to recreate them using complete ML libraries. This would demand a problematic training process to achieve similar final networks. This section will present the ONNX interface and explain how it was implemented inside Madanalysis5.

6.2.1 ONNX

ONNX, for Open Neural Network Exchange [208], is a Microsoft project launched in 2017 and which has become a major API (Application Programming Interface) in the machine learning domain. As an open-source initiative, it is nurtured by a collaborative community comprising contributors from diverse organizations and individuals advancing machine learning. Functioning as a universal framework for deep learning model representation, ONNX facilitates seamless interoperability across various platforms and frameworks. This enables researchers to train models in one framework and deploy them in another, obviating the need for redundant implementation efforts. By standardizing model representation, ONNX improves collaboration with ML research and development. In essence, ONNX catalyzes expediting the development and deployment of machine learning solutions, offering a shared language for model exchange.

This API is increasingly utilized within the Atlas analysis communities as an efficient means of sharing the exact model in the auxiliary material.
A set of ATLAS analysis sharing ONNX material is presented below :

- **ATLAS-SUSY-2019-04:**
  - Search of R-parity-violating supersymmetry
  - Published trained networks in ONNX format on HEPData.
  - Uses 64 high-level variables plus a continuous b-tag score.
- **ATLAS-SUSY-2018-30:**
  - Search for supersymmetry in final states with many b-jets
  - Published trained NN in ONNX format.
  - SimpleAnalysis code details input variables and their normalization.

- **ATLAS-EXOT-2019-23:**
  - ATLAS search for neutral long-lived particles
  - Published ONNX records of NNs and standalone executables of BDTs on HEPData.
  - Provides 6-dimensional efficiency maps for public use.

Another crucial aspect of leveraging ONNX for Atlas analyzers is the ability to develop and train models in powerful environments that provide access to machine learning libraries like PyTorch or Keras and subsequently save them as .onnx files for integration into C++ code. This .onnx can encapsulate the model's architecture, input and output layers, relevant information, all weights and biases, and the activation functions. Given that many analyses are written in C++ for speed convenience or necessity because of ROOT, Athena, or other dependencies, ONNX offers the capability to load these essential model files into such environments quickly. Otherwise, analyzers should use the implemented MVA (Multivariate Analysis) tools present in the ATLAS analysis software ecosystem based on C++.

6.2.2 ONNX Runtime

ONNX Runtime (ORT) [212] is the main component in the ONNX ecosystem, designed to execute ONNX models across various hardware platforms efficiently. It provides a runtime environment optimized for running models with high performance and low latency. This API enables the deployment of ML models in various environments, ensuring consistent and reliable performance across different operating systems and devices. This process is referred to as inferencing. ORT is considered an inference engine. ORT also supports a wide range of hardware accelerators, including CPUs, GPUs, and special inference chips. Thus allowing each user to leverage the full potential of their hardware infrastructure. Its flexibility and scalability make it an essential tool for deploying machine learning solutions across diverse use cases. In essence, ONNX Runtime empowers developers to unlock more potential of their ONNX models and deliver efficient machine learning applications.

ONNX Runtime is available in multiple programming languages, including C++, Python, and C# [212]. This ensures compatibility with a wide range of development environments and platforms, allowing analyzers and other users to integrate ONNX models into their applications. In fact, to load and execute ONNX files containing pre-trained models, one only needs the runtime API. There is no need for additional dependencies or complex setup procedures. This streamlined approach simplifies the deployment of machine learning solutions, enabling users to leverage the capabilities of models and implement them in existing frameworks in a straightforward way. Furthermore, the ONNX Runtime API is very compact; in fact, for a given programming language and a given OS platform, the API can be run only by using a very low number of files. Let's take the example of the API for C++. One only needs to link the correct library and include one header file in the compilation to unlock the loading and running functionalities of ML models saved in the .onnx files.

Implementing this API inside the Madanalysis5 framework implies that one can load models saved as .onnx files. This is an essential step for the recasting framework because it opens up the opportunity to reproduce ML-dependent cutflows. Many ATLAS/CMS analyses utilize ML algorithms, and the phenomenology community needs to open reinterpretation frameworks for ML. Furthermore, taking into account the complexity of modern LHC data taking and the future searches that will be conducted in the subsequent runs, one concludes that ATLAS and CMS analyses must maximize the transparency of ML implementation. By sharing the models with tools like ONNX, the reinterpretation potential and utility of the results are greatly enhanced.

6.2.3 Madanalysis SampleAnalyser

Madanalysis5 has two main operating methods: manual and expert. The first method is a user-friendly version capable of analyzing input samples by defining signal regions, building variables and applying cuts, creating histograms, and outputting statistical results. This method is operated through a specific MA interpreter. The interpreter is controlled via a terminal and is a simple Python interface to the core of the recasting framework called SampleAnalyser running on the back end. When commands are applied to the interpreter, a C++ file is generated and executed with SampleAnalyser. This C++ analyzer kernel is optimized for recasting software needs. MA5 expert mode is more similar to standard analysis frameworks used in ATLAS or CMS. It gives the user more freedom and the possibility to create complex functions. Operating in expert mode is done by writing a main script in C++, which will be added to the SampleAnalyser compiling sequence.

As one can see in figure 6.1, the two main components, the interface, and the SampleAnalyser kernel, collaborate at various stages in the standard operational mode. In expert mode, the user directly implements the analysis inside the recasting kernel. This expert mode offers the possibility to include other header and C++ files as well as add new libraries in the compiling sequence by changing the Makefile. Essentially, the expert mode operates as a classical C++ analysis framework.

Using the simple mode with the interface, one can do fast phenomenology studies. In contrast, a full ATLAS or CMS search recasting is done in expert mode due to the possible high levels of complexity. The flexibility of the expert mode, together with the compactness of the ORT API, provides a straightforward implementation of ML functionalities.

By manually including the necessary libraries in the SampleAnalyser compiling sequence, one can obtain new features and get interesting results, as shown in figure 6.2

6.2.4 Madanalysis packages

In Madanalysis5, whenever an expert mode analysis is set up, an automatic makefile is built. This Makefile guides the compilation of the SampleAnalyser script to build an executable madanalysis job. Through such a make-file, one can manually add all necessary files and libraries to add functionalities from other software. After verifying compatibility between compiler versions and OS architectures, ONNX can be integrated straightfor-

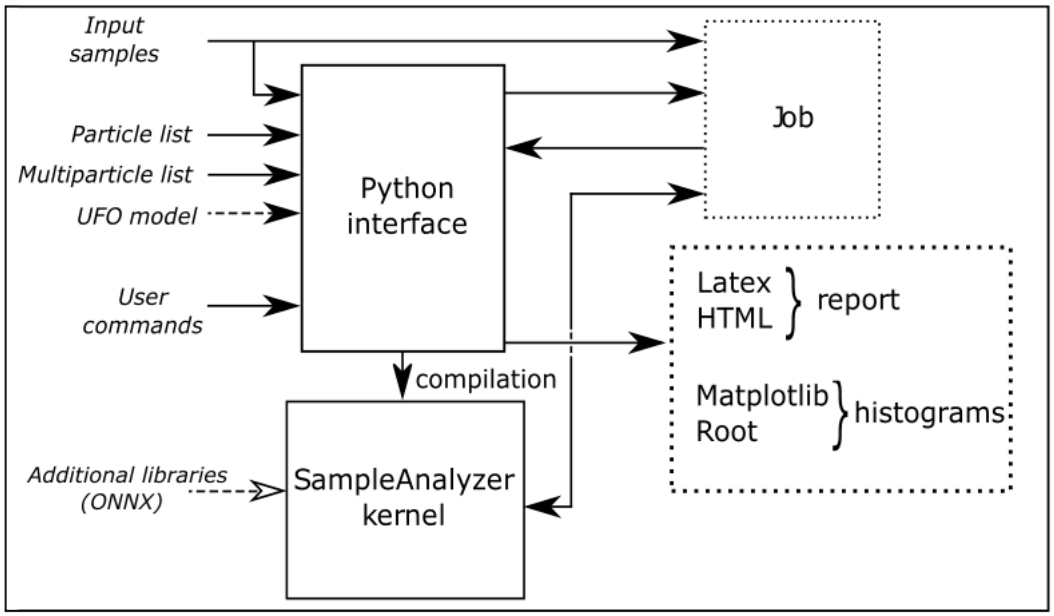


Figure 6.1: The madanalysis5 manual mode flowchart. Additional libraries can be added to the SA kernel manually. However, recent developments have directly included ORT within the framework.

wardly by modifying the SampleAnalyser makefile. However, this approach is not very user-friendly since it requires each user to download the appropriate ORT API files and add them to the Makefile with the associated private paths.

Madanalysis5 offers the possibility to download, install, and set up multiple optional packages to add functionalities to the SampleAnalyser kernel. These optional packages include analysis-specific algorithms for object reconstruction (FastJet) [213], libraries designed for statistical modeling and hypothesis testing (pyHF) [214], utilities for compressing and decompressing data in various formats (Zlib) [215] and more.
Some of these functionalities are primordial for recasting certain ATLAS and CMS analyses, and users need to have a simple, user-friendly way to import and use them. These optional packages are downloaded, installed, and configured for madanalysis using a single command in the interpreter on manual mode. The MA5 source code was modified to accommodate one more optional package: ONNX Runtime API.

From ONNX's GitHub page [208], a compressed file for every published ONNX release version can be downloaded. It is important to note that the ONNX file depends heavily on the platform in which it is being deployed, i.e., the operating system and CPU/GPU architecture. It is also important to notice that different ONNX libraries must be downloaded if one wants to do standard inference, GPU utilization, model training acceleration, etc.



Figure 6.2: New impressive feature of MA5 using pre-trained NeuralNetworks and ONNX.

Checking the system platform when launching madanalysis5 enables one to save relevant architecture information of the user machine. The information is used to determine the correct ONNX files to be downloaded and added to the SampleAnalyser core. Currently, MA5 supports inference on CPU resources for both Linux and Mac operative systems. In the future, other options can be added to select a specific ORT release or install training libraries and possibly GPU hardware utilization during inference and training.

Madanalysis 5 is finally set up to use ML functionalities straightforwardly. A user needs to prompt *install onnx* in the interpreter to download and correctly set up the appropriate ONNX version and libraries for their system. This provides quick access to ML model inference using CPU on both Linux and Mac machines and creates the possibility of recasting ML-based analyses.
Nevertheless, to assess the feasibility of using ONNX in Madanalysis 5 for reinterpretation projects, it is essential to recast an ML-based analysis effectively. The rest of the current chapter addresses this task.

6.3 Recasting an ML-based SUSY search

The ATLAS analysis used for concept proving the recasting of ML-based searches in Madanalysis5 is a search for R-parity-violating (RPV) supersymmetry [207]. The search was conducted using $139 fb^{-1}$ of run 2 data and targets events with a high jet multiplicity, at least one isolated lepton, and either zero or at least three b-tagged jets. The search was interpreted in the context of multiple SUSY RPV models, including different SUSY particles.

6.3.1 R-parity and R-parity Violation

R-parity is a discrete symmetry in the Minimal Supersymmetric Standard Model (MSSM) defined as:

$$R_p = (-1)^{3(B-L)+2s} \tag{6.1}$$

where B is the baryon number, L is the lepton number, and s is the spin of the particle.

R-parity has two primary consequences: Proton Stability and ensuring a Dark Matter Candidate.
R-parity prevents rapid proton decay by forbidding terms that violate B and L, which allow proton decay at rates much faster than the observed limits. R-parity conservation also ensures the stability of the Lightest Supersymmetric Particle (LSP). This allows the LSP to be a viable dark matter candidate since it cannot decay into SM particles. In typical Supersymmetric (SUSY) scenarios, signals often include the production of heavy superpartners of Standard Model particles, which promptly decay into a cascade of lighter supersymmetric particles. A key feature of SUSY signals is the presence of large missing transverse energy (MET) due to the undetectable Lightest Supersymmetric Particle (LSP), which escapes the detector. Other characteristic signatures include high-energy jets, leptons, and possibly photons, depending on the decay chain involved

However, RPV searches are conducted as an alternative way to probe SUSY. The associated processes can yield unique signatures. When R-parity is violated, the possibility of the LSP, such as a neutralino, decaying into SM particles becomes possible. Additionally, the associated couplings can result in processes that violate the baryon number (B), leading to a high jet multiplicity in the final state. The decay of the LSP can be represented as:

$$\tilde{\chi}_1^0 \to \text{jets} + \text{leptons} \tag{6.2}$$

where $\tilde{\chi}_1^0$ is the neutralino, a common candidate for the LSP in MSSM.

Additionally, RPV coupling allows for searches of LLPs where SUSY particles would decay in an SM channel after a macroscopic displacement.

6.3.2 Benchmark models

In the investigated models, RPV couplings and SUSY particle masses are fixed to guarantee the prompt decay of the associated SUSY particles. The models include the gluino, which is the partner of the SM gluon, the stop quark, the partner of the right-handed top quark, and one or more electroweakinos. Electroweakinos are massive fermions formed through the mixing of the partners of SM electroweak and Higgs bosons.
In total, five models yielding different RPV processes were used as benchmark scenarios in the analysis. Results were interpreted in the context of each model. A specific selection channel was implemented for the electroweakino models using neural networks. Figure 6.3 shows multiple Feynman diagrams describing processes induced by the different models leading to the investigated final state.
A reminder on the link between electroweakinos and the neutralino is done below since they are a main component of the target signals.

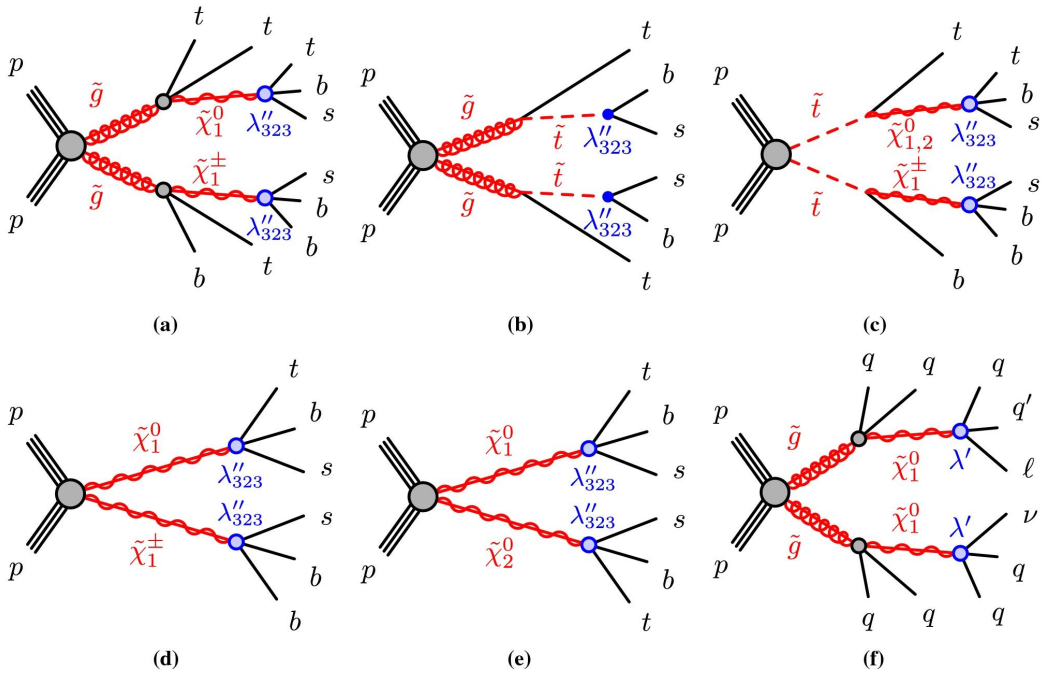


Figure 6.3: From [207]. Several simplified signal models were investigated during the analysis, including gluino, stop quark, and electroweakino decays. Anti-particle notation is omitted.

Neutralino as a Mix of Electroweakinos In the MSSM, neutralinos are the mass eigenstates formed from the mixing of electroweakinos. These electroweakinos include:

- Bino ($\tilde{B}$): The supersymmetric partner of the $U(1)_Y$ gauge boson.
- Wino ($\tilde{W}^3$): The neutral component of the supersymmetric partner of the $SU(2)_L$ gauge bosons.
- Higgsinos ($\tilde{H}$): The supersymmetric partners of the Higgs.

These states mix through a mass matrix to form the four neutralinos ($\tilde{\chi}_i^0$, where $i = 1, 2, 3, 4$), which are the physical mass eigenstates in the MSSM.

This RPV run2 analysis is divided into two main sections. The first part is based on a classical jet counting analysis with cuts on kinematic variables accounting for two of the b-jet event cases with either 0 or 3 b-jets. The second part utilizes ML techniques to improve the sensitivity to signal. Multiple neural networks (NN), representing various jet multiplicity cases, are used as discriminators to separate background events from the signal. The training procedure of these NN classifiers considers electroweakinos samples as signal and $t\bar{t}$ as background. ONNX files for all the NN classifiers were published as well, making this analysis a good choice for the validation of ONNX functionalities in MA5.

The search final results do not provide significant deviations with respect to the SM predictions. No excesses were observed, and exclusion plots were produced for the gluino, stop quark and electroweakino models. Nevertheless, this analysis offers a high reinterpretation capacity since the ATLAS collaboration has published important auxiliary material. This crucial information was to replicate the analysis in a recasting script correctly. The resources cover the ML models as .onnx files, detailed cutflows for each benchmark signal model, and parameter cards to generate the same signal models.

Previous recast attempts were conducted on this search but have failed to reproduce correctly the NN-related cuts [216]. In fact, through informal private communications with the authors, it was noticed that a significant amount of important information concerning the analysis script, the NN, and its input variables was omitted in the paper and the additional public resources. This missing information has a significant impact on the capacity to use the NN discriminators as intended and impeded reinterpretation work from the phenomenology community. Extensive communications have brought up the relevant missing information that enables one to recast the analysis correctly. This highlights the importance of correctly sharing all necessary analysis details for reinterpretation purposes.

The NN-based analysis was recast in madanalysis5, showing low discrepancies when compared to the published cutflows as presented in the result section 6.6.2.

6.4 Signal event generation

Simulated signal samples were generated for the different SUSY RPV models used for benchmarking. The analyzers published, as auxiliary material, the cutflows for each model and parameter cards for event generators. These files are used to correctly parameterize a given generator by fixing relevant masses, lifetimes, and mixtures of electroweakinos and interaction strengths of the SUSY signal. Using these parameter cards with event generators such as Madgraph [217], one can produce benchmark samples, which will be used for validating the recasting script.

Madgraph is often used in conjunction with other software like Pythia8 [218] for shower development modeling, and SFS [197] is taken for detector simulation, respectively. When used in conjunction, one can provide a complete simulation of ATLAS-like events. A list of the main steps accomplished by each software is presented below.

1. **MadGraph [217]**:

    - **Feynman Diagram Calculation**: Feynman diagrams are generated from the parametrization of the model of interest based on user-specified processes. Models are typically provided in the Universal FeynRules Output (UFO) [219] format, which includes the necessary information such as particle content, interactions, and parameters. The UFO format is widely used in high-energy physics simulations, allowing for easy import and manipulation of models in various Monte Carlo event generators.

- **Matrix Element Generation**: generates matrix elements corresponding to the calculated Feynman diagrams, representing the probability amplitudes for different interaction outcomes.
- **Event Generation**: MadGraph utilizes matrix elements to generate hard-scattering at parton-level event samples, including information about the types of particles involved and their momenta, and performs particle decays, with MadSpin [220] ensuring proper treatment of spin correlations in the decays.

2. **Pythia [218]**:

   - **Parton Showering**: Pythia takes the parton-level event samples generated by MadGraph and simulates the emission of additional partons (parton showering) due to QCD radiation.
   - **Hadronization**: It models the process by which partons fragment and combine to form protons, pions, kaons, and other possible hadrons
   - **Underlying Event Simulation**: Pythia also simulates the additional soft interactions between particles in the collision environment.

3. **Delphes [198]**:

   - **Detector Simulation**: Delphes takes the simulated particle-level event samples from MadGraph and Pythia as input and provides a simplified response of a particle detector. This includes the tracker, which calculates the particle propagation and the associated tracks, and the calorimeters using configurable layer granularity and energy resolution dependencies to stochastic, constant, and noise terms.
   - **Particle Reconstruction**: Finally, it reconstructs the observed particles based on the simulated detector response, including their energies, momenta, charges, and types. Allowing for different jet reconstruction algorithms.

4. **Simple Fast Simulator (SFS) [197]**:

   - **Differences from Delphes**: SFS also performs detector simulation using the transfer function, and it does particle reconstruction implementing transform functions. However, it is designed to be faster and less complex, offering flexibility for quick studies and prototyping.

To produce signal samples for recasting the full detector simulation step, as done in Geant4 by considering radiation lengths and other particle-material interactions, is not necessary. Using Madanalysis5, the detector, object reconstruction, and tagging efficiencies are effectively reproduced with simpler techniques. In general, transform functions techniques can be applied to account for uncertainties and limitations of the detector's responses as well as efficiencies of tagging and reconstruction of physics objects. This process involves simply convoluting the true simulated distribution with a probability distribution function (PDF) representing the detection and reconstruction effect. For the analysis of interest studied in this PhD, such techniques were implemented on the b-tagging of jets as presented in the next section 6.6.1.

The neutralino is often considered stable by standard SUSY models. Thus, some tweaking in Madgraph configuration files was necessary to force the neutralino decay by unlocking its width value, usually fixed at 0. Various mass points ranging from $m_\chi = 250$ and 300 GeV were produced since they were used in different benchmarking steps of the analysis (cutflows and exclusion plots). The masses were fixed and set equal between all neutralinos and charginos.

Multiple processes were included by considering all Feynman diagrams offering combinations of neutralinos (χ_1^0, χ_2^0) and charginos (χ_1^+, χ_1^-) :

6.5 NN discriminator

As presented in the first part of this section, the Machine-Learning part of the analysis improves the sensitivity of the search for models involving electroweakino production. The classifiers are used for events presenting one lepton, at least four b-tagged jets, and a total number of jets in the [4-8] range. For each one of the five jet multiplicities, one neural network is used to classify the event between the higgsino signal and $t\bar{t}$ background. This results in 5 independent NN that were trained on different jet-multiplicity signal events. The NNs are simple classifiers with a total number of 65 inputs and one output, which varies from 0 to 1. The inputs are a mixture of simple kinematic variables such as the leading lepton momentum and higher-level variables; for instance, the scalar p_t sum of all jets (H_t); a more detailed description of the input variables is done in section 6.6.1.
Each NN has an associated output cut used for the classification of signal and background events. Events yielding an NN output superior to that specific threshold pass the signal selection. In the analysis flow, these ML cuts are implemented as the last classification criterion, with values of around 0.7 changing between each NN.

The NN training is performed under the constraint that the NN output distribution for the background remains invariant concerning the b-jet multiplicity. This feature is visible on one of the NN output distributions depicted in figure 6.4. This property was utilized to estimate the background from data in the analysis [207]. This distribution varies from what is often represented in NN classifiers. To maximize separation between signal and background the background distribution should peak at 0 while signal one should peak at 1. A flat distribution would mean that the neural network has no preferred output value for this type of input event. However, this effect is due to a choice of binning of the histogram.

The bins in figure 6.4 are defined in the paper as *'four bins of equal width with approximately equal signal fractions'*. This definition lacks the exact bin values used by the analysis team Additionally, the only available NN distribution is represented with this binning Thus rendering impossible the correct reproduction of the histogram and the estimation of the real NN output shape on signal and background.

The bin values were obtained following private communication with the authors. These bins were manually chosen to flatten the signal distribution completely to work with equally populated regions. Additionally, the bins were shown with equal widths in figure

6.4 for visual purposes only. This hides key features of the real distribution, which are crucial to verifying that the reproduction is done properly.

The real width of bins 1,2,3 and 4 are, respectively: **0.52, 0.17, 0.13, 0.19**.
Resulting in the bin limits : bin1 = [0,0.52]; bin2 = [0.52,0.69]; etc.

These values raise more questions as one would expect each bin size to get smaller when going towards 1 for standard signal/background classifiers. In fact, for an optimized classifier, the distribution for signal peaks at one since it is the target. Therefore, to build 4 bins that are equally populated in signal, the bin sizes should decrease while getting closer to 1 to compensate for the distributions ramp up to 1.

These bin values point out the fact that the signal distribution does not peak at 1, suggesting that the target for classifying signal events is lower. This type of information should be included in the analysis paper.

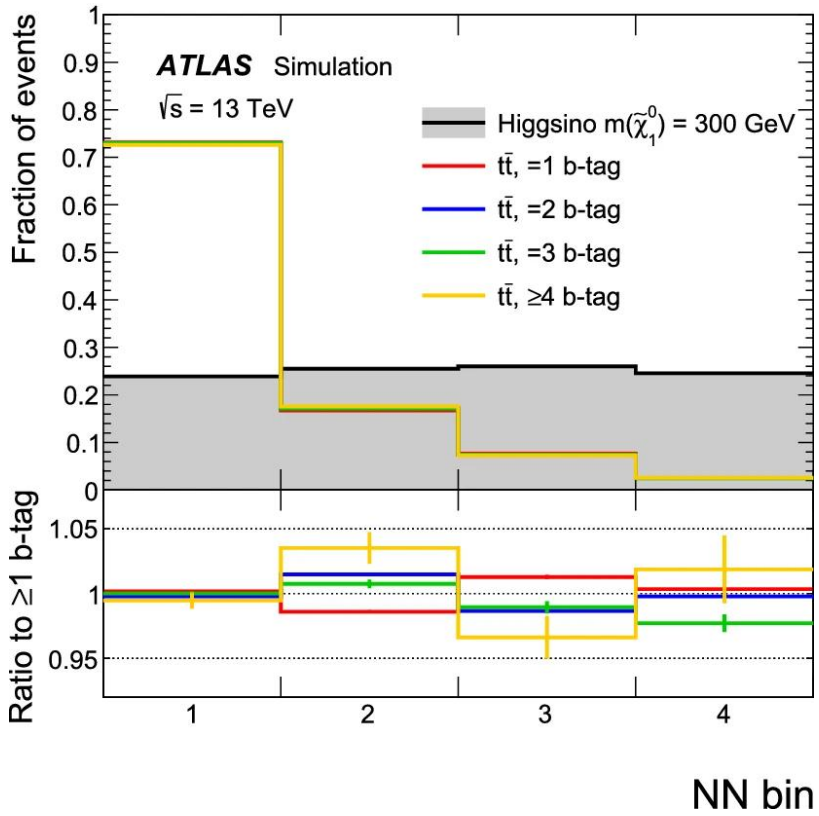


Figure 6.4: From [207]. Distribution of the NN output used for 6 jets events Higgsino signal is set with a neutralino mass of 300 GeV. Background events with diverse b-jet multiplicities peak at low values. Bins are chosen to artificially flatten the distribution.

The exact NN output distribution was obtained through private communications but is still unpublished and remains ATLAS internal information.
Important features of the full NN distribution that were not visible in the "4-bin" version

of the plot were discovered. This was an essential piece of information as it allowed for more rigorous validation of the reproduced distribution in MA5 with the same benchmark signal model.

Multiple communications with the authors brought up a lot of important material. This material is essential to implement a correct replication of the analysis. For instance, the paper mentions a penalty term introduced in the loss function, which is said to optimize sensitivity to the signal. Nevertheless, it is not explained that this term biases the signal classification to peak at 0.8 instead.

The encountered difficulties while trying to reproduce ML-based results show persistent difficulties in many published analyses. The depth of auxiliary resources can often be under-invested, leaving the utilization of the results for reinterpretation projects challenging. This is a significant concern for analysis involving ML tools. ML algorithms are extremely sensitive to how the input information is computed, and they are constructed to work in very specific manners. All information associated with its input and outputs should always be in the published resources to guarantee reinterpretation potential. The next part of this section presents important recast-sensitive steps of the analysis and how some crucial missing information on NN inputs strongly impacts the classifier results.

6.6 Recasting Validation

To ensure that the results are properly replicated, they must be compared to what the reference analysis obtained (for the same benchmark signal). Indeed, the typical workflow includes writing the first version of the analysis script, including all pertinent selection cuts, verifying the obtained results, and then refining the script. Many steps of an analysis are approximated for recasting purposes. Differences can arise from transform functions that are too approximate or from the wrong replication of complex variables. Some cuts can be strongly impacted by these effects. Optimizing these points is crucial to validate the recasting algorithm. Nevertheless, some approximations can reflect a lack of detail in published resources. The impact-full steps and parameters must be understood. Multiple adjustments are made to render these key points. Much closer to what is performed in the reference analysis.

The resource material includes a C++ code snippet [221] showing an example of recasting under the SimpleAnalysis framework. This file is used to better understand the analysis flow and is used as a basis to build a new recasting code in Madanalysis5. This extra material also allows one to understand how the neural networks are used, how input variables are treated, and what selection cuts are applied. This type of additional material is very complementary to the published papers as it encapsulates relevant technical details.

6.6.1 Sensitive steps

This section aims to highlight the main parts of the recasting work that called for important tweaking. Indeed, the approximation of some steps shows a significant impact on the

final outputs. To optimize the recasting script, tunning was performed to imitate better the ATLAS analysis. This was possible mainly by finding additional information.

Input samples verification

The first important part of the full recasting workflow to be controlled concerns the signal samples used as input. As mentioned in section 6.4, parameter cards containing information related to the models used for benchmarking are shared. However, utilizing it for the Higgsino model requires guaranteeing neutralino decays. In most models, the neutralinos are considered stable and do not decay.
Furthermore, after generating the hepmc files, Pythia8 log files can be consulted to verify that neutralinos indeed have daughter particles.

It is of the utmost importance to understand what processes were generated with each signal model to reproduce as closely as possible the input samples used for the benchmarking results. The cutflows, accessible in hepdata [222], indicate the precise processes allowed, but the NN output distribution plot does not. In fact figure 6.4 only mentions that the higgsino signal is using a mass point of 300 GeV for $\widetilde{\chi}_1^0$ By communicating with the authors it was understood that samples associated with this histogram include the three processes: $pp \rightarrow \chi_1^{\pm}\chi_1^0$, $\chi_1^{\pm}\chi_2^0$, χ_1^0, χ_2^0.

It is crucial to ensure that the input samples fed to the recasting script are the same as those investigated during the analysis. Essentially, if the input samples lack a given process, the final yields can become very difficult to compare to the reference. Such situations impede a true assessment of the reinterpretation feasibility.

NeuralNetwork inputs

All 5 NNs associated with the jet multiplicity categories (4 - 8) present the same architectures and have the same input vector. The inputs contain standard variables and custom ones. The following list indicates the 65 variables :

- Number of jets and number of b-jets
- Custom category of b-jet multiplicity.
- Invariant mass of three leading jets system
- Invariant mass of three leading jets + missing momentum + leading lepton system
- p_T sum of all jets and b-jets : H_T and $H_T b$
- Minimum mass difference between jets.
- Missing transverse energy and its azimuthal angle (ϕ)
- All jets : E, p_T, η, ϕ, and custom b-tag score (described lower)
- Minimum ΔR between lepton and jet
- Leading lepton : E, p_T, η, and ϕ

All variables associated with masses, energies, and momenta are normalized to the same energy scale of 100 GeV. It has been demonstrated that NN performs better when using normalized inputs, especially when using energies [223] [224] [225].

Note that all the neural networks have the same number of inputs, no matter the number of jets. Each jet parameter has an associated input. This implies that events with a low number of jets have a lot of "empty" inputs that are artificially set to a low value, which depends on the parameter. This is sub-optimal as the neural network training process, through backpropagation, will consider many useless neurons and their associated weights. It is important to ensure that all jet input variables are set to the proper low value whenever there are not enough jets.

Jet b-tag score

The b-tag score associated with each jet is a pseudo-continuous value representing the confidence in the b-tagging. The scores are linked to different ATLAS b-tagging working points. The paper suggests that they are connected to 5 pseudo-continuous bins delimited by b-tagging efficiencies (described in a b-tagging performance paper [226]). Nevertheless, there is no precise information on how to link a given b-score NN input to the ATLAS pseudo-continuous b-tag efficiency bins.
The only accessible information about this score definition is found in the snippet code of the analysis in hepdata. Here the score is defined as **5** if the jet is b-tagged with 70% efficiency and **1** otherwise.

The first recasting attempts considered the b-tag in this binary approach but have shown unsatisfying results.

Private exchanges with the authors have provided the important missing information concerning this score. The b-scores of each jet follow these different working points (WP) of the DL1r b-tagging algorithm [226] :

1. not tagged with an 85% efficiency WP
2. tagged with 85%, not tagged with 77%
3. tagged with 77%, not tagged with 70%
4. tagged with 70%, not tagged with 60%
5. tagged with 60%

Note that 5 is the highest score, passing the tight working point, while 1 is associated with the loosest working point.

Using Athena and other ATLAS-specific software, one can easily recover which WP a jet has passed for the b-tagging algorithms. However, inside Madanalysis5, the b-tagging is purely based on the true information of the simulations. To represent this tagging efficiency on jets, transform functions on truth b-jets were added. Such transform functions can be dependent on the jet's kinematics. For example, a b-tagging algorithm can lose

efficiency on softer jets or in high η regions of the calorimeter. These effects should be taken into account to imitate the b-tagging behavior of the experiment properly. ATLAS's DL1r algorithm tagging efficiencies have shown an approximately flat distribution, at first order, with respect to P_t and η [226]. Figure 6.5 depicts the evolution of the efficiency with respect to P_t for two different b-tagging algorithms. This indicates that the associated transform functions can remain simple and do not require dependencies on jet kinematics

To effectively simulate the behavior of the b-tagging algorithm for each truth b-jet, a random value between 0 and 1 is generated. This random value is directly used to determine the associated b-score by considering a uniform probability distribution. The number is pulled between 0 and 1. Depending on the value, it will land on a different b-score. Table 6.1 illustrates how each jet is receiving its associated b-tag score.

Score	**Lower Limit (Inclusive)**	**Upper Limit (Exclusive)**
5	0.00	0.60
4	0.60	0.70
3	0.70	0.77
2	0.77	0.85
1	0.85	1.00
1	If truth b-tag is false	

Table 6.1: Score assignment based on random [0,1] value and b-tag status.

Note that no miss-tagging rate is considered for non-b-jets.

Number of b-jets

The number of b-jets is an important parameter throughout the analysis. Many selection cuts depend on this value, which also impacts the NN inputs. According to the pseudo code file, the considered scale factor for counting b-jets is 70%. Using this detail, one can ensure that the counting strategy reflects this experimental defect. In the recasting script, the number of b-jets is defined as the number of jets with a b-jet score higher than 4.

Summary

Recovering key information about these impact-full parameters of the analysis was of the utmost importance. One can see a tremendous difference in the outcome of the ML-based tools after implementing the correct b-jet score or after finding what Feynman diagrams should be included for the Higgsino signal. Ensuring proper communication and legacy code must be a main priority of LHC's experiments. Especially when a search involves the usage of ML tools. The studies that determine the impact of these parameters have further confirmed the high sensitivity an NN has to the definition of its inputs. Additionally, constructing the transform functions serves as an illustrative example of the typical challenges encountered in recasting ATLAS analyses. The next section will focus on the main results obtained to validate the recasting script.

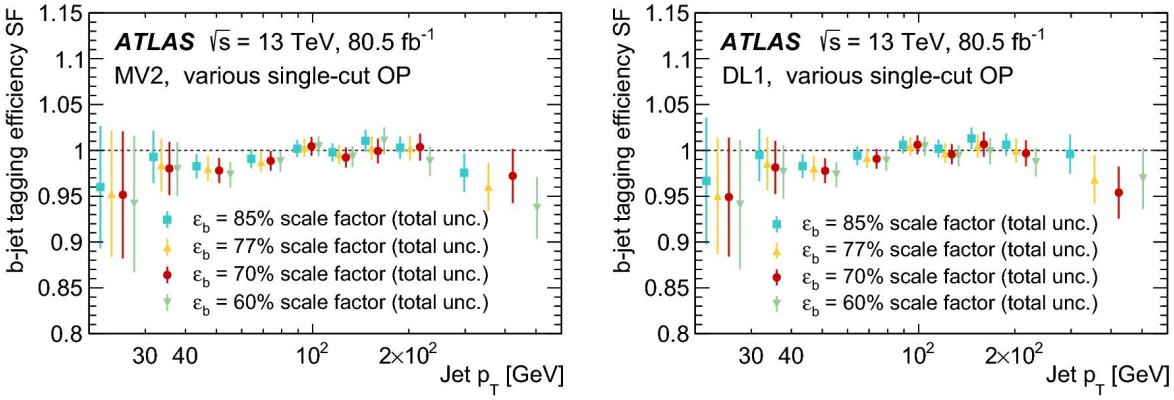


Figure 6.5: B-tagging efficiency on 4 different working points. Two Btaggign algorithms are presented. DL1 on the left panel refers to the b-tagging used for the analysis. The dependence on Pt remains flat at first order. From an ATLAS b-jet identification performance paper [226]

6.6.2 Results

Efficiency flow

Once all important modifications are correctly applied to the most sensitive selection steps, the results must be validated. To confirm the selection efficiencies, one can compare them to the available reference cutflows. These include different signal models targeting specific processes. There are two cutflows associated with the Higgsino model (which uses the NN cut): one for the neutralino process and one for charginos. The following results focus on the neutralino decays.

These Neutralino decays ($\tilde{\chi}^0_{1,2} \rightarrow t, b, s$) for a mass point of 250 GeV. Around 350k events were generated using Madgraph and Pythia8 and inputted into the optimized recasting script. The resulting yields for important initial and final selection cuts are compared to the reference analysis in table 6.2.

The uncertainties of the reference selection efficiencies can be deduced from the number of initial events. The total number of raw and weighted events are $N_{raw} = 269512$ and N_{evt}=14491.03.
If one considers N_{raw} as the initial count, the number of selected counts ($N_{\text{selected}} = \epsilon * N_{raw}$) and their uncertainties on each selection can be deduced. The uncertainty is given by Poisson statistics: $\sigma_{\text{selected}} = \sqrt{N_{\text{selected}}}$

The uncertainty in efficiency σ_ϵ can be calculated using the propagation of uncertainty formula and results in :

$$\sigma_\epsilon = \sqrt{\frac{\epsilon(1-\epsilon)}{N_{raw}}}$$

The computed efficiency uncertainties on the NN cuts are one order of magnitude lower than the efficiencies number of digits in the reference file. This indicates that some rounding was done at values higher than the Poisson uncertainty. To stay consistent, the

computed uncertainties were brought up to the same order of magnitude and might be more conservative. This is not a major concern since recasting procedures are always an approximation of the reference analysis. Very fine comparisons of efficiencies are not the objective. The same strategy is applied for computing the recast efficiency uncertainties.

The tightest last NN cut yields about 40 selected events. While this number is low, it is enough to provide a relative statistical error of only 15 %.

Looking at table 6.2, important differences in the initial cuts remain. On the recast results, an excess in signal leptons efficiency and a lower one for hard leptons cuts is observed. These are potentially due to discrepancies in signal lepton definition and lepton reconstruction effects that can be further refined in the fast detector effect simulations to account for a correct imitation of reconstructed objects. Undisclosed information with respect to other involved processes or other configurations of event generators on the benchmark samples could have such an impact. Further optimization of lepton transform functions could also potentially reduce these differences. However, the recast results are much more in agreement with what is expected concerning the final NN cuts that populate the electroweakino signal regions. This suggests a strong potential for reinterpreting the RPV analysis with other models.

Reproducing to perfection an analysis is a very difficult task when complex ATLAS reconstruction and analysis algorithms are involved. The approximations made throughout the recasting script have consequently impacted the cutflows. However, the level of proximity is satisfying for validation purposes.

Cuts	**recast**	**Expected**
Signal leptons ≥ 1	43.14% ± 0.08%	38.18% ± 0.09%
Leading lepton Pt > 27 GeV	33.14% ± 0.08%	37.36% ± 0.09%
# jets > 4 (>20 GeV) + 1 lepton	29.21% ± 0.08%	30.8% ± 0.09%
4 jets : NN cut	0.01% ± 0.01%	0.02% ± 0.01%
5 jets : NN cut	0.04% ± 0.01%	0.06% ± 0.01%
6 jets : NN cut	0.08% ± 0.01%	0.12% ± 0.01%
7 jets : NN cut	0.12% ± 0.01%	0.13% ± 0.01%
8 jets : NN cut	0.10% ± 0.01%	0.10% ± 0.01%

Table 6.2: Cutflow from the recasting script compared to the expected values from [222]. The initial number of recast events is 352 785.

ML-tool behaviour

The NN output signal distribution is an important parameter for validating the recasting script. The original histogram 6.4 was reproduced with the same 4 custom bins, which should include 25% of signal each. As mentioned in section 6.6.1, the signal of this histogram includes multiple higgsino processes with 300 GeV mass.

Figure 6.6 shows the recast distribution. The custom NN bins do not align precisely with the 25% target but fluctuate around it, with the first and last bins deviating the most. During the full optimization process of the recasting script, reproducing this plot was the main difficulty to surpass. In fact, before implementing the necessary modifications, the bin population deviated significantly from the 25% target.

The 4-bin version of the histogram is the only accessible information one can find on the neural network outputs. Consequently, the complete shape of the NN for this given Higgsino signal can be difficult to understand. Thankfully, through exchanges with the authors, comparisons between the full histogram of the recast network (figure 6.7) and the original were conducted. Thus offering a much finer and more unambiguous verification of this distribution on the same signal.

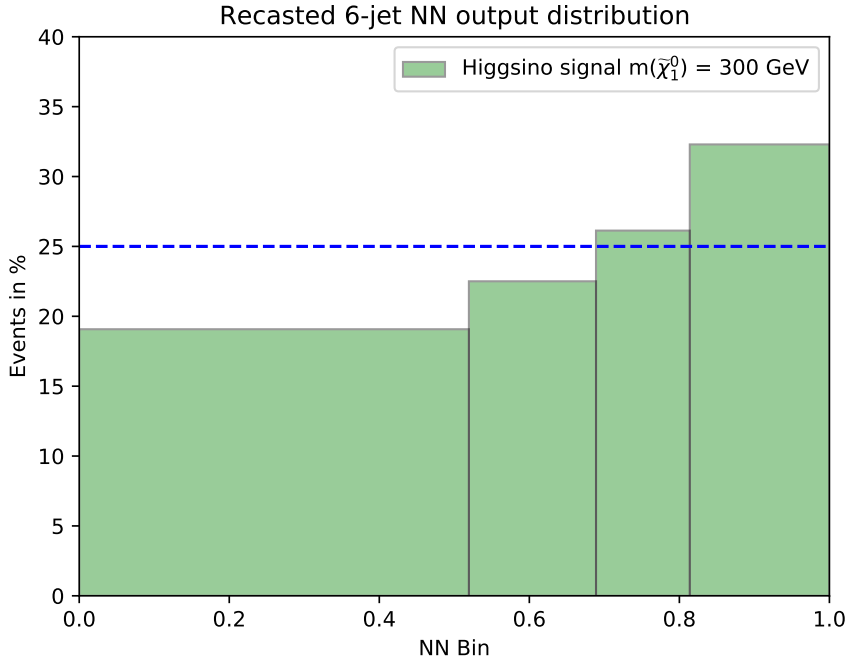


Figure 6.6: A reproduction of figure 6.4. The horizontal blue line represents the target of 25%. Each bin should contain an equal percentage of the higgsino signal population. The bins are : [0.0, 0.52, 0.69, 0.81, 1.0]

The full recast distribution of the 6jet NN on the higgsino benchmark signal (figure 6.7) reveals very similar features to the internal ATLAS one. This plot cannot be shown in this document as it remains ATLAS internal. However, current efforts led by this project are being conducted to render it public.

The maximum value, which describes the actual target for classifying signal events, is found indeed at 0.8 in both cases. Moreover, the behavior of tails before and after the peak is similar. Nevertheless, an expected bump at low output values, clearly visible in the original distribution, is less obvious to deduce from the recast output. The observed differences between the histograms reflect the shortage and excess in NN bins 1 and 4,

which can be seen in figure 6.6. One can also compare the mean and standard deviations of both distributions. They are very close, indeed the relative difference between both is of the order of one percent implying the NN is being correctly implemented in the recasting algorithm.
The relative differences are :

Mean: 3.13% Standard Deviation: 1.27%

This comparison manifests acceptable deviations and strongly secures the recasting MA5 scripts. Similar key features of the NN are observed on the same signal samples between the reference distribution and the one obtained by Madanalysis5. Even if some discrepancies persist, specifically at lower classifier values, the important factor is that the signal classification peaks remain at the same NN output value. This ensures that the fixed threshold value for accepting and rejecting events is in agreement with the classifier's performance. Therefore, similar efficiencies were maintained on the NN selection cuts.

These histograms and the cutflow (table 6.2) firmly validate the recasting code in Madanalysis5.

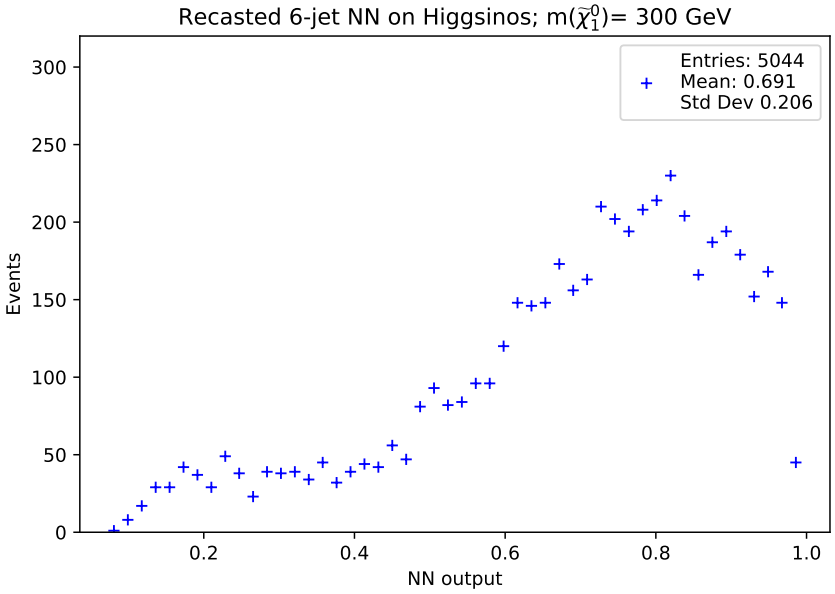


Figure 6.7: NN output for the 6 jet slice. Binned from 0 to 1 with 50 bins. Obtained in Madanalysis5.

Exclusion plots

The final plot to consider for validation is a reproduction of exclusion plots. Parameter space limits are set on the Higgsino and Wino model using the ATLAS observations in the NN-based signal region. Madanalysis5 allows for the computation of the expected number of events in each signal region for a given integrated luminosity by using the

recast cutflows. Using this functionality, one can compare the number of events observed by ATLAS to the recasting prediction. By picking a few mass points and obtaining their associated cutflows, Figure 6.8 was obtained. This figure shows the relevant exclusion limits obtained by MA5 and observed by the experiment.

This result is preliminary, but it shows that the recasting procedure produces consistent results. The cross-section limit mass dependence is reproduced. A shift towards higher cross-sections is present for all mass points. An investigation of these remaining differences would require a complete evaluation of the fast simulation performance used in MadAnalysis with respect to ATLAS full simulation and reconstruction. This is beyond the scope of the present work but points towards a need for precise simulations in recasting programs. This led to a new project between the MadAnalysis team and LPNHE to use fast simulation AI solutions trained on full simulation samples to be more precise while providing an affordable CPU performance. Additionally, the observed differences could be caused by the input samples. In fact, fine details of the Madgraph configuration are still missing from the auxiliary material.

Nevertheless, this plot validates the recasting effort made in this thesis and demonstrates for the first time that ML-based searches can be recast within MA5.

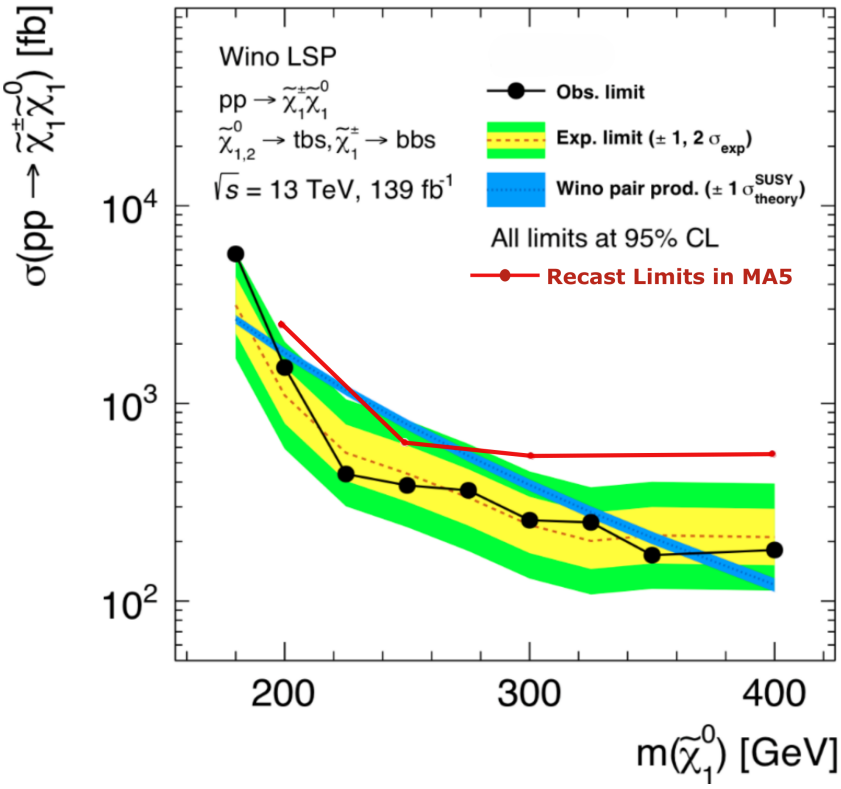


Figure 6.8: Resulting cross-section limits obtained with the recasting script. Overlapped with the ATLAS measurement exclusion plot [207]. Limits computed on simulated events of the RPV wino LSP model.

6.7 Conclusion

As machine learning becomes prevalent in LHC analyses, publishing trained models in a reusable format along with legacy code has become essential for reinterpretation purposes. The complexity of these models presents practical challenges in accurately reusing them and ensuring their consistent performance across various environments. A crucial aspect of recasting frameworks is to develop functionalities that incorporate machine learning inference.
The ONNX runtime API [212] offers high flexibility with its cross-platform capabilities and supports both CPU and GPU performance optimizations. It enables efficient training and inference processes, is open-source, and is under constant development and optimization with backward compatibility. This adaptability makes ONNX increasingly standard in LHC experiments, where models are trained using PyTorch [209] and then loaded into C++-based internal analysis software. This approach also replaces the usage of ROOT's TMVA libraries [211]. Utilizing machine learning tools in this format simplifies the exchangeability of models and will become more prevalent over time. This will benefit the reinterpretation of results as standardized procedures will help the flow of recasting ML-based searches.

MadAnalysis5 presents all necessary capacities for recasting classical, cut-based analyses. And adding ONNX functionalities opens a wider phase space for analysis recasting. This integration has now been set up and works as intended. In the future, specific MadAnalysis functions could be implemented to interface with ONNX, further enhancing its capabilities and offering a long term usability of LHC limits derived from ML-based analysis to assess the constraint from the LHC legacy data on any potential future models.

To validate these functionalities, an ML-based analysis was successfully recast. The R-parity-violating supersymmetry [207] search ATLAS-SUSY-2019-04 on Run 2 data has published trained networks in ONNX format as well as a truth-level implementation in SimpleAnalysis [221], which was crucial for understanding the NN input variables. However, there remained uncertainties about how to reproduce some of the main variables and verify that the benchmark signals from other fast-simulation yield the expected ML responses within acceptable uncertainties. For such reasons, this analysis has never been reinterpreted. Still, it offers many reinterpretation potentials with an overall of 139 fb^{-1} of Run 2 data which is now achievable through the efforts provided in this project. This is a major step since it validates the possibility of recasting ML-based analyses.

Extra information was retrieved from private exchanges to fully implement the NN and complete a correct recasting. This experience should raise more awareness of the importance of auxiliary resources, especially for ML-based analyses. While simple cut-and-count analyses can often be described straightforwardly within papers, providing a precise description of an ML tool, its behavior, input variables, and how to compute them correctly is much more challenging to include in a paper.
Additionally, it is equally important to ensure that plots containing the expected NN output are public.
LHC experiments are responsible for ensuring that phenomenologists can extract the maximum benefit from published analysis results. Extensive usage of inference software

such as ONNX Runtime must become a standard way of sharing NN. Extra documents specifically indicating how to manipulate the ML tool inputs should always support the network files. Furthermore, a precise description of how the algorithms react to a given benchmark sample is necessary to correctly validate the recasting tools.
These points are still quite open, as there is no standard workflow for optimizing the reinterpretation power of ML searches. The phenomenology community has put together recent guidelines to indicate how to transmit better legacy code regarding ML-based searches of ATLAS and CMS [196].

The study presented in this chapter has led to internal procedures within the ATLAS collaboration to extend the published material of analysis SUSY-2019-04 by including all relevant information mentioned in this thesis. This particular project demonstrates the need to improve ATLAS auxiliary resources protocols. It will benefit the recasting community in the near future by opening the range of reinterpretation of ATLAS experimental results.

Bibliography

[1] Planck-Collaboration, N. Aghanim, Y. Akrami, M. Ashdown, J. Aumont, C. Baccigalupi, M. Ballardini, A. J. Banday, and et al., "Planck 2018 results. v. cmb power spectra and likelihoods," *Astronomy & Astrophysics*, vol. 641, p. A5, 2020. Published online 11 September 2020.

[2] Planck-Collaboration, N. Aghanim, Y. Akrami, F. Arroja, M. Ashdown, J. Aumont, C. Baccigalupi, M. Ballardini, and et al., "Planck 2018 results. i. overview and the cosmological legacy of planck," *Astronomy & Astrophysics*, vol. 641, p. A1, 2020. Published online 11 September 2020.

[3] Planck-Collaboration, N. Aghanim, Y. Akrami, M. Ashdown, J. Aumont, C. Baccigalupi, M. Ballardini, and et al., "Planck 2018 results. vi. cosmological parameters," *Astronomy & Astrophysics*, vol. 641, p. A6, 2020. Published online 11 September 2020.

[4] J. Diao and et al., "The impact of the dark matter on galaxy formation," *Journal of Physics: Conference Series*, vol. 2441, p. 012025, 2023.

[5] J. R. Primack, "Dark matter and structure formation in the universe," *arXiv preprint arXiv:astro-ph/9707285*, 1997.

[6] E. Aprile, K.-L. Giboni, M. Monzani, G. Plante, M. Yamashita, R. Gaitskell, S. Fiorucci, P. Sorensen, L. DeViveiros, A. Bernstein, N. Madden, C. Winant, T. Shutt, J. Kwong, A. Bolozdynya, E. Dahl, U. Oberlack, P. Shagin, R. Gomez, D. McKinsey, A. Manzur, R. Hasty, K. Ni, F. Arneodo, A. Ferella, L. Baudis, J. Angle, J. Orboeck, A. Manalaysay, J. Lopes, L. Coelho, L. Fernandes, and J. Santos, "Xenon," *Nuclear Physics B - Proceedings Supplements*, vol. 173, pp. 113–116, 2007. Proceedings of the 7th UCLA Symposium on Sources and Detection of Dark Matter and Dark Energy in the Universe.

[7] A. Z. on behalf of the DarkSide-20k collaboration, "The darkside-20k experiment," *Journal of Instrumentation*, vol. 19, p. C03058, 2024. Published 27 March 2024.

[8] I. Arnquist, N. Avalos, D. Baxter, X. Bertou, N. Castelló-Mor, A. E. Chavarria, J. Cuevas-Zepeda, J. C. Gutiérrez, J. Duarte-Campderros, A. Dastgheibi-Fard,

O. Deligny, C. De Dominicis, E. Estrada, N. Gadola, R. Gaïor, T. Hossbach, L. Iddir, L. Khalil, B. Kilminster, A. Lantero-Barreda, I. Lawson, S. Lee, A. Letessier-Selvon, P. Loaiza, A. Lopez-Virto, A. Matalon, S. Munagavalasa, K. J. McGuire, P. Mitra, D. Norcini, G. Papadopoulos, S. Paul, A. Piers, P. Privitera, K. Ramanathan, P. Robmann, M. Settimo, R. Smida, R. Thomas, M. Traina, I. Vila, R. Vilar, G. Warot, R. Yajur, and J.-P. Zopounidis, "First constraints from damic-m on sub-gev dark-matter particles interacting with electrons," *Phys. Rev. Lett.*, vol. 130, p. 171003, Apr 2023.

[9] M. Collaboration, P. Brun, A. Caldwell, *et al.*, "A new experimental approach to probe qcd axion dark matter in the mass range above 40 μev," *Eur. Phys. J. C*, vol. 79, p. 186, 2019.

[10] B. M. Roach, S. Rossland, K. C. Y. Ng, K. Perez, J. F. Beacom, B. W. Grefenstette, S. Horiuchi, R. Krivonos, and D. R. Wik, "Long-exposure nustar constraints on decaying dark matter in the galactic halo," *Phys. Rev. D*, vol. 107, p. 023009, Jan 2023.

[11] K. Abe, H. Fuke, S. Haino, T. Hams, M. Hasegawa, K. Kim, M. Lee, Y. Makida, J. Mitchell, J. Nishimura, M. Nozaki, R. Orito, J. Ormes, N. Picot-Clemente, K. Sakai, M. Sasaki, E. Seo, R. Streitmatter, J. Suzuki, K. Tanaka, N. Thakur, A. Yamamoto, T. Yoshida, and K. Yoshimura, "The results from bess-polar experiment," *Advances in Space Research*, vol. 60, no. 4, pp. 806–814, 2017. Solar Energetic Particles, Solar Modulation and Space Radiation: New Opportunities in the AMS-02 Era.

[12] H. e. a. Abdalla, "Search for dark matter annihilation signals in the h.e.s.s. inner galaxy survey," *Phys. Rev. Lett.*, vol. 129, p. 111101, Sep 2022.

[13] C. consortium, "Ricap18, 7th roma international conference on astroparticle physics," *EPJ Web of Conferences*, vol. 209, p. 01038, 2019. Published online: 13 May 2019.

[14] M. Di Mauro, J. Pérez-Romero, M. A. Sánchez-Conde, and N. Fornengo, "Constraining the dark matter contribution of γ rays in clusters of galaxies using fermi-lat data," *Phys. Rev. D*, vol. 107, p. 083030, Apr 2023.

[15] A. Leopold, *Dark Matter Searches in Association with a Higgs Boson using s = 13 TeV ATLAS Data and Performance Evaluation of the High-Granularity Timing Detector*. PhD thesis, Sorbonne Université, 2020. Presented 16 Dec 2020.

[16] A. Blanchard, J.-Y. Héloret, S. Ilić, B. Lamine, and I. Tutusaus, "cdm is alive and well," *The Open Journal of Astrophysics*, vol. 7, 5 2024.

[17] E. Corbelli and P. Salucci, "The extended rotation curve and the dark matter halo of M33," *Monthly Notices of the Royal Astronomical Society*, vol. 311, pp. 441–447, 01 2000.

[18] M. Markevitch, "Chandra observation of the most interesting cluster in the universe," *arXiv preprint astro-ph/0511345*, 2005.

[19] Wikipedia-contributors, "Standard model of elementary particles," 2023.

[20] P. W. Higgs, "Broken symmetries and the masses of gauge bosons," *Phys. Rev. Lett.*, vol. 13, pp. 508–509, Oct 1964.

[21] F. L. Wilson, "Fermi's theory of beta decay," *American Journal of Physics*, vol. 36, no. 12, pp. 1150–1160, 1968.

[22] M. Milgrom, "Mond theory," *Canadian Journal of Physics*, vol. 93, no. 2, pp. 107–118, 2015.

[23] J. D. Bekenstein, "Tensor-vector-scalar-modified gravity: from small scale to cosmology," *Philosophical Transactions of the Royal Society A: Mathematical, Physical and Engineering Sciences*, vol. 369, no. 1957, pp. 5003–5017, 2011.

[24] B. D. Fields, K. Freese, and D. S. Graff, "Massive compact halo objects viewed from a cosmological perspective: contribution to the baryonic mass density of the universe," *New Astronomy*, vol. 3, no. 6, pp. 347–361, 1998.

[25] A. Arbey, "Primordial black holes, a small review," *arXiv preprint arXiv:2405.08624*, 2024. 8 pages, 7 figures. Contribution to the 2024 Very High Energy Phenomena in the Universe session of the 58th Rencontres de Moriond.

[26] B. Carr, K. Kohri, Y. Sendouda, and J. Yokoyama, "Constraints on primordial black holes," *Reports on Progress in Physics*, vol. 84, no. 11, p. 116902, 2021.

[27] S. D. McDermott, H.-B. Yu, and K. M. Zurek, "Constraints on scalar asymmetric dark matter from black hole formation in neutron stars," *Phys. Rev. D*, vol. 83, p. 063509, 2011.

[28] S. D. McDermott, H.-B. Yu, and K. M. Zurek, "Turning off the lights: How dark is dark matter?," *Phys. Rev. D*, vol. 83, p. 063509, Mar 2011.

[29] S. Tremaine and J. E. Gunn, "Dynamical role of light neutral leptons in cosmology," *Phys. Rev. Lett.*, vol. 42, pp. 407–410, 1979.

[30] E. Armengaud *et al.*, "Constraining sterile neutrino warm dark matter with decam multi-band optical data," *Mon. Not. Roy. Astron. Soc.*, vol. 471, no. 4, pp. 4606–4614, 2017.

[31] M. A. Monroy-Rodríguez and C. Allen, "The end of the macho era: Limits on halo dark matter from stellar halo wide binaries," *Astrophys. J.*, vol. 790, no. 2, p. 159, 2014.

[32] D. Harvey, R. Massey, T. Kitching, A. Taylor, and E. Tittley, "The nongravitational interactions of dark matter in colliding galaxy clusters," *Science*, vol. 347, no. 6229, pp. 1462–1465, 2015.

[33] K. M. Zurek, "Multicomponent dark matter," *Phys. Rev. D*, vol. 79, p. 115002, Jun 2009.

[34] B. Hoeneisen, "A study of warm dark matter, the missing satellites problem, and the uv luminosity cut-off," *International Journal of Astronomy and Astrophysics*, vol. 13, no. 1, pp. 1–10, 2023.

[35] G. Steigman, B. Dasgupta, and J. F. Beacom, "Precise relic wimp abundance and its impact on searches for dark matter annihilation," *Phys. Rev. D*, vol. 86, p. 023506, Jul 2012.

[36] H. E. Haber and L. S. Haskins, *Supersymmetric Theory and Models*, ch. Chapter 6, pp. 355–499.

[37] T. C. collaboration, A. Tumasyan, W. Adam, *et al.*, "Search for electroweak production of charginos and neutralinos in proton-proton collisions at $\sqrt{s} = 13$ tev," *J. High Energ. Phys.*, vol. 2022, p. 147, 2022.

[38] J. Arakawa and T. M. P. Tait, "Is a Miracle-less WIMP Ruled out?," *SciPost Phys.*, vol. 11, p. 019, 2021.

[39] M. Dutra, *Origins for dark matter particles : from the "WIMP miracle" to the "FIMP wonder"*. Theses, Université Paris Saclay (COmUE), Feb. 2019.

[40] V. S. Rychkov and A. Strumia, "Thermal production of gravitinos," *Phys. Rev. D*, vol. 75, p. 075011, Apr 2007.

[41] S. Navas *et al.*, "Particle data group," *Phys. Rev. D*, vol. 110, no. 030001, 2024.

[42] M. Shaposhnikov, "Sterile neutrinos as dark matter," *Nuclear Physics B*, vol. 1003, p. 116496, 2024. Special Issue of Nobel Symposium 182 on Dark Matter.

[43] S. Böser, C. Buck, C. Giunti, J. Lesgourgues, L. Ludhova, S. Mertens, A. Schukraft, and M. Wurm, "Status of light sterile neutrino searches," *Progress in Particle and Nuclear Physics*, vol. 111, p. 103736, 2020.

[44] C. S. Kim, G. López Castro, and D. Sahoo, "Discovering intermediate mass sterile neutrinos through $\tau^- \to \pi^-\mu^-e^+\nu(\text{or}\overline{\nu})$ decay," *Phys. Rev. D*, vol. 96, p. 075016, Oct 2017.

[45] K. Petraki, "Small-scale structure formation properties of chilled sterile neutrinos as dark matter," *Phys. Rev. D*, vol. 77, p. 105004, May 2008.

[46] H. Rasmussen, A. McNichol, G. M. Fuller, and C. T. Kishimoto, "Effects of an intermediate mass sterile neutrino population on the early universe," *Phys. Rev. D*, vol. 105, p. 083513, Apr 2022.

[47] P. D. Bolton, F. F. Deppisch, and P. B. Dev, "Probes of Heavy Sterile Neutrinos," *arXiv preprint arXiv:2206.01140*, 2022. Contribution to the 2022 EW session of the 56th Rencontres de Moriond, Author Accepted Manuscript.

[48] K. Abazajian and S. M. Koushiappas, "Constraints on sterile neutrino dark matter," *Phys. Rev. D*, vol. 74, p. 023527, Jul 2006.

[49] M. Aker, K. Altenmüller, J. Amsbaugh, M. Arenz, M. Babutzka, J. Bast, S. Bauer, H. Bechtler, M. Beck, A. Beglarian, *et al.*, "The design, construction, and commissioning of the katrin experiment," *Journal of Instrumentation*, vol. 16, no. 08, p. T08015, 2021.

[50] S. Hagstotz, P. F. de Salas, S. Gariazzo, S. Pastor, M. Gerbino, M. Lattanzi, S. Vagnozzi, and K. Freese, "Bounds on light sterile neutrino mass and mixing from cosmology and laboratory searches," *Phys. Rev. D*, vol. 104, p. 123524, Dec 2021.

[51] R. D. Peccei and H. R. Quinn, "CP conservation in the presence of pseudoparticles," *Phys. Rev. Lett.*, vol. 38, pp. 1440–1443, Jun 1977.

[52] J. E. Kim and G. Carosi, "Axions and the Strong CP Problem," *arXiv preprint arXiv:0807.3125*, 2009. Revised version published in Rev. Mod. Phys. 82:557-602, 2010 and Rev. Mod. Phys. 91:049902, 2019.

[53] C. B. A. et al., "Axion dark matter," *arXiv preprint arXiv:2203.14923*, 2023. Submitted to Snowmass 2021 White Paper.

[54] T. Hiramatsu, M. Kawasaki, T. Sekiguchi, M. Yamaguchi, and J. Yokoyama, "Improved estimation of radiated axions from cosmological axionic strings," *Phys. Rev. D*, vol. 83, p. 123531, Jun 2011.

[55] R. K. et al, "Axion dark matter experiment: Detailed design and operations," *arXiv preprint arXiv:2010.00169*, 2020. FERMILAB-PUB-20-331-AD-E-QIS.

[56] E. A. et al., "Solar axion search with the cast experiment," *Proceedings of the ICHEP 2008 conference*, 2008.

[57] I. G. Irastorza, F. T. Avignone, G. Cantatore, S. Caspi, J. M. Carmona, T. Dafni, M. Davenport, A. Dudarev, G. Fanourakis, E. Ferrer-Ribas, J. Galan, J. A. Garcia, T. Geralis, I. Giomataris, S. Gninenko, H. Gomez, D. H. H. Hoffmann, F. J. Iguaz, K. Jakovcic, M. Krcmar, B. Lakic, G. Luzon, A. Lindner, M. Pivovaroff, T. Papaevangelou, G. Raffelt, J. Redondo, A. Rodrıguez, S. Russenschuck, J. Ruz, I. Shilon, H. T. Kate, A. Tomas, S. Troitsky, K. van Bibber, J. A. Villar, J. Vogel, L. Walckiers, and K. Zioutas, "The international axion observatory (iaxo)," 2012.

[58] S. Shakeri, D. J. Marsh, and S.-S. Xue, "Light by light scattering as a new probe for axions," *arXiv preprint arXiv:2002.06123*, 2020.

[59] H.-Y. Zhang, C.-X. Yue, Y.-C. Guo, and S. Yang, "Searching for axionlike particles at future electron-positron colliders," *Phys. Rev. D*, vol. 104, p. 096008, Nov 2021.

[60] N. Song, L. Su, and L. Wu, "Polarization signals from axion-photon resonant conversion in neutron star magnetospheres," *arXiv:2402.15144*, February 2024.

[61] I. Batković, A. D. Angelis, M. Doro, and M. Manganaro, "Axion-like particle searches with iacts," *Universe*, vol. 7, no. 6, p. 185, 2021.

[62] A. Berlin, S. Gori, T. Lin, and L.-T. Wang, "Pseudoscalar portal dark matter," *Phys. Rev. D*, vol. 92, p. 015005, Jul 2015.

[63] M. Bauer, U. Haisch, and F. Kahlhoefer, "Simplified dark matter models with two higgs doublets: I. pseudoscalar mediators," *arXiv preprint arXiv:1701.07427*, 2017. Submitted on 25 Jan 2017 (v1), last revised 8 Jun 2017 (this version, v3).

[64] T. A. collaboration, G. Aad, B. Abbott, *et al.*, "Search for dark photons from higgs boson decays via zh production with a photon plus missing transverse momentum signature from pp collisions at $\sqrt{s} = 13$ tev with the atlas detector," *J. High Energ. Phys.*, vol. 2023, p. 133, 2023.

[65] C. Arina, B. Fuks, L. Mantani, H. Mies, L. Panizzi, and J. Salko, "Closing in on t-channel simplified dark matter models," *Physics Letters B*, vol. 813, p. 136038, 2021.

[66] S. P. Liew, M. Papucci, A. Vichi, and K. M. Zurek, "Mono-x versus direct searches: simplified models for dark matter at the lhc," *Journal of High Energy Physics*, vol. 2017, no. 6, pp. 1–37, 2017.

[67] G. Aad, B. Abbott, D. C. Abbott, A. Abed Abud, K. Abeling, D. K. Abhayasinghe, S. H. Abidi, O. AbouZeid, N. L. Abraham, H. Abramowicz, *et al.*, "Search for new phenomena in events with an energetic jet and missing transverse momentum in pp collisions at s= 13 tev with the atlas detector," *Physical Review D*, vol. 103, no. 11, p. 112006, 2021.

[68] M. Aaboud, G. Aad, B. Abbott, B. Abeloos, S. Abidi, O. AbouZeid, N. L. Abraham, H. Abramowicz, H. Abreu, R. Abreu, *et al.*, "Search for dark matter and other new phenomena in events with an energetic jet and large missing transverse momentum using the atlas detector," *Journal of High Energy Physics*, vol. 2018, no. 1, pp. 1–53, 2018.

[69] M. Aaboud, G. Aad, B. Abbott, J. Abdallah, O. B. o. Abdinov, B. Abeloos, S. H. Abidi, H. AbouZeid, N. L. Abraham, H. Abramowicz, *et al.*, "Search for dark matter at= 13 tev in final states containing an energetic photon and large missing transverse momentum with the atlas detector," *European Physical Journal C*, vol. 77, 2017.

[70] A. M. Sirunyan, A. Tumasyan, W. Adam, *et al.*, "Search for new physics in events with a leptonically decaying z boson and a large transverse momentum imbalance in proton-proton collisions at $\sqrt{s} = 13$ tev," *Eur. Phys. J. C*, vol. 78, p. 291, 2018. Received: 01 November 2017; Accepted: 16 March 2018; Published: 11 April 2018.

[71] e. a. Sirunyan, A. M., "Search for new physics in final states with an energetic jet or a hadronically decaying w or z boson and transverse momentum imbalance at $\sqrt{s} = 13$ TeV," *Phys. Rev. D*, vol. 97, p. 092005, May 2018.

[72] T. A. collaboration, G. Aad, B. Abbott, *et al.*, "Search for dark matter produced in association with a standard model higgs boson decaying into b-quarks using the full run 2 dataset from the atlas detector," *J. High Energ. Phys.*, vol. 2021, p. 209, 2021.

[73] T. A. collaboration, G. Aad, B. Abbott, *et al.*, "Search for dark matter in events with missing transverse momentum and a higgs boson decaying into two photons in pp collisions at $\sqrt{s} = 13$ tev with the atlas detector," *J. High Energ. Phys.*, vol. 2021, no. 13, pp. 1–13, 2021.

[74] T. C. collaboration, A. M. Sirunyan, A. Tumasyan, *et al.*, "Search for dark matter produced in association with a single top quark or a top quark pair in proton-proton collisions at $\sqrt{s} = 13$ tev," *J. High Energ. Phys.*, vol. 2019, p. 141, 2019.

[75] N. Trevisani, "Collider searches for dark matter (atlas + cms)," *Universe*, vol. 4, no. 11, p. 131, 2018.

[76] T. A. collaboration, G. Aad, B. Abbott, *et al.*, "Search for invisible higgs-boson decays in events with vector-boson fusion signatures using 139 fb^{-1} of proton-proton data recorded by the atlas experiment," *J. High Energ. Phys.*, vol. 2022, p. 104, 2022.

[77] M. Aaboud, G. Aad, B. Abbott, J. Abdallah, O. Abdinov, B. Abeloos, S. Abidi, O. AbouZeid, N. Abraham, H. Abramowicz, *et al.*, "Search for new phenomena in dijet events using 37 fb^{-1} of pp collision data collected at $\sqrt{s} = 13$ tev with the atlas detector," *Phys. Rev. D*, vol. 96, p. 052004, 2017.

[78] F. Bartels, *Search for Low-Mass Dijet Resonances Using Trigger-Level Jets at the ATLAS Detector*. PhD thesis, 2024.

[79] N. M. T. A. Bauer, M., "Collider probes of axion-like particles," *J. High Energ. Phys.*, vol. 2017, p. 44, 2017.

[80] G. A. et al. (ATLAS Collaboration), "Search for higgs boson decays into a pair of pseudoscalar particles in the bb final state with the atlas detector in pp collisions at s = 13 tev," *Phys. Rev. D*, vol. 105, p. 012006, 2022.

[81] A. Collaboration, "Search for decays of the higgs boson into a pair of pseudoscalar particles decaying into bb+ using pp collisions at s = 13 tev with the atlas detector," *arXiv:2407.01335 [hep-ex]*, 2024.

[82] G. G.-P. G. Cobal M., Giordani M. P., "Search for a new pseudoscalar decaying into a pair of muons in events with a top-quark pair at formula presented with the atlas detector," *arXiv*, 2023.

[83] G. A. et al, "Search for the decay of the higgs boson to a z boson and a light pseudoscalar particle decaying to two photons," *Physics Letters B*, vol. 850, p. 138536, 2024.

[84] A. Collaboration, "Search for short- and long-lived axion-like particles in $h \to aa \to 4\gamma$ decays with the atlas experiment at the lhc," *arXiv*, 2023.

[85] A. Ringwald, "Searching for axions and alps from string theory," *J. Phys.: Conf. Ser.*, vol. 485, p. 012013, 2014.

[86] S. Alexander, T. Manton, and E. McDonough, "The field theory axiverse," *arXiv:2404.11642*, April 2024.

[87] A. Keshavarzi, K. S. Khaw, and T. Yoshioka, "Muon g- 2: A review," *Nuclear Physics B*, vol. 975, p. 115675, 2022.

[88] V. Brdar, S. Jana, J. Kubo, and M. Lindner, "Semi-secretly interacting axion-like particle as an explanation of fermilab muon g2 measurement," *Physics Letters B*, vol. 820, p. 136529, 2021.

[89] R. Daido, F. Takahashi, and W. Yin, "The alp miracle: unified inflaton and dark matter," *Journal of Cosmology and Astroparticle Physics*, vol. 2017, no. 05, p. 044, 2017.

[90] A. Mariotti, D. Redigolo, F. Sala, and K. Tobioka, "New lhc bound on low-mass diphoton resonances," *Physics Letters B*, vol. 783, pp. 13–18, 2018.

[91] I. Brivio, M. Gavela, L. Merlo, R. del Rey, and O. M. Sumensari, "Alps effective field theory and collider signatures," *Eur. Phys. J. C*, vol. 77, no. 8, p. 572, 2017.

[92] H. Song, H. Sun, and J. Yu, "Effective field theories of axion, alp and dark photon," *J. High Energ. Phys.*, vol. 2024, no. 1, p. 161, 2024.

[93] T. A. collaboration, G. Aad, B. Abbott, and et al., "Measurements of the higgs boson production and decay rates and constraints on its couplings from a combined atlas and cms analysis of the lhc *pp* collision data at $\sqrt{s} = 7$ and 8 tev," *J. High Energ. Phys.*, vol. 2016, p. 45, 2016.

[94] H. M. N. M. e. a. Bauer, M., "Axion-like particles at future colliders," *Eur. Phys. J. C*, vol. 79, p. 74, 2019.

[95] C. Arina, M. Backović, J. Heisig, and M. Lucente, "Solar γ rays as a complementary probe of dark matter," *Phys. Rev. D*, vol. 96, p. 063010, Sep 2017.

[96] M. Lucente, C. Arina, M. Backović, and J. Heisig, "Probing dark matter long-lived mediators with solar rays," in *Proceedings of Science*, 2017.

[97] C. Alpigiani and M. Proffitt, "Mathusla," *An Update to the Letter of Intent for MATHUSLA: Search for Long-Lived Particles at the HL-LHC*, 2024.

[98] "Radiofrequency cavities," 2012.

[99] A. Horvath, "This w3c-unspecified vector image was created with inkscape." https://commons.wikimedia.org/w/index.php?curid=679693, 2006. CC BY-SA 2.5.

[100] The ATLAS Collaboration, "The ATLAS Experiment at the CERN Large Hadron Collider," *Journal of Instrumentation*, vol. 3, p. S08003, 2008.

[101] "Cern image." CERN, Jan. 2011. CERN-EX-1101010-03.

[102] R. M. Bianchi and A. Collaboration, "Atlas experiment schematic or layout illustration." https://cds.cern.ch/record/2837191, Oct. 2022. ATLAS-PHOTO-2022-055.

[103] G. e. a. Aad, "The ATLAS Inner Detector commissioning and calibration. The ATLAS Inner Detector commissioning and calibration," *Eur. Phys. J. C*, vol. 70, pp. 787–821, 2010. Comments: 34 pages, 25 figures.

[104] M. Battaglia, "Performance of the ATLAS Pixel Detector at the start of LHC Run 3," tech. rep., CERN, Geneva, 2023.

[105] "Technical Design Report for the ATLAS Inner Tracker Pixel Detector," tech. rep., CERN, Geneva, 2017.

[106] J. N. Jackson, "The ATLAS semiconductor tracker (SCT)," *Nucl. Instrum. Meth. A*, vol. 541, pp. 89–95, 2005.

[107] A. Sfyrla *et al.*, "The detector control system for the atlas semiconductor tracker assembly phase," *Nuclear Science, IEEE Transactions on*, vol. 52, pp. 938–943, Sept. 2005.

[108] A. Vogel, "Atlas transition radiation tracker (trt): Straw tube gaseous detectors at high rates," tech. rep., CERN, Geneva, Apr. 2013. https://cds.cern.ch/record/1537991.

[109] ATLAS Collaboration, "Experiment briefing: Keeping the atlas inner detector in perfect alignment." https://cds.cern.ch/record/2723878, July 2020. ATLAS-PHOTO-2020-045.

[110] G. A. B. e. a. The ATLAS collaboration, Aad, "Search for long-lived, massive particles in events with displaced vertices and multiple jets in pp collisions at $\sqrt{s} = 13$ TeV with the ATLAS detector," *J. High Energ. Phys.*, vol. 2023, p. 200, 2023.

[111] J. Pequenao, "Computer generated image of the atlas calorimeter." https://cds.cern.ch/record/1095927, Mar. 2008. CERN-GE-0803015.

[112] "ATLAS liquid argon calorimeter: Technical design report," 12 1996.

[113] "ATLAS Liquid Argon Calorimeter Phase-II Upgrade: Technical Design Report," tech. rep., CERN, Geneva, 2017.

[114] G. B. Kopp, C. Tully, K. E. Kennedy, W. P. Chung, S. Hoienko, J. M. Mans, M. D. Krohn, B. J. Crossman, J. Hiltbrand, A. Skuja, and L. Wang, "A Novel Timing Trigger with the CMS Hadron Calorimeter," 2023.

[115] *ATLAS tile calorimeter: Technical Design Report*. Technical design report. ATLAS, Geneva: CERN, 1996.

[116] A. M. Henriques Correia, "The ATLAS Tile Calorimeter," tech. rep., CERN, Geneva, 2015.

[117] E. Khramov *et al.*, "Study of the response of the hadronic barrel calorimeter in the atlas combined test-beam to pions of energies from 20 to 350 gev for beam impact points from 0.2 to 0.65," Tech. Rep. ATL-TILECAL-PUB-2009-007, ATL-COM-TILECAL-2009-006, CERN, Geneva, Apr. 2009.

[118] ATLAS Collaboration, "Tile calorimeter public plots." https://twiki.cern.ch/twiki/bin/view/AtlasPublic/TileCaloPublicResults. Accessed: 2024-10-23.

[119] "Atlas muon spectrometer: Technical design report," tech. rep., CERN, Geneva, 1997.

[120] ATLAS Collaboration and S. Bressler, *Technical Design Report for the Phase-II Upgrade of the ATLAS Muon Spectrometer*. Technical Design Report ATLAS, July 2022. Report number - CERN-LHCC-2017-017 ; ATLAS-TDR-026.

[121] P. Jenni, M. Nordberg, M. Nessi, and K. Jon-And, "Atlas forward detectors for measurement of elastic scattering and luminosity," 2008.

[122] S. A. Khalek, B. Allongue, F. Anghinolfi, P. Barrillon, G. Blanchot, S. Blin-Bondil, A. Braem, L. Chytka, P. C. Muíño, M. Düren, *et al.*, "The alfa roman pot detectors of atlas," *Journal of Instrumentation*, vol. 11, no. 11, p. P11013, 2016.

[123] S. White, "The atlas zero degree calorimeter," *Nucl. Instrum. Meth. A*, vol. 617, pp. 126–128, 2010.

[124] D. Caforio, "Luminosity measurement using cherenkov integrating detector (lucid) in atlas," in *10th ICATPP Conference on Astroparticle, Particle, Space Physics, Detectors and Medical Physics Applications*, pp. 413–417, 2008.

[125] A. Sidoti, "Minimum bias trigger scintillators in atlas run ii," *JINST*, vol. 9, p. C10020, 2014.

[126] V. Cindro *et al.*, "The atlas beam conditions monitor," *Journal of Instrumentation*, vol. 3, pp. P02004–P02004, feb 2008.

[127] S. Grinstein, A. Collaboration, *et al.*, "The atlas forward proton detector (afp)," *Nuclear and particle physics proceedings*, vol. 273, pp. 1180–1184, 2016.

[128] G. e. a. Aad, "The atlas trigger system for lhc run 3 and trigger performance in 2022," *Journal of Instrumentation*, vol. 19, p. P06029, June 2024.

[129] J. Pequenao, "Event cross section in a computer generated image of the atlas detector." https://cds.cern.ch/record/1096081, Mar. 2008.

[130] R. Atkin, "Review of jet reconstruction algorithms," *Journal of Physics: Conference Series*, vol. 645, p. 012008, sep 2015.

[131] M. Cacciari, G. P. Salam, and G. Soyez, "The anti-k_t jet clustering algorithm," *Journal of High Energy Physics*, vol. 2008, p. 063, 2008.

[132] G. A. et al, "The atlas experiment at the cern large hadron collider: a description of the detector configuration for run 3," *Journal of Instrumentation*, vol. 19, p. P05063, may 2024.

[133] E. Kay, "Commissioning the Phase-1 LAr Upgrade," tech. rep., CERN, Geneva, 2021.

[134] I. Gnesi, "Micromegas chambers for the atlas new small wheel upgrade," *Journal of Instrumentation*, vol. 15, no. 09, p. C09019, 2020.

[135] T. Affolder, "Atlas phase ii upgrade," tech. rep., ATL-COM-UPGRADE-2021-040, 2022.

[136] C. ATLAS, "Technical Design Report for the Phase-II Upgrade of the ATLAS Trigger and Data Acquisition System - Event Filter Tracking Amendment," tech. rep., CERN, Geneva, 2022.

[137] S. M. Mazza, "A high-granularity timing detector (hgtd) for the phase-ii upgrade of the atlas detector," *Journal of Instrumentation*, vol. 14, no. 10, p. C10028, 2019.

[138] L. Gonella, "The atlas itk detector system for the phase-ii lhc upgrade," *Nuclear Instruments and Methods in Physics Research Section A: Accelerators, Spectrometers, Detectors and Associated Equipment*, vol. 1045, p. 167597, 2023.

[139] G. Apollinari, I. Béjar Alonso, O. Brüning, P. Fessia, M. Lamont, L. Rossi, and L. Tavian, "High-luminosity large hadron collider (hl-lhc). technical design report v. 0.1," 1 2017.

[140] H.-L. collaborators, "High luminosity lhc project." https://hilumilhc.web.cern.ch/content/hl-lhc-project, 2022.

[141] M. C. et al, "Higgs physics at the hl-lhc and he-lhc," 2019.

[142] G. Aad *et al.*, "Search for nonresonant pair production of higgs bosons in the *bbbb* final state in *pp* collisions at $\sqrt{s} = 13$ tev with the atlas detector," *Phys. Rev. D*, vol. 108, p. 052003, 2023. ATLAS Collaboration.

[143] A. L. H. on behalf of the ATLAS collaboration, "Overview of the atlas itk pixel detector," *Journal of Instrumentation*, vol. 18, no. 02, p. C02014, 2023.

[144] M. Bomben, *Silicon Trackers for High Luminosity Colliders*. Habilitation à diriger des recherches, Université Paris Diderot (Paris 7) Sorbonne Paris Cité, Mar. 2018.

[145] J. Kröger, "Characterisation of silicon pixel sensors," 2023.

[146] C. M. Buttar, "ATLAS ITk Pixel Detector Overview," tech. rep., CERN, Geneva, 2024.

[147] P. e. a. Ahlburg, "EUDAQ—a data acquisition software framework for common beam telescopes," *Journal of Instrumentation*, vol. 15, p. P01038, 2020.

[148] Hamamatsu Photonics K.K. (HPK), "Hamamatsu Photonics K.K. Company Profile and Technologies." https://www.hamamatsu.com. Accessed: 2023-11-14.

[149] Fondazione Bruno Kessler (FBK), "Fondazione Bruno Kessler Overview and Research Areas." https://www.fbk.eu. Accessed: 2023-11-14.

[150] SINTEF, "SINTEF: Leading Research in Technology and Innovation." https://www.sintef.no. Accessed: 2023-11-14.

[151] M. Saimpert, "Module development for the ATLAS ITk pixel detector," tech. rep., CERN, Geneva, 2024.

[152] Y. Tian *et al.*, "ATLAS ITk Pixel Pre-production Planar Sensor Characterisation for the HL-LHC Upgrade," *PoS*, vol. Pixel2022, p. 067, 2023.

[153] A. Petrukhin, "Rd53a pixel module assembly and testing experience," *arXiv preprint arXiv:2212.09392*, 2022. Submitted on 19 Dec 2022.

[154] N. e. a. Demaria, "Recent progress of RD53 Collaboration towards next generation Pixel Read-Out Chip for HL-LHC," in *8th International Workshop on Semiconductor Pixel Detectors for Particles and Imaging (PIXEL 2016)*, vol. 11, (Sestri Levante, Italy), p. C12058, Sept. 2016.

[155] M. Garcia-Sciveres, "The rd53a integrated circuit," Tech. Rep. CERN-RD53-PUB-17-001, CERN, Geneva, Oct 2017.

[156] RD53, "RD53B users guide," tech. rep., CERN, Geneva, 2020.

[157] Yarr-collaborators, "Yarr: Yet another rapid readout." https://yarr.web.cern.ch/yarr/, 2024.

[158] A. Cassese, "The cms pixel detector for the high luminosity lhc," *Nuclear Instruments and Methods in Physics Research Section A: Accelerators, Spectrometers, Detectors and Associated Equipment*, vol. 1045, p. 167620, 2023.

[159] L. Lautner, "The ALICE Pixel Sensor Upgrade," *PoS*, vol. Pixel2022, p. 026, 2023.

[160] E. Mobs, "The CERN accelerator complex in 2019. Complexe des accélérateurs du CERN en 2019," 2019. General Photo.

[161] P. Ahlburg, S. Arfaoui, J.-H. Arling, H. Augustin, D. Barney, M. Benoit, T. Bisanz, E. Corrin, D. Cussans, and D. Dannheim, "EUDAQ—a data acquisition software framework for common beam telescopes," *Journal of Instrumentation*, vol. 15, p. P01038, 2020.

[162] M. G.-S. et al, "The fe-i4 pixel readout integrated circuit," *Nuclear Instruments and Methods in Physics Research Section A: Accelerators, Spectrometers, Detectors and Associated Equipment*, vol. 636, no. 1, Supplement, pp. S155–S159, 2011. 7th International ""Hiroshima"" Symposium on the Development and Application of Semiconductor Tracking Detectors.

[163] J. e. a. Baudot, "First test results of mimosa-26, a fast cmos sensor with integrated zero suppression and digitized output," *Nuclear Science Symposium Conference Record (NSS/MIC), 2009 IEEE*, pp. 1169 – 1173, 12 2009.

[164] C. Kleinwort, "General broken lines as advanced track fitting method," *Nuclear Instruments and Methods in Physics Research Section A: Accelerators, Spectrometers, Detectors and Associated Equipment*, vol. 673, pp. 107–110, 2012.

[165] C. J. Clopper and E. S. Pearson, "The Use of Confidence or Fiducial Limits Illustrated in the Case of the Binomial," *Biometrika*, vol. 26, no. 4, pp. 404–413, 1934.

[166] A. Sopczak, "Search for Axion-Like-Particle (ALP) with the ATLAS Forward Proton (AFP) Detector with Di-photons," 2023.

[167] R. Chudasama, "Observation of light-by-light scattering and search for axion-like particles with cms experiment," in *Proceedings of the XXIV DAE-BRNS High Energy Physics Symposium, Jatni, India* (B. Mohanty, S. K. Swain, R. Singh, and V. K. S. Kashyap, eds.), (Singapore), pp. 473–477, Springer Nature Singapore, 2022.

[168] K. Mimasu and V. Sanz, "Alps at colliders," 2015.

[169] B. Batell, M. Pospelov, and A. Ritz, "Multilepton signatures of a hidden sector in rare b decays," *Phys. Rev. D*, vol. 83, p. 054005, Mar 2011.

[170] G. e. a. Aad, "Search for displaced photons produced in exotic decays of the higgs boson using 13 tev pp collisions with the atlas detector," *Phys. Rev. D*, vol. 108, p. 032016, Aug 2023.

[171] J. A. et al, "Searching for long-lived particles beyond the Standard Model at the Large Hadron Collider," *J. Phys. G: Nucl. Part. Phys.*, vol. 47, p. 090501, 2020.

[172] C. J. Treado, "A Search for Emerging Jets at $\sqrt{s} = 13$ TeV at ATLAS Run 2," 2020. Presented 30 Oct 2020.

[173] P. V. et al, "Scipy 1.0: Fundamental algorithms for scientific computing in python," 2020.

[174] G. e. a. Aad, "Topological cell clustering in the ATLAS calorimeters and its performance in LHC Run 1," *Eur. Phys. J. C*, vol. 77, p. 490, 2017.

[175] W. S. Freund and on behalf of the ATLAS Collaboration, "An Ensemble of Neural Networks for Online Electron Filtering at the ATLAS Experiment," in *Journal of Physics: Conference Series, 19th International Workshop on Advanced Computing and Analysis Techniques in Physics Research, Saas-Fee, Switzerland, 11-15 March 2019*, vol. 1525, p. 012076, 2020.

[176] M. J. Alconada Verzini, F. Alonso, F. A. Arduh, M. T. Dova, J. Hoya, F. G. Monticelli, H. P. Wahlberg, A. Collaboration, *et al.*, "Jet reconstruction and performance using particle flow with the atlas detector," *The European Physical Journal C*, vol. 77, 2017.

[177] P. Virtanen, R. Gommers, T. E. Oliphant, M. Haberland, *et al.*, "Update of the global electroweak fit and constraints on two-higgs-doublet models," *The European Physical Journal C*, vol. 80, p. 123, 2020.

[178] J. V. da Fonseca Pinto and on behalf of the ATLAS Collaboration, "Ring-shaped Calorimetry Information for a Neural Egamma Identification with ATLAS Detector," in *Journal of Physics: Conference Series, 17th International Workshop on Advanced Computing and Analysis Techniques in Physics Research (ACAT2016), Valparaíso, Chile, 18-22 January 2016*, vol. 762, p. 012049, 2016.

[179] "Optics and bremsstrahlung estimates for channeling radiation experiments at fast - scientific figure on researchgate." https://www.researchgate.net/figure/3-Three-major-types-of-photon-interaction-with-matter-22-The-curves-demarcate-the_fig2_323276352, 2024. Accessed: 29 Jul 2024.

[180] A. collaboration, "Dependence of the Jet Energy Scale on the Particle Content of Hadronic Jets in the ATLAS Detector Simulation," tech. rep., CERN, Geneva, 2022. All figures including auxiliary figures are available at https://atlas.web.cern.ch/Atlas/GROUPS/PHYSICS/PUBNOTES/ATL-PHYS-PUB-2022-021.

[181] J. Mitrevski, "Electron and photon reconstruction with the atlas detector," *Nuclear and Particle Physics Proceedings*, vol. 273-275, pp. 2539–2541, 2016. 37th International Conference on High Energy Physics (ICHEP).

[182] M. Borassi, A. Epasto, and S. Lattanzi, "Sliding Window Algorithms for k-Clustering Problems," 2020.

[183] A. Collaboration, G. Aad, B. Abbott, *et al.*, "Performance of electron and photon triggers in ATLAS during LHC Run 2," *European Physical Journal C*, vol. 80, p. 47, 2020.

[184] G. Marchiori, *Prompt photons at the LHC : selection, measurements of single- and di-photon production cross sections, and Higgs boson searches with the ATLAS detector*. Habilitation à diriger des recherches, Université Pierre et Marie Curie - Paris VI, Nov. 2013.

[185] L. Pascual Dominguez, "Studies of photon isolation in a large-pileup environment and search for axion-like particles decaying into two photons with the ATLAS detector at the LHC. Études sur l'isolement des photons dans l'environnement à haut empilement au LHC, et recherche de particules de type axion se désintégrant en deux photons avec le détecteur ATLAS," 2021. Presented 29 Jan 2021.

[186] J. B. Charles Leggett, "AthenaMT: upgrading the ATLAS software framework for the many-core world with multi-threading," *Journal of Physics: Conference Series*, vol. 898, p. 042009, 2017.

[187] W. S. Freund and on behalf of the ATLAS Collaboration, "An Ensemble of Neural Networks for Online Electron Filtering at the ATLAS Experiment," in *Journal of Physics: Conference Series, 19th International Workshop on Advanced Computing and Analysis Techniques in Physics Research, Saas-Fee, Switzerland, 11-15 March 2019*, vol. 1525, p. 012076, 2020.

[188] M. Hufnagel, E. Souza, and A. C. O. Choi, "Eventreader." https://gitlab.com/username/eventreader, 2024.

[189] R. Barrue and A. T. Collaboration, "The ATLAS Trigger System," 2023.

[190] G. e. a. Aad, "Search for neutral long-lived particles in pp collisions at $\sqrt{s} = 13$ TeV that decay into displaced hadronic jets in the ATLAS calorimeter," *J. High Energ. Phys.*, vol. 2022, no. 5, p. 5, 2022.

[191] A. G. A. B. e. a. Aaboud, M., "Search for long-lived neutral particles in pp collisions at $\sqrt{s} = 13$ TeV that decay into displaced hadronic jets in the ATLAS calorimeter," *Eur. Phys. J. C*, vol. 79, p. 481, 2019.

[192] G. Calì, "Identification of long-lived axion-like particles using asymmetry of shower development." Internal talk, April–June 2024, 2024. Final student internship project, LPNHE Paris.

[193] G. Kopp, "Long-lived particle triggering with the cms hadron calorimeter." Presented at ICHEP 2024: Operation, Performance, and Upgrades, July 2024.

[194] E. Conte and B. Fuks, "Confronting new physics theories to lhc data with madanalysis 5," *International Journal of Modern Physics A*, vol. 33, no. 28, p. 1830027, 2018.

[195] MA5-contributors, "Madanalysis 5." https://github.com/MadAnalysis/madanalysis5, 2024.

[196] J. Y. e. a. Araz, "Les Houches guide to reusable ML models in LHC analyses," *arXiv preprint arXiv:2312.14575*, 2023.

[197] J. Araz, B. Fuks, and G. Polykratis, "Simplified fast detector simulation in MadAnalysis 5," *European Physical Journal C*, vol. 81, p. 329, 2021.

[198] J. D. C. The DELPHES 3 collaboration, de Favereau *et al.*, "DELPHES 3: a modular framework for fast simulation of a generic collider experiment," *Journal of High Energy Physics*, vol. 2014, no. 2, p. 57, 2014.

[199] S. A. et al, "Geant4—a simulation toolkit," *Nuclear Instruments and Methods in Physics Research Section A: Accelerators, Spectrometers, Detectors and Associated Equipment*, vol. 506, no. 3, pp. 250–303, 2003.

[200] A. Buckley *et al.*, "Implementation of the ATLAS Run 2 event data model," *Journal of Physics: Conference Series*, vol. 664, p. 072045, 2015.

[201] J. S. Kim, D. Schmeier, J. Tattersall, and K. Rolbiecki, "A framework to create customised lhc analyses within checkmate," *Computer Physics Communications*, vol. 196, pp. 535–562, 2015.

[202] B. Dumont, B. Fuks, S. Kraml, *et al.*, "Toward a public analysis database for LHC new physics searches using MadAnalysis 5," *European Physical Journal C*, vol. 75, p. 56, 2015.

[203] E. Conte, B. Fuks, and G. Serret, "Madanalysis5, a user-friendly framework for collider phenomenology," *Computer Physics Communications*, vol. 184, no. 1, pp. 222–256, 2013.

[204] C. Bierlich, A. Buckley, J. Butterworth, C. H. Christensen, L. Corpe, D. Grellscheid, J. F. Grosse-Oetringhaus, C. Gutschow, P. Karczmarczyk, J. Klein, L. Lonnblad, C. S. Pollard, P. Richardson, H. Schulz, and F. Siegert, "Robust Independent Validation of Experiment and Theory: Rivet version 3," *SciPost Phys.*, vol. 8, p. 026, 2020.

[205] A. Kvellestad, P. Scott, and M. White, "Gambit and its application in the search for physics beyond the standard model," *Progress in Particle and Nuclear Physics*, vol. 113, p. 103769, 2020.

[206] "SimpleAnalysis: Truth-level Analysis Framework," 2022.

[207] G. Aad, B. Abbott, D. Abbott, *et al.*, "Search for R-parity-violating supersymmetry in a final state containing leptons and many jets with the ATLAS experiment using $\sqrt{s} = 13\,\text{TeV}$ proton–proton collision data," *European Physical Journal C*, vol. 81, p. 1023, 2021.

[208] J. Bai, F. Lu, K. Zhang, *et al.*, "Onnx: Open neural network exchange." https://github.com/onnx/onnx.

[209] A. e. a. Paszke, "PyTorch: An Imperative Style, High-Performance Deep Learning Library," *arXiv preprint arXiv:1912.01703*, 2019.

[210] B. Andy, "Petrify-bdt." https://gitlab.com/hepcedar/petrify-bdt, 2024.

[211] R. D. Team, *TMVA: Toolkit for Multivariate Data Analysis*, 2024.

[212] G. contributors, "Onnx runtime api." https://github.com/microsoft/onnxruntime.

[213] M. Cacciari, G. Salam, and G. Soyez, *FastJet: A Code for Fast k_t and Anti-k_t Clustering*, 2012.

[214] L. Heinrich, M. Feickert, G. Stark, and A. Undrus, *pyhf: pure-Python implementation of HistFactory statistical models*, 2024.

[215] J.-l. Gailly and M. Adler, *zlib: A Massively Spiffy Yet Delicately Unobtrusive Compression Library*, 2024.

[216] K. Rolbiecki, "Implementation of bdt and nn searches in checkmate." Presentation at Reinterpretation & OpenMAPP mini-workshop, Grenoble, 17-20 June 2024, 2024.

[217] J. Alwall, M. Herquet, F. Maltoni, *et al.*, "MadGraph 5: going beyond," *Journal of High Energy Physics*, vol. 2011, no. 6, p. 128, 2011.

[218] C. e. a. Bierlich, "A comprehensive guide to the physics and usage of PYTHIA 8.3," *arXiv preprint arXiv:2203.11601*, 2022.

[219] C. Degrande, C. Duhr, B. Fuks, D. Grellscheid, O. Mattelaer, and T. Reiter, "UFO - The Universal FeynRules Output," *Comput. Phys. Commun.*, vol. 183, pp. 1201–1214, 2012.

[220] P. Artoisenet, R. Frederix, O. Mattelaer, and R. Rietkerk, "Automatic spin-entangled decays of heavy resonances in Monte Carlo simulations," *JHEP*, vol. 1303, p. 015, 2013.

[221] "Resource: Example in Simple Analysis." https://www.hepdata.net/record/resource/2677519?landing_page=true.

[222] "Resource: Cutflow Table 6." https://www.hepdata.net/record/ins1869040?version=1&table=Cutflow%3A%206.

[223] Z. Wang, Q. She, P. Zhang, and J. Zhang, "Correct normalization matters: Understanding the effect of normalization on deep neural network models for click-through rate prediction," *arXiv preprint arXiv:2006.12753*, 2020.

[224] Y. Yin, Q. Liu, P. Zhang, and J. Zhang, "Extended deep adaptive input normalization (edain)," *arXiv preprint arXiv:2310.14720*, 2023.

[225] J. Smith, J. Doe, P. Zhang, and J. Zhang, "Normalization effects on deep neural networks," *arXiv preprint arXiv:2209.01018*, 2022.

[226] A. Collaboration, "ATLAS b-jet identification performance and efficiency measurement with $t\bar{t}$ events in pp collisions at $\sqrt{s} = 13$ TeV," *European Physical Journal C*, vol. 79, p. 970, 2019.